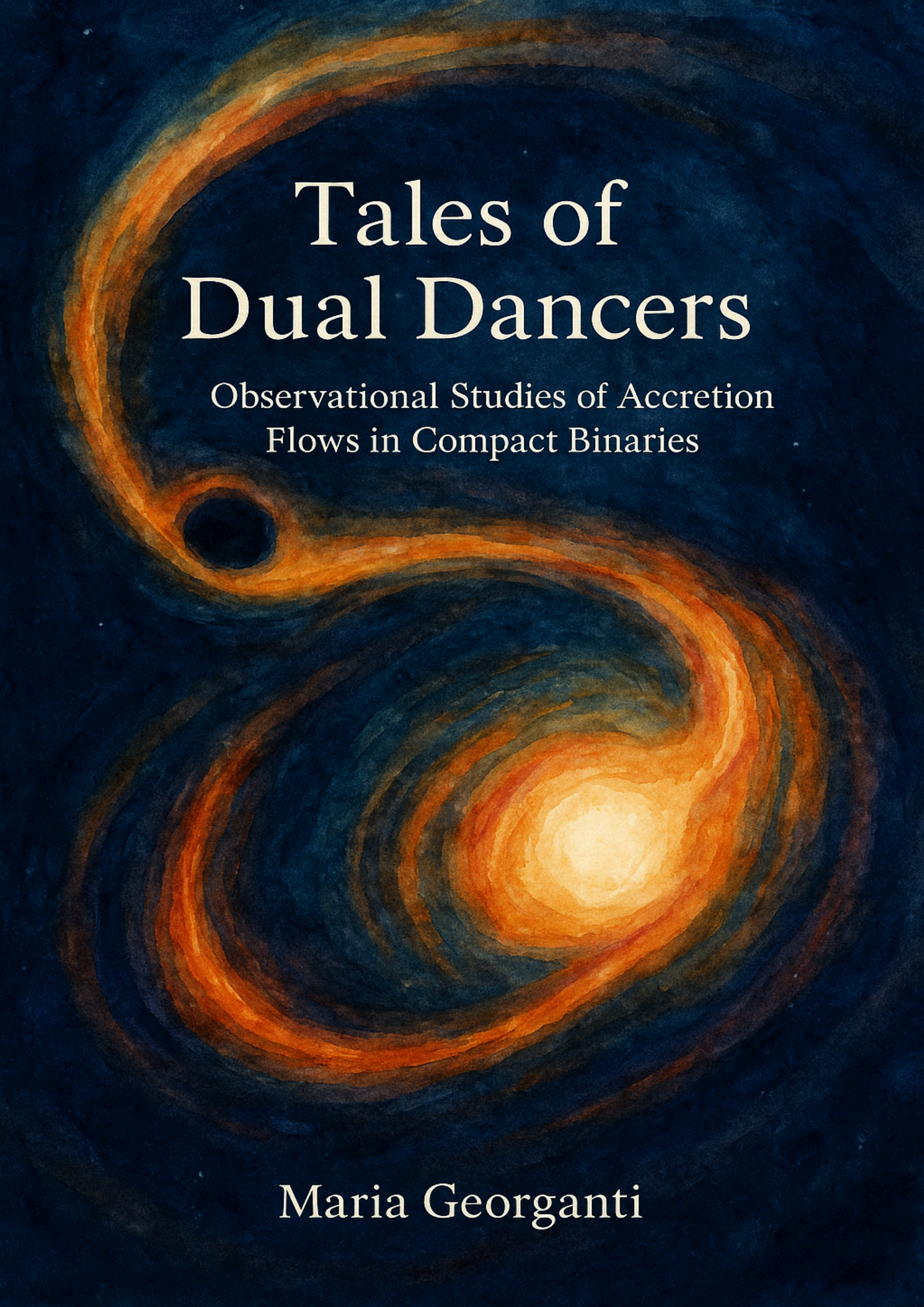

Tales of Dual Dancers

Observational Studies of Accretion Flows in Compact Binaries

Maria Georganti

UNIVERSITY OF SOUTHAMPTON

Faculty of Engineering and Physical Sciences
School of Physics and Astronomy

Tales of Dual Dancers: Observational Studies of Accretion Flows in Compact Binaries

by

Maria Georganti

MSc in Astronomy and Astrophysics

ORCiD: 0000-0002-3776-9652

A thesis for the degree of
Doctor of Philosophy

June 8, 2025

University of Southampton

Abstract

Faculty of Engineering and Physical Sciences
School of Physics and Astronomy

Doctor of Philosophy

Tales of Dual Dancers: Observational Studies of Accretion Flows in Compact Binaries

by Maria Georganti

This thesis presents an observational study of accreting compact binaries, whose radiation is emitted across the entire electromagnetic spectrum. Each wavelength probes a different binary component, providing insights into the physical processes at play. Ultraviolet (UV) emission, in particular, has been proven crucial in understanding the structure and dynamics of accretion discs, as well as tracing inflow and outflow processes. This work focuses on studying two spectacular objects: the dwarf nova WZ Sge and the black hole X-ray transient MAXI J1820+070, using primarily time-resolved observations from the Hubble Space Telescope (HST).

For WZ Sge, my research presents the first UV characterisation of the source during three distinct stages of its 2001 superoutburst. The system exhibits an unusual dip in its light curve, and a key focus of this study is to investigate whether this dip results from its transition to a magnetic propeller state. Instead of finding evidence of magnetic propeller signatures, this work proposes the existence of a veiling curtain − material along the line-of-sight − surrounding the system. The properties of the material are characterised by a moderate-temperature, high-density, low-velocity absorbing profile. This result is of high importance as it highlights a previously unknown physical component, always present around the source.

For MAXI J1820+070, I present the first multi-epoch UV spectral and temporal characterisation during its outburst, covering both hard and soft states. Using HST and complementary AstroSat observations, this work constitutes a unique opportunity to define the UV response to luminosity changes and state transitions in black hole binaries. It is shown how the UV spectrum and the stochastic and aperiodic variability change among these states. The HST spectra provide meaningful insights about the physical conditions of the accretion disc and the possible emergence of outflows. This research also quantifies the reprocessing efficiency in the outer disc using irradiated disc models. These avenues are explored due to the low extinction to the system, which is also determined.

The findings of this thesis significantly advance our understanding of accreting compact binaries. The discovery of the veiling curtain in WZ Sge opens new routes for investigating similar features in other systems, while the detailed UV characterisation of MAXI J1820+070 enhances our understanding of state transitions and disc dynamics in black hole binaries. These results signify the importance of UV observations in unraveling the complex processes occurring in these systems.

Contents

List of Figures

List of Tables

Declaration of Authorship

I declare that this thesis and the work presented in it is my own and has been generated by me as the result of my own original research.

I confirm that:

1. This work was done wholly or mainly while in candidature for a research degree at this University;
2. Where any part of this thesis has previously been submitted for a degree or any other qualification at this University or any other institution, this has been clearly stated;
3. Where I have consulted the published work of others, this is always clearly attributed;
4. Where I have quoted from the work of others, the source is always given. With the exception of such quotations, this thesis is entirely my own work;
5. I have acknowledged all main sources of help;
6. Where the thesis is based on work done by myself jointly with others, I have made clear exactly what was done by others and what I have contributed myself;
7. The second chapter of my thesis has been published on:
   Georganti M., Knigge C., Castro-Segura N., Long K.S., "Plateaus, dips, and rebrightenings during the outbursts of WZ Sge: no magnetic propeller, but a veiling curtain", 2022, MNRAS, 511, 4, 5385

   The third and fourth chapters are based on an already submitted work:
   Georganti M., Knigge C., Castro-Segura N., Long K.S., Dewangan G.C., Banerjee S., Hynes R.I., Gandhi P., Altamirano D., Patterson J., Zurek D.R., "Ultraviolet spectroscopy of the low-mass X-ray binary MAXI J1820+070 before, during and after a state transition"

Signed:..... Date:.....

Acknowledgements

I would like to take this opportunity to express my deepest gratitude to those who have supported, motivated, and guided me throughout my academic career and during the process of writing this thesis.

First and foremost, I am extremely thankful to my supervisor, Christian Knigge, for his invaluable guidance, insightful conversations and unwavering support. His scientific expertise and encouragement have been instrumental in enhancing my critical thinking and shaping both my research journey and academic growth. Christian, thank you for mentoring me. You inspired me like no other. I will always cherish your lessons and carry them beyond the world of academia.

I also acknowledge my collaborator Knox Long for his constructive conversations and guidance on my research. His feedback and insights played a crucial role in challenging me to become a better researcher. Furthermore, I would like to thank the members of the viva committee, Deanne Coppejans and Tony Bird, for the stimulating discussion during my viva and their constructive comments that helped improve my thesis.

While my time at the University of Southampton may be coming to an end, I am grateful to have been a part of the Astronomy group. Many thanks to my colleagues for our discussions, assistance, and the enjoyable moments we shared.

Perhaps the real treasure was the friends we made along the way. Here, I would like to thank my friends in Southampton that kept me alive, supported me and shaped my personality over the last years. Special thanks to Andrés, Noel, Cory, Giorgos, Shenli, Josep, Arianna, Shubhani. A particular thanks to Hao − beyond being a great office mate, he became one of my best friends.

Beyond my friends in England, I would also like to thank my friends from Greece. Maria V, Olympia, Maria M., Eirini, Chara, Panagiotis have always supported me and spent time with me, making the distance feel smaller. A special shout-out to Eleftheria and Fey − our journey together, your friendship, from studying physics to planning for the future, has been always in my heart. I would not be where I am without you.

I could not close this section without mentioning my friend and partner in life/crime, Jakub. From being one of my good friends over the years to becoming an irreplaceable member of my life, you have been my source of support and love. Thank you for all the moments we have shared and continue to live together. Dziękuję, że jesteś sobą.

Τέλος, ένα μεγάλο ευχαριστώ στην οικογένειά μου για την αγάπη και την στήριξή τους. Δεν θα μπορούσα να κάνω αυτό το ταξίδι χωρίς αυτούς αν δεν στήριζαν τις αποφάσεις μου. Σας ευχαριστώ που μου δώσατε την ευκαρία να ακολουθήσω το όνειρό μου.

Στις γιαγιάδες μου Μαρία και Ευαγγελία

To my family, and to the people that became family along the way

Part I

Literature review

Chapter 1

Introduction

"So once you do know what the question actually is, you'll know what the answer means"

-Douglas Adams, The Hitchhiker's Guide to the Galaxy

1.1 The path to the stellar graveyard

It is noted that the main sources of reference for these sections, if not specified otherwise, are Salaris and Cassisi (2005), Peters and Hirschi (2013), Karakas and Lattanzio (2014).

Our trip begins at stellar nurseries, a name that describes high-density molecular clouds composed primarily from hydrogen (and helium). A cloud collapses under its own gravity on the *free-fall timescale* ($t_{ff} \propto \rho^{-1/2}$) when its mass has reached a critical value. At this point, hydrostatic equilibrium breaks down as the gas pressure is no longer able to support the cloud against gravity. The mass needed for the immediate collapse is known as the *Jeans mass*[1]. As gravity takes over, the cloud most likely will break into smaller pieces − a process called *fragmentation*. Each of these fragments will start to shrink and contract by releasing gravitational energy, and their temperature and density will increase. This process eventually leads to hydrogen (^{1}H) fusing into helium (^{4}He) in the core of a fragment. The onset of the thermonuclear reactions signals the fragment's arrival as a *star* on the *Zero-Age Main Sequence* (ZAMS) or for short here, *Main Sequence* (MS). Stars remain on the MS until they run out of their hydrogen fuel in their cores. This occurs over the *nuclear timescale* (expressed in years for convenience), which is defined as

$$t_{nucl} = \frac{0.007 M_{core} c^2}{L}, \tag{1.1}$$

where M_{core} is the core's mass of the star at MS, L its luminosity, and c the speed of light.

[1]The Jeans mass is often recognised as the *Jeans criterion* or *instability* and it is proportional to powers of the temperature and density of the cloud as $M_J \propto T^{3/2}\rho^{-1/2}$.

The predominant factors, which determine the evolution of a *single* star, are its *mass* and, as a secondary effect, its *metallicity*. Stellar evolution modelling, though, is hampered by several uncertainties and approximations regarding key physical processes like heat transport, mixing, mass loss and the impact of the exact stellar composition. Therefore, theoretically predicted evolutionary tracks are somewhat model dependent. This is important to note here as, for example, the mass ranges mentioned in the following sections, are only rough estimates and can vary between different models. This section is devoted to present both the standard evolutionary trajectories of low-/intermediate-mass stars ($M_{init} \leq 8 - 10M_{\odot}$), as well as the one of massive ones ($M_{init} \geq 10M_{\odot}$), as a prelude to the discussion of binary star evolution later in this chapter. As we are going to see, low- and intermediate-mass stars (Section 1.1.1), in most cases, leave behind a *white dwarf* (WD), whereas massive stars (Section 1.1.2) end their lives through a supernova (SN) explosion that results in the formation of a *neutron star* (NS) or a *black hole* (BH). In order to be consistent throughout my description, I am going to employ the mass ranges given by Karakas and Lattanzio (2014) – the respective graph of plausible stellar trajectories of the employed masses is shown below in Figure 1.1. The formed compact objects, remnants of stellar journeys, will constitute one of the stellar components in my study of interacting binaries.

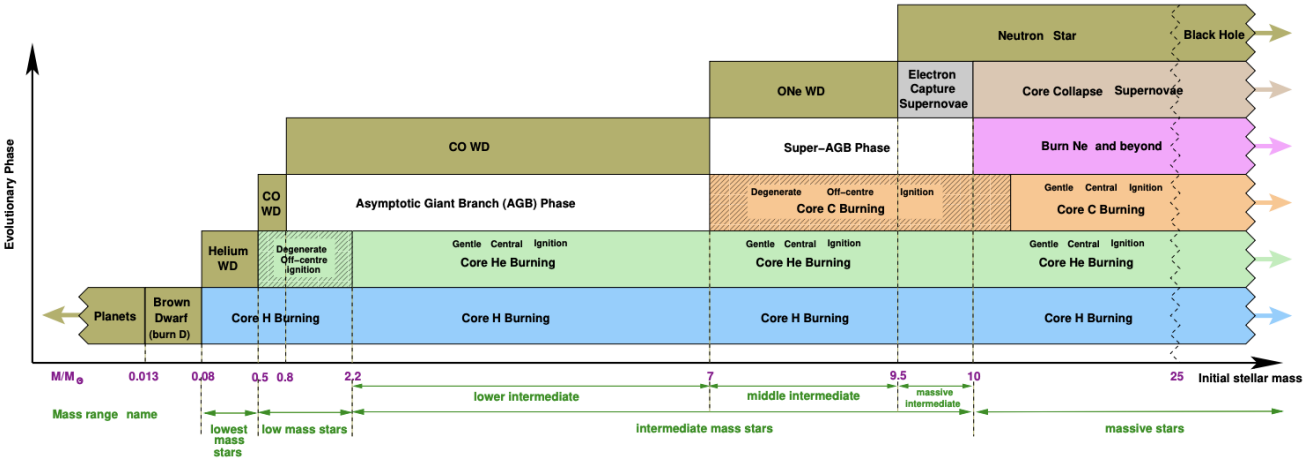

FIGURE 1.1: Basic illustrative chart that demonstrates the evolutionary stages of *solar-metallicity* stars with respect to their *initial* mass. The mass range which is employed at the current illustration is between $0.08M_{\odot}$ – star's minimum needed mass to ignite hydrogen at its core – to approximately $30M_{\odot}$. Beyond that mass, the stars are susceptible to significant mass loss through stellar outflows with characteristic examples the short-lived Wolf-Rayet stars and/or the luminous blue variables. However, it is noteworthy to mention that the showcased mass ranges are only estimates as their calculation is dependent on the input physics ingredients of the performed modelling such as metallicity, mass loss, convection or mixing processes. Figure taken from Karakas and Lattanzio (2014).

1.1.1 Low and intermediate-mass stars

Low and intermediate-mass stars represent the majority of the stellar population (e.g. Salpeter, 1955; Kroupa, 2001), and their longevity offers us a unique opportunity to study evolution processes in different stages of their lives. The MS is a period of stability for these objects, as they

spend most of their MS lifetime without significantly changing their physical properties such as their temperature, radius or luminosity. The Hertzsprung-Russell (HR) diagram, perhaps the most popular diagram in astronomy, sketches the evolutionary tracks of stars of different mass, in which the luminosity of a star is plotted against its surface temperature (Figure 1.2). The low mass[2] stars are characterised by different internal structures based on their initial mass. In particular, stars between $0.075M_\odot < M_{init} < 0.35M_\odot$ are *fully convective* whereas stars in the range of $0.35M_\odot < M_{init} < 1.5M_\odot$ are described by a *radiative* core and a *convective* envelope during their time on the MS. In both cases, the proton-proton (p-p) chain mechanism is responsible for the ^{1}H fusion onto ^{4}He. On the other hand, the increased core temperatures in higher mass stars cause the CNO cycle to dominate for masses $\geq 1.5M_\odot$. The CNO cycle is an alternative hydrogen-to-helium fusion mechanism, that uses the carbon, nitrogen, oxygen isotopes as catalysts. The temperature dependence of the CNO cycle results in an enhanced energy production rate as the temperature in the core rises. The structure of these stars differs from the structure of their lower-mass counterparts and is described by a *convective* core and a *radiative* envelope.

The stars will remain on the MS until their hydrogen is exhausted in their cores. This may be the endpoint, for example, of stars between $0.075M_\odot \leq M_{init} \leq 0.5M_\odot$, where they finish their lives as He WDs[3]. Somewhat higher mass stars, however, let's say roughly up to $7M_\odot$, will continue to evolve until a CO WD is created. In these objects, the newly-formed ^{4}He core is initially inert − there is no hydrogen fuel to burn and the core is not hot enough to commence the fusion of helium into carbon (^{12}C). Radiation pressure therefore cannot support the core to act against gravity, so the core *contracts*, causing the central temperature and pressure to rise. Still, at this stage, nuclear fusion takes places only in a shell around the core, in which ^{1}H fuses to ^{4}He (H-shell burning). Radiation reaches the outer layers of the envelope, causing it to expand. The star therefore becomes bigger and redder (as its temperature decreases) − it has reached the *red giant branch* (RGB).

Meanwhile, the core continues to shrink until it reaches the critical temperature, of the order of $\sim 10^8$K, required to ignite ^{4}He. In stars of $0.5M_\odot \leq M_{init} \leq 2.2M_\odot$, an *electron-degenerate*[4] core

[2]The lowest mass bound corresponds to the minimum mass that permits nuclear fusion. Below that mass, we find sub-stellar−brown dwarf objects. The most recent determination of the hydrogen-burning limit is by Chabrier et al. (2023).

[3]Helium white dwarfs (He WDs) are only observed as part of binary systems (first observed by Marsh et al., 1995). Even though modelling of single star progenitors in the range of $0.075M_\odot \leq M_{init} \leq 0.5M_\odot$ forms He WDs at the end of their lives, observationally, this is not so obvious. The life span of these objects exceeds the Hubble time even though there is evidence that He WDs can be found in metal-rich environments (Kilic et al., 2007). Undoubtedly, metallicity influences the conditions of their surrounding regions as stars evolve.

[4]Electron degeneracy pressure is exerted in specific conditions of high densities or low temperatures (Fowler, 1926). At high densities, as the ones created in stellar cores, electrons are obliged to occupy different bound states of higher and higher energy levels since otherwise Pauli's exclusion principle is violated. Pauli's principle states that two electrons cannot occupy the same bound state. The electrons have high kinetic energy (as a result of their compression and based on Heisenberg's uncertainty principle) and exert great pressure. The pressure is dependent only on the particle density and not the temperature (contrary to the scaling for gas pressure, for example). For the case where the electrons are relativistic, the electron degeneracy pressure it is given by $P_e \propto \rho_e^{4/3}$. This pressure can act against gravitational collapse in stars up to $1.4M_\odot$. This limit defines the maximum white dwarf mass, known as the Chandrasekhar limit. The same principles are extended to all fermions − nucleons (protons, neutrons) and the rest of the leptons (e.g. neutrinos), particles that are generated at the cores of massive stars (as it will be mentioned in Section 1.1.2.)

is formed, in which electron degeneracy pressure provides the support against gravity. The core starts *fusing* ^{4}He into ^{12}C through the triple-alpha process, but the release of the generated energy, and the steep rise of the core temperature, lead to a "runaway effect", accelerating the production rate. These cascade processes cause ^{4}He ignition to turn on *rapidly*, in the so-called *helium flash*. In the HR diagram, this marks the peak of the RGB. The helium flash constitutes the beginning of ^{4}He fusion in the star's core. It is worthwhile to mention that the helium flash is not apparent at the star's surface, as the released energy is absorbed by the enclosing layers. Stars with masses $\geq 2.2 M_\odot$ do not develop degenerate conditions, so they do not undergo a helium flash and instead ignite ^{4}He gradually. The period that the stars burn ^{4}He stably (into ^{12}C) in their cores is called the *horizontal branch* (HB).

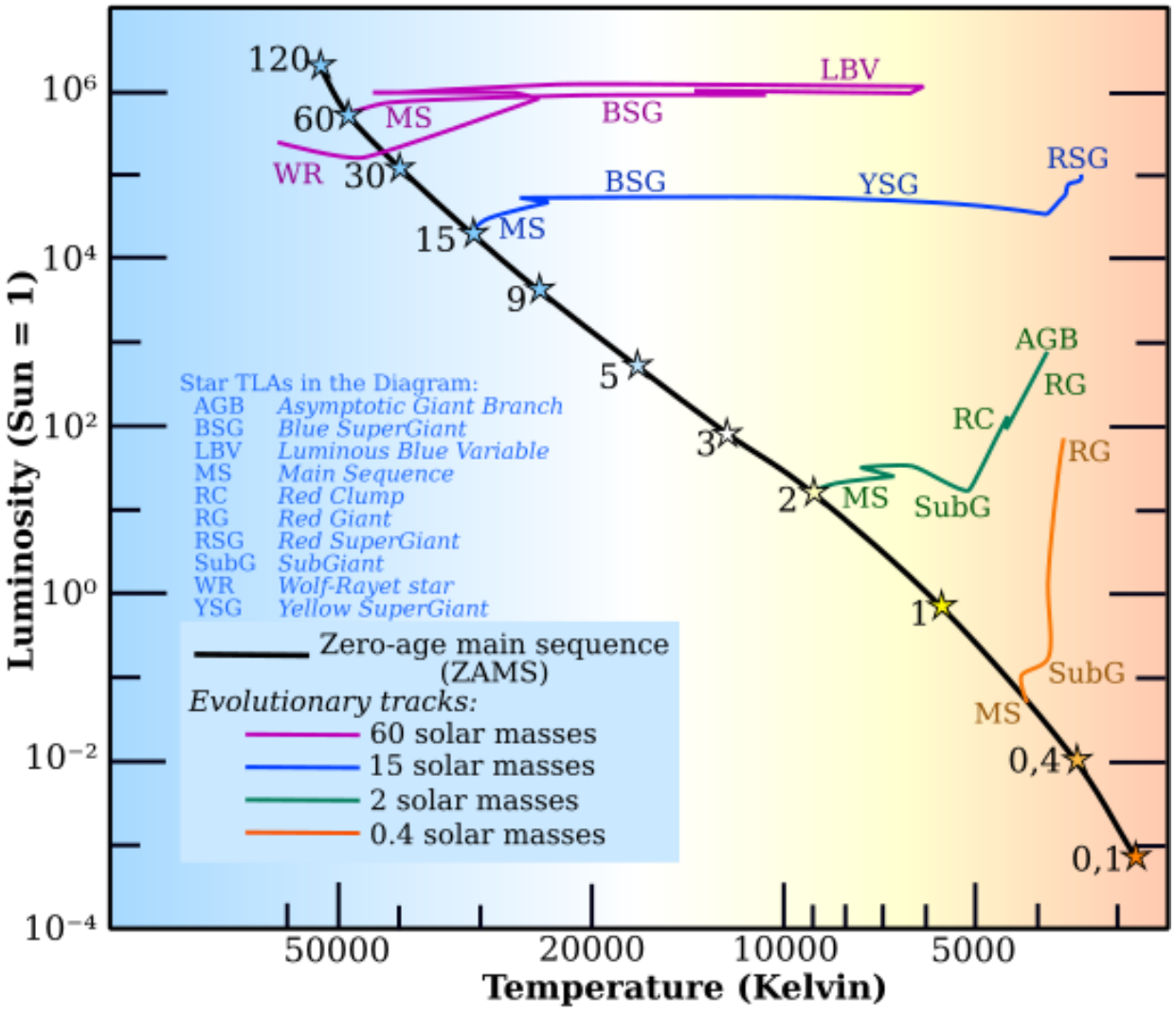

FIGURE 1.2: The stellar evolutionary paths of different mass stars can be illustrated through a Hertzsprung-Russell (HR) diagram, like the one seen above. Here, the luminosity of a star is plotted against its temperature. The provided HR diagram showcases characteristic evolutionary tracks of $0.4 M_\odot$, $2 M_\odot$, $15 M_\odot$, $60 M_\odot$. The different stages have been named along the track while a legend is already provided with the different abbreviations. Figure taken from Wikipedia Commons.

A similar pattern will be followed as the star climbs from the HB up the *asymptotic giant branch* (AGB). A star in this phase has an inert ^{12}C core (a small admixture of oxygen, ^{16}O, is also created in the core through α-capture i.e. carbon's reaction with the remaining ^{4}He-nuclei), surrounded by an inner He-burning and an outer H-burning shell. The shell-burning causes the star to expand and cool, so it moves back to the top right of the HR diagram, towards lower temperature and higher luminosity. The AGB is a quite short-lived phase and is characterised by strong mass loss. During the AGB, the star ejects most of its envelope to form a *planetary nebula*, leaving behind only the dense, degenerate CO core. This nearly-formed CO WD slowly cools down and becomes dimmer and dimmer. The ejected layers carry heavy elements − the result of mixing processes at the later stages of the star's life (e.g. via slow *n*-capture process aka s-process) − that enhances the nucleosynthesis fraction of its environment.

A fraction of intermediate-mass stars, usually of $M_{init} \geq 7 - 10 M_{\odot}$, will ignite ^{12}C at their degenerate cores. These stars will eventually reach the *super-AGB* stage. Here, the star's structure consists of a degenerate ONe core, surrounded by an envelope of ^{12}C,^{4} He,^{1} H burning shells. They eventually end their lives either as ONe WDs − if they lose their envelopes before their core reaches the Chandrasekhar limit (i.e. $M_{ch} = 1.4 M_{\odot}$; Karakas and Lattanzio, 2014) or as low-mass NSs − through the *electron-capture supernova* (ECSN) formation channel (e.g. Nomoto, 1984, 1987; Jones et al., 2013; Leung et al., 2020). The details of these channels and the percentage of intermediate-mass stars that actually lead to CO/ONe WDs or ECSNe are still uncertain, as they depend on the input physics and the detailed implementation of various complex processes (e.g. thermal pulsations, mixing, composition).

1.1.2 High-mass stars

Massive (early-type, young O/B) stars, despite their rarity (Kroupa, 2001) and short life, influence the dynamics and evolution of their surrounding regions and, in general, their host galaxies. They enrich their environments and constitute sources of stellar feedback and nucleosynthesis. This happens either through mass loss (stellar winds) − cases of Wolf-Rayet (WR) stars or luminous blue variables (LBVs) that they lose their outer layers quite early in their lives − or SN explosions.

Unlike their low-mass counterparts, though, massive stars are described by a *convective* core and a *radiative* envelope. After the H-depletion of the core during the MS phase, they become *red supergiants* (RSGs). In this stage, similar to the one sketched in Section 1.1.1, fusion takes place only in an H-burning layer, surrounding the inert ^{4}He core. As the core contracts and heats up, the envelope expands and cools down. Eventually, conditions in the core reach the point where the fusion of ^{4}He into ^{12}C, through the triple-alpha process, is ignited. These stars then evolve to the *blue supergiant* (BSG) branch. In the subsequent burning stages, the same pattern continues as heavier and heavier elements are ignited and typically burn more and more rapidly. Throughout these burning cycles, the outer layers expand (RSG phase) and contract (BSG phase), creating back

and forth tracks at the HR diagram. This is the case, for example, for stars $\geq 15M_{\odot}$, as can be seen in Figure 1.2.

After all of the available fuel for fusion reactions is exhausted, the final state for such a star is an inert iron-nickel (^{56}Fe/^{56}Ni) core, surrounded by thin burning shells of ^{28}Si, ^{20}Ne, ^{16}O, ^{12}C, ^{4}He and ^{1}H (multiple shell-burning). The fusion of elements heavier than ^{56}Fe requires energy rather than releasing it, and therefore ^{56}Fe-fusion extracts energy from the system. The degenerate core soon enough becomes unstable and contracts $-$ if it exceeds the Chandrasekhar limit, it must collapse. Beyond this point, the continuous core contraction increases both temperature and density. These conditions cause the disintegration of ^{56}Fe-nuclei to α-particles and unbound nucleons (electrons and protons). These nucleons quickly fuse to form neutrons and neutrinos through *e*-capture (neutronisation). The core is compressed until it reaches nuclear densities ($\rho \approx 10^{14}$gr cm^{-3}). At this stage, *neutrino losses* guide the imminent explosion (e.g. Janka et al., 2007; Janka, 2012) as the outer layers collapse and rebound off the newly-formed neutron core, resulting in a powerful explosion. This phenomenon is known as a *core-collapse supernova* (CCSN). The material once at the core of this massive star is ejected and travels outwards, thus enriching the interstellar medium (ISM) with heavy elements.

What happens to the core left behind during the SN explosion? Its contraction may be halted as *neutron degeneracy pressure* acts against gravity. If that is the case, a NS is formed. The maximum (non-rotating) NS mass that can be supported by neutron degeneracy pressure, known as the *Tolman-Oppenheimer-Volkoff limit* (TOV limit), is calculated between $2.2 - 2.9M_{\odot}$ (Kalogera and Baym, 1996); the most recent estimate is $M_{TOV} = 2.25^{+0.08}_{-0.07}M_{\odot}$ (Fan et al., 2024). A stellar remnant of this mass corresponds to a progenitor mass between $10M_{\odot}$ and $25M_{\odot}$. On the other hand, beyond the TOV limit, neutron degeneracy pressure cannot prevent further contraction, and the core collapses into a BH. This is the destiny of stars $\geq 25M_{\odot}$.

1.2 Cosmic pairs

The discussion so far has treated stars as individual objects. The majority though of the stellar population in the Milky Way is found in binaries and several times, in a configuration of more than two stellar components (e.g. Sana et al., 2012; Duchêne and Kraus, 2013; El-Badry et al., 2021). Nevertheless, these binary systems may interact or not. This depends on their orbital separation, the distance of their mass centres. If the separation between the two objects is quite large, then both companions evolve independently as they are in isolation (Section 1.1). These binaries are named *non-interacting* binaries. Conversely, *interacting* binaries are close systems where binarity affects the evolution of at least one of the two components. This thesis revolves around interacting binary systems, where one component is already a compact object, i.e. a WD, NS or a BH, and it is accreting material from a companion star. The evolution of binary systems in such a state typically involves common envelope phases, i.e. periods of dynamically unstable mass transfer, during which the whole system is embedded in the envelope of the more massive component.

This section is devoted to provide to the reader the appropriate ingredients regarding the different aspects of binary evolution and the formation of the systems in question.

1.2.1 The family of interacting compact binaries

No classification scheme is perfect, and the taxonomy of compact binaries is no exception. In particular, there is always a tension between making classifications granular enough to capture the diversity of the population, yet simple enough to reflect their underlying commonalities. Part of the issue is that classification schemes are no longer solely an observational (i.e. phenomenological) tool, but often involve the intersection of theory, observations and computational modelling. In the case of interacting compact binaries, the primary classification criteria are (i) the nature of the binary components (the accretor and the donor star) and (ii) the mechanisms responsible for driving mass transfer between them. Beyond these factors, observational properties such as the persistence (or not) of outburst episodes provides us additional information, allowing us to subdivide these systems as *persistent* or *transient* sources. In this section, I will describe the main categories of interacting compact binaries, starting with the distinction between different types of *accretors* (WD, NS or BH). More detailed classification based on additional characteristics are discussed further below, and a summary of the classification scheme is provided in Figure 1.3.

Accreting white dwarfs (AWDs) are interacting binaries where a WD primary accretes mass either from a Roche-lobe filling low-mass MS star, an evolved red giant or a (semi-)degenerate secondary (Hellier, 2001; Warner, 2003). The most common category of AWDs is the one called *cataclysmic variables* (CVs), semi-detached systems with short orbital periods, ranging from 80 minutes[5] to 2 days. In CVs, a *low-mass* ($\leq 1 M_\odot$) (near-)*MS star* fills its Roche lobe and transfers mass to the WD usually via an accretion disc. As we will see, orbital angular momentum losses, either through magnetic braking or gravitational radiation, drive the binary evolution in these systems. The majority of the CV population consists of *dwarf novae* (DNe), systems that show outbursts due to a thermal-viscous disc instability (e.g. Hameury et al., 2000; Buat-Menard et al., 2001; Lasota, 2001; Hameury, 2020). DNe are further divided in U Gem, Z Cam and SU UMa systems based on the morphology of their outburst light curve. I am going to discuss more in depth about their characteristics and their outburst manifestation in Chapter 2, a chapter that it is dedicated to WZ Sge (a subcategory of the SU UMa systems).

Apart from DNe, the non-magnetic CV classification tree includes the *nova-like variable* (NLs) systems. They are considered persistent sources, where the accretion rate is so high (of the order of $\dot{M}_{acc} \geq 10^{-9} M_\odot \ yr^{-1}$) that it suppresses the instability that causes the DN behaviour (sustenance of a hot, ionised disc). The presence of a magnetic field can significantly affect the accretion process and the environment around the WD. If present, two subgroups of CVs arise based on its strength, *polars* ($B_{WD} \geq 10^7 G$) and *intermediate polars* (IPs; $10^5 G \leq B_{WD} \leq 10^7 G$). The strong

[5]The smallest orbital period corresponds to the observed *period minimum* of CVs, marking the transition of a low-mass companion to a brown dwarf (e.g. Barker and Kolb, 2003; Knigge, 2006; Knigge et al., 2011).

magnetic field in polars will prevent the formation of an accretion disc whereas in IPs, a disc is created until the magnetosphere is reached. The distinction between magnetic systems and the role of the magnetic field will be discussed later in Section 1.5.

The other main AWD classes are the *symbiotic binaries*, the *supersoft X-ray sources* and the *AM CVn* systems. Symbiotic binaries are hosts to a WD (albeit there is a NS subclass − defining them as symbiotic X-ray binaries), orbiting an *evolved red giant*. They are typically wide, wind-fed systems (due to the size of the secondary), even though mass transfer through Roche lobe overflow has also been observed (Iben and Tutukov, 1996). Supersoft X-ray sources (SSS), now, are persistent systems where the WD accretes from a more massive MS star, i.e. $M_2 > M_{WD}$, through Roche lobe overflow. As we will see later in Section 1.2.3, systems with more massive secondaries are susceptible to unstable mass transfer. SSS are considered *thermal timescale mass transfer* systems. Stable nuclear burning onto the WD's surface may result in its *accretion-induced collapse* as it surpasses the Chandrasekhar limit ($M_{ch} \geq 1.4 M_{\odot}$). Both of these classes are considered plausible single-degenerate routes for being Type Ia SN progenitors (e.g. Mikołajewska and Shara, 2017; Liu et al., 2019). On the other hand, AM CVn are the most compact semi-detached systems − orbital periods between 5 to 65 minutes − where the WD orbits either WD or He-rich secondaries (e.g. Solheim, 2010; Ramsay et al., 2018). They may constitute strong low-frequency gravitational wave (GW) sources (e.g. Nelemans et al., 2004; Liu et al., 2022), some of which will be detectable from future missions such as the Laser Interferometer Space Antenna (LISA; Amaro-Seoane et al., 2023). Of particular note, I mention the *classical novae* (CNe) and the *recurrent novae* (RNe), both of which are known as *thermonuclear runaways*. In these systems, an explosion is triggered when inflowing hydrogen-rich material burns onto the WD's surface after reaching a critical mass.

In contrast, systems with NS and BH accretors, commonly known as *X-ray binaries* (XRBs), are divided into three main categories based on the mass of the companion star: the *High-mass X-ray binaries* (HMXBs), the *Intermediate-mass X-ray binaries* (IMXBs) and the *Low-mass X-ray binaries* (LMXBs). In HMXBs, luminous, early-type O/B donors ($M_2 \geq 8 - 10 M_{\odot}$) orbit most likely a NS primary − the absence of BH accretors in most cases is expected from binary evolution. The anatomy of these systems involves the NS either accreting mass during its periastron passage through the equatorial decretion disc of a Be-star, giving rise to *Be X-ray binaries* (BeXRBs) or it is wind-/disc-fed from its O/B supergiant companion, in systems called *Supergiant X-ray binaries* (SgXBs). The latter category contains the *Supergiant Fast X-ray Transients* (SFXTs), wind-fed systems that display short eruptions, in contrast to the persistent nature of the broader SgXB category (e.g. Pradhan et al., 2018). Note that only a few SgXB systems harbour BHs (e.g. Orosz et al., 2007, 2009, 2014; Miller-Jones et al., 2021; van den Heuvel, 2019, and references therein). Key examples include the BH SgXBs Cygnus X-1 (the first discovered BH X-ray source) and M33 X-7 (to date, the one containing the most massive BH accretor).

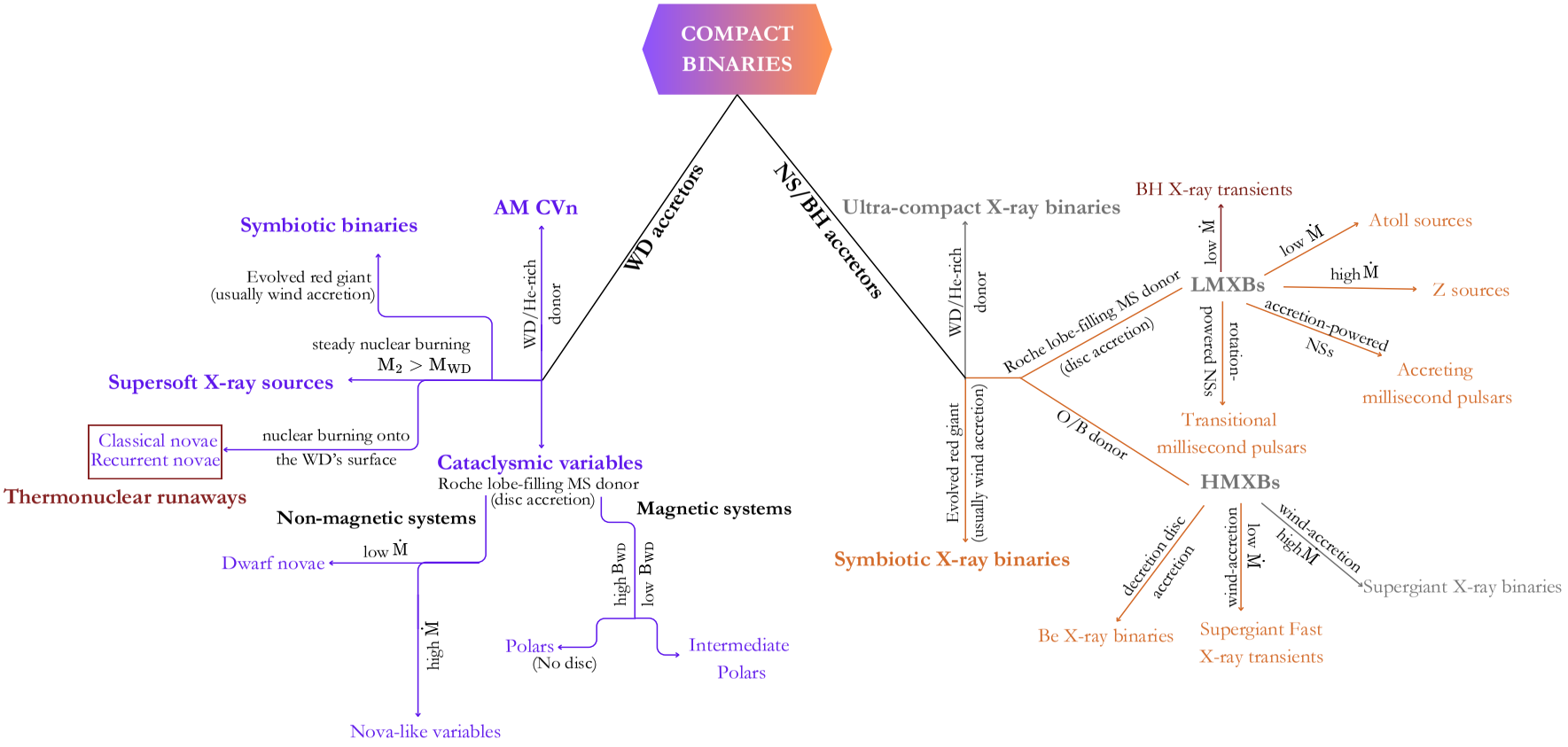

FIGURE 1.3: The classification tree of interacting compact binaries. The primary distinction is based on the nature of the accretor. It is noted that there is a colour distinction among the systems with different primaries. In particular, the WD systems are illustrated in purple, the NS systems in orange while the BH binaries are in dark red. The categories which may include both NS/BH systems are displayed in grey. Each of these systems are then categorised based on the nature of donor. Complementary distinctive annotations for each class are also given. These annotations include the mass transfer mechanism that takes place between the two objects of the binary (disc accretion as opposed to wind-accretion) or properties such as the magnetic field or mass accretion rate. It is noted that in WD binaries, apart from the SSS that have more massive secondaries, in all the other categories $M_2 < M_{WD}$. I do not also include purposefully the IMXBs in this classification, as this phase constitutes a short-lived stage before the descent of these systems to the LMXB class.

Analogously to CVs, LMXBs are accreting binary systems with orbital periods ranging from a few hours (systems with MS donors) to days/weeks (systems with red giant companions). However, in LMXBs, the accretor is a NS or BH. As of today, almost 200 confirmed and candidate LMXB systems have been discovered in the Milky Way (Bahramian and Degenaar, 2023). The majority of them are transients, i.e. they display *outburst episodes*, similar to the ones seen in DNe. During these outbursts, they can reach luminosities of the order of $10^{36} - 10^{37}$erg s^{-1}, compared to $\leq 10^{33}$erg s^{-1} at their quiescent state (Bahramian and Degenaar, 2023). The taxonomy can be quite complex, as we can see in Figure 1.3, in the case of NSs. The sub-classifications here can be based on either spectral and temporal X-ray signatures (e.g. as for the split between Atoll and Z sources) or the magnetic field strength and the existence (or not) of an accretion disc. BH systems, though, are simpler in that extent, giving rise only to *BH X-ray transients* (BHXTs). Finally, IMXBs constitute a short-lived phase while unstable mass transfer takes place, and these systems transition into the LMXB regime. A schematic example of an LMXB system can be seen in Figure 1.4.

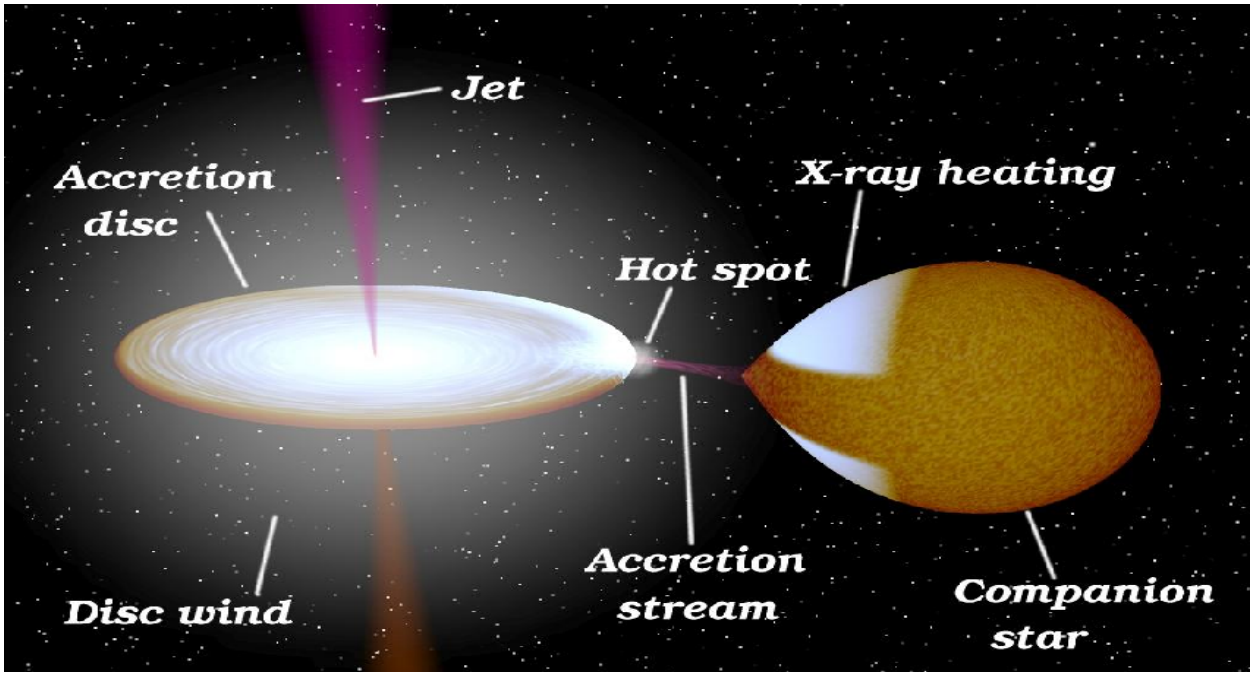

FIGURE 1.4: Schematic of a low-mass X-ray binary (LMXB) system. In these systems, the companion star transfers mass through the formation of an accretion disc into the NS or BH. The different components of the system are already identified as it is seen in the figure. Figure produced by Rob Hynes.

Other categories of compact binaries with NS/BH primaries include the aforementioned *symbiotic X-ray binaries* and the equivalent to the AM CVn sources, the *ultra-compact X-ray binaries* (UCXBs).

1.2.2 Roche geometry

In this thesis, I am mainly interested in semi-detached binary systems. The basic geometry we typically consider in studying them is the so-called *Roche geometry*.

Let us consider two massive bodies, with masses M_1 and M_2, orbiting one another. The two objects are approximated as *point sources*, as their mass is centrally-concentrated, while they are moving in Keplerian *circular* orbits around the common centre of mass (CM). Let us imagine a test particle under the influence of the gravitational wells of these two bodies. In the co-rotating reference frame, a centrifugal force is acting on the particle that modifies the effective gravitational potential. This effective potential – which is called the *Roche potential* – accounts for both gravitational and rotational effects.

In the non-inertial frame, the effective Roche potential is defined as

$$\Phi_R(\vec{r}) = -\frac{GM_1}{|\vec{r}-\vec{r_1}|} - \frac{GM_2}{|\vec{r}-\vec{r_2}|} - \frac{1}{2}(\vec{\omega}\times\vec{r})^2, \tag{1.2}$$

where $\vec{r_1}$ and $\vec{r_2}$ are position vectors from the centres of the two stars. The last term in the Roche potential represents the centrifugal force per unit mass. Here, ω is the angular velocity of the binary, relative to an inertial frame, given by $\omega = \left[G(M_1+M_2)/a^3\right]^{1/2}$.

Important features of the Roche geometry are the equipotential surfaces, i.e. surfaces of constant Φ_R, as well as saddle points, known as *Lagrangian points*, where $\nabla\Phi_R$=0. These features are demonstrated in Figure 1.5, and their structure is connected to the mass ratio, $q = M_2/M_1$, between the two components. It can be seen that circular equipotential surfaces arise either at large distances (much greater than the binary separation) or around the centres of each of the two objects. In both of these limits, the material is governed by the gravitational field of a point-like source. The spherical shape of the equipotentials is distorted, however, for locations influenced significantly by both stars.

Furthermore, the Lagrangian (equilibrium) points can be divided into two categories, based on their stability. The *unstable* Lagrangian points, i.e. L_1, L_2, L_3, are on the line connecting the two stars while the remaining two, i.e. L_4, L_5, are *stable*[6] and located at the vertex of the two equilateral triangles, created by the two stellar masses. In a semi-detached configuration, mass transfer occurs through the inner Lagrangian point, L_1, which creates a two-lobed figure-eight shape with each lobe centred around one of the two stars. Indeed, as the donor *fills* its Roche lobe, material passes through L_1 and falls into the gravitational well of the accretor. This situation marks the onset of Roche lobe overflow (RLO).

1.2.3 Mass transfer through RLO

Accretion via RLO is the most common mass transfer mechanism in interacting binaries, as seen in CVs and LMXBs. Here, the donor fills its Roche lobe and transfers mass to a compact object, i.e.

[6] I note in passing that the mass ratio, q, between the two bodies controls the structure of the Roche geometry and, therefore, plays a role in the stability of the Lagrangian points. In particular, the stability of the L_4 and L_5 points is valid under the requirement that $q < 0.0385$. This is true, for example, for the Trojan asteroids that are located at the L_4, L_5 points of the Sun-Jupiter system.

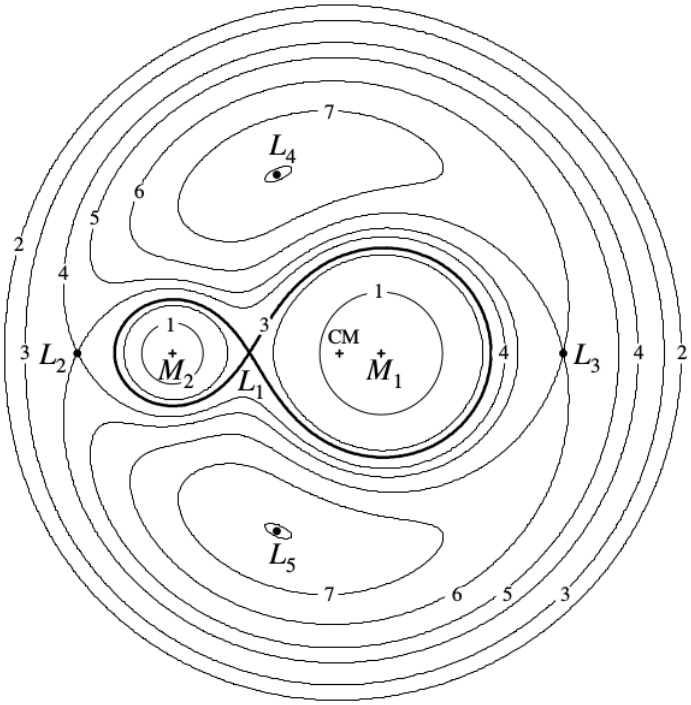

FIGURE 1.5: Cross-section of the Roche lobe geometry of a binary system with q=0.25. The mass ratio between the two stellar components defines the shape of the resulting geometry. The contours correspond to equipotential surfaces in the orbital plane of the system while the presented numbers, 1-7, indicate levels of increasing potential. The Lagrange points, $L_1 - L_5$, are also presented in the figure. Mass transfer occurs through the inner Lagrangian point, L_1, which allows, material to cross from one star to the other. Figure taken from Frank et al. (2002).

a WD, NS or a BH (see the different formation channels in Figure 1.6 for more details). However, as the donor approaches the Roche lobe, its shape diverges from that of a sphere, and it becomes increasingly deformed. For a fully Roche lobe-filling star, i.e. the donor in a semi-detached binary, the *Roche lobe radius*, R_L, is the *maximum* radius that the star can acquire. As a consequence, accretion continues as long as the donor adjusts its structure to maintain contact with its Roche lobe radius over time (Frank et al., 2002).

Due to the lobe's divergence from spherical symmetry, its size is typically parameterised by considering the radius of a sphere with the same volume as the lobe. This value is mostly approximated analytically or numerically, with the most widely used analytical formulae in different mass ratio regimes being those derived by Eggleton (1983)

$$\frac{R_{L,2}}{a} = \frac{0.49q^{2/3}}{0.6q^{2/3} + ln(1+q^{1/3})} \qquad 0 < q < \infty, \tag{1.3}$$

and Paczyński (1971)

$$\frac{R_{L,2}}{a} = 0.462\Big(\frac{q}{1+q}\Big)^{1/3} \qquad 0.1 < q < 0.8. \tag{1.4}$$

The above expressions (Equations 1.3 and 1.4) highlight that, during mass transfer, the binary orbit will evolve, as it is linked to the mass ratio, q, of the two objects and the orbital separation, a, between them.

The evolutionary stage of the donor at the time it fills its Roche lobe, defines three distinct cases of mass transfer, known as cases A, B and C. In *Case A*, for example,the star is on the MS when the mass transfer begins. This happens either when the donor expands or the orbit shrinks through angular momentum losses. It typically applies to short-period binaries, like the Algol-type systems. On the other hand, Cases B and C correspond to mass transfer beginning at later stages of the donor's evolution. *Case B* signifies a (sub-)giant donor that burns hydrogen in a shell and/or fuses helium in its core, whereas *case C* arises in wide binaries, where the donor reaches its supergiant stage (inert CO core, He- and H-burning shells). The latter scenario is particularly important for the formation of LMXBs through the common envelope phase, as we shall see later in Section 1.2.4.

The motion of material from one star to the other will change the mass ratio of the binary, causing the orbital parameters to change as mass and angular momentum are redistributed. The stability of mass transfer depends on the interplay of three factors coming together. These factors concern how the properties of the system respond and readjust in response to mass transfer. Specifically, these factors are the stellar and Roche lobe radii, as well as the orbital separation of the system. To decipher how these properties will change then, it is often assumed that the mass transfer is *conservative*, i.e. that the total angular momentum and mass are conserved, $\dot{J} = 0$, $\dot{M} = 0$ (there is no mass loss from the system). Conservative mass transfer is considered to be the simplest useful framework. Strictly speaking, this applies only in certain specific cases, like the Algol-type systems. In many systems, however, angular momentum and perhaps mass are lost via outflows.

In order to gain insight and intuition into the evolution of interacting binary systems, it is nevertheless useful to derive some of the key results for the conservative mass transfer case. The following discussion follows Frank et al. (2002). We start by considering the orbital angular momentum of the system, $J = mr^2\omega$, which can be written as

$$J = (M_1 a_1^2 + M_2 a_2^2)\omega \Rightarrow J = M_1 M_2 \Big(\frac{Ga}{M_1 + M_2}\Big)^{1/2}. \tag{1.5}$$

The separations of the two components from the centre of mass, a_1, a_2 are expressed in terms of the total binary separation, a, as $a_1 = a(M_2/M_1 + M_2)$ and $a_2 = a(M_1/M_1 + M_2)$. We have also made use of Kepler's third law, $4\pi^2 a^3 = G(M_1 + M_2)P_{orb}^2$, to substitute for the angular velocity, ω.

Logarithmically differentiating Equation 1.5 with respect to time, we derive that

$$\frac{\dot{a}}{a} = \frac{2\dot{J}}{J} - \frac{2\dot{M}_2}{M_2}(1 - q). \tag{1.6}$$

As the secondary conservatively transfers mass to the primary (i.e. $\dot{M}_2 = -\dot{M}_1$ and $\dot{J} = 0$), it is evident from Equation 1.6 that the binary orbit must expand ($\dot{a} > 0$) whenever $M_2 < M_1$. Indeed, since the transferred material is moved closer to the CM, the donor has to expand its orbit in order to conserve angular momentum. On the contrary, in the case that $M_2 > M_1$, the orbit shrinks ($\dot{a} < 0$). The minimum binary separation for conservative mass transfer to take place is in the case that the two masses are equal, i.e. $M_2 = M_1$.

The Roche lobe radius of the secondary, $R_{L,2}$, must respond to the mass loss and the associated changes to the orbit. To quantify this, we employ the same mathematical trick as we logarithmically time-differentiate the Paczyński relation (Equation 1.4). The simpler form of the Paczyński approximation (Paczyński, 1971) is usually preferred in these cases as it offers us invaluable insights despite the fact that the Eggleton approximation (Eggleton, 1983) covers a broader range of mass ratios. The following relation then describes the time evolution of these properties as mass transfer occurs

$$\frac{\dot{a}}{a} = \frac{\dot{R}_{L,2}}{R_{L,2}} - \frac{\dot{M}_2}{3M_2}. \tag{1.7}$$

Combining both Equations 1.6 and 1.7, we find that

$$\frac{\dot{R}_{L,2}}{R_{L,2}} = \frac{2\dot{J}}{J} - \frac{2\dot{M}_2}{M_2}\left(\frac{5}{6} - q\right). \tag{1.8}$$

The above expression, i.e. Equation 1.8, signifies the response of the Roche lobe radius (either through expansion or shrinkage) to mass loss. We can immediately identify two different regimes, depending on the mass ratio of the system. *Less-massive secondaries* ($q < 5/6$ systems) are susceptible to the expansion of their Roche lobe with respect to time ($\dot{R}_{L,2}/R_{L,2} > 0$). In this case, RLO can only be maintained via two different channels: either the secondary star expands ($\dot{R}_2 > 0$) as part of its evolutionary process (on a nuclear timescale) or the binary orbit shrinks due to angular momentum losses ($\dot{J} < 0$). These situations lead to *stable mass transfer*.

The two main angular momentum loss (AML) mechanisms that take place during stable mass transfer periods are *gravitational radiation* and *magnetic braking*. Gravitational radiation (GR) is released from binary systems, thereby removing angular momentum, as they spiral towards one another (Kraft et al., 1962). Hence despite being always present, GR-driven orbit shrinkage dominates mostly in *close* binaries as $\dot{J}/J|_{GR} \propto a^{-4}$ (Landau and Lifshitz, 1951; Paczyński, 1967). On the other hand, magnetic braking (MB; Kraft, 1967; Skumanich, 1972) occurs in systems where the companion star is a late-type star. The magnetic fields in these objects play a crucial role as they channel the donor's ionised wind, which therefore removes angular momentum out of the system. Here, the rate at which this process takes place is less certain, as it is estimated mainly observationally (e.g. see Skumanich, 1972, for some of the initial studies on magnetic braking).

In systems with more *massive donors* ($q \geq 5/6$), the Roche lobe will shrink ($\dot{R}_{L,2}/R_{L,2} < 0$) in response to mass loss. The secondary then has to either rapidly *contract* to maintain its radius equal

to the Roche lobe radius or encounter runaway mass loss that drives the star out of equilibrium. This *unstable mode of mass transfer* eventually terminates when enough material has been accreted to the companion, and the mass ratio of the system has been reversed. At this point, mass transfer can become stable again. Unstable mass transfer can occur on either the thermal or dynamical timescale, depending on the donor's mass and radius, as well as its evolutionary stage. Let us briefly consider these two cases.

Dynamically unstable?

Low-mass MS stars are described by a radiative core and a convective envelope, whereas in higher-mass MS stars, a convective core is surrounded by a radiative envelope (see Section 1.1). The response of a star to rapid (adiabatic) mass loss is sensitive to these structural differences. Stars with convective envelopes are expected to expand (or maintain constant radius) in response to adiabatic mass loss, while radiative envelopes shrink.

Based on these considerations, we can expect to encounter dynamically unstable mass transfer in binary systems with $q \geq 5/6$ (so that the Roche lobe shrinks in response to mass loss) and donor stars with convective envelopes (so that the star expands in response to rapid mass loss). Mass transfer will then take place on the dynamical timescale (of the envelope), which is defined as

$$t_{dyn} = \frac{R}{c_s}, \tag{1.9}$$

where c_s the local speed of sound.

Thermally unstable?

If the donor in a $q \geq 5/6$ binary *can* maintain hydrostatic equilibrium (e.g.because it has a radiative envelope), the mass transfer rate is likely to be set by the timescale on which the donor attempts to maintain thermal equilibrium. This thermal timescale is given by

$$t_{th} \approx \frac{GM_2^2}{2R_2L_2}, \tag{1.10}$$

where M_2, R_2, L_2 the mass, radius and luminosity of the secondary star (mainly we consider the envelope and not the star as a whole).

1.2.4 Origin of CVs and LMXBs

The common envelope (CE) phase is one of the most characteristic manifestations of a *dynamically* unstable mass transfer configuration. It is critical for explaining the origin of CVs, supersoft X-ray sources and LMXBs, but is also relevant to other types of systems. For example, it constitutes a possible formation channel for type Ia SNe or double compact binaries (check Figure 1.6 for a

schematic chart of some of the aforementioned formation channels). A review by Ivanova et al. (2013) provides a thorough description of the fundamental principles of the CE phase. Nevertheless, here, I would like to give a small overview due to its importance to the formation of the studied systems.

The CE formation channel was first introduced by Van Den Heuvel (1976) and Paczynski (1976) as a mechanism to help explain the origin and evolution of close binaries. However, later studies in the field (e.g. Webbink, 1984; Livio and Soker, 1988; de Kool, 1990; Taam and Sandquist, 2000; Dewi and Tauris, 2000; Ivanova et al., 2013, 2020) established the importance of the CE phase as an inevitable part of the binary evolution. A first encounter with a CE stage may be the case where two MS stars orbit one another, and the more massive one first evolves and encloses the companion at its envelope. Loss of the established synchronisation between the stellar components along with the appearance of a drag force due to the companion's movement within the envelope cause the orbit to shrink and the two stars to spiral-in. As this process takes place, energy and angular momentum are redistributed and transferred to the hydrogen-rich envelope. The most employed formalism that describes the CE evolution, commonly referred to as the α-formalism (Webbink, 1984; de Kool, 1990), works under the premise that the envelope would be *ejected* if its binding energy, denoted as E_{bind}, is less than or equal to the orbital energy difference, ΔE_{orb}, between the initial and final stages of the CE phase, $E_{bind} \leq \Delta E_{orb}$. Otherwise, in the opposite case, the outcome of the CE process would lead to a merger of the two stars. They parameterise the efficiency of this energy balance, accounting for our lack of knowledge of the included uncertainties, by using the α_{CE} parameter as

$$E_{bind} = \alpha_{CE} \Delta E_{orb} \Rightarrow \alpha_{CE} = \frac{E_{bind}}{\Delta E_{orb}}, \tag{1.11}$$

where the envelope binding energy is expressed as

$$E_{bind} = \frac{-GM_2 M_{2,env}}{\lambda R_{L,2}}, \tag{1.12}$$

with M_2 the mass of the more massive star, $M_{2,env}$ its envelope mass, $R_{L,2}$ its Roche lobe radius while λ, an introduced numerical factor (e.g. de Kool, 1990; Dewi and Tauris, 2000) to account for different structures of its envelope (which depend on the evolutionary stage of the evolved star).

On the other hand, the orbital energy dissipation between the onset and final product of the CE is given by the following relation

$$\Delta E_{orb} = E_{orb,f} - E_{orb,i} = \left[-\frac{GM_{core} M_1}{2a_f} + \frac{GM_2 M_1}{2a_i} \right], \tag{1.13}$$

where, now, M_{core} the core mass of the more massive star, defined as $M_{core} = M_2 - M_{env}$, M_1 the companion's mass while $a_f < a_i$ the orbital separations of the system at these stages.

The final outcome of this process would be a close binary, which consists of the core of the evolved star as the donor and the companion star as the accretor. Other formalisms, such as the γ-formalism (conservation of angular momentum, c.f. Nelemans et al., 2000), have also been proposed. Even though these approaches are simplistic, it is quite challenging to fully simulate these types of binary populations and evolve stars through the whole CE phase due to the plethora of implemented processes and lack of computational power. The key point that I am trying to convey is that we have to recognise the complexity of such rapid phenomena in order to decipher the observed properties of such systems.

1.3 Accretion discs - in a nutshell

1.3.1 Disc formation

Accretion discs are efficient structures for extracting gravitational potential energy and converting it into radiation. But how are they formed? We saw in previous sections how mass transfer takes place between the two binary components, and how material is transferred through the inner Lagrangian point onto the primary star. The gas stream, though, being supersonic and carrying still substantial angular momentum, will follow elliptical, *precessing*[7] trajectories, instead of falling directly onto the compact object.

To be more precise, let us imagine the orbits of a particle stream coming through the L_1 point. Each particle will follow, as mentioned, such a trajectory that would lead, eventually, to their orbits' intersection. The particles will start colliding with each other, dissipating their energy via shocks. Gas still maintains its angular momentum (as it has to be conserved), but as energy is lost from the system, the infalling material will be concentrated at the orbit of the lowest energy for its angular momentum, i.e. a Keplerian circular [8] orbit. The radius of that orbit is known as the *circularisation* radius, R_{circ}, and it is given by

$$\frac{R_{circ}}{a} = (1+q)\frac{R_{L,1}}{a}. \tag{1.14}$$

[7] The presence of the companion changes the effective potential from the exact R^{-1} dependence which is required for closed periodic orbits.

[8] This configuration is easily justified if we consider that the orbit's eccentricity, e, is related to its specific orbital energy, ϵ, and specific angular momentum, h, as

$$e = \left[1 + \frac{2\epsilon h^2}{(GM)^2}\right]^{1/2}.$$

As orbital energy is decreased and the angular momentum is conserved, the eccentricity should be adjusted appropriately. Here, the term "specific" signifies that the relevant properties have been divided by the reduced mass of the system.

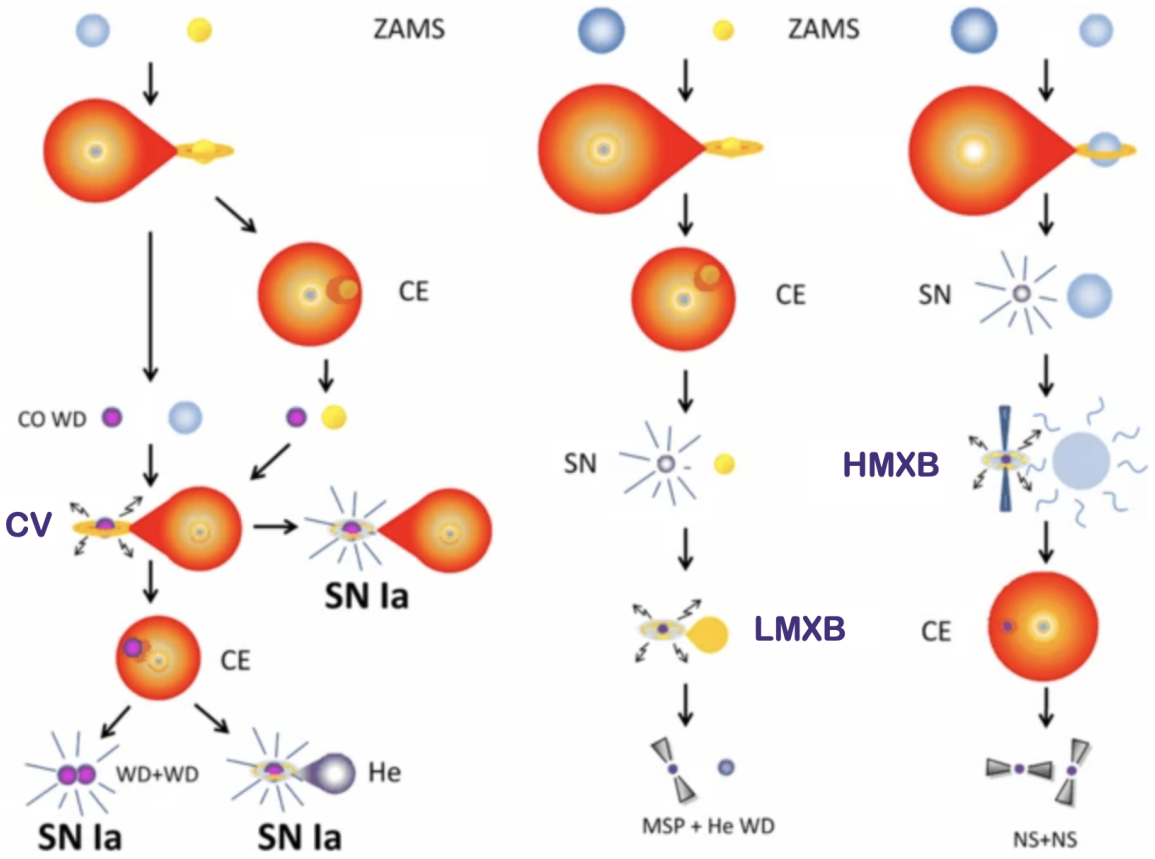

FIGURE 1.6: A representative, schematic illustration of various evolutionary formation channels that include stages of accretion onto compact objects (denoted as the CV, LMXB and HMXB stages at the charts above). The left panel showcases potential paths to form type Ia SNe either through the single- or double-degenerate scenarios. On the other hand, the right panel displays formation of NS XRBs with the LMXB to lead to the creation of millisecond pulsar (MSP) orbiting a WD whereas the HMXB binary forms a double NS system (pulsar system). It is evident, in all cases, the transition through a CE phase as the initial MS pair evolves while some channels also go through a second round of CE before the final products are formed. For clarity, it is noted that, at the second stage, there is not an involved mass transfer phase but only that the donor star fills its Roche lobe. These formation channels are not exclusive. Figure adapted from Ivanova et al. (2013).

At the circularisation radius, gas will continue to lose energy through its interactions with neighbouring particles while *viscous stresses* will redistribute its angular momentum. The original circular ring will spread towards both larger and smaller radii, thereby forming an *accretion disc*. The undefined nature of *viscosity*, though, presents a challenging issue to address, but it is possibly associated with the existent turbulence of the disc. The most accepted mechanism responsible for the transport of angular momentum in such flows is the *magnetorotational* instability (MRI; Balbus and Hawley, 1991), even though other mechanisms have been proposed, e.g. *spiral waves* (e.g. Ju et al., 2016, 2017). In the MRI-based picture, ionised gas elements of adjacent annuli are coupled with the magnetic field lines. Differential rotation provides an additional, yet crucial ingredient of

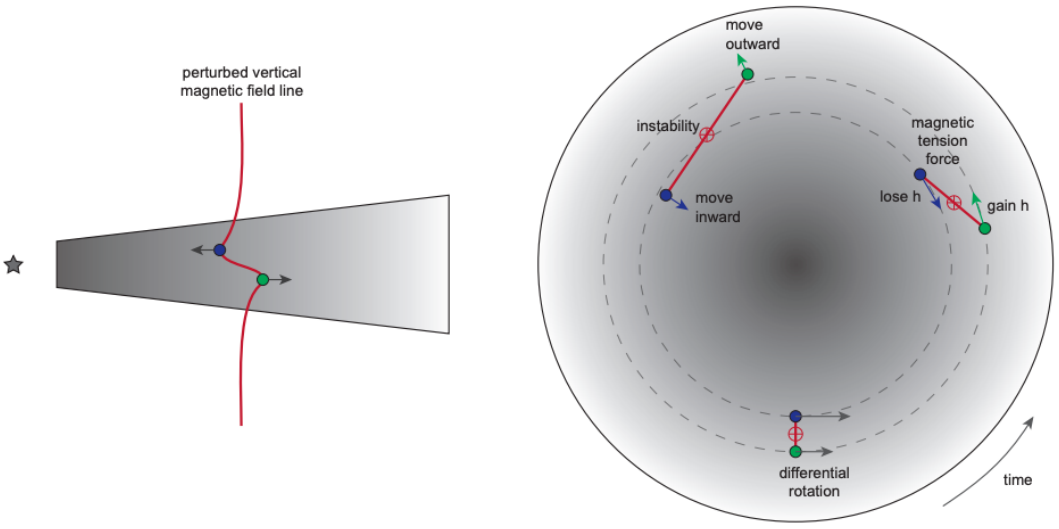

FIGURE 1.7: Both edge- and face-on illustration of the magnetorotational instability (MRI; Balbus and Hawley, 1991) in an accretion disc. Magnetic fields and differential rotation are essential ingredients to drive accretion onto the compact object. The differential rotation (parts of the disc are rotating with different angular velocities) perturbs and stretches the magnetic field lines, embedded vertically in the plasma. Magnetic tension forces are trying to restore the bent field lines by transporting angular momentum outwards. Figure taken from Armitage (2022).

how momentum is transported radially, as different parts of the disc are rotating at different velocities. Let us not forget that Keplerian velocities have a $R^{-3/2}$ radial dependence, and therefore, the rotational velocity drops as we move further away from the central object.

The angular momentum transport mediated by the MRI is illustrated in Figure 1.7, where we can see how two elements of adjacent annuli are displaced as time progresses. Initially, due to differential rotation, the *inner* element (blue circle) will rotate *faster* than the one located further away (green circle). Magnetic tension will arise as a restoring force and will try to bring the two elements back together (left side of Figure 1.7). Hence, the inner element will slow down while the outer element will speed up. Slowing the inner element down removes energy from it, and therefore it causes its displacement to an even lower orbit. Overall, a runaway process emerges — for any given radius on the disc, a fraction of particles gains angular momentum as they move outwards, allowing a particle fraction to move inwards and be deposited closer to the compact object. This is easy to understand if we realise that the angular momentum scales as $R^{1/2}$ with the radius.

In practice, the viscosity in accretion discs is often modelled via the simple $\alpha-$*prescription*. Shakura and Sunyaev (1973) described the nature of viscosity via this single parameter, α, and parameterised their uncertainty about how the angular momentum is transferred outward and how the different accretion rings interact. This *prescription* establishes the kinematic viscosity in the disc as

$$\nu = \alpha c_s H, \tag{1.15}$$

where α ranges between $0 \leq \alpha \leq 1$, c_s is the local sound speed and H its scale-height. The discs that fall under this prescription are called *standard* discs. A standard disc is the simplest kind of accretion flow − and the one we will be concerned with in this thesis − and describes a *steady* (constant mass accretion rate from the companion star), *geometrically thin* ($H/R << 1$) and *optically thick* ($\tau >> 1$) disc.

The total (maximum) luminosity that the infalling accreted material of such a disc *radiates* as it swirls around the compact object is set by the mass accretion rate, $\dot{M}_{acc}$, as

$$L_{disc,max} = \frac{GM\dot{M}_{acc}}{2R}, \tag{1.16}$$

which is half of the accreted luminosity, $L_{acc} = GM\dot{M}_{acc}/R$ (as we also see later on). The other half is expected to be released in a thin boundary layer, at the surfaces of at least WD and NS accretors, in which the material spins from Keplerian velocities to nearly zero. For BHs, the drop in angular velocity occurs at the innermost stable circular orbit (ISCO)[9]. Note that in these boundaries, as $\dot{\Omega}$=0, the torque is considered zero.

Especially, in XRBs, the total (or disc) luminosity is often described by the efficiency with which they release rest mass energy as

$$L_{rad} = \eta \dot{M}_{acc} c^2. \tag{1.17}$$

It is easy to see between these relations that the efficiency, η, is directly dependent on the *compactness* of the accretor, i.e. M/R, since $\eta \propto M/R$. Typical values range from η=0.001 for accretion on to WDs while higher values are met on XRBs. Characteristic efficiency approximation value of accretion on to BHs is considered η=0.1.

Alternatively, the radiative luminosity is also often expressed as a fraction of the *Eddington luminosity*. The Eddington luminosity (aka the Eddington limit) is the *maximum* luminosity that a spherical object can emit isotropically before radiation pressure will overwhelm the object's self-gravity. Assuming that the disc consists only of *ionised hydrogen*, accretion provides the luminosity and this limit ($L_{acc} = L_{edd}$) is written as

$$L_{edd} = \frac{4\pi GMm_p c}{\sigma_T} = 1.26 \times 10^{38} \Big(\frac{M}{M_\odot}\Big) \text{erg s}^{-1}, \tag{1.18}$$

[9]The innermost stable circular orbit (ISCO) is the smallest stable circular orbit that a particle can be found around a black hole and its location is dependent on the black hole spin. For example, for a (non-spinning) Schwarzschild black hole, the ISCO is located at $6GM/c^2$, where the term GM/c^2 is defined as the gravitational radius, R_G.

where m_p the proton's mass and σ_T the electron scattering (Thomson) cross-section. In reality, the considered assumptions are far from what happens in real objects, such as accretion discs, but this limit provides us with a reasonable estimate of the maximum luminosity an accreting object is likely to reach.

In the sub-Eddington regime ($L << L_{edd}$), which is relevant for the work in this thesis, Shakura and Sunyaev (1973) derived the disc structure and the emitted spectrum, as we will see in the following section. The Shakura and Sunyaev (1973) work was primarily focused on observational properties of BH binaries in the framework of classical (non-relativistic) mechanics. Novikov and Thorne (1973) expanded the previous study by taking into account relativistic effects in the vicinity of the BH and beyond the ISCO. In my description, though, I will purely stay at the classical Shakura-Sunyaev disc implementation, rather than the Novikov-Thorne one, as GR-effects are not relevant in this work.

1.3.2 Standard discs - geometrically thin, optically thick accretion flows

The transient nature of many accreting systems and the appearance of their eruptions are a reminder that the standard, steady-state Shakura and Sunyaev model (Shakura and Sunyaev, 1973) is just a simplification. However, it is useful to gain valuable insights. The *thin* approximation allows us to disentangle the vertical and radial disc structure, while the thinness of the accretion flow imposes that the local Keplerian velocity of each annulus is *supersonic* as $H/R = c_s/\Omega_K << 1$. On the other hand, the emitted radiation is approximated as *blackbody* radiation. This is a valid approximation in an *optically thick* disc, where the photons and gas particles are in local thermal equilibrium (LTE), and therefore, the gas heating and cooling rates are in balance.

The solutions of the (mass, angular momentum) conservation equations can help us to compute the rate of dissipated energy throughout the disc and define the luminosity emitted from its surface. Viscous dissipation in a steady, thin disc is expressed as

$$D(R) = \frac{3GM_1\dot{M}_{acc}}{8\pi R^3}\left[1 - \left(\frac{R_{in}}{R}\right)^{1/2}\right], \tag{1.19}$$

where the last term, i.e. the one in brackets, arises from the usage of a zero-torque boundary condition to the innermost radius of the disc, R_{in}. This is related to the fact, as already mentioned, that the accretors are rotating slowly with respect to the rotational (Keplerian) velocity of the inner disc. Note that the viscous dissipation has a R^{-3} radial dependence. Consequently, most of the energy is deposited towards smaller radii, closer to the compact object, thereby making these regions emitting at higher energies.

The energy dissipation rate through the disc drives the radiative flux, released from the system, as the potential energy is converted to radiation. Requiring that these two contributions should

be equal, we can find that the effective temperature distribution due to viscosity is given by

$$D(R) = \sigma_{SB} T^4_{eff,visc}(R) \Rightarrow T_{eff,visc}(R) = \left\{ \frac{3GM_1\dot{M}_{acc}}{8\pi\sigma_{SB}R^3} \left[1 - \left(\frac{R_{in}}{R} \right)^{1/2} \right] \right\}^{1/4}. \tag{1.20}$$

where σ_{SB} is the Stefan–Boltzmann constant.

For such discs, since each annulus of the disc emits at a different temperature, $T_{eff,visc}(R)$, the spectral energy distribution (SED) is usually constructed as a superposition of local blackbody profiles, a *multi-temperature* blackbody spectrum (Mitsuda et al., 1984; Makishima et al., 1986). Here, the specific intensity from each ring follows Planck's law, described as

$$I(\nu, T) = \frac{2h\nu^3}{c^2} \frac{1}{e^{h\nu/k_B T_{eff,visc}} - 1}, \tag{1.21}$$

where ν is the frequency, and h and k_B are Planck's and Boltzmann's constants, respectively.

The monochromatic flux, F_ν, which an observer of a distance D and an inclination i receives is then given by the following relation

$$F_\nu = \frac{4\pi h \cos i \nu^3}{c^2 D^2} \int_{R_{in}}^{R_{out}} \frac{R dR}{e^{h\nu/k_B T_{eff,visc}} - 1}. \tag{1.22}$$

At intermediate frequencies, the flux scales as $F_\nu \propto \nu^{1/3}$ and this is often considered to be the characteristic accretion disc spectrum. The turnover on either side of this regime is due to the temperature range being limited by the presence of the inner and outer disc radii. Specifically,

$$\text{for} \quad \frac{k_B T_{eff,visc}(R_{out})}{h} < \nu < \frac{k_B T_{eff,visc}(R_{in})}{h} : \qquad F_\nu \propto \nu^{1/3}. \tag{1.23}$$

The detailed disc structure (e.g. the radial distribution of density, scale-height, mid-plane temperature, etc) as derived by Shakura and Sunyaev (1973), mainly depends on the specific opacities that dominate in a given regime, as well as the relative strengths of gas and radiation pressure[10]. Figure 1.8 provides a comprehensive overview of the different regimes. At the smallest radii (closer to the compact object), temperatures are high, radiation pressure dominates, and opacity is mainly due to electron scattering. At larger radii, the temperature is much lower, so the gas pressure surpasses the radiation pressure, and free-free and bound-free emission processes dominate the opacities (which can then be described by Kramer's law).

[10]Opacity constitutes a measure of the photon's penetrability through a medium and it is considered temperature-dependent. The relevant opacity laws that we take into account in the current thesis are a) the electron scattering opacity that dominates in high temperatures, defined as $\kappa_{es} = \sigma_T n_e$ with σ_T the Thomson cross-section and n_e the electron density, and b) the Kramer's opacity, result of free-free (photon absorbed by a free electron) and bound-free (photon absorption from a bound electron) processes. The latter law powers with density and temperature as $\kappa_{kramers} \propto \rho T_c^{-7/2}$, where T_c the central temperature on the disc. In general, it is expected that $T_c \geq 10^4$K.

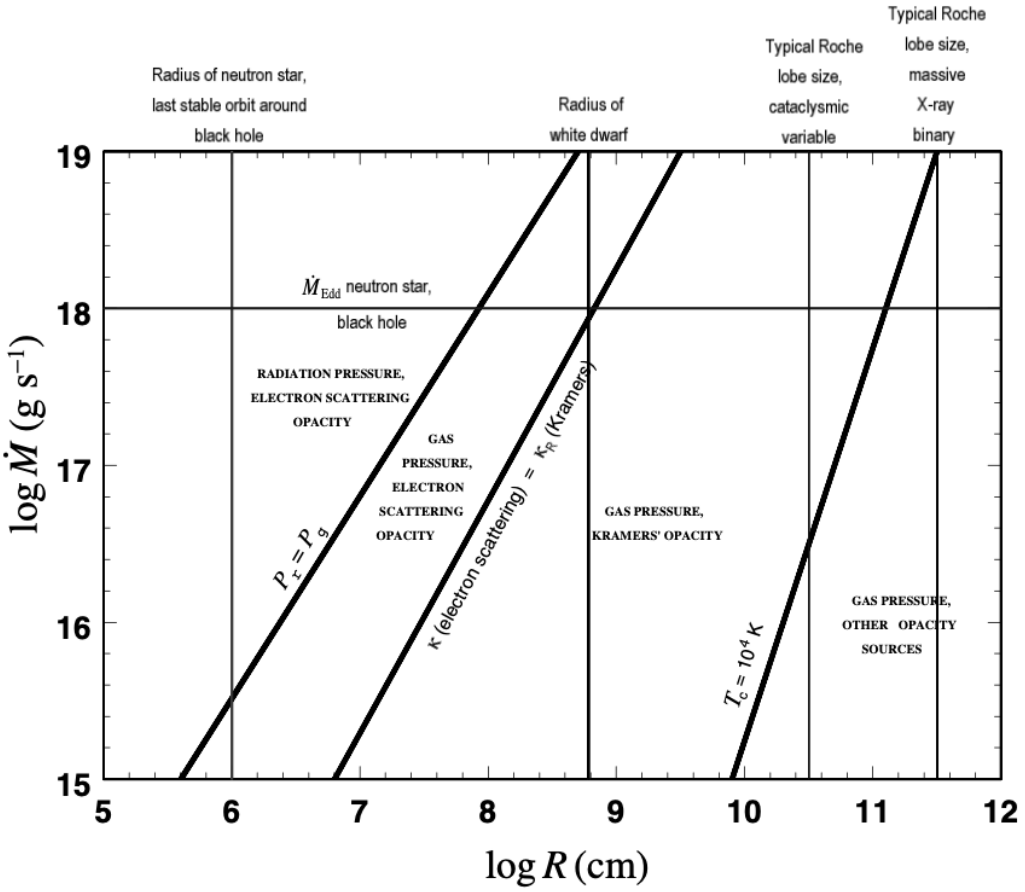

FIGURE 1.8: Different regimes in an accretion disc based on the Shakura and Sunyaev (1973) model, where the disc radius is plotted against the mass accretion rate at each radii. The relevant properties of each regime and their limits are highlighted (pressure, opacity laws, temperature) while at the upper x-axis, characteristic length scales (compared to the size of the binary) are mentioned. Figure taken from Frank et al. (2002).

Despite the model's simplicity, strong evidence of geometrically thin and optically thick discs is apparent at the soft states of CV and LMXB outbursts (see Section 1.4.1 for more information). For example, the disc temperatures may vary between 0.5-1.0 keV for the case of LMXBs. The blackbody approximation should be modified, though, if emission line formation is needed to be captured. The only way to form emission lines is via a vertical temperature inversion in the disc, i.e. there has to be a hot layer on top of a cooler optically thick disc. Furthermore, one should consider effects such as relativistic distortions of the disc emission in the case of BH transients or spectral hardening (caused by Compton scattering in the disc atmosphere[11] – Shimura and Takahara, 1995; Davis and El-Abd, 2019).

On the other hand, the standard disc model fails for extremely low- and extremely high-mass accretion rates, where the accretion flow is unable to radiate away all of the gravitational potential energy that is released. In these cases, much of the energy can be carried with the flow (as internal

[11]The Planck's law neglects the effect of the disc's atmosphere (optically thin regime – $\tau << 1$) in redistributing the radiation over frequency. There is an underestimation of atmospheric opacity as a function of frequency.

heat) via advection. It is important to remember that in the standard Shakura-Sunyaev disc model, advection is not included (since radiative cooling is assumed to be sufficient to balance viscous dissipation). At the low-accretion regime, studies by Narayan and Yi (1994, 1995), for example, tried to elucidate these optically thin, *advection-dominated accretion flows* (ADAFs), when $H/R << 1$. In contrast, at the high-accretion, (super-)Eddington end, the disc is sustained by radiation. Here, *slim* ($H/R \leq 1$; Abramowicz et al., 1988) and *thick* ($H/R > 1$; Abramowicz et al., 1980) disc solutions exist and describe the respective accretion flows.

In general, the luminosity radiated by a steady, thin disc is found by integrating Equation 1.19. This shows that the disc radiates half of the accreted luminosity as

$$L_{disc,max} = 2\int_{R_{in}}^{\infty} 2\pi RD(R)dR \Rightarrow L_{disc,max} = \frac{GM_1\dot{M}_{acc}}{2R} = \frac{1}{2}L_{acc}. \tag{1.24}$$

The other half, either is released as thermal radiation at the boundary layer of accretors with a solid surface i.e. WDs and NSs or it is advected into the event horizon of BHs.

1.3.3 Outburst episodes

1.3.3.1 The disc instability model

CVs and LMXBs alternate between extended periods of quiescence and sudden dramatic eruptions, during which the luminosity increases by several orders of magnitude within short timeframes (which can last from days to months). This transient behaviour is normally interpreted in the framework of the *disc instability model* (DIM; see e.g. Osaki, 1996; Buat-Menard et al., 2001; Lasota, 2001; Hameury, 2020, for recent reviews). The DIM is based on the recognition that accretion discs are susceptible to a thermal-viscous instability associated with the ionisation of hydrogen. This instability is driven by the steep dependence of the opacity on temperature in the partially-ionised hydrogen disc, thereby making the disc *unstable*. Note that DIM is based on the standard disc implementation, introduced by Shakura and Sunyaev (1973).

In order to illustrate the basic concepts of the model, we are going to consider a DN outburst, following the evolution sketched below in Figure 1.9. In general, CV discs are preferred to test basic accretion models, as they are not affected by ultra-strong magnetic fields or relativistic effects (unlike their NS and BH counterparts). The figure also showcases the $\Sigma - T_{eff,visc}$ plane, known as *S-curve*, where the different green lines correspond to a family of thermal equilibrium solutions during an eruption (as a function of disc radius).

During *quiescence*, the disc is located at the stable *cold branch* on which hydrogen is neutral, and the mass transfer rate through the disc, denoted as $\dot{M}_{tr}$,is low everywhere (lower left panel of Figure 1.9). As its mass builds up, the disc's surface density and mass accretion rate increase until the point, where the latter reaches a critical value, $\dot{M}_{tr} = \dot{M}_{cr}$, on a *viscous* timescale. The

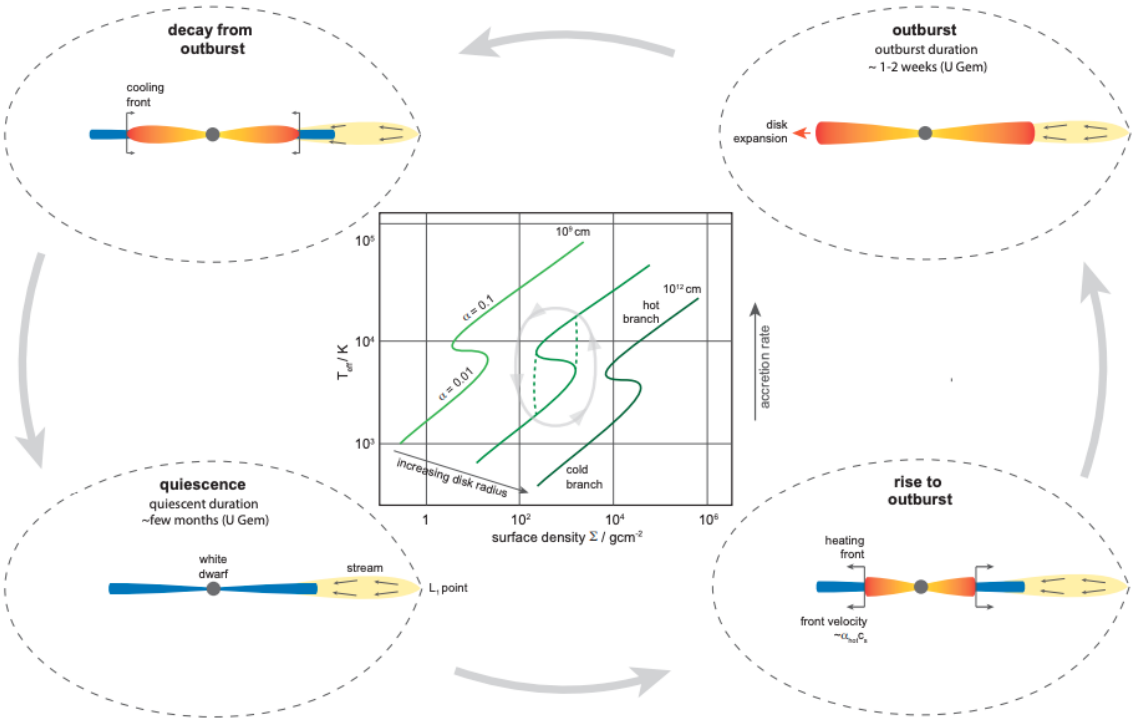

FIGURE 1.9: Evolution of a DN outburst where we can see four different stages: a) quiescence, b) rise to outburst, c) outburst and d) outburst decay. A limit cycle is created during these stages, as demonstrated by the $\Sigma - T_{eff,visc}$ plane, known as S-curve (surface density-temperature plane). Its secondary y-axis represents the mass accretion rate, scaling as $\dot{M}_{tr} \propto T^4_{eff,visc}$. The distinct green lines represent thermal equilibrium solutions as a function of radius. Here, the disc is stable as long as its heating rate is less or equal to its cooling rate. The disc starts at the stable cold branch (quiescence) but as $\dot{M}_{tr} = \dot{M}_{cr}$, it becomes unstable and transitions into the hot branch on thermal timescale (outburst). As the disc mass gets depleted through accretion onto the WD surface, the disc returns back to quiescence. Noted that the viscosity parameter, α, is different at the two branches, i.e. $\alpha_c = 0.01$ and $\alpha_h = 0.1$. Figure taken from Armitage (2022).

gas opacity raises as the disc heats up (as $T_{eff,visc} \propto \dot{M}_{tr}^{1/4}$) and the *hydrogen-ionisation instability* is triggered ($T_{eff,visc,H} = 6500K$). Two *heating fronts* propagate in the disc (at a speed of $\sim \alpha_h c_s$) − one inwards that reaches the inner disc, and one outwards that reaches the outer edge (lower right panel of Figure 1.9). Once in outburst, the disc becomes fully ionised (upper right panel of Figure 1.9) and it is located to the stable *hot branch* of the S-curve on the *thermal* timescale. Finally, the surface density starts to decrease as the rate at which mass is transferred through an annulus is larger than the rate at which the donor supplies mass to the disc. The outburst finishes when the disc is back to the stable *cold branch* by the propagation of a *cooling front* (of a speed $\sim \alpha_c c_s$). The cooling front begins at the outer disc and propagates, in our case, towards the WD, thereby bringing the disc to its quiescent state (upper left panel of Figure 1.9) on a *thermal* timescale.

The observed light curve phenomenology of these systems can help us infer where the thermal-viscous instability is initially triggered. In "outside-in" outbursts, the instability begins in the cooler, outer disc regions and the heating front propagates towards the WD. In contrast, in "inside-out" outbursts, it is triggered in the hotter, inner regions of the disc, causing the disc to transition

to a hot, ionised state. The corresponding light curves are characterised by a slow ("outside-in" outbursts) or faster ("inside-out" outbursts) brightness rise and a slower, broader (due to the slower speed of the cooling front) decline.

The timescales that govern these transitions are essential to probe the structure of the accretion disc and the evolution of these events. In quiescence, mass accumulates in the outer disc, slowly moves inwards, and drives perturbations at its surface density profile, as mentioned, on a viscous timescale. In other words, it corresponds to the time required to move along a stable branch. The timescale can be approximated as

$$t_{visc} \sim \frac{1}{\alpha}\left(\frac{R}{H}\right)^2 \frac{1}{\Omega_K}. \tag{1.25}$$

On the other hand, the thermal timescale refers to the time it takes the disc to respond to temperature variations and readjust its thermal equilibrium and stability during an outburst. The timescale needed to move between the two (stable) branches of the S-curve can be expressed as

$$t_{th} \sim \frac{1}{\alpha}\frac{1}{\Omega_K}. \tag{1.26}$$

For thin ($H/R << 1$) discs, both timescales can be expressed with respect to the dynamical timescale ($t_{dyn} = 1/\Omega_K$, with Ω_K the local Keplerian velocity), which is the fastest time a change in the azimuthal direction takes place. Indeed, in these discs, the viscous timescales are several orders of magnitude longer than the other two at the same radius ($t_{dyn} \leq t_{th} \leq t_{visc}$). Consequently, the eruption recurrence timescale varies from months to years.

In a gas-dominated accretion disc, the gas opacity and its strong temperature dependence, as we have seen, play an essential role in the manifestation of these outburst episodes. Moreover, the viscosity efficiency, as given by the α-prescription, is required to be greater, at least an order of magnitude, during the outburst compared to its value in quiescence, i.e. $\alpha_h/\alpha_c = 10$ to reproduce the observed light curves. Indeed, shearing-box simulations have shown that convection boosts the angular momentum transport during high states and introduces vertical gradients and time fluctuations, resulting in $\alpha_h = 0.1$ (e.g. Hirose et al., 2014; Coleman et al., 2016; Scepi et al., 2018) for DN and $\alpha_h = 0.2 - 1.0$ (Tetarenko et al., 2018c) for LMXB discs. This discrepancy of the viscosity mechanism is justified as MRI requires fully ionised discs to take place.

1.3.3.2 Beyond the standard DIM

The standard DIM and the hydrogen-ionisation instability explain the outburst light curve phenomenology of the majority of DNe. They also constitute a reliable approach to describe the observed light curve profiles of LMXBs. However, other ingredients had to be taken into account in order to decipher the wide range of outburst characteristics of the documented light curves. This

is mandatory to interpret phenomena such as the long duration and high luminosity of BHXTs or the appearance of superoutbursts in DNe (see Hameury, 2020, for a review). This section is intended to be a brief summary of the most important modifications that have been proposed to explain key observational features in DNe and transient LMXBs. Life is not that simple though, as there is not only one game in town. We should keep in mind that more than one of these ingredients may sometimes be needed to understand the behaviour, even for a single system.

Perhaps the most obvious assumption to relax is that of a constant mass supply from the donor star. *Variations in its mass transfer rate* can be either *intrinsic* (e.g. stellar spots, flares) or *extrinsic* (e.g. irradiation) (e.g. Hameury et al., 2000; Buat-Ménard et al., 2001). In fact, transfer rate variations are essential to explain the DN light curves of the U Gem and Z Cam-type systems (Schreiber et al., 2003; Buat-Ménard et al., 2001) even though exceptions arise (e.g. Szkody et al., 2013; Hameury and Lasota, 2014; Kato, 2019). On the other hand, the *irradiation of the donor* by the inner accretion flow and/or the accretor itself accounts for some of the observed features in both DNe and X-ray transients. *Truncation of the inner disc* was also an important addition to the model, and, as we will see later, it is of great interest to us to decipher the light curves of WZ Sge-type systems (see Chapter 2 for more details). Truncation can occur either due to the existence of a magnetic field in the case of WD and NS accretors, disc evaporation (Meyer and Meyer-Hofmeister, 1994), ADAF (e.g. Narayan and Yi, 1994, 1995) or jet formation (e.g. Markoff et al., 2003; Marcel et al., 2022).

Furthermore, a variation of the DIM that incorporates the perturbation of the outer disc by the donor's tidal forces is accounting for the *tidal-thermal instability* (TTI; e.g. Whitehurst, 1988; Osaki, 1989, 1995). TTI was introduced to explain the superoutbursts and appearance of superhumps − optical brightness modulations with a period of a few percent of the orbital period of the system − of the SU UMa DN family (e.g. Hameury et al., 1998; Buat-Menard et al., 2001). The outburst light curves of these systems are described by the appearance of superoutbursts every few normal outbursts. At the standard picture, the TTI is most likely triggered by a normal outburst when the disc is already expanded. The moment its outer edge reaches the 3:1 resonance radius, tidal stresses would cause its orbit to precess and increase its angular momentum transport rate − the enhanced angular momentum (transport) rate would last until the disc shrinks back below the resonance radius. Due to this requirement, the TTI may be the predominant mechanism in low-mass ratio systems, i.e. $q \leq q_{crit} = 0.22$ (Smak, 2020), as the 3:1 resonance is only achieved in such mass ratios. Even though it is certainly a possibility, the fact that superoutbursts and superhumps are also detected in $q \geq q_{crit}$ systems is concerning. Characteristic is the example of U Gem and its 1985 superoutburst (Smak and Waagen, 2004).

Beyond DNe, in XRBs, *irradiation of the accretion disc* plays a significant role in shaping their light curves. The reprocessing of X-ray photons by the outer disc's surface acts as an additional heat source, thereby changing the thermal equilibrium curves of the accretion disc. It is worthwhile to mention here that if irradiation is taken into account, Coriat et al. (2012) showed that the DIM

does a very good job distinguishing transient from persistent XRB sources. The following section, Section 1.3.4, provides a more detailed description of irradiated discs and how irradiation modifies the disc temperature profile.

1.3.4 Irradiated discs

Irradiation of the accretion disc by the central (X-ray) source is known to be important in LMXB systems, where the outer disc regions absorb and re-emit hard photons at longer (UVOIR) wavelengths (van Paradijs and McClintock, 1994; van Paradijs, 1996; King and Ritter, 1998; Dubus et al., 1999, 2001; Tetarenko et al., 2018b). The radiative heating associated with the incident radiation modifies the disc's temperature distribution, thereby influencing its spectral energy distribution, stability, and its evolution across an outburst.

The absorbed portion of the irradiating flux, F_{irr}, that heats the disc can be expressed in terms of an effective temperature, $F_{irr} = \sigma_{SB} T^4_{eff,irr}$, and written as

$$\sigma_{SB} T^4_{eff,irr} = \left(\frac{L_{irr}}{4\pi R^2}\right)\left(\frac{H}{R}\right)\gamma\,(1-A) \Rightarrow T_{eff,irr} = \left\{\left(\frac{L_{irr}}{4\pi\sigma_{SB} R^2}\right)\left(\frac{H}{R}\right)\gamma\,(1-A)\right\}^{1/4}, \quad (1.27)$$

where L_{irr} is the luminosity of the irradiating source, which is assumed to emit isotropically. A is the albedo (a measure of the body's reflectivity, so that (1-A) is the *absorbed* fraction of the flux). The quantity γ ranges between $1/8$ and $2/7$ for a viscous-dissipation-dominated ($H \propto R^{9/8}$) and an irradiation-dominated disc ($H \propto R^{9/7}$), respectively. The pressure scale-height of the disc, H/R, scales as

$$\frac{H}{R} = \left(\frac{H}{R}\right)_{R_{disc}} \left(\frac{R}{R_{disc}}\right)^{\gamma}. \quad (1.28)$$

Overall, the disc temperature distribution considering both *viscous dissipation* (Equation 1.20) and *irradiation* (Equation 1.27) can then be written as

$$T_{eff} = (T^4_{eff,visc} + T^4_{eff,irr})^{1/4}, \quad (1.29)$$

with the two contributions scaling as $T_{eff,visc} \propto R^{-3/4}$ and $T_{eff,irr} \propto R^{-1/2}$. This shows that irradiation inevitably becomes more and more important as we go to larger and larger radii since $T_{eff,irr}$ drops less steeply than $T_{eff,visc}$. Of course, to what extent irradiation modifies the temperature profile of the disc is linked to its shape as it defines the fraction of the X-ray reprocessing. For instance, if we assume the irradiating source is in the middle of the disc, its light intercepts a bigger solid angle in a flared or a convex disc than in an equatorial, flat disc.

1.4 The transient nature of accreting systems

The previous section highlighted the DIM and its different flavours, which is thought to be responsible for the transient behaviour in CVs and LMXBs. In general, systems in *quiescence* (low-accretion regime) are less-explored, since these phases are quite challenging observationally due to their faintness. In quiescence, the disc is cold and faint while radiation from the donor star dominates. Advection is likely to play a crucial role in this low-accretion regime, and the inner disc may be characterised by an optically thin ADAF (e.g. Narayan and Yi, 1994, 1995). On the other hand, the outburst periods of these sources are well-explored. Their high luminosity permits us to study their broad-band emission as their spectral energy distribution (SED) ranges from radio to X-ray wavelengths. In particular, in LMXBs, the innermost[12] regions around the NS or BH emit mainly in X-rays, while in CVs, for example, the same regions emit in the extreme UV (EUV).

In LMXBs, X-ray observations have shown that the outburst evolution is *hysteretic*, as these sources cycle between two distinct accretion states, the *hard* and the *soft* state, via two different paths. This behaviour sketches a "q-shaped" curve in the *hardness-intensity diagram* (HID), where the spectral hardness[13] of the source is plotted against its X-ray luminosity. A characteristic example is displayed in Figure 1.10, which showcases the HID of the BH LMXB GX 339-4 during its 2002-2003 outburst (Belloni et al., 2005; Romero et al., 2017). The X-ray behaviour of this system during the same outburst, as monitored by *Rossi X-ray Timing Explorer* (RXTE), is shown in Figure 1.11 (Belloni et al., 2005). It is worthwhile to mention that a similar hysteretic pattern has also been discovered in CVs (Körding et al., 2008, for the case of the DN SS Cygni), although it is not clear whether this can be interpreted in the same way as for LMXBs (Hameury et al., 2017).

The interchange between the hard and the soft state, though, mainly concerns BH binaries, rather than NS systems. Aql X-1, for example, is one typical case that a NS system may display hysteretic behaviour (Körding et al., 2008). In the majority of (weakly-magnetised) NS LMXBs, though, the observed behaviour may be completely different, presenting a clear dichotomy in mass accretion rates. Having said that, two subclasses arise, i.e. the atoll and Z sources, which sketch defined paths at the X-ray colour diagram (e.g. van der Klis, 1989). As NS binaries are not discussed in this thesis, this section aims to bring familiarity to the reader only about the outburst evolution in BHXTs.

[12] The mentioned innermost regions include both the inner disc and the boundary layer in the case of solid accretors, i.e. WDs and NSs.

[13] The X-ray spectral hardness or hardness ratio defines the energetics of the X-ray emission and is expressed as

$$\mathrm{X-ray\ hardness\ ratio} = \frac{\mathrm{Hard} - \mathrm{Soft}}{\mathrm{Hard} + \mathrm{Soft}} \times \mathrm{X-ray\ photon\ rate}.$$

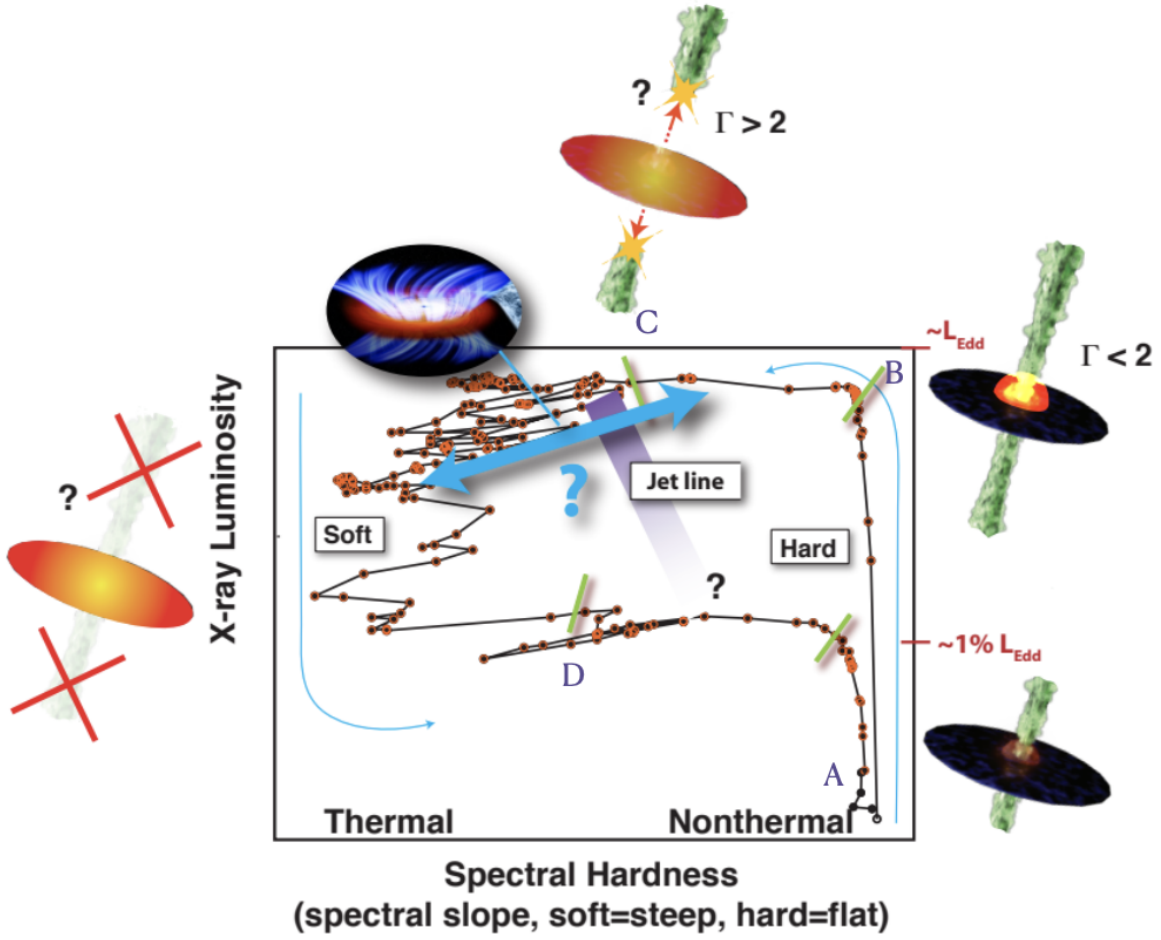

FIGURE 1.10: HID of the LMXB GX339-4, where the x-axis represents the spectral hardness of the source and the y-axis, its X-ray luminosity. The source presents a hysteretic behaviour (follow the blue arrow between the different states), as it transitions from the hard state to the soft state and returns back to the hard state at the end of the outburst (hard → soft → hard). The nature of the radiation (thermal/non-thermal) and the spectral indices of the dominant component at each case are also highlighted. The appearance (or not) of different type of outflows (jets: hard state, winds: soft state) are displayed through schematic illustrations. The A-D letters identify the transitions between the two states during the eruption. In particular, A signifies the low-hard state, B the transition between the hard and soft state (encompassing the intermediate states), C represents the beginning of the soft state and D the transition back to the hard-intermediate/low hard state. Figure adapted from Romero et al. (2017).

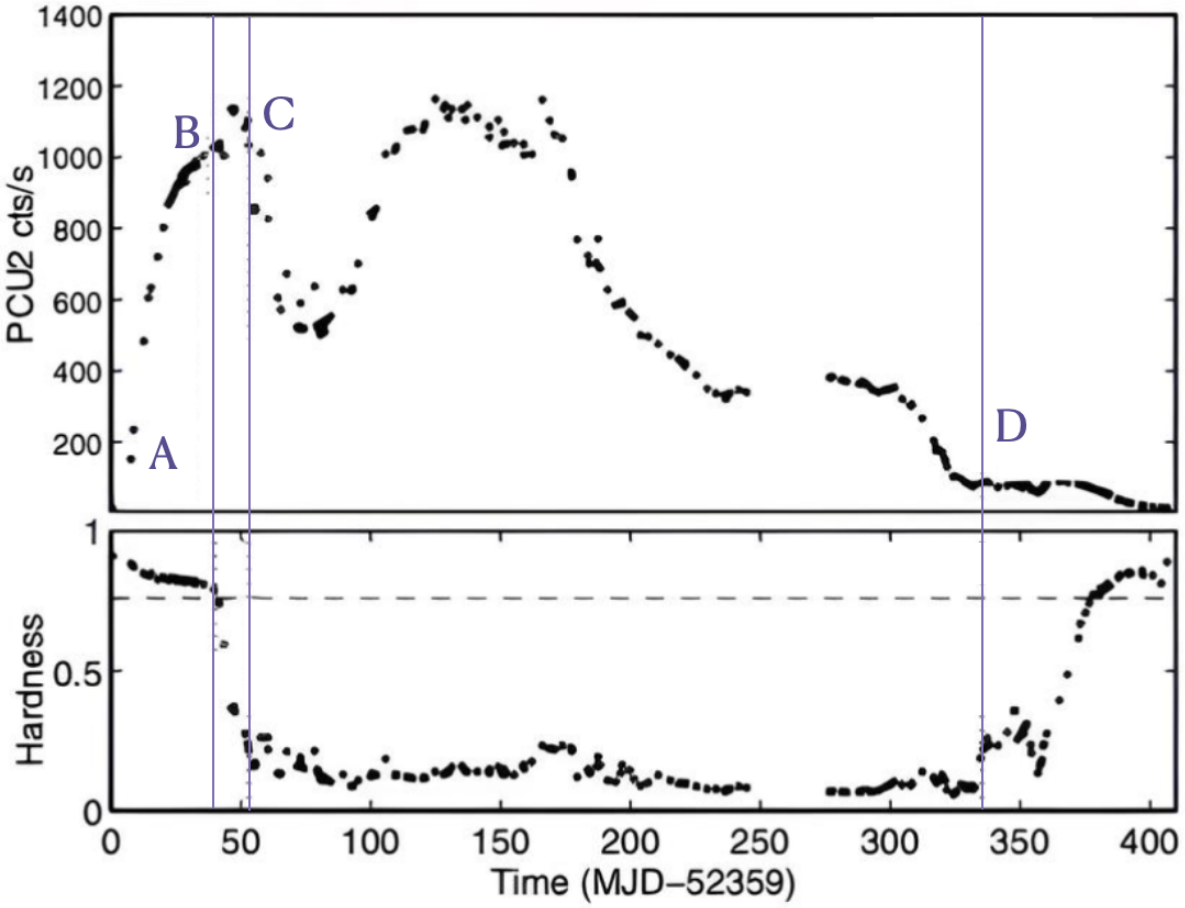

FIGURE 1.11: The upper panel demonstrates the X-ray light curve of the LMXB GX339-4 during its 2002-2003 outburst, as was observed by *RXTE*/PCA while the lower panel its respective hardness. The three vertical lines correspond to transitions between the states. The used notation (A,B,C and D) has been explained in Figure 1.10, which shows the corresponding HID of the source. It is noted that the horizontal line at the hardness panel signifies the hardness value, as the system evolves from the right to the left side of the HID. Figure adapted from Belloni et al. (2005).

1.4.1 The BHXT properties along the outburst

The accretion states of BHXTs are defined by their X-ray spectral and temporal properties (e.g. Esin et al., 1997; Homan et al., 2001; Zdziarski and Gierliński, 2004; Homan and Belloni, 2005; Remillard and McClintock, 2006; Done et al., 2007; Gilfanov, 2010; Belloni and Motta, 2016). They evolve in the course of an eruption as the geometry of the accretion flow changes. The majority of these systems succeed in completing the full hysteresis outburst cycle, although there are systems that fail to accomplish this. For example, some BH binaries undergo the so-called *failed-transition outbursts*, during which they never reach a soft state before their return back to quiescence (e.g. Alabarta et al., 2021, for a comprehensive study on these systems). Throughout a canonical outburst though, a source will pass through four main accretion states: the *low-hard state* (LHS), the

hard-intermediate state (HIMS), the *soft-intermediate state* (SIMS) and the *high-soft state* (HSS), creating an HID as the one seen in Figure 1.10. This figure will be my reference point throughout this section as I describe both the spectral and timing properties of a typical BHXT.

At the beginning and end of the eruption (lower right part of Figure 1.10), the source is in the LHS. Here, the accretion disc is thought to be located far away from the BH, and the mass accretion rate is fairly low, e.g. $\sim 0.01 L_{edd}$ for GX 339-4. The X-ray spectrum is dominated by non-thermal radiation in the form of a hard power-law ($\Gamma < 2$) component with a high-energy cutoff (around 100 keV). This is usually interpreted as the result of inverse Compton scattering of low-energy photons by relativistic electrons in a hot "corona", i.e. a Comptonisation region. The concept of the corona is essentially that of a hot cloud around the BH for which different geometrical configurations have been proposed (e.g. Bambi et al., 2021). A weak thermal component is also apparent at low-energies (e.g. Grove et al., 1998), a feature attributed to the radiation from the accretion disc. In this state, strong X-ray aperiodic variability − on the order of 20%-50% (e.g. Belloni et al., 2005; Muñoz-Darias et al., 2011; Belloni and Stella, 2014; Motta, 2016) is typically seen in variability studies. A useful tool in this context is the *rms-intensity diagram* (Muñoz-Darias et al., 2011), which tracks the variability evolution throughout the eruption and shows its tendency to decrease as the source proceeds to the HSS. In the LHS, the *power density spectra* (PDS) are characterised by band-limited (red) noise, but broad peaks, known as *quasi-periodic oscillations* (QPOs), may also be present.

As the outburst progresses, and the luminosity rises, the source moves upwards in the HID (at constant spectral hardness). At some luminosity, i.e. $\sim L_{edd}$ for GX 339-4, it is going to turn to softer hardness ratios, signifying its arrival at the HIMS (upper right part of Figure 1.10). The X-ray spectrum becomes softer, as the accretion disc moves closer to the BH. Here, the PDS are described by the appearance of QPOs on top of the band-limited noise. These signals are primarily prominent in the low-frequency regime (LF-QPOs), but high-frequency QPOs (HF-QPOs) have also been discovered in the hard state (e.g. Casella et al., 2004; Motta et al., 2011; Belloni et al., 2012). The low-frequency oscillations in this state are called *type-C* QPOs (ν_{QPO}=few mHz-10 Hz) and are most likely associated with either geometrical effects, such as the Lense-Thirring precession of the hot accretion flow in the vicinity of the BH (e.g. Stella and Vietri, 1998; Stella et al., 1999; Schnittman et al., 2006; Ingram et al., 2009; Ingram and Motta, 2019), instabilities such as the accretion/jet instability (e.g. Tagger and Pellat, 1999; Varnière et al., 2002, 2012; Ferreira et al., 2022), or corona oscillations (e.g. Titarchuk and Fiorito, 2004; Cabanac et al., 2010). Collimated, relativistic jets (e.g. Markoff et al., 2001; Corbel et al., 2003; Fender et al., 2004, 2009; Fender and Gallo, 2014) are observed in the radio and infrared bands.

The transition between HIMS and SIMS (*jet line* in Figure 1.10) is difficult to detect and may coincide with the quenching of the radio jet (e.g. Gallo et al., 2003; Corbel et al., 2003; Fender et al., 2009) and the appearance of a *type-B* QPO (ν_{QPO}=5-6 Hz) at the PDS (e.g. Belloni and Motta, 2016). The distinct timing properties between these short-lived phases elucidate the passage from one stage to the other (as the luminosity is mostly constant). At the SIMS, the disc thermal emission

begins to dominate, the aperiodic X-ray variability decreases even more (compared to the previous stages), and the PDS may display *type-A* ($\nu_{\rm QPO}$ =6-8 Hz; Miyamoto et al., 1993; Belloni et al., 2005) or *type-B* QPOs (e.g. Belloni and Motta, 2016). Eventually, the HSS is reached (upper left part of Figure 1.10). The luminosity of the system will start to drop and it will move vertically down the HID until it reaches the lower part of the HSS. Here, the accretion disc has reached the ISCO. The X-ray spectrum is dominated by blackbody emission ($\Gamma > 2$) from a geometrically thin, optically thick accretion disc, whereas the power-law component contributes only few % of the total flux, extending in a coronal tail beyond 500 keV. On the other hand, in the timing domain, variability during the soft state is limited to amplitudes of a few % (commonly between 1%-5%; e.g. Casella et al., 2004; Belloni et al., 2005; Muñoz-Darias et al., 2011; Belloni and Stella, 2014; Motta, 2016), while the QPO signatures are broader and weaker than the ones found in the hard state. In HSS, highly ionised X-ray disc winds emerge (e.g. Miller et al., 2006b, 2008; Neilsen and Lee, 2009; Ponti et al., 2014, 2016; Díaz Trigo and Boirin, 2016; Higginbottom et al., 2018) instead of jets seen before (see more in Section 1.4.2). After the HSS is over, the system passages through HIMS until its final transition back to the LHS (horizontal line at the HID). At the end of the outburst, this transition seems to occur near $\sim 0.02 L_{\rm edd}$. The HIMS and LHS share the same properties and characteristics as their respective state in the beginning of the eruption.

Reflection signatures are also observed in the X-ray spectra of BHXTs, mostly taken during the *hard* state. Hard X-ray photons produced in the Comptonisation region can intercept the accretion disc and either be scattered by free electrons (Compton scattering) or absorbed by heavy elements in the disc (like iron) and then re-emitted. These processes procure discrete features at the X-ray spectrum, such as the Compton hump (which is mostly seen between 20-30 keV) and the fluorescent Fe Kα emission line (at 6.4 keV) or K-edge. Inextricably linked to relativistic distortions in the vicinity of the BH, the shape of these signatures are influenced by phenomena such as gravitational redshift and (relativistic) Doppler shifts as the disc rotates. Nevertheless, these reflection signatures are useful as we can extract information about the plunging region (region between ISCO and the event horizon of the BH, where material is in free-fall motion) and the ionisation state of the disc. For example, the velocity width of the relativistically broadened Fe Kα line depends primarily on the inner disc radius (the ISCO) and, therefore, on the BH's spin.

1.4.2 Outflows: jets and winds

Outflows impact the accretion flow and provide mechanisms for feedback between systems and their environments. In BHXTs, the standard picture is that outflows come in two flavours, based on the accretion state of the system (e.g. Miller et al., 2006a, 2008; Neilsen and Lee, 2009). Indeed, when the source is in the hard state (right branch of the HID in Figure 1.10), compact, relativistic jets are seen, and synchrotron (radio) radiation is emitted. As the inner disc moves inwards towards the ISCO, and the source transitions from the hard to soft state, the jet properties change. There is no detection of steady jets, but as the jet line is crossed, luminous radio flares are produced (e.g. Fender et al., 2004, 2009; Miller-Jones et al., 2012). These are thought to be associated

with the ejection of the inner accretion flow in distinct "blobs", which are sometimes resolved spatially later on during the soft state, as they move out and interact with the ISM. Characteristic is the case of the microquasar GRS 1915+105 and its superluminous ejecta (Mirabel and Rodríguez, 1994). The soft state is also characterised by a suppression of the jet, while ionised X-ray winds take its place (e.g. Gallo et al., 2003; Fender et al., 2009; Neilsen and Lee, 2009; Miller-Jones et al., 2012). By the end of the outburst, the X-ray spectrum becomes harder again, and the radio jet reappears.

The seen connection between the accretion state and the emergence of radio jets is known as the *disc-jet coupling*. This may be illustrated through the found correlation in the hard state between the X-ray and radio luminosities of such systems. This phenomenon is not mutually exclusive to BHXTs, but also observed in NS LMXBs (e.g. Corbel et al., 2003; Gallo et al., 2003; Migliari and Fender, 2006; Gallo et al., 2014, 2018). For completeness, I note that the emission from a partially self-absorbed (optically thick) jet, found at the hard state, can be described by a flat/inverted spectrum. This constitutes the superposition of frequency-dependent synchrotron spectra ranging from radio to the infrared. The infared component, in particular, corresponds to the base of the jet and can be used to infer the location of its release (e.g. Markoff et al., 2003) from an optically thin disc (e.g. Marino et al., 2021; Marcel et al., 2022). As we go towards the radio though, the emission originates from higher and higher layers of the jet as we move outwards.

On the other hand, wind signatures in the form of *blue-shifted* X-ray absorption lines are mainly found in the soft state, where (hot) ionised, equatorial X-ray winds are present, and mostly absent in the hard state, where synchrotron emission from the jet dominates. Winds may remove both mass and angular momentum away from the system as the material becomes unbound from the atmosphere of the accretion disc. The three contestants that can battle against gravity are thermal, magnetic, and radiation pressure. To see this quantitatively, we can use the general equation describing the conservation of angular momentum in magnetohydrodynamics, which is

$$\rho \frac{\mathrm{d}\vec{v}}{\mathrm{d}t} = -\nabla \mathrm{P} + \frac{(\nabla \times \vec{\mathrm{B}}) \times \vec{\mathrm{B}}}{4\pi} + \rho \vec{\mathrm{g}}_{\mathrm{rad}} + \rho \vec{\mathrm{g}}. \tag{1.30}$$

Here, all of the force/pressure terms have been summed to the right part of the equation. The forces that may act against gravity, $\rho\vec{\mathrm{g}}$, are the thermal pressure, $-\nabla \mathrm{P}$, the magnetic pressure $(\nabla \times \vec{\mathrm{B}}) \times \vec{\mathrm{B}}/4\pi$ or the radiation pressure, $\rho\vec{\mathrm{g}}_{\mathrm{rad}}$. Thus *thermally-driven*, *magneto-centrifugal* and *radiatively-driven* winds can, in principle, be formed, respectively, depending on which of these terms dominates. For example, in BHXTs, strong X-ray irradiation can lead to the formation of a *thermally-driven* wind (e.g. Begelman et al., 1983; Higginbottom et al., 2017, 2018). The heating of the upper layers of the outer disc's atmospheres by the central X-ray emitting source results in gas acquiring thermal velocities that surpass the local escape velocity of the medium, enabling it to escape.

Even though wind signatures are inclination dependent (e.g. Ponti et al., 2012, 2014; Díaz Trigo and Boirin, 2016), the anticorrelation between wind and jet signatures has long been recognised.

It is still not understood, however. It may be associated with the nature of the outflows or how they are triggered in the course of the outburst, as the accretion flow evolves. Of course, there is also the possibility that the absence of observational signatures is merely a type of selection effect. For example, a wind could be present, but too highly ionised in some states to produce spectral signatures (e.g. Díaz Trigo et al., 2014; Díaz Trigo and Boirin, 2016).

In any case, simultaneous wind and jet signatures in the hard state have been found in a number of high-luminosity sources (e.g. Homan et al., 2016; Higginbottom et al., 2020, including both BH and NS systems). This suggests that there is a luminosity dependence in the expression of these signatures over the course of the outburst (Higginbottom et al., 2019). This fact may point to radiation pressure being at least an important factor in driving these outflows.

Wind signatures in bands, other than X-rays, have also been seen in states other than the HSS. Optical/near-infrared (cold) winds have been detected through their *blue-shifted absorption* or *P-Cygni profiles* of the Balmer series and/or He I lines in the hard state of LMXB systems. These systems include V404 Cyg (Muñoz-Darias et al., 2016), V4641 Sgr (Muñoz-Darias et al., 2018), Swift J1357.2-0933 (Jiménez-Ibarra et al., 2019) and MAXI J1820+070 (Muñoz-Darias et al., 2019). Similarly, hard-state UV winds have been detected in two NS systems, Swift J1858.6-0814 (Castro Segura et al., 2022) and UW Crb (Fijma et al., 2023). Soft-state wind signatures are also not restricted to the X-ray band – e.g. Sánchez-Sierras and Muñoz-Darias (2020) have found near-IR winds (Paschen series spectral signatures) in the soft state of MAXI J1820+070. The last system is of great interest to us, since it is the focus of much of this thesis (see Chapters 3 and 4). In Chapter 3, I specifically search for UV disc wind signatures in different stages of the source's 2018 outburst via the UV resonance lines.

1.5 Magnetically-controlled accretion onto white dwarfs

Accretion onto magnetised objects has been a subject of considerable theoretical research, via both analytical studies (e.g. Ghosh et al., 1977; Ghosh and Lamb, 1979a,b; Shu et al., 1994; Lovelace et al., 1995; D'Angelo and Spruit, 2010, 2012) and magnetohydrodynamical simulations (e.g. Romanova et al., 2002, 2003; Zanni and Ferreira, 2013). Although the majority of these studies have been focused on the extreme accretion in NSs, in this section, I am going to focus my attention on the basic principles of the disc-magnetosphere interaction, as well as on the observational characteristics of magnetic CVs. This is going to lay the foundation for our discussion in Chapter 2 about WZ Sge and its possible magnetic nature.

As a reminder, magnetic WD systems can be classified into two main categories, the *polars* ($B_{WD} \geq 10^7$G) and the *IPs* (10^5G $\leq B_{WD} \leq 10^7$G), even though subclasses and outliers exist particularly near the intersection between these regimes. Examples of these more unusual magnetic CVs are the asynchronous polars (e.g. Stockman et al., 1988; Silber et al., 1992; Schwope et al., 1997; Schwarz et al., 2004) or the disc-less IPs (e.g. Buckley et al., 1995; Hellier and Beardmore, 2002).

The current section will not delve into details of these exotic objects, but will focus on the fundamental distinction between polars and IPs, as well as on their different spectral and temporal properties (e.g. Hellier, 2001; Warner, 2003; Ferrario et al., 2015; Mukai, 2017; Page and Shaw, 2022).

1.5.1 The role of the magnetic field

Strong magnetic fields affect the behaviour of the surrounding ionised material and can interact with the inner parts of an accretion disc. If there is an accretion disc surrounding the primary, the magnetic field starts to dominate the dynamics of the system, defining its own "sphere" of influence or *magnetosphere*, at the point where the disc's ram pressure is in equilibrium with the magnetic pressure exerted by the accretor (Pringle and Rees, 1972). Inside this *magnetospheric* radius (R_m), the field guides the gas into the star's surface in free-fall. The exact location of R_m depends on the strength of the magnetic field, with stronger fields resulting in larger magnetospheric radii.

For a spherically symmetric inflow, pressure equilibrium gives

$$P_{ram} = P_{mag} \Rightarrow \rho v_{ff}^2 = \frac{B^2}{8\pi} \Rightarrow \frac{(2GM_{WD})^{1/2}\dot{M}_{acc}}{4\pi R^{5/2}} = \frac{B_{WD}^2 R_{WD}^6}{8\pi R^6}. \tag{1.31}$$

Here, we have assumed *steady-state accretion*, $\rho v_{ff} = \dot{M}_{acc}/4\pi R^2$, where v_{ff} the free-fall velocity ($v_{ff}^2 = 2GM/R$) of the inflowing material. We have also taken the magnetic field to be dipolar, $B(R) = B_{WD}R_{WD}^3/R^3$, where B_{WD} is the WD's magnetic field, and R_{WD} is its radius (Frank et al., 2002).

Under these assumptions, rearranging Equation 1.31, the magnetospheric radius at which these pressures are balanced is also called *Alfvén* radius, R_A, and is given by

$$R_m \equiv R_A = \left(\frac{B_{WD}^4 R_{WD}^{12}}{2GM_{WD}\dot{M}_{acc}{}^2} \right)^{1/7}. \tag{1.32}$$

It is important to note that in some models (e.g. Ghosh et al., 1977; Shu et al., 1994; D'Angelo and Spruit, 2012), the interaction between the field lines and the disc is expressed through a slight modification of the above relation, $R_m = \xi R_A$. The dimensionless normalisation factor, $\xi \simeq 1$, is included to recognise the simplistic nature of the spherical inflow scenario described above. The nature of the rotating accretor constrains its value to lie in the range ξ=0.5-1 for magnetised NSs (e.g. Ghosh et al., 1977) and 0.4-0.5 for magnetised WDs (e.g. Long et al., 2005). In general, for magnetic accretion from a disc, a value of ξ=0.5 is often assumed.

The relationship between the magnetospheric and circularisation radius (Equation 1.14) provides us with a criterion for deciding whether a disc should be formed at all. In polars, for example, it

is expected that the magnetospheric radius lies beyond the circularisation radius of the accretion disc, $R_m > R_{circ}$, and therefore, an accretion disc is *not* formed. Instead, material is strongly-coupled to the magnetic field lines (at or near L_1) and is deposited onto the WD's polar caps in a collimated accretion column (e.g. Frank et al., 2002; Warner, 2003). In IPs, on the other hand, a (partial) disc is created as $R_m < R_{circ}$. The following figure, Figure 1.12, compares different accretion flows in various types of CVs: a non-magnetic CV (left), an IP (center), and a polar (right).

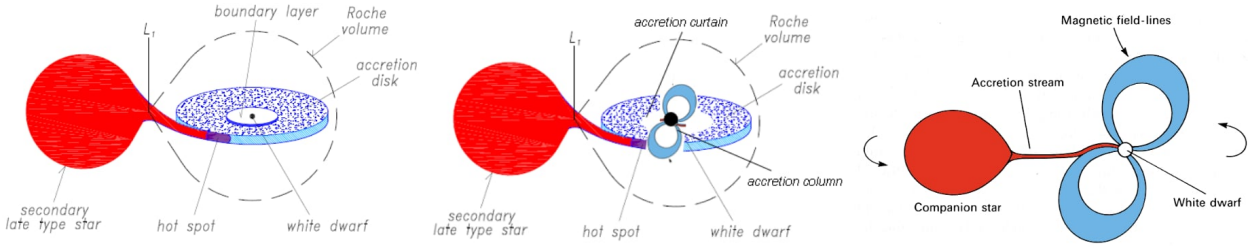

FIGURE 1.12: Illustrative sketches of accretion mechanisms in CVs. The left panel shows the case of a non-magnetic CV undergoing Roche lobe overflow. The center and right panels show magnetised WD systems: in the IP case (center), the strong magnetic field disrupts the inner accretion disc, channeling material along magnetic field lines, whereas in the polar case (right), the accretion stream directly follows the field lines without the formation of the disc. Figure taken from Giovannelli (2017).

How does the magnetic field actually change the accretion flow in these systems? At $R \simeq R_m$, the field truncates the inner disc regions. What happens next depends on whether R_m is smaller or larger than the *corotation radius*, R_{co}. This is the radius in the disc where the Keplerian angular velocity – $\Omega_K(R) = (GM_{WD}/R^3)^{1/2}$ – matches the angular velocity of the accretor – $\Omega_{WD} = 2\pi/P_{spin}$, where P_{spin} is the spin period of the WD. The corotation radius is therefore defined by the condition $\Omega_K(R_{co}) = \Omega_{WD}$, giving

$$R_{co} = \left(\frac{GM_{WD}P_{spin}^2}{4\pi^2}\right)^{1/3}. \tag{1.33}$$

The criterion that determines whether material is accreted or expelled from the system is whether the inner edge of the disc rotates *faster* or *slower* than the star. As a result, two accretion regimes can be identified:

- If $R_m < R_{co}$, matter at the inner edge of the disc is moving faster than the star, $\Omega_{WD} < \Omega_K(R_m)$. In this case, we are going to have *channeled accretion*, where the magnetic field lines will guide the gas onto the star's magnetic poles in an *accretion column*. Upon collision with the upper layers of the WD photosphere, a shock is formed, thermalising ($T_{shock} \approx 3GM_{WD}m_H/8k_BR_{WD}$ =10-50keV) and decelerating the infalling material (Frank et al., 2002). In the steady state, the accreting gas releases the fraction of L_{acc} that has not already been released in the disc as it moves along the accretion column and impacts on the star. Thermal

bremsstrahlung[14] (hard X-rays) and *cyclotron*[15] emission (optical/infrared) are primarily radiated throughout the column. In addition, close to the WD surface, a significant portion of the bremsstrahlung and cyclotron radiation is reprocessed, i.e. absorbed and re-emitted in longer wavelengths (soft X-rays/UV radiation). Smaller contributions to the overall spectral energy distribution may also be observable from the post-shock region (soft X-rays) or we may observe line emission throughout the column (e.g. Mukai, 2017). The interplay between the two prominent cooling mechanisms (bremsstrahlung/cyclotron) depends on the strength of the magnetic field and the mass accretion rate per unit area[16] (also known as the specific mass accretion rate, $\dot{m}$). These parameters permit a clear distinction between different types of magnetic accretion flows. In WD systems with moderate B_{WD} and high $\dot{m}$, like IPs for instance, the cyclotron cooling contribution is negligible. In this case, material in the hot post-shock region (mostly electrons and ions) exchanges energy much faster than the electrons' radiative loss timescale, allowing us to treat them as a unified one-temperature plasma (e.g. Aizu, 1973; Lamb and Masters, 1979; Wu et al., 1994). Note that the radiative cooling is primarily carried out by electrons rather than ions, as electrons have smaller mass and, consequently, higher interaction cross-sections. Cyclotron cooling becomes important as the field becomes stronger and/or the specific mass accretion rate drops, breaking the simplicity of the above treatment as ions and electrons can attain different temperatures (e.g. Wu, 2000; Saxton et al., 2005, and references therein).

- If $R_m > R_{co}$, the object rotates faster than material at the inner disc edge, $\Omega_{WD} \geq \Omega_K(R_m)$. A "centrifugal barrier" is created, which prevents the material from accreting onto the rotating object. Instead, it gets ejected out to large radii. Of course, preceding this outcome, the gas will be forced to corotate for potentially quite a while with the field. This means that it can be accelerated effectively all the way out to some radius, R_a. In order to become unbound, the only thing which is required is that $v_{outflow} > v_{esc}(R_a)$, where $v_{esc}^2 = GM_{WD}/2R_a$ is the local escape velocity at the radius where acceleration stops. The system resides in a *propeller state*, characterised by an observed drop in luminosity in its light curve (e.g. Illarionov and Sunyaev, 1975; Syunyaev and Shakura, 1977). This drop happens because a lot of the accretion luminosity is not released radiatively in the propeller state. Instead, it goes into ejecting the material and into spinning down the WD (since that supplies the torque for the outflow). It is straightforward to estimate the mass accretion rate, $\dot{M}_{lim}$, reaching the centrifugal barrier and hence the limiting luminosity, L_{lim}, of different systems by the apparent distinctive

[14] Bremsstrahlung (or free-free) radiation is emitted as a (free) charged particle decelerates when encounters the electric field of another (free) charged particle, i.e. an electron or an atomic nucleus. The field will force the particle to divert its trajectory by losing energy. In our case, electrons do decelerate when deflected by ions at the WD's photosphere.

[15] Cyclotron radiation is emitted by acceleration of charged particles, e.g. electrons, due to the presence of the magnetic field. The acceleration is procured by the exerted Lorentz force as particles spiral around the field lines. The constructed spectrum is discrete as emission is radiated at the cyclotron frequency and its harmonics. The cyclotron frequency is given by $\omega_c = nqB/mc$ (cgs units), where n=1,2,3,...n the number of the harmonics, B the magnetic field's strength, m and q the particle's mass and charge and c the speed of light.

[16] The specific mass accretion rate, $\dot{m}$, is usually used in this context (rather than $\dot{M}_{acc}$) since it is important to account for the channeling effect of the magnetic field as it accretes onto the WD surface.

drops in their light curves. Following Campana et al. (2002), the limiting luminosity can be expressed as

$$R_m = R_{co} : L_{lim}(R) = \frac{GM\dot{M}_{lim}}{R} \Rightarrow L_{lim}(R) \sim 1.97 \times 10^{38} \xi^{7/2} \mu_{30}^2 P_{spin}^{-7/3} M^{-2/3} R_6^{-1}, \quad (1.34)$$

where μ, P_{spin}, M, R are the magnetic moment, spin period, mass and radius of the involved object, respectively. Transitions into and out of the propeller regime have been suggested to occur in accretors of all scales, including LMXBs, HMXBs, IPs and YSOs, as demonstrated in Figure 1.13. It is worth noting that this is – in principle – a direct observational method to estimate the magnetic field strength of rotators, if everything else is known.

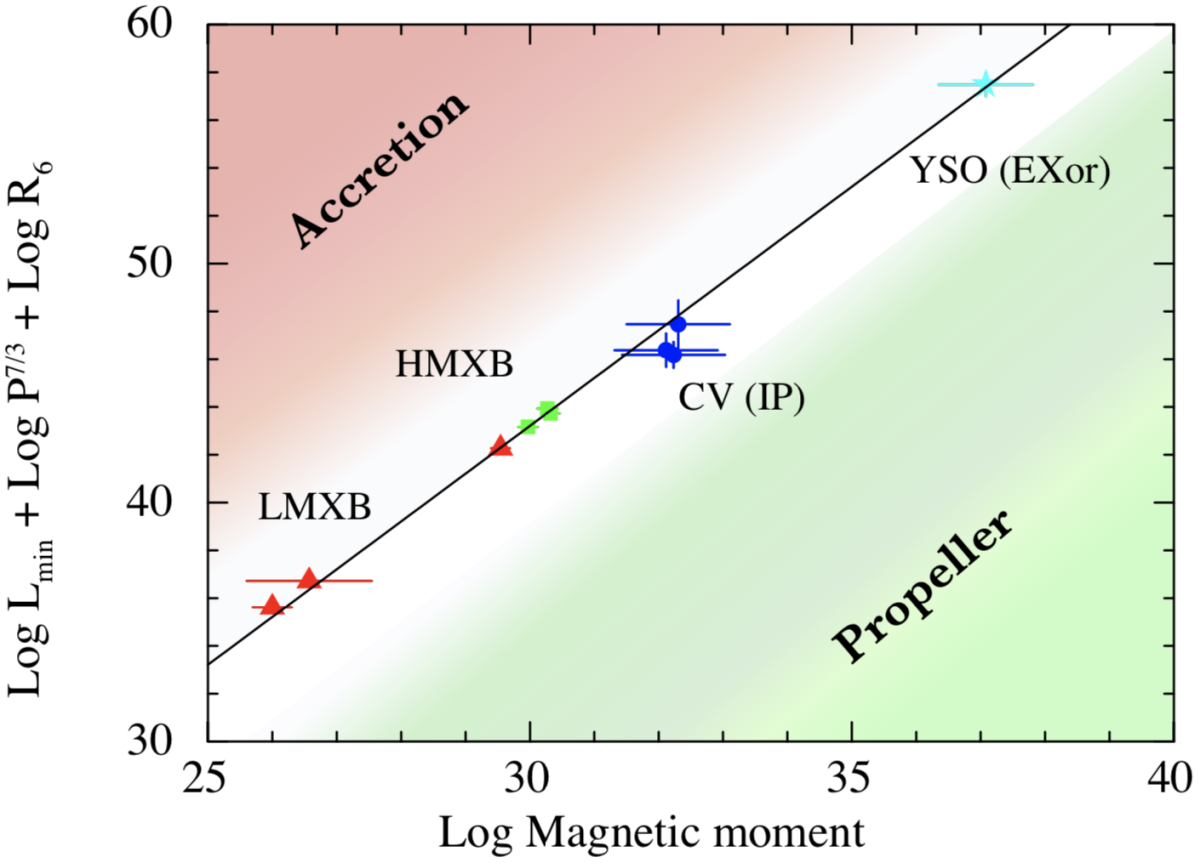

FIGURE 1.13: Correlation between physical parameters of rotators of all scales, such as the magnetic moment, spin period and radius at the point where the outburst light curves appear a drop in the luminosity, L_{min} (onset of the propeller regime, Equation 1.34). Different classes of sources are sketched in this diagram: the red triangles represent the LMXBs, the green squares the HMXB systems, the blue dots the IPs and the cyan stars the YSOs. The black solid line divides the region where accretion onto the system's surface takes place with the region where the propeller dominates. Figure taken from Campana et al. (2018).

1.5.2 Magnetic cataclysmic variables

Magnetic WD systems are remarkably common, although the field's origin and evolution are still under investigation (Schreiber et al., 2021). Volume-limited (d $<$ 150 pc) CV demographics have shown that more than one-third (36%) of the local CV population consists of magnetic WD binaries (Pala et al., 2020). Here, my aim is to give a brief overview of the observational properties regarding these two classes of CVs (e.g. Warner, 2003; Hellier, 2001; Ferrario et al., 2015; Mukai, 2017; Page and Shaw, 2022). The following section is based on information found in the aforementioned studies, if not otherwise stated.

1.5.2.1 Polars

Polars (or AM Her systems − named after AM Herculis, the prototype system that showed similar characteristics), are close, disc-less systems, where the magnetic field is strong enough, $B_{WD} \geq 10^7$G, that magnetic torques have *synchronised* (tidally-locked) the orbit with the WD rotation, i.e. $P_{orb} = P_{spin}$. Hence this is the period of the observed variability in their light curves (e.g. Cropper, 1990, for a detailed review). In this strong B_{WD}/low $\dot{m}$ regime, the post-shock region is described by radiative losses via optically thick (circularly and linearly) polarised cyclotron emission − radiated at optical, near-infrared and sometimes, UV wavelengths. UV cyclotron emission has been detected only in few systems, whose magnetic field is quite strong (e.g. Gänsicke et al., 2001; Ferrario et al., 2003, for the case of AR UMa). These polarisation signatures constitute not only an essential tool to measure the field strength of these objects, but are crucial to our understanding of the structure and the geometry of their accretion flows (e.g. Cropper, 1990; Ferrario et al., 2015). On the other hand, bremsstrahlung radiation acts complementary to the overall radiative cooling of the post-shock region, contributing only a small percentage to the hard X-ray luminosity of the system.

Among magnetic WD binaries, the magnetic field strength can be determined observationally only in polars. Methods such as Zeeman splitting of photospheric optical absorption lines (e.g. Balmer series − low-mass accretion rates), modelling of cyclotron harmonic features (apparent at the optical/infrared spectra) or finally, polarisation measurements (ratio of the linear to circular polarisation) are typically employed (Cropper, 1990). Note that although estimating field strength is beyond the scope of the current thesis, these methods are mentioned here for completeness.

1.5.2.2 Intermediate polars

IPs are accreting WDs with weaker magnetic fields that do not prevent the formation of an accretion disc. Instead, the material that reaches the magnetosphere is channeled into the WD's poles through the formation of *accretion curtains* (larger effective area covered by the accretion column). The (partial) disc may still be susceptible to the thermal-viscous instability, as seen in other DNe.

Indeed, a fraction of IPs shows outburst episodes, although these are rarer and much shorter in duration due to the impact of the field (Hameury and Lasota, 2017).

In these systems, the magnetic torque has *not synchronised* the WD with the orbit ($P_{orb} > P_{spin}$) either due to the WD's internal weaker magnetic field or the large separation of the two components (the magnetic field drops as R^{-3} with distance). Observationally, it is certainly true that the orbital periods of IPs are very different from those of polars (e.g. Patterson, 1994; Ferrario et al., 2015). A controversial, at the time, idea was when Chanmugam and Ray (1984) emphasised that the IPs may be progenitors of polars, i.e. that their weaker magnetic field had not allowed the system's synchronisation − yet (e.g. Chanmugam and Ray, 1984; Pretorius et al., 2013). The evolutionary connection between these two classes, currently, is a fairly unexplored domain.

Due to their asynchronous rotation and the misalignment between their rotator and magnetic axes, multi-periodic variability is detected in both X-ray and optical bands. In particular, these signals are found at both the orbital and spin periods, and, sometimes, also in an orbital sideband, expressed as $P_{syn}^{-1} = P_{spin}^{-1} - P_{orb}^{-1}$ (synodic period). The detection of variability in the sideband periods may be the result of reprocessing of radiation in various parts of the system, such as the disc itself. Spectroscopically, in this moderate B_{WD}/high $\dot{m}$ regime, much of the accretion luminosity is released at the WD's surface through optically thin bremsstrahlung radiation (Section 1.5.1). Circular polarisation is not an obvious feature in the spectra of IPs (Wickramasinghe et al., 1991), but it has been detected in few systems (e.g. Butters et al., 2009; Katajainen et al., 2010; Potter et al., 2012). Due to lack of simultaneous optical/near-infrared polarisation measurements (e.g. Wickramasinghe et al., 1991; Ferrario et al., 2015), magnetic field strength determination is quite difficult in these systems.

1.6 Open questions and thesis outline

This introductory chapter has given us the essential ingredients in our quest to understand accreting compact binaries a bit better and it serves as our guideline to establish the proper background for the upcoming chapters. In particular, we have explored how these binaries are formed and evolve, how accretion discs around compact objects are produced and the way they convert gravitational potential energy to radiation. Furthermore, it was introduced that these discs are most likely unstable and susceptible to erupt briefly while they are "sleeping" for long periods. Finally, we focused our attention on understanding the observational properties of BH binaries during these eruptions and in the end, how magnetic fields may influence the accretion flow around WDs.

Even though I would like to provide an introduction consistent and self-constrained, there are many instances, where interpreting the related phenomena is impeded by uncertainties of various factors. These factors may include the lack of simultaneous multi-wavelength observations in order to characterise its different components at the same time and trace the binary as a whole

body, simplistic approximations of the underlying physics or even observational effects. Some of the *open questions* that we may still have and were expressed throughout this chapter are the following

- Are the DIM modifications enough to explain the wide range of characteristics between DNe and LMXBs? What other factors should be taken into account?
- What is the origin of hysteresis in disc-accreting systems?
- What are the driving mechanisms for the manifestation of disc winds?
- Is the clear anticorrelation between jets in the hard state and disc winds in the soft state still valid?
- What causes the periodic and aperiodic variability in these systems?

This thesis presents an effort to tackle some of these issues and discuss their implications through time-resolved UV spectroscopic observations on two objects, the prototypical DN WZ Sge and the BHXT MAXI J1820+070. To be more specific, in *Chapter 2*, I study the outburst evolution of the DN WZ Sge in the aftermath of its outburst. My goal is to explain the process that may be responsible for creating such a peculiar feature, a dip, at the source's eruption decline. Here, I test the idea that this drop in luminosity is due to the transition into a propeller state, as was hinted by Campana et al. (2018). To test and interpret such an idea, I create both time-averaged and variability (RMS) spectra of the source in all of the epochs that I have in my disposal. This is the *first attempt* to look the UV spectral signatures at different stages of the eruption decay and characterise each one of them. This study is a milestone in this path, and an immediate contribution right before the next superoutburst is due.

On the other hand, *Chapters 3 and 4* are devoted to the BHXT MAXI J1820+070. I present, here, the first multi-epoch characterisation of a LMXB in the UV wavelengths. This is a unique opportunity, as most of the LMXBs suffer from high extinction along the line-of-sight. MAXI J1820+070 allows us to study it throughout the whole outburst and compare its signatures between both hard and soft states. Characteristically, I analyse two hard state observations − the first epoch is close to the peak brightness of the source, the second epoch is some days before the hard-to-soft state transition − and a soft state. The UV observations, taken by both the HST and complementary, by AstroSat (covers alone the soft state), permit us to properly characterise the system by measuring its extinction, its spectral and temporal (stochastic and/or UV QPOs) properties throughout the outburst along with the standard reprocessing picture at the outer part of the accretion disc among others. Here, the HST spectra will also allow us to search for UV winds at the hard state while we can characterise the properties of the line-forming regions by modelling the observed emission lines.

Finally, the last chapter, Chapter 5, summarises my results while highlighting the main conclusions and what it has to be done so we can go further.

Part II

Research projects

Chapter 2

Searching for a magnetic propeller in the prototypical DN WZ Sge

...but finding a veiling curtain

"Don't adventures ever have an end?"
"I suppose not. Someone else always has to carry on the story."

-J.R.R.Tolkien, The Lord of the Rings

This chapter is based on the following work published at the MNRAS:

Georganti M., Knigge C., Castro-Segura N., Long K.S., "Plateaus, dips, and rebrightenings during the outbursts of WZ Sge: no magnetic propeller, but a veiling curtain", 2022, MNRAS, 511, 4, 5385

Abstract

WZ Sge is the prototype of highly evolved, low-accretion rate DNe. During the decline from eruptions, its light curve displays a "dip" followed by $\simeq$ 10 "echo-outbursts". The standard DIM does not account for this behaviour, which is also seen in other low-accretion rate DNe. One recent interpretation for these rapid brightness changes is that they represent transitions into and out of a magnetic propeller regime. Here, I test this scenario with time-resolved, ultraviolet spectroscopy taken with the *Hubble Space Telescope* (HST) just before, during and after the dip in WZ Sge's 2001 eruption. I find no distinctive or unique signatures that could be attributed to a propeller in either the time-averaged UV spectrum or the variability spectrum. Thus the data do not support the magnetic propeller scenario. Instead of resolving the mystery of WZ Sge's outburst light curve, my study has actually added another: the origin of the narrow absorption features seen in all outburst phases. I show explicitly that these features are likely formed in a high-density "veiling curtain" with a characteristic temperature T $\simeq 17,000$ K. However, the nature and origin of this veil are unclear.

2.1 Introduction

DNe represent a subcategory of CVs that exhibit eruptions with amplitudes in the range of 2-5 mag (and sometimes even larger) and with recurrence timescales ranging from days to years. The taxonomy of these systems, initially, was purely phenomenological as they were categorised by the morphology of their outburst light curves. Even today, this basic scheme still persists. Based on this type of classification then, three distinct subclasses arise: the U Gem, the Z Cam and the SU UMa systems (see e.g. Hellier, 2001; Warner, 2003, for more information), named after the prototype system of each subclass. The SU UMa stars are subdivided further into different classes, with the WZ Sge-type binaries being of particular interest to us, especially their prototype WZ Sge.

The light curves of systems belonging to these different categories are quite different, as demonstrated in Figure 2.1. For example, U Gem systems are characterised by periodic eruptions, during which their amplitude increases between 2-5 mag in a matter of days before their subsequent return to quiescence (upper panel of Figure 2.1). Z Cam systems show long standstill periods after some outbursts, during which their luminosity lies pretty close to their acquired maximum brightness (middle panel of Figure 2.1). The light curves of SU UMa systems exhibit both normal eruptions and superoutbursts. The superoutbursts are brighter and last longer than normal eruptions and usually appear every few outbursts (lower panel of Figure 2.1). On the other hand, the WZ Sge-type stars exhibit only superoutbursts (Figure 2.5 for WZ Sge's studied 2001 superoutburst).

As noted in Section 1.3.3.2, the variety of additional observed light curve signatures, as the ones portrayed in Figure 2.1, are not always captured by the standard DIM (e.g. as described by Osaki, 1996; Buat-Menard et al., 2001; Lasota, 2001; Hameury, 2020) but can be explained through a combination of factors such as mass transfer fluctuations, donor's irradiation and disc truncation (e.g. Hameury et al., 2000; Smak, 2000). In particular, U Gem-type light curves are typically explained through the DIM successfully, even though disc truncation and a variable mass transfer rate from the secondary are required to reproduce the succession of the outbursts in the U Gem-type DN SS Cygni (e.g. Schreiber et al., 2003). On the other hand, the discs in the Z Cam systems are located on the threshold of being unstable as $\dot{M}_{tr} \approx \dot{M}_{crit}$. The seen standstill periods are due to an increased mass transfer rate from the donor star such that $\dot{M}_{tr} > \dot{M}_{crit}$ (Buat-Ménard et al., 2001).

In SU UMa sources, now, the complexity of the light curves together with the emergence of superhumps have been proven more challenging to decipher. Observationally, superhumps are associated with the manifestation of a superoutburst but there are cases, which may suggest otherwise (Imada et al., 2012; Kato and Osaki, 2013). However, both the TTI and/or irradiation-enhanced mass transfer are considered concrete candidates for producing the observed signatures. Apart from the already mentioned considerations for the manifestation of the TTI in these systems (Section 1.3.3.2), the irradiation-enhanced mass transfer scenario requires the accretion disc to be warped (e.g. Smak, 2009b) for the detection of the superhumps (e.g. Hameury et al., 2000; Smak, 2009a; Hameury, 2020). However, disc warping − the disc's axis is not aligned with

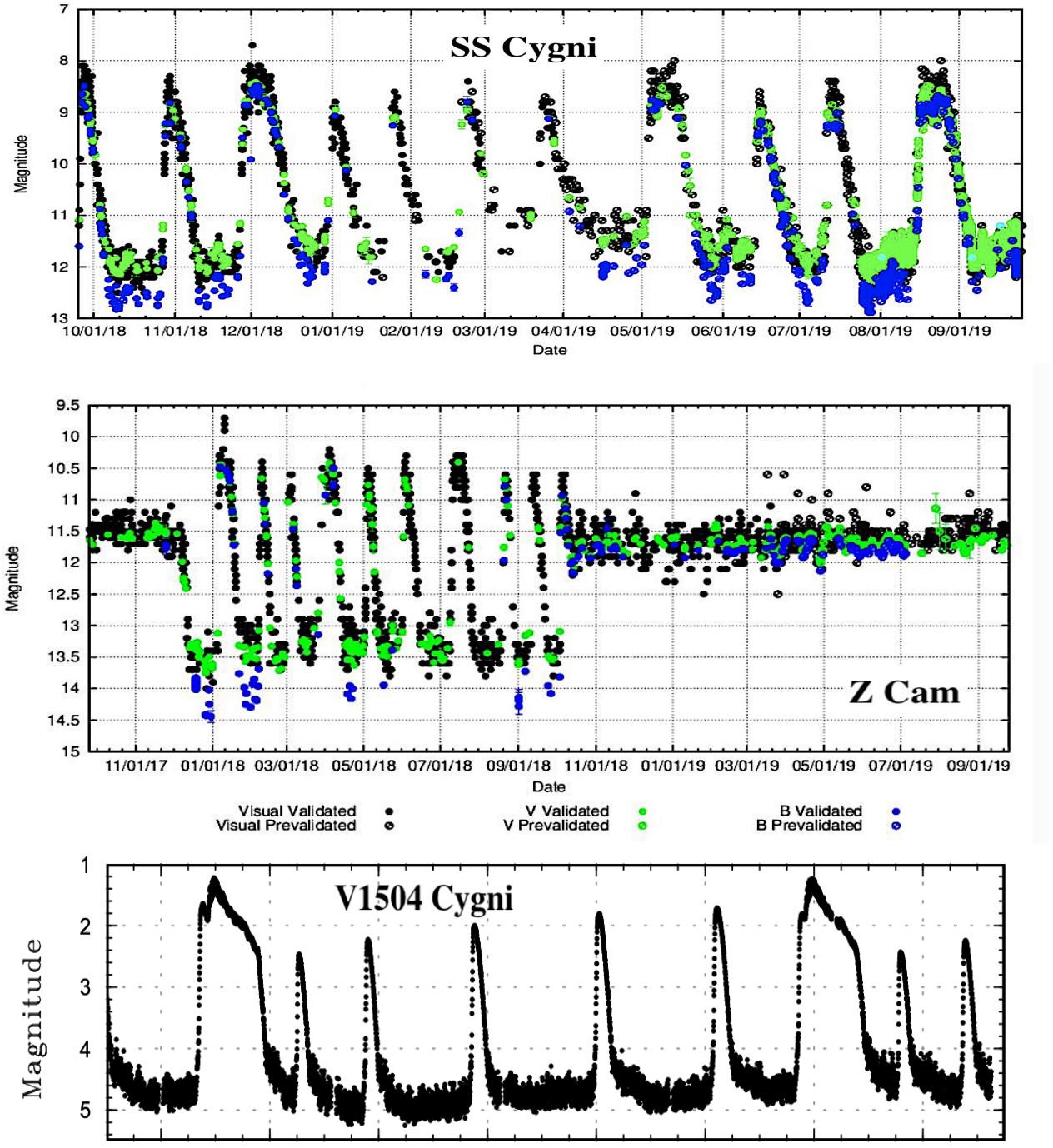

FIGURE 2.1: Optical light curves of different type of DNe. As it is seen, there is a broad range of distinct features that may not be explained through the same mechanism. *Upper panel:* Optical light curve of SS Cygni, a U Gem-type DN, where normal eruptions are seen. *Middle panel:* Optical light curve of Z Cam, where the eruptions are interrupted by a standstill, during which the disc is hot and ionised. These two figures have bee taken from AAVSO. The three colours correspond to different bands (visual: black, V:green, B:blue, see also the legend below the figures). *Lower panel:* Optical light curve of the superoutburst of the SU UMa DN V1504 Cygni. The system produces both normal outbursts as well as superoutbursts where different structures can be seen both in rise and the decline after each eruption. Figure taken from Osaki and Kato (2014).

the spin of the compact object − is something which is not yet explored in CVs. Lastly, in WZ Sge-type systems − these highly-evolved, low-accretion DNe − their superoutburst light curves are described by a distinctive "dip", preceding a series of rebrightening(s) before the systems' return back to quiescence. In this chapter, the goal is to test a recently proposed explanation for one such signature, the demonstrated "dip", seen in the superoutburst decline of WZ Sge.

WZ Sge constitutes one of the closest CVs, located at a distance of d=45.2 $\pm$ 0.1 pc (Gaia Collaboration et al., 2021). It consists of a highly-evolved (brown dwarf) secondary (e.g. Patterson, 2001; Patterson et al., 2005; Steeghs et al., 2007) orbiting a moderate massive WD (Echevarría et al., 2008) with an orbital period of 82min (Krzeminski, 1962). WZ Sge shows spectacular high-amplitude ($\simeq$ 7 mag), long superoutbursts with a recurrence time of almost 30 years (e.g. Kato, 2015, for a detailed review of WZ Sge-type stars).

Its nature was a matter of controversy but it was initially classified as a RN. However, the appearance of *superhumps* (Patterson et al., 1981) at the beginning of the 1978 superoutburst led to the reclassification of the system as part of the SU UMa family. The discovery of these *double-peaked* variations, first discovered in WZ Sge, was attributed by Patterson et al. (1981) to an enhanced mass transfer from the companion star. It is now known that these "early superhumps", as they are called − let us not be confused with the ordinary (single-peaked) superhumps that we have also in SU UMa stars − are a characteristic property of *moderate-* and *high-inclination* WZ Sge-type binaries (e.g. Ishioka et al., 2002, 2003; Pavlenko, 2007; Kato, 2015, and references therein). They are most likely produced as the disc expands and reaches the 2:1 resonance during outburst (e.g. Lin and Papaloizou, 1979; Osaki and Meyer, 2002; Uemura et al., 2012).

The discovery of early superhumps in WZ Sge (e.g. Patterson et al., 1981; Ishioka et al., 2002; Patterson et al., 2002) was just the beginning, as its observed superoutburst light curves were nothing as seen beforehand. For WZ Sge, only four (1913, 1946, 1978, 2001) superoutbursts have been reported and only the last two are well-described. The first three are demonstrated in Figure 2.2 by combining data from Mayall (1946) for the first two events and the American Association of Variable Star Observers (AAVSO) for the last one. The respected datasets have been extracted from Patterson et al. (1981). The 2001 superoutburst is displayed in Figure 2.5 using data from the Variable Star NETwork (VSNET; Kato et al., 2004). It is really astonishing how four superoutbursts of the same system can be so distinctive even though the observational technique and setup(s) are not similar for all the eruptions and should be taken into account (follow discussion on Kato, 2015). A few general patterns can be spotted though. The last two eruptions (1978, 2001) are both described by a slow viscous decline, referred to as the *plateau* phase, a characteristic *dip* and a series of rebrightenings ($\sim$ 1 mag), the so-called *echo-outbursts*. The first two observation series are more elusive, especially the 1946 superoutburst where the dip is not discernible and the lack of echo-outbursts is prominent. Note that there is an observational gap during the supposed rebrightening phase. However, if there was a reflaring phase following the 1946 eruption, it must have been shorter than those seen following the two subsequent superoutbursts (Mayall, 1946; Kato, 2015).

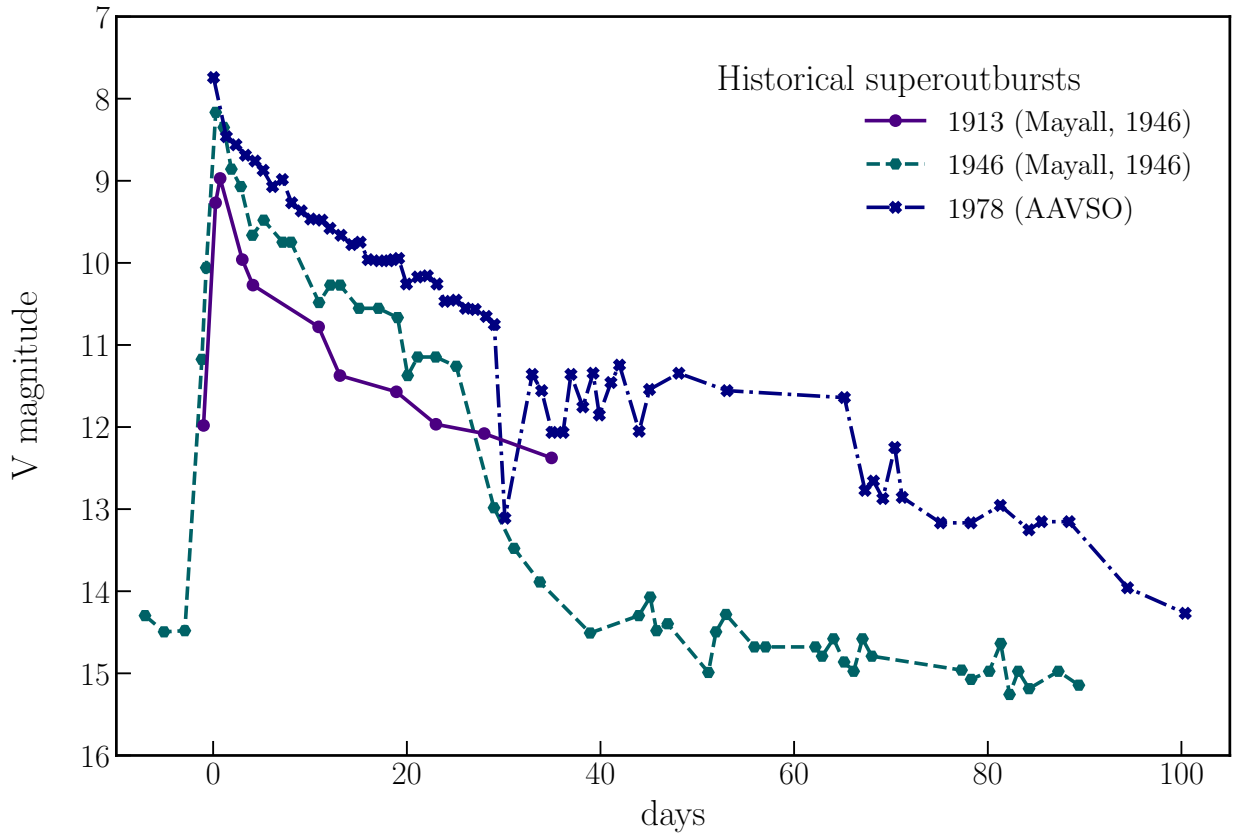

FIGURE 2.2: Optical light curves, binned by day, of the three historical superoutbursts of WZ Sge, extracted from Patterson et al. (1981). Photographic data are employed to create the 1913 and 1946 light curves (Mayall, 1946) whereas the 1978 superoutburst made use of AAVSO observations. For illustration reasons, the magnitude axis of the 1913 and 1946 observations is shifted. The 1913 superoutburst is two magnitudes while the 1946 superoutburst one magnitude brigher. It is worthwhile mentioning the discussion in Kato (2015) regarding the magnitude conversion to modern system standards of the first two recorded superoutbursts, leading to an overestimation of the mentioned magnitudes, if this is not properly conducted.

It was soon realised that additional ingredients – beyond the standard DIM – are needed to explain the intricate and complex patterns of the WZ Sge light curves. The TTI model presents a challenge as it requires an extremely small viscosity α_c value during quiescence (e.g. Smak, 1993; Osaki, 1995) to reproduce the recurrence timescale between superoutbursts and the observed mass accretion rate, $\dot{M}_{acc}$. On the other hand, enhanced mass transfer, disc truncation, donor irradiation, or a combination of all these have been suggested (Lasota et al., 1995; Warner et al., 1996; Hameury et al., 1997). Inner disc truncation in *quiescence* is plausible in WZ Sge, either via evaporation of the inner disc (Meyer and Meyer-Hofmeister, 1994) or by the existence of a magnetic field (Livio and Pringle, 1992). Indeed, the discovery of coherent, fast optical (Robinson et al., 1978; Patterson, 1980), UV (Skidmore et al., 1999) and X-ray oscillations in quiescence (Patterson et al., 1998) around 27.87s may indicate the presence of a magnetic WD, rotating with this spin period.

In contrast, the WD spin period was not identified during either the 1978 or the 2001 superoutburst. Knigge et al. (2002) reports the detection of strong but incoherent 15s UV oscillations as well as weaker 6.5s signals during the echo-outburst phase of its 2001 superoutburst. This study signifies the first attempt to analyse the UV observations of WZ Sge following its 2001 superoutburst, using the same dataset that it is utilised in the current work. The discovery of such features challenges existing models for WZ Sge's variability during outburst, as they are distinct from what has been observed in quiescence. Their origin remains unclear as they do not align with either the pulsating WD or magnetic rotator frameworks, presenting results that are distinct from what has been observed in quiescence. Kuulkers et al. (2011) argue that the 27.87s pulses are only detected during quiescence, as the magnetosphere is suppressed during eruptions (due to the increased mass transfer rate). In this case, WZ Sge would be an IP in quiescence (but probably not in outburst). The nature of WZ Sge − and, in particular, the presence (or not) of a dynamically important magnetic field associated with the WD − is still a matter of debate (also see, for example, Lasota et al., 1999; Matthews et al., 2007; Warner and Pretorius, 2008).

If in fact WZ Sge constitutes an IP system, like the one shown in Figure 2.3, the distinct dip in its outburst light curve (seen in the last two eruptions) might be the observational signature of the system that transitions into and out of a propeller state (Campana et al., 2018). Even though this mechanism is most commonly considered in the context of NS X-ray binaries (e.g. Gilfanov et al., 1998), the propeller transition has been suggested to occur in many accreting transient sources that harbour accretion discs, including objects such as LMXBs, HMXBs, IPs and YSOs. Campana et al. (2018) provide a universal relation between the minimum luminosity (in the dip) and the stellar (accretor) parameters by investigating the distinctive luminosity drops during the outburst decays of magnetic stars of different scales (c.f. Figure 1.13).

The present study seeks to test whether a transient magnetic propeller is, in fact, present in WZ Sge (and, consequently, perhaps also in similar systems). The test is based on the UV spectral signatures observed before, during and after the dip in its 2001 superoutburst light curve. If the system transitions to a propeller state during the dip, it is anticipated that this would produce strong changes in the UV spectrum, relative to spectra associated with disc-dominated phases. Since magnetic propellers are expected (and observed) to be highly variable, these signatures should be most apparent in the *root-mean-square* (RMS) spectra (since constant components, e.g. the accretion-heated WD, are suppressed in these). The variable spectral component can also be isolated via a linear decomposition of the time-resolved spectra, and this provides an additional technique for testing this scenario (as well as a consistency check). The spectral signatures associated with the propeller state are expected to resemble those observed in another WD binary, AE Aqr, which is permanently in the propeller mode (Eracleous et al., 1994; Eracleous and Horne, 1996; Wynn et al., 1997).

In the section below, Section 2.2, I will give a brief overview of AE Aqr and its unique UV signatures, before evaluating whether the comparison between these two systems is justified. Next, the

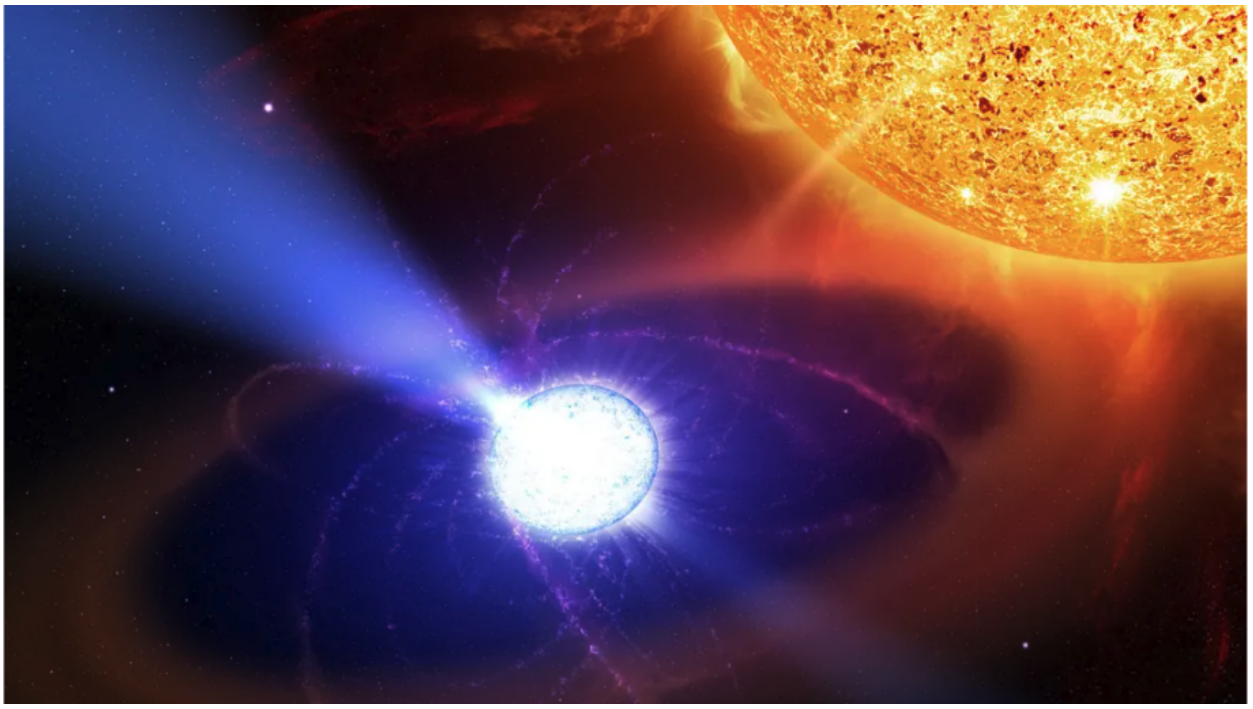

FIGURE 2.3: Artistic illustration of the magnetic nature of WZ Sge. Here, the brown dwarf secondary transfers mass to the WD, while the inner accretion disc is truncated due to the existence of the magnetic field. Credit: Casey Reed/NASA.

description of the observational setup(s), analysis and findings of my study follow in the subsequent sections. If propellering could be confirmed, WZ Sge would be one of the fastest-spinning WD systems with a spin period of 27.87s.

2.2 AE Aqr: a guide to magnetic propeller systems

Until recently, AE Aqr was the only known example of a magnetic propeller WD system (Eracleous et al., 1994; Eracleous and Horne, 1996; Wynn et al., 1997) [1]. As a result, it has been very well-studied observationally. It therefore provides us with the best available laboratory for studying the observational signatures of such systems. For reference, the WD in AE Aqr has a spin period of 33.08s (Patterson, 1979) and orbits an evolved, late-type (red dwarf) secondary (Welsh et al., 1995) in a 9.88-hour orbit (Patterson, 1979).

Studies back in the '90s and early '00s (Wynn and King, 1995; Wynn et al., 1997; Meintjes and de Jager, 2000) have shown that AE Aqr does not follow the traditional IP configuration. Material is coupled to the magnetic field lines of the WD at the magnetospheric radius, but it is subsequently mostly *expelled* from the system, allowing only a small fraction to be accreted. This mass ejection process is thought to be responsible for most of the observed spectral and temporal peculiar properties seen in this system. Of great interest to us here is the presence of aperiodic,

[1] The first "AE Aqr-twin", LAMOST J024048.51+195226.9, was finally discovered a few years ago (Garnavich et al., 2021; Pelisoli et al., 2022).

high-amplitude flares on timescales of minutes, observed in the UV (Eracleous and Horne, 1996). Note that the flaring activity in AE Aqr is a distinctive phenomenon as it appears across the entire electromagnetic spectrum from radio (e.g. Abada-Simon et al., 1993) to γ-rays (e.g. Bowden et al., 1992; Meintjes et al., 1994, but also Aleksić et al. 2014).

Indeed, AE Aqr provides evidence of inhomogeneous accretion in the form of diamagnetic blobs (Wynn et al., 1997) even though a highly-variable, transient disc around the WD is supported through 3D magnetohydronamical simulations (Isakova et al., 2016; Blinova et al., 2019). The observed flares are thought to occur either when diamagnetic blobs interact with the WD's magnetic field and are ejected at larger radii (Eracleous and Horne, 1996) or when ejected blobs collide with each other (Welsh et al., 1998). In any case, the expelled material is expected to produce the observed emission line spectrum of the system, which is extremely distinctive (Pearson et al., 2003). The loss of energy and angular momentum from the system via the outflow is reflected in the enormous spin-down power of the WD (de Jager et al., 1994; Mauche, 2006). This power is consistent with the expected accretion luminosity (and therefore mass accretion rate) but much larger than the radiative power, observed in the system. This fact confirms that most of the mass is ejected (Eracleous and Horne, 1996).

Eracleous and Horne (1996) isolated the spectrum of these flares in the UV, as shown in Figure 2.4. The same figure also showcases the time-averaged spectrum of the system for comparison. These results are based on an observational campaign where the system was observed on 1992 November 27-28 over nine HST orbits. The spectra on the first eight orbits were obtained using the G160L first-order grating of the *Faint Object Spectrograph* (FOS; Harms et al., 1979) on board HST at the 1150-2510Å range, having a spectral resolution of 9.2Å (FWHM). However, in the last orbit, the G160L grating was replaced by *PRISM*, an instrument covering the 1500-6015Å spectral range with low and wavelength-dependent spectral resolution (e.g. 44Å at Mg_{II} λ2800Å, 92Å at Balmer edge and 140Å at Hγ; Sirk and Bohlin 1986; Evans 1993). This distinction on the instrumental setups is explicitly cited in Figure 2.4 as well.

It is evident that the shorter wavelengths ($\lambda < 2000$Å) are densely populated with strong, single-peaked, broad emission lines, encompassing both high- and low-ionisation states in environments of different densities. Notable features in the high-density, high-ionisation regime include N_V λ1240Å, Si_{IV} λ1400Å, and He_{II} λ1640Å. Conversely, low-ionisation species with lower densities give rise to semi-forbidden transitions such as $O_{III]}$ λ1663Å and $Si_{III]}$ λ1892Å.

By contrast, the near-UV region ($\lambda > 2000$Å) primarily displays the Fe_{II} complex and the Mg_{II} λ2800Å features. These emission lines are not stable, but vary in the same fashion with respect to time. This behaviour may imply that these lines are produced in the same region or, in the case that there are two line-emitting regions (due to the density profile inconsistency), that the two regions are responding together to the mechanism driving the line emission (Eracleous and Horne, 1996).

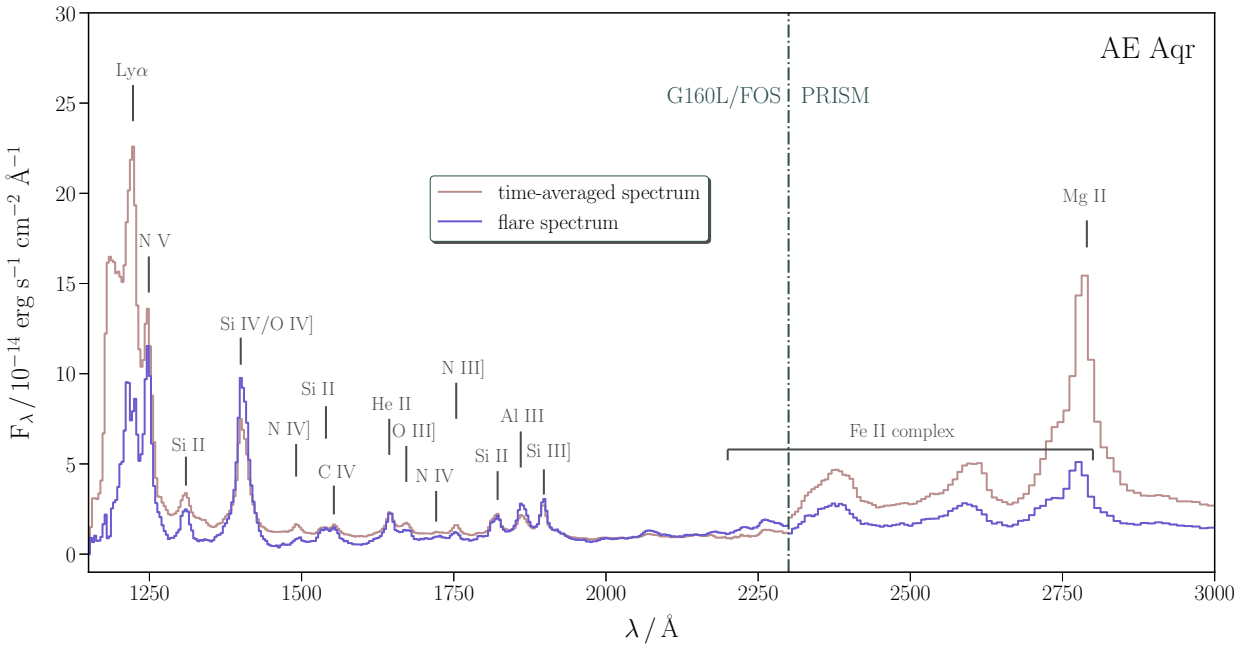

FIGURE 2.4: The time-averaged (dusty pink) and flare/variability (purple) UV spectra of AE Aqr, as reproduced from Eracleous and Horne (1996). The spectra between 1150–2300Å are obtained by using the G160L grating of *FOS* on board the HST whereas their 2300–3000Å part is acquired by exploiting PRISM. The shorter wavelengths are described by a wide range of ionisation states and semi-forbidden emission lines. At longer wavelengths though only the Fe_{II} complex and the Mg_{II} line are clearly visible.

As noted above, our goal is to test the magnetic propeller scenario for WZ Sge by checking for the presence of AE Aqr-like spectral signatures during the times when the system should be in a propeller state. However, while it may be enticing to compare the two systems in question, we first have to ask whether this is a fair comparison. Over the years, there were several times that these two systems were compared to one another, especially in terms of the possible magnetic nature of WZ Sge and plausibly, similar characteristics (e.g. Matthews et al., 2007; Warner and Pretorius, 2008). The primary areas of concern for such a comparison are described below, and the properties of the systems' components − donor, WD accretor, accretion disc − are summarised in Table 2.1.

The most obvious issue to consider is that there are different types of accretion flows between the two systems. For example, WZ Sge harbours at least a partial accretion disc around the WD while observationally, there is no evidence for a disc around AE Aqr. However, recent magnetohydrodynamical simulations propose the possible presence of a transient and turbulent disc around its highly-spinning WD (Isakova et al., 2016; Blinova et al., 2019). Moreover, further evidence to support the comparison between these two systems is provided by the transitional millisecond pulsar (tMSP)[2] PSR J1023+0038 (Archibald et al., 2009). PSR J1023+0038 displays the same extraordinary distinctive UV emission line spectrum, which is thought to be the result of the ejection of the inner

[2]Transitional millisecond pulsars (tMSPs) are referred to as fast-spinning NS systems, with spin periods at the millisecond range, that alternate between two primary states: i) a radio state and ii) an accreting state. According to the predominant "recycling scenario", these states are linked in such a way that when the accretion onto the pulsar

parts of the disc (Hernández Santisteban, 2016). In fact, the inner disc in this system is disrupted at a distance from the central object that is comparable to the size of AE Aqr's magnetosphere. The mass transfer rate from the donor star is also comparable in PSR J1023+0038 and AE Aqr. This shows that similar UV emission line spectra are produced whenever material is ejected at roughly the same rate from similar radii.

TABLE 2.1: Summary of the estimated physical parameters and properties of WZ Sge and AE Aqr for their in-between comparison. The references, presented in the table, are only examples of the various works refer to the topic in question. The text provides a better representation of the current literature.

	WZ Sge	AE Aqr	References
	Stellar components		
	WD + brown dwarf	WD + red dwarf	1,2,3,4,5
	Accretor		
WD mass / P_{spin} period	$0.63M_\odot$/27.87s	$0.8M_\odot$/33.08s	2,3,4,6
	Donor		
CNO processed?	No	Yes	1,7
	Accretion disc		
	Yes	No?	8,9
Mass transfer rate, $\dot{M}_{tr}$	$10^{-9}M_\odot$ yr^{-1}	$(1-3)\times10^{-9}M_\odot$ yr^{-1}	10,11

References: (1) Steeghs et al. (2007), (2) Echevarría et al. (2008), (3) Patterson (1980), (4) Patterson (1979), (5) Welsh et al. (1995), (6) Casares et al. (1996), (7) Mauche et al. (1997), (8) Isakova et al. (2016), (9) Blinova et al. (2019), (10) Eracleous and Horne (1996), (11) Long et al. (2003)

Furthermore, both WZ Sge and AE Aqr seem to host moderately massive (Echevarría et al., 2008) and fast-rotating (e.g. Patterson, 1979; Patterson et al., 1998) WDs, with comparable mass transfer rates near the inner edges of their respective discs. In AE Aqr, this rate is dictated by the secondary star (Eracleous and Horne, 1996). In contrast, in WZ Sge, the donor feeds the disc at a considerably lower rate (Smak, 1993), but the mass transfer rate through the inner disc near the end of the plateau phase is comparable to the mass transfer rate from the donor in AE Aqr (Long et al., 2003). The nature of the donor stars is different, however. Specifically, the transferred material in AE Aqr originates from an evolved secondary, which means it has undergone CNO processing (Welsh et al., 1995). Nevertheless, this will not impact the emergence of characteristic emission lines even for different abundance ratios (e.g. Mauche et al., 1997; Mauche, 2004; Gänsicke et al., 2003).

Taking all of this into account, the aim of the current project is to find *any* observational evidence for an unusual (and perhaps AE Aqr-like) UV emission line spectrum in the dip phase of WZ Sge's 2001 superoutburst. The comparison to AE Aqr is convenient as a *reference point*, since it is the only well-studied accreting WD system in a magnetic propeller state and shares many key properties. However, our observational study is, of course, agnostic to this – i.e. we are sensitive to *any* distinctive and variable signature in our spectra.

terminates (LMXB configuration), the transferred angular momentum enables it to spin-up and behave as a radio pulsar (e.g. Bhattacharya and van den Heuvel, 1991).

2.3 Observations

2.3.1 HST observations

The HST observed the DN WZ Sge on 2001 August 8, 19 and 22 after its outburst peak on July 24, with the goal to investigate the immediate aftermath and decline phase of its superoutburst. The observations (Proposal ID: 9287, PI: Knigge) were taken with the *Space Telescope Imaging Spectrograph* (STIS; Kimble et al., 1998; Woodgate et al., 1998) both at the far- and near-UV part of the spectrum using the Multi-Anode Microchannel Array (MAMA) detectors. Each epoch consists of a four-orbit HST visit, covering three key points of the source's outburst: the "plateau" (HST-1), the "dip" (HST-2) and the "echo-outburst" (HST-3) phase. The timing of the observations can be seen in Figure 2.5, overlaid on WZ Sge's 2001 superoutburst optical light curve.

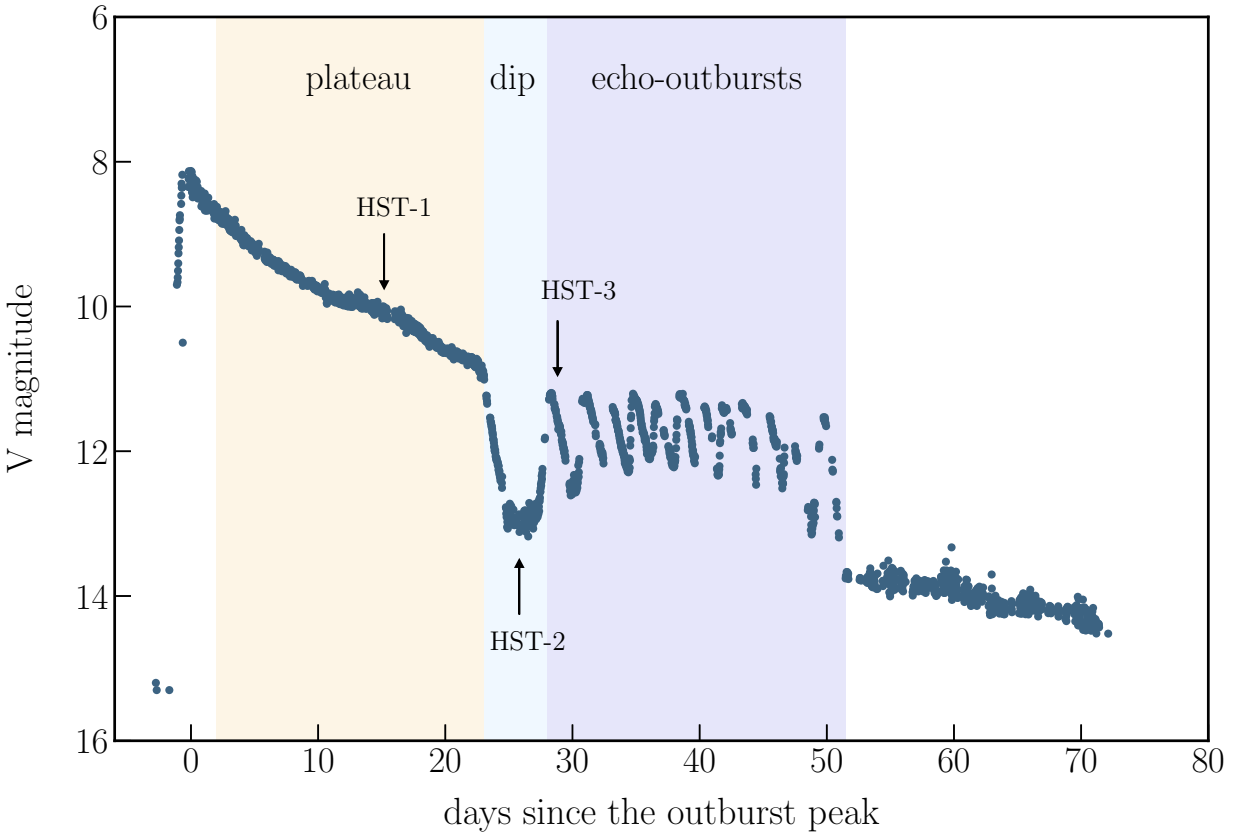

FIGURE 2.5: The optical light curve of the 2001 superoutburst of WZ Sge as it is given by VSNET with respect to days since its outburst peak. Three different regions, at the outburst decay, are background highlighted: the plateau (beige), the dip (light blue), and the echo-outburst phase (purple). The times of our HST observations are marked by arrows and cover all the decline stages of the superoutburst. The outburst peak (Ishioka et al., 2002) corresponds to 2001 July 23.565 (UTC).

Time-resolved spectroscopy was acquired *only* at the far-UV part of the spectrum as the observations were taken with the FUV-MAMA detector in TIME-TAG mode, providing us with time resolution of relative accuracy of 125 μs. The spectra were acquired with the E140M/1425Å echelle

grating at the wavelength range of 1144−1710Å. This instrumentation setup offers a spectral resolution of R = 45.800, which corresponds to a velocity resolution of $\simeq$ 7 km s^{-1}. The near-UV observations are obtained in ACCUM mode, and therefore timing information is not available. In these wavelengths, the respective E230M/1978Å and the E230M/2707Å echelle gratings exploited the R = 30.000 resolution, resulting to a velocity resolution of $\simeq$ 10 km s^{-1}. Overall, the $0''.2 \times 0''.06$ slit was used for the plateau and the $0''.2 \times 0''.2$ slit for the other two epochs. It is worthwhile mentioning the difference on the used target slit between the first and the subsequent two epochs, since as we shall see, it is responsible for some of the induced variability, seen only at the plateau phase. The *calstis* pipeline was used to extract one-dimensional spectra, both at the far-and near-UV regions. In each case, blaze correction was performed on the individual orders of the *echelle* spectra while the overlapping regions among orders were trimmed before I combined them into a single spectrum.

The immediate comparison between the two systems has already considered the employed instrumental setups. The search for magnetic propeller signatures limit us at the far-UV wavelengths as timing information is only available at this regime. AE Aqr is observed by *FOS*, an instrument of a much lower resolution than the employed *STIS* of the WZ Sge observations considered here. The take-home message though, but quite crucial at the conducted analysis, is that the emission lines in the far-UV range (G160L grating) are *resolved*. Note that the FWHM of the λ1640Å line, corrected for the instrumental resolution, is close to 1700 km s^{-1} (Eracleous and Horne, 1996).

The WZ Sge HST observations were retrieved from the Mikulski Archive for Space Telescopes (MAST) and a summarised description of them can be found in Table 2.2. On the other hand, the AE Aqr data products were given to us after a private communication with M.Eracleous.

2.4 Data Analysis

2.4.1 Construction of light curves

I constructed wavelength-integrated light curves from the time-resolved observations using a customised version of the LIGHTCURVE package[3], which included both background subtraction while it excluded the time windows affected by buffer dumps. An overall view of the procured light curves for the three studied stages of the superoutburst is demonstrated in Figure 2.6, incorporated along with the orbital phase of the system (secondary x-axis). The system's ephemeris is the one employed by Patterson et al. (1998) and expressed as

$$\text{mid} - \text{eclipse} = \text{HJD}\ 2,437,547.72840 + 0.0566878460(3)\text{E} \tag{2.1}$$

[3]The LIGHTCURVE package constitutes an astronomical tool for extracting lightcurve datasets, operating in "TIME-TAG" mode. This tool is only appropriate for HST's *COS* and *STIS* instruments. Originally found source: https://github.com/justincely/lightcurve.

TABLE 2.2: Log of observations of discussed in this work. The last column represents the notation that we are going to use throughout this thesis.

ObsID	Setup (grating/aperture)	Start Time (UT) (hh:mm:ss)	Start Time (MJD)	Exposure (s)	Central wavelength (Å)	Notation
PLATEAU						
o6j711010	E230M/0″.2 × 0″.06	15:09:01	52129.63126157	144	near-UV/1978Å	
—"—020	—"—	15:16:52	52129.63671296	144	near-UV/2707Å	
—"—030	E140M/—"—	15:26:22	52129.64331019	548	far-UV/1425Å	
—"—040	—"—	16:22:24	52129.68222222	2756	—"—	HST-1
o6j712010	E230M/—"—	18:21:35	52129.76498843	144	near-UV/1978Å	
—"—020	—"—	18:29:26	52129.77043981	144	near-UV/2707Å	
—"—030	E140M/—"—	18:38:56	52129.77703704	593	far-UV/1425Å	
—"—040	—"—	19:35:04	52129.81601852	2850	—"—	
DIP						
o6j723010	E230M/ 0″.2 × 0″.2	06:14:58	52140.26039352	120	near-UV/1978Å	
—"—020	—"—	06:22:25	52140.26556713	120	near-UV/2707Å	
—"—030	E140M/—"—	06:31:31	52140.27188657	1180	far-UV/1425Å	
—"—040	—"—	07:39:51	52140.31934028	2730	—"—	HST-2
o6j724010	E230M/—"—	09:27:32	52140.39412037	120	near-UV/1978Å	
—"—020	—"—	09:34:59	52140.39929398	120	near-UV/2707Å	
—"—030	E140M/—"—	09:44:05	52140.40561343	1180	far-UV/1425Å	
—"—040	—"—	10:52:31	52140.45313657	2730	—"—	
ECHO-OUTBURSTS						
o6j725010	E230M/ 0″.2 × 0″.2	06:28:26	52143.26974537	120	near-UV/1978Å	
—"—020	—"—	06:35:53	52143.27491898	120	near-UV/2707Å	
—"—030	E140M/—"—	06:44:59	52143.28123843	1180	far-UV/1425Å	
—"—040	—"—	07:53:43	52143.32896991	2730	—"—	HST-3
o6j726010	E230M/—"—	09:41:03	52143.40350694	120	near-UV/1978Å	
—"—020	—"—	09:48:30	52143.40868056	120	near-UV/2707Å	
—"—030	E140M/—"—	09:57:36	52143.415	1180	far-UV/1425Å	
—"—040	—"—	11:06:20	52143.46273148	2730	—"—	

We see that the light curves are characterised by short-timescale, rapid variability during all stages while evidence for $\simeq$ 15s oscillations were found (only) at the echo-outburst phase (Knigge et al., 2002). Initially, it is noteworthy though to focus on the plateau phase and investigate the count rate drop between the first and second orbit and again between the third and fourth orbit of this phase's light curve. Remarkably, in both cases, the count rates were gradually recovered back to their previous level. I suspect that this is an artefact due to the object's motion in and out of slit, which is used only at this epoch. However, after discussion with the STScl office and inspection of the target acquisition and jitter files, I did not identify any evident long-term drifts. In order to confirm the validity of this raised speculation, I have extracted spectra separately for the first and second halves of the orbits in question, i.e. second and fourth orbits of the plateau phase. The ratios of these spectra are almost flat, with sharp, narrow "P-Cygni"-like features that are most likely associated due to movement in the dispersion direction. This is not the case, though, for the stochastic variability seen, for instance, during the fourth orbit of the dip phase. The spectrum ratios, extracted from high and low count rate states of the dip phase, resemble the transmission spectrum of an absorber, a *veil*, found in the system in all stages of the superoutburst (discussed later in Section 2.5.3). Hence I specify that the variability seen in the first epoch was indeed likely due to the target moving within the slit but the remaining stochastic variability in this and other orbits is intrinsic to the source.

2.4.2 Methods: detection of spectral variability

2.4.2.1 Time-averaged and RMS spectra

Identification of spectral variability constitutes a crucial element in our overall understanding of astronomical sources as it characterises temporal-dependent processes and how they influence (through spectral line variations) the source's environment with respect to time. Construction of RMS spectra is considered to be a powerful spectral variability tool as it disentangles and isolates features that exhibit strong time variations, such as the magnetic propeller signatures, from those that do not, as all constant components are eliminated. In the current framework, the disentanglement between the binary's constant and variable components is necessary as the accretion-heated WD could conceivably swamp the mean propeller signature.

I construct, first, time-averaged and variability (RMS) *far-UV* spectra of WZ Sge before, during and after the dip of the source's light curve in order to test the magnetic propeller scenario, suggested by Campana et al. (2018). The aforementioned process involves assigning timing information to respective wavelengths bins in the specified spectral range, which in our case is between 1200-1700Å. Then, the time-averaged mean flux and the RMS around it are separately computed for each wavelength bin. The time and wavelength resolution, used in this analysis, are chosen to be Δt = 60s and $\Delta\lambda$=1Å as these choices best reflect the line fluctuations, even though several alternatives were also tested. Nevertheless, the specific choices for time and wavelength resolution

do not significantly affect our results. The time-averaged and RMS spectra for all our epochs are demonstrated in Figures 2.7 and 2.8, respectively.

It is worthwhile to mention that the RMS spectra do not highlight the direction of the variable line − in other words, they do not distinguish between variable absorption or emission − but only the fact that there is an *excess*, an "emission line", in that particular wavelength. Thus, they cannot be treated as "normal" spectra. To be more precise, "P-Cygni" or "inverse P-Cygni" features in an RMS spectrum cannot be taken as outflow or inflow signatures, for example. Instead, they are most likely the result of velocity shifts between spectra. As a reminder, I mention that we should be cautious regarding the RMS spectrum for the plateau phase as it may be affected by the slit-motion-induced variability noted above. On the other hand, last but not least, I refer to the fact that in *near-UV wavelengths*, only mean spectra are created (as the observations in the near-UV are taken in ACCUM mode). These spectra can be seen in Figure 2.9.

2.4.2.2 Linear decomposition

As previously mentioned, propeller signatures are time-dependent and highly variable. These signatures are anticipated to emerge during the dip epoch (HST-2) of the WZ Sge superoutburst, where they would be superimposed on the steady, constant emission coming from the WD. This suggests that the propeller effect, which is linked to the interaction between the accretion disc and the magnetic field of the WD, could cause fluctuations in the observed emission during specific phases of the outburst, especially when the system undergoes a dip in brightness. An additional method to elucidate the two different components is to carry out a linear decomposition, following a similar analysis performed by Eracleous and Horne (1996) for the case of AE Aqr.

The observed time-resolved spectra, $F_{obs}(t, \lambda)$, for each epoch, are decomposed into constant, $C(\lambda)$, and variable, $V(\lambda)$, components so as to

$$F_{obs}(t, \lambda) = C(\lambda) + D(t)\, V(\lambda), \tag{2.2}$$

where $D(t)$ is the driving light curve for the variable component, for which I adopted a scaled and slightly smoothed version of the far-UV continuum light curve. In other words, it represents the continuum fluctuations, where, in here, it is estimated from the $1450-1500$Å wavelength interval. The modelling and the optimal parameter estimation of the time-resolved spectra are achieved through unbinned maximum likelihood estimation (MLE) fits, as the performed implementation allows me to work directly with the TIME-TAG photon stream sets.

The nature of our data (individual photons) allows us to treat them as discrete events, each tagged with a specific position (wavelength) and time arrival. We try to find the best-fit model that maximises the likelihood function ($\mathcal{L}$). The likelihood of observing this photon stream is determined by multiplying the probabilities of all bins, assuming that each bin is independent. It is common practice, though, to work with the negative log-likelihood for numerical convenience and

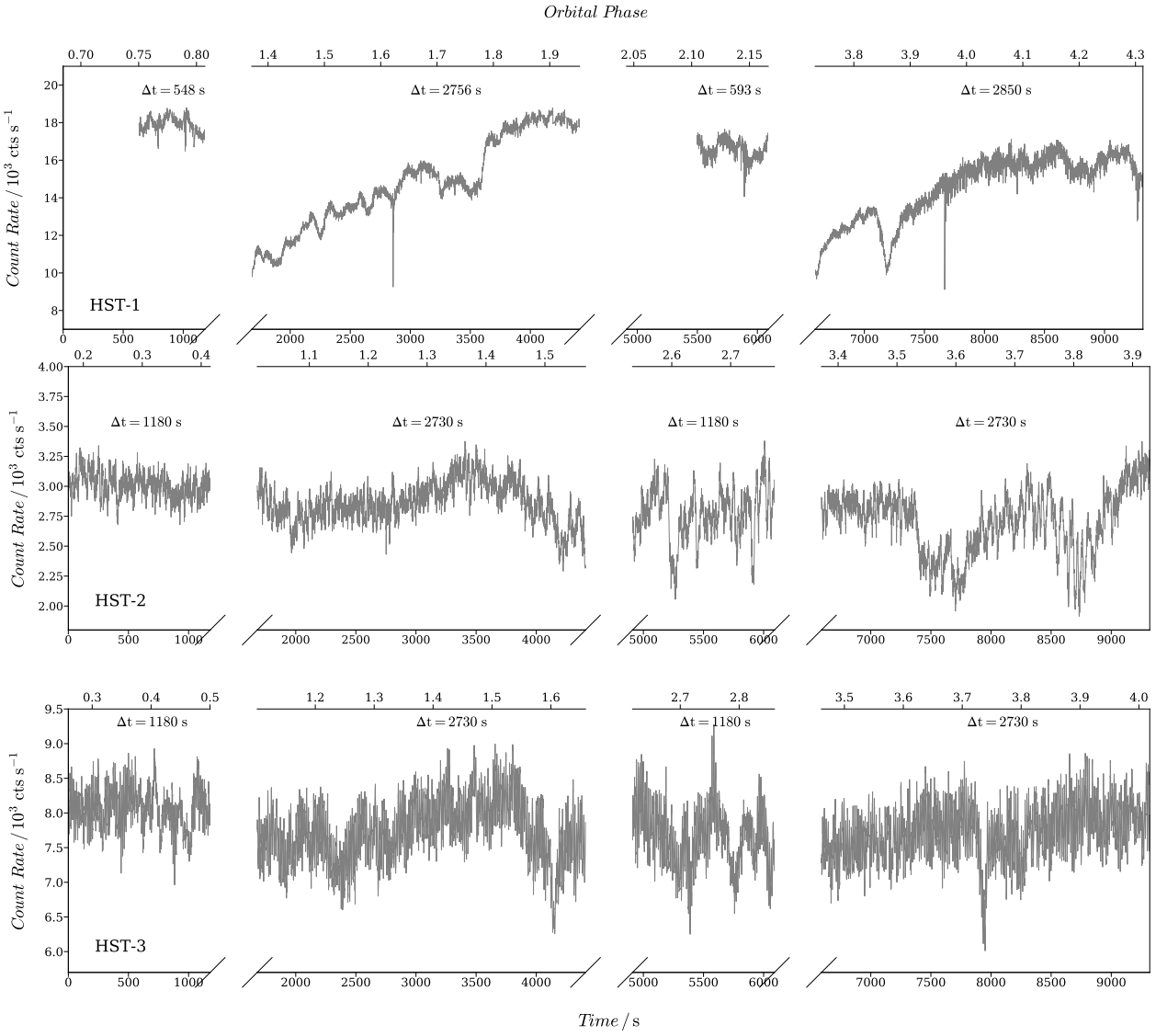

FIGURE 2.6: Extracted one-second resolution light curves of WZ Sge for the three studied epochs, each one of them composed of four different orbits. The duration of each orbit as well as the orbital phase of the system are noted. The orbital phase was calculated by exploiting the ephemeris given by Patterson et al. (1998). The broken axes specify time discontinuity between the observations. Each epoch is indicated by using the HST notation scheme.

facilitation of optimisation problems. Following the recipes given by Nelson and Nelson (1998) and Poisson statistics (discrete distributions), it can be shown that, for the model described in Equation 2.2, the unbinned negative log-likelihood can be written as

$$\ln\mathcal{L} = \left[\sum_{i=0}^{N} \ln[C(\lambda) + D(t)V(\lambda)]\right] - \mathcal{N} \tag{2.3}$$

where $\mathcal{N}$ the number of counts predicted by the model in all of the bins. It is noted that N in the sum represents the number of the observed events.

This method corrects the slit-motion-induced variability in the plateau phase − something that could not be avoided in the construction of the mean and RMS spectra. Of course, due to the fact that $D(t)$ is a scaled and smoothed version of the "true" far-UV light curve, a caveat in this analysis is that its form is uncertain with an offset and overall scaling and therefore, there is unavoidable mathematical degeneracy between the two components. In particular, the inferred $C(\lambda)$ will, in general, be a linear combination of the "true" constant and variable components. By contrast, the inferred $V(\lambda)$ is always just a scaled version of the "true" variable component. This mathematical degeneracy between them will not alter the later discussion and the nature of my results. Having said that, the spectral shape and absorption/emission lines will always be correct (to the extent the model itself is valid, of course).

The findings of this analysis are overlaid in Figures 2.7 and 2.8. In particular, in Figure 2.7, I overplot the constant component with respect to the time-averaged spectrum while in Figure 2.8, the variable component with respect to the RMS spectrum.

2.5 Results and discussion

2.5.1 Spectral evolution through the outburst's decline

Far-UV part of the spectrum

Overall, there is good agreement between the time-averaged spectra and the constant component, result of the applied decomposition in all the epochs. The time-averaged far-UV spectra, depicted in Figure 2.7, are characterised by intrinsically *narrow* absorption lines (FWHM $=$ 550 km s^{-1}) while the continuum rises towards the UV (blue continuum). The continuum flux level is measured at 1450Å and it fluctuates between 5×10^{-12} erg s^{-1} cm^{-2} $^{-1}$, during the plateau phase, to 7×10^{-13}erg s^{-1} cm^{-2} $^{-1}$, at the dip, until it rises to a level of 1.7×10^{-12}erg s^{-1} cm^{-2} $^{-1}$ during the first rebrightening of the source. The demonstrated lines in the spectra range from low to high ionisation states, while strongly absorbed are the various transitions of silicon (Si_{II} λ1263, 1527, 1533Å, Si_{III} λ1299Å, Si_{IV} λ1400Å) and carbon (C_{I} λ1658Å, C_{II} λ1335Å, C_{IV} λ1550Å). In contrast, evident is the presence of some weak P-Cygni structures, mostly at the first and the third epoch, such as the ones of N_{V} λ1240Å and C_{IV} λ1550Å. These lines are plausibly formed in an accretion wind (Rosen et al., 1998) during high mass transfer periods.

Near-UV part of the spectrum

At the near-UV part of the spectrum, the time-averaged spectra show intrinsically narrow lines as seen in Figure 2.9. Moderate ionisation transitions, such as the N_{IV} λ1721Å and Al_{III} λ1860Å, as well as semi-forbidden lines, such as $O_{III]}$ λ1672Å and $N_{III]}$ λ1754Å, are discernible at shorter wavelengths. This fact suggests the existence of lower-density line-forming regions at the accretion disc's atmosphere. In contrast, at the other end of the spectrum, the only visible lines are Mg_{II} λ2800Å and the broad, Fe_{II} complex. The stronger multiplets in this complex were identified

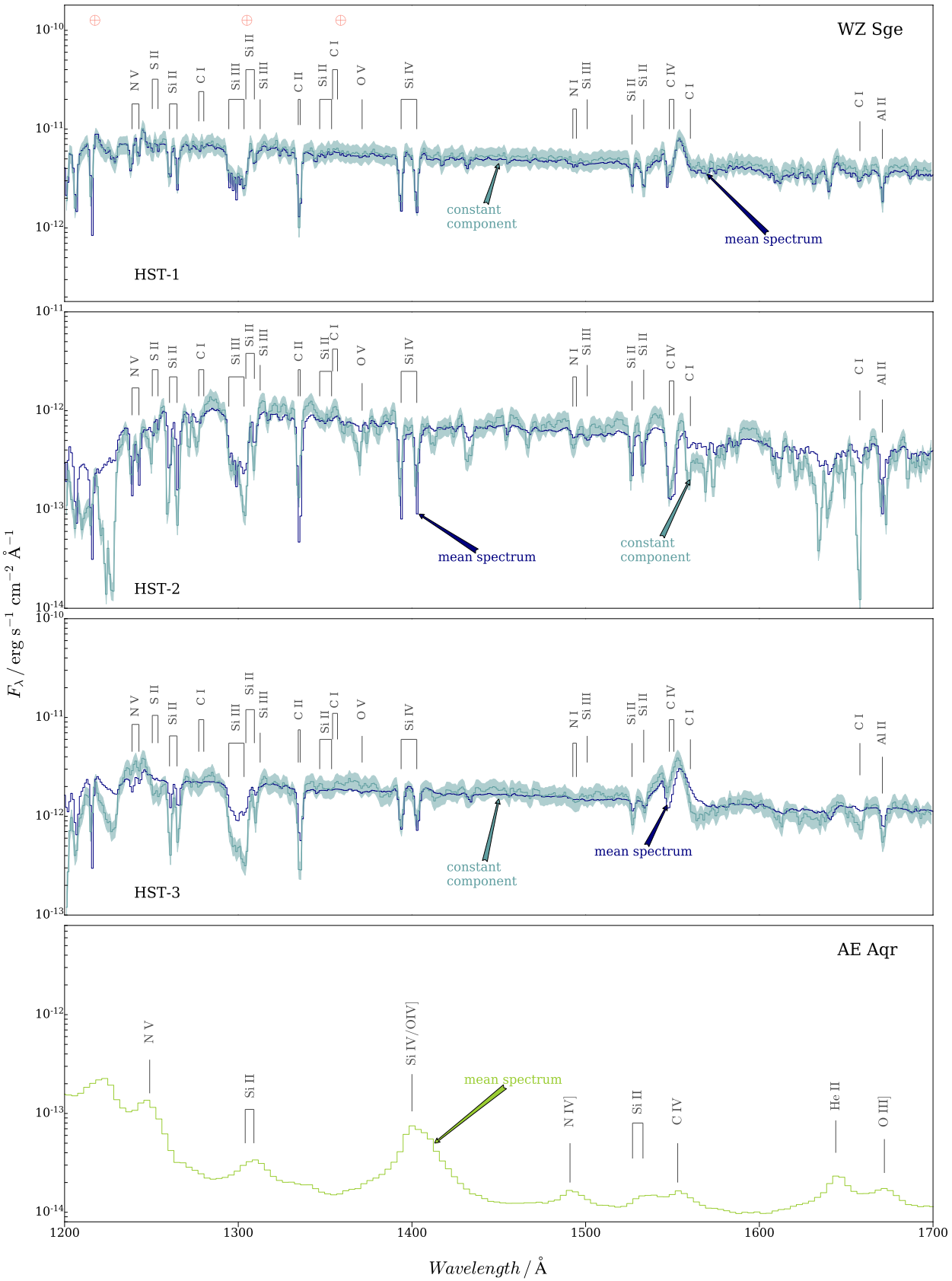

FIGURE 2.7: Flux-calibrated far-UV mean spectra (navy) for all of our epochs, plotted with respect to the constant component (teal), suggested by our linear decomposition model. The teal-shaded area corresponds to 20% of the constant component's flux in both directions. The line identifications, including the geocoronal species – represented by ⊕ – are shown on top of these plots. The last panel indicates the mean AE Aqr spectrum for comparison.

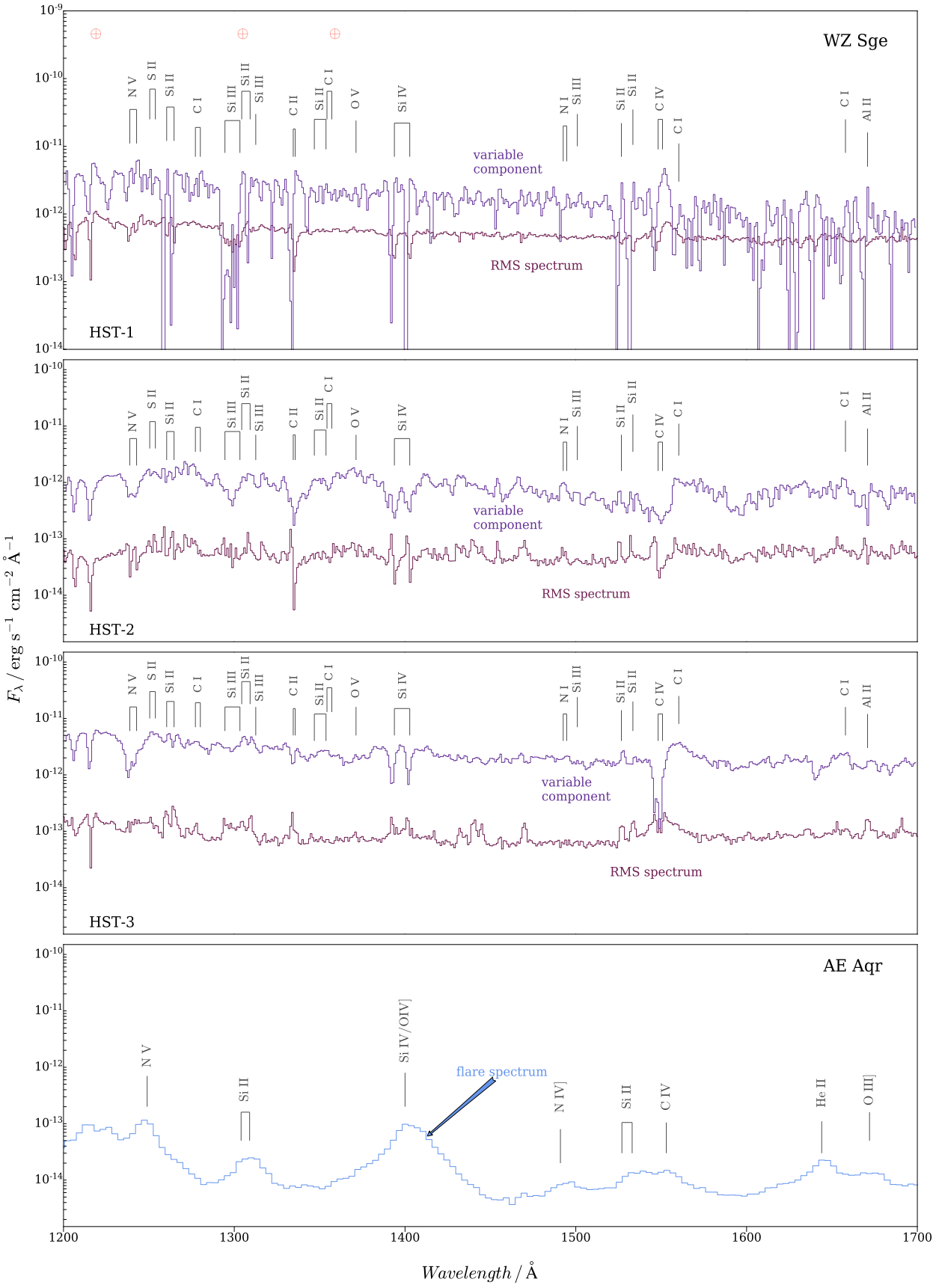

FIGURE 2.8: Flux-calibrated far-UV RMS spectra (dark magenta) for our three epochs plotted with respect to the variable component (purple) of our linear decomposition. The line identifications, including the geocoronal species — represented by ⊕ — are shown on top of these plots. The last panel indicates the flare AE Aqr spectrum for comparison.

and put them also in Figure 2.9. These multiplets are: UV1 (2600-2629Å), UV2 (2383-2405Å), UV3 (2344-2345Å) and UV64 (2563-2595Å).

2.5.2 Existence of magnetic propeller

The primary aim of the current project was to test whether the magnetic propeller scenario is responsible for the distinctive dip of the light curves of WZ Sge (and similar systems) by trying to find any unique observational UV signature in its spectra. Here, AE Aqr − a well-studied magnetic propeller system − has been taken as a reference point to guide the immediate comparison and subsequent discussion of my findings. As demonstrated, comparing the spectra of these two systems, though, they are nothing alike.

To be more specific, none of the features seen in either the mean or the variability spectrum of WZ Sge in the dip phase are exclusive to this phase. If the system was in a propeller phase (only) during the dip, it would be expected to see a distinctive line spectrum in this phase, including features associated with shock-excited emission produced during blob–blob or blob-magnetosphere collisions (Eracleous and Horne, 1996; Welsh et al., 1998; Pearson et al., 2003). Secondly, all of the lines observed in the dip phase are seen in *absorption*, whereas AE Aqr exhibits strong, highly variable emission lines. Thirdly, all of the absorption features observed in WZ Sge are narrow (FWHM $\approx$ 550 km s^{-1} both in the far- and near-UV range) by contrast to the broad (FWHM $\approx$ 1700 km s^{-1}), emission lines expected from propeller kinematics and seen, for example, in AE Aqr (Eracleous and Horne, 1996). The current behaviour is present both at the mean/constant and RMS/variability spectra and therefore, masking of an underlying propeller signature by the hot WD in WZ Sge is also unlikely. Of course, it should be emphasised that, due to difference of instrumental resolution, the narrow absorption features, visible in WZ Sge, would not be detectable − and certainly not resolved − in the *FOS* spectrum of AE Aqr.

Someone may wonder, where do these results lead us? If not a propeller, then what? Do we need to instigate additional physics in order to address and understand the complex pattern of the light curves, seen in WZ Sge itself (e.g. Patterson et al., 1981; Patterson et al., 2002) and WZ Sge-like systems (e.g. Nakata et al., 2013; Kato, 2015). Several such ingredients have been already proposed, usually based on modifications to the standard DIM (Section 1.3.3.2). For example, Hameury et al. (2000) and Buat-Menard et al. (2001) suggested that rebrightenings may be associated with enhanced mass transfer due to the irradiation of the secondary star during an outburst. Osaki et al. (2001) proposed that echo outbursts are connected to viscosity variations in the disc and Meyer and Meyer-Hofmeister (1994); Meyer and Meyer-Hofmeister (2015), argued that the evaporation of the inner parts of the accretion disc may be responsible. Hence the magnetic propeller scenario sketched by Campana et al. (2018) – which my analysis tends to rule out – is not the only potential candidate.

Recently, Hameury and Lasota (2021) have taken a new and comprehensive look at what modifications to the DIM are required in order to account for echo-outbursts. They find that, in order to

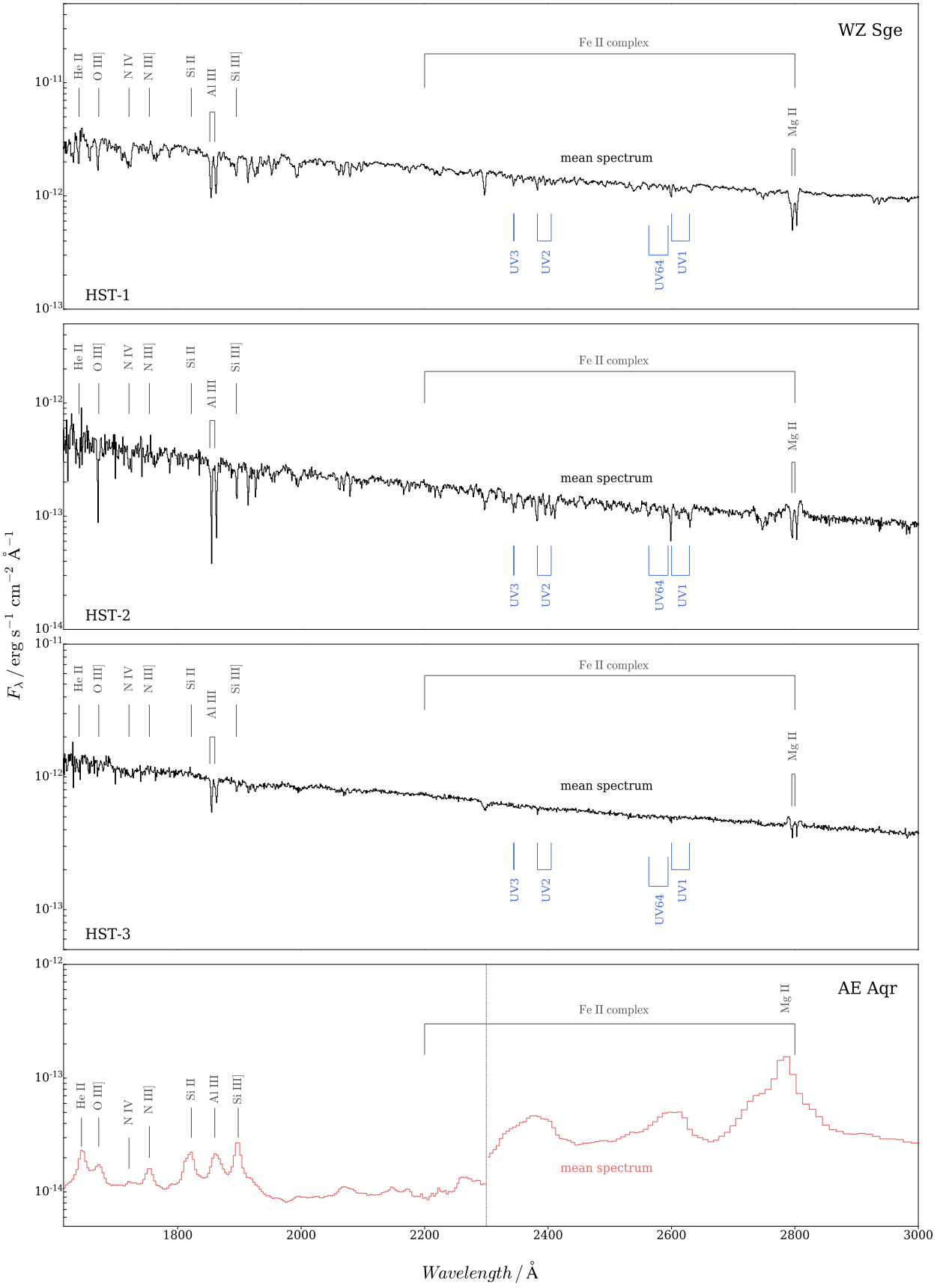

FIGURE 2.9: Near-UV mean spectra of WZ Sge (dark grey) for all our epochs along with the most prominent line identifications. At longer wavelengths, we identify the stronger Fe_{II} multiplets (UV1, UV2, UV3, UV64). The last panel again demonstrates the mean AE Aqr spectrum for comparison.

explain the full range of observed outburst phenomenologies, several conditions must be met: (i) the disc must be on the lower stable branch of the S-curve in quiescence, implying that outbursts are not triggered by the DIM itself, but by enhanced mass transfer from the secondary, (ii) the disc must be truncated in quiescence, (iii) mass transfer during the outburst must be sustained 'externally' (e.g. by irradiation), beyond the duration the DIM would naturally support as it should be close enough to the critical accretion rate, (iv) stream overflow must be significant, depositing material closer to the WD than the outer disc edge. These are strong, but perhaps not unreasonable requirements. Now that the propeller model has been ruled out, these requirements, too, will need to be subjected to stronger observational tests.

2.5.3 The mystery of the narrow absorption lines

Intrinsically narrow absorption features are detected at all stages of the superoutburst's decay. However, this is not the first time that similar structures are observed in WZ Sge. Long et al. (2004) did observe them in their UV analysis, using observations on a later date of WZ Sge's 2001 superoutburst. The earliest spectrum in their work is taken on 2001 September 11, which is roughly three weeks after the last observation considered here (on August 22). That date coincides with the dip between the last two echo-outbursts associated with the 2001 eruption (Godon et al., 2004). The rest of their observations were obtained much later, when the source was almost close to its quiescent level. Steeghs et al. (2007) also found indications of these narrow absorption features also in quiescence.

But where are these structures formed? To quantify this, I have measured the velocity offsets of several relatively isolated narrow absorption lines (in particular, Si_{IV} λ1393.76Å, Si_{IV} λ1402.77Å, Si_{II} λ1533.43Å) from their rest wavelengths in the time-averaged spectrum for each of the three epochs. These turn out to be $\simeq -73 \pm 3$ km s^{-1}, which is consistent with the systemic velocity of the binary system (-72 ± 2 km s^{-1}; Spruit and Rutten 1998; Steeghs et al. 2001). However, it is worth noting that the narrow UV absorption lines seen in quiescence by Steeghs et al. (2007) were centred on -16 ± 4 km s^{-1}. The difference between this and the systemic velocity was attributed to the effect of gravitational redshift. The narrow absorption lines in our data are closer to the systemic velocity, suggesting that the line-forming region was located further from the WD.

Long et al. (2004) characterised the physical conditions under which these lines were formed, considering a model in which these lines are absorbed in a slab of material with electron density in local thermodynamic equilibrium (LTE). Indeed, this model is not that far off from describing their input spectrum, thereby giving us some insights at the same time. In particular, they found that the temperature, T, of their model slab decreased from T=11500K in September to T $\approx$ 7200K in October, to T $\approx$ 6500K at later times. Across the same interval, the column density of the absorber dropped from logN_H $\approx$19.5 to $\approx$19. The turbulent velocities required to account for the width of the lines were always modest, in the range of $v_t \approx 150 - 450$ km s^{-1}.

In this work, I carried out a similar analysis using the TLUSTY and SYNSPEC packages (Hubeny and Lanz, 2017). As noted above, the narrow absorption features are present in all of our epochs – plateau, dip and echo-outburst. However, the UV spectra during the plateau and echo-outburst phases are much harder to model, since they are dominated by disc emission and partially reprocessing in a disc wind (Knigge et al., 1997, 1998; Noebauer et al., 2010; Matthews et al., 2015). Hence I restrict my analysis here to the dip phase, where the accretion-heated WD is expected to be the dominant UV source. Of course, it has to be taken into account that a fixed-density LTE slab model can only be expected to provide rough characteristic values for the physical parameters in the line-forming region.

I describe, below, the different steps of the performed modelling of the UV spectrum. Initially, a solar abundance, logg=8.5 (Steeghs et al., 2001), WD model is fitted to the far-UV through near-UV spectrum, trying to isolate the regions contaminated with strong absorption features that are clearly not associated with the WD. The resulting estimate of the WD temperature is $T_{WD} \approx$ 27300K, a comparable estimate to the one obtained by Long et al. (2004) during the final dip phase in September 2001. Then, I estimated the transmission spectrum of the veil by dividing the observed HST spectrum (dip phase) by the WD model. In order to remove any remaining large-scale trends that are not linked with absorption, I divided this spectrum by a highly smoothed version of itself. I used a very broad ($\approx$ 500Å) Savitzky–Golay filter for this purpose. Finally, I performed the final modelling where I fitted this transmission spectrum with that expected for an LTE slab, varying the temperature (T), electron density (n_e), turbulent velocity (v_t) and column density (N_H).

The results are demonstrated in Figure 2.10 where the spectrum is fitted by both the WD contribution and the absorbing curtain. The best-fitting LTE slab produces most of the observed features, and it is characterised by T = 17200K, $\log n_e \approx 15.7$, $v_t = 120$ km s^{-1} and $\log N_H \approx 20.4$. It is worth mentioning that there is a strong degeneracy between T and n_e in LTE slab models, especially in the high-density, mostly ionised regime (Long et al., 2004). If I follow them and fix $\log n_e \approx 11$, then I find that T $\approx$ 14400K, $v_t \approx 260$ km s^{-1} and $\log N_H \approx 20.7$. Of course, there are several uncertainties that should be considered such as the thickness of the slab, absorbing this material but the basic result does not change. Indeed, these observed narrow absorption features suggests the presence of *moderate temperature, high-density, low-velocity* absorbing material along the line-of-sight. The temperature of this veil declines monotonically as the outburst progresses.

Surprisingly, the presence of the same ubiquitous features is discernible in all stages of the outburst, even in the disc-dominated plateau and echo-outburst phases. This fact implies that the existent veil is always present throughout the eruption. During the disc-dominated phases, i.e. plateau and echo-outburst phases, the UV emission comes mainly from the inner disc, a region spanning a few R_{WD}. Since at least part of this emission is absorbed, the veil is likely to have a lateral extent that is at least this wide. This strongly suggests that the veil is not connected with the WD itself, but is probably located in the *outer* disc regions.

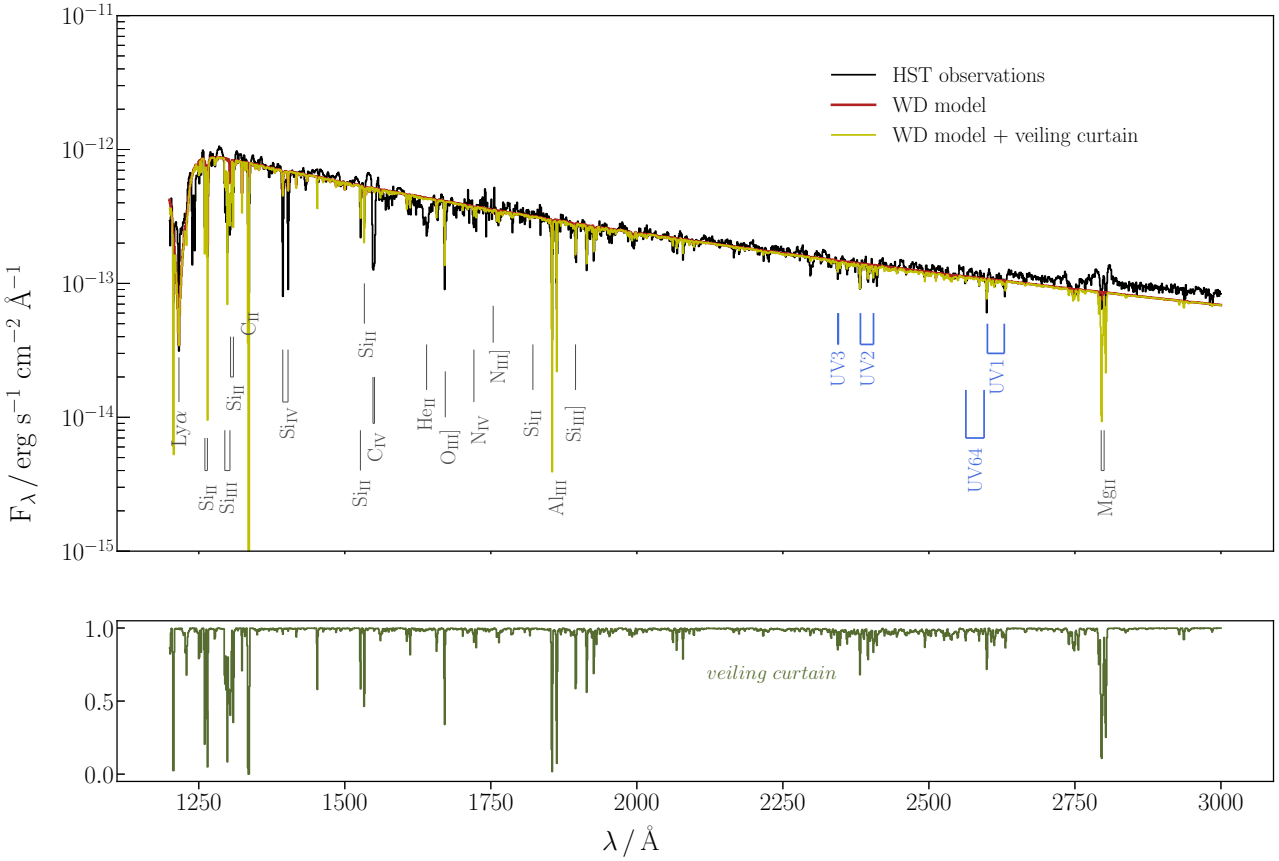

FIGURE 2.10: *Upper panel*: combined far- and near-UV spectrum, taken during the dip phase, of WZ Sge (grey) compared to the applied pure WD model (dark red) and the combination of the WD model and the veiling curtain (yellow). The most important lines are again identified at both parts of the spectrum. It is discernible that the addition of the veiling curtain is successful in reproducing the observed features. *Bottom* panel: demonstration of the absorbing veiling curtain (olive green) for comparison.

WZ Sge is viewed fairly edge-on – its outer disc is partially eclipsed (Ritter and Schroeder, 1979) – and absorption features associated with veiling material have also been seen in other high-inclination CVs. This includes both low-state systems, such as the 'Fe curtain' reported by Horne et al. (1994) in the eclipsing DN OY Car, and high-state ones, such as the absorption lines in the nova-likes UX UMa (Baptista et al., 1998) and V348 Pup (Froning et al., 2003). Whether all of these veiling structures are physically related is an important open question though but understanding their physical nature should be a matter of priority.

2.6 Summary

This study has tested the idea that the presented dip in the superoutburst light curve of WZ Sge stars is caused by a switch to a magnetic propeller state (Campana et al., 2018). Using time-resolved UV spectroscopy obtained just before, during and after the dip in the 2001 eruption of WZ Sge itself, I have constructed spectra representing both the constant and variable components

in all three outburst phases. The constructed spectra were, then, compared to the time-averaged and flaring components in the well-known magnetic propeller system AE Aqr (Eracleous and Horne, 1996).

As I have shown, none of WZ Sge's UV spectra show evidence for the distinctive broad emission line signatures seen in AE Aqr. This includes the spectra obtained for the dip phase, when the propeller should be active, and notably the variable component, which should isolate any time-dependent propeller signatured from the constant WD spectrum. Instead, all of WZ Sge's spectra display more or less the same set of narrow, (mostly) low-ionisation absorption features. All of this argues strongly against the propeller scenario in WZ Sge and the magnetic nature of its WD.

The narrow UV absorption lines in the spectra of WZ Sge are almost certainly the counterpart to the features noted by Long et al. (2004) later on in the same outburst. They cannot be formed in the atmosphere of the WD itself and therefore demand the existence of an absorbing "veil" in the system. The temperature of this material declines over the course of the outburst – my performed modelling suggests $T \simeq 14,000 - 17,000$ K during the dip phase, compared to the highest value found by Long et al. (2004), $T \simeq 11,500$ K, in the interval between the final two echo-outbursts. Importantly, the signature of the veil can be seen even during the disc-dominated plateau and echo-outburst phases. This suggests that the absorber is linked to a system component that is present throughout (at least) all of the super-outburst. An association with material in the outer disc seems likely, but the nature and origin of the absorber remain unknown.

I conclude by stressing the importance of resolving both of these mysteries: the peculiar outburst light curves and the nature of the absorbing veil.

Acknowledgements
I would like to acknowledge the contribution of Mike Eracleous for providing the data products of AE Aqr for the implementation of the current project and the immediate comparison with WZ Sge. Furthermore, I would like to thank my supervisor Christian Knigge that helped me with the modelling of the narrow absorption features presented in this work.

Chapter 3

An ultraviolet characterisation of the BHXT MAXI J1820+070

...before, during and after a transition

We live in a rainbow of chaos.

Paul Cezanne

The following two chapters are based on the work:

Georganti M., Knigge C., Castro-Segura N., Long K.S., Dewangan G.C., Banerjee S., Hynes R.I., Gandhi P., Altamirano D., Patterson J., Zurek D.R., "Ultraviolet spectroscopy of the low-mass X-ray binary MAXI J1820+070 before, during and after a state transition", submitted to MNRAS

Abstract

I present ultraviolet (UV) spectroscopic observations covering three distinct accretion states of the low-mass X-ray binary (LMXB) MAXI J1820+070: the luminous hard state, a hard-intermediate state and the soft state. The observations were obtained during the 2018 outburst of MAXI J1820+070 with the *Hubble Space Telescope* (HST) and AstroSat satellite observatory. The extinction towards the source turns out to be low – $E_{B-V} = 0.20 \pm 0.05$ – making it one of the best UV accretion laboratories among LMXBs. Remarkably, I observe only moderate differences between all three states, with all spectra displaying similar continuum shapes and emission lines. Moreover, the continua are not well described by physically plausible irradiated disc models. All of this challenges the standard reprocessing picture for UV emission from erupting LMXBs. The UV emission lines are double-peaked, with high-ionisation lines displaying higher peak-to-peak velocities. None of the lines display obvious outflow signatures, even though blue-shifted absorption features have been seen in optical and near-infrared lines during the hard state. The emission line ratios are consistent with normal abundances, suggesting that the donor mass at birth was low enough to avoid CNO processing ($M_{2,i} \lesssim 1.0 - 1.5 M_{\odot}$).

3.1 Introduction

MAXI J1820+070 (=ASASSN-18ey) is one of the closest, brightest and least-reddened Galactic black hole X-ray transients (BHXTs). It was discovered after its outburst onset on 2018 March (Tucker et al., 2018; Kawamuro et al., 2018). Since it is an excellent target for studying black hole (BH) accretion, unprecedented monitoring has been carried out across the entire electromagnetic spectrum, covering the main outburst of the source and the subsequent reflaring episodes (e.g. Baglio et al., 2018; Atri et al., 2020; Stiele and Kong, 2020; Tetarenko et al., 2021a; Özbey Arabacı et al., 2022; Yoshitake et al., 2022; Banerjee et al., 2024).

At a distance of d $= 2.96 \pm 0.33$kpc (Atri et al., 2020), the system was categorised quite early as part of the BH population family due to its unique X-ray properties (Kawamuro et al., 2018; Chakraborty et al., 2020). The details regarding the respective X-ray properties and characteristics of such systems as they follow a "q-track" between the hard and the soft state at the HID have been presented in Section 1.4.1. The binary inclination was calculated to be between $66^{o} \leq i \leq 81^{o}$ (Torres et al., 2020) while the jet inclination gives a slightly smaller estimate $i = 64^{o} \pm 5^{o}$ (Wood et al., 2021).

MAXI J1820+070 reached peak optical brightness around March 28, but remained at the hard state until (early) July. During that period, the X-ray spectrum was mostly described by a hard component, originated at the time-varying corona, and reflection features (e.g. Buisson et al., 2019; Kara et al., 2019; De Marco et al., 2021). In the timing domain, there was a frequency evolution of the observed QPOs both in X-rays (e.g. Mudambi et al., 2020; Mereminskiy et al., 2018; Yu et al., 2018b; Stiele and Kong, 2020) and optical (e.g. Yu et al., 2018b,a; Zampieri et al., 2018; Mao et al., 2022; Thomas et al., 2022), as their frequency was increasing with respect to time. The system then started its transition to the soft state, characterised by a rapid softening of the X-ray spectrum (Homan et al., 2018c,b, 2020) and a decrease of the radio and infrared flux, thereby indicating the quenching of the compact jet (Tetarenko et al., 2018a; Casella et al., 2018). It stayed at the soft state until (late) September, where it started its transition back to the hard state (Negoro et al., 2018; Bright et al., 2018; Motta et al., 2018; Homan et al., 2018a). Its outburst finished when the source reached its quiescent level on March 2019 (Russell et al., 2019).

The X-ray behaviour of BHXTs, as seen, is well-determined and serves as a probe to the inner disc regions in the vicinity of the compact object. However, a significant challenge for the study of these systems is that interstellar extinction usually prevents us from exploring the ultraviolet (UV) response to changes in X-ray luminosity and state transitions. This is unfortunate, as the UV band is a critical link between the inner accretion flow (the corona and the hot, viscously-dominated disc) and the outer one (the cool, irradiation-dominated disc). To date, only six BHXTs have been observed in the far-UV part of the spectrum near outburst peak in the soft state (Hynes, 2005). Increasing the size of this sample is important for understanding how the disc evolves and responds to the changing X-ray irradiation during eruptions, what drives the presence of disc wind signatures in specific wavelengths during different states (e.g. Muñoz-Darias et al., 2016,

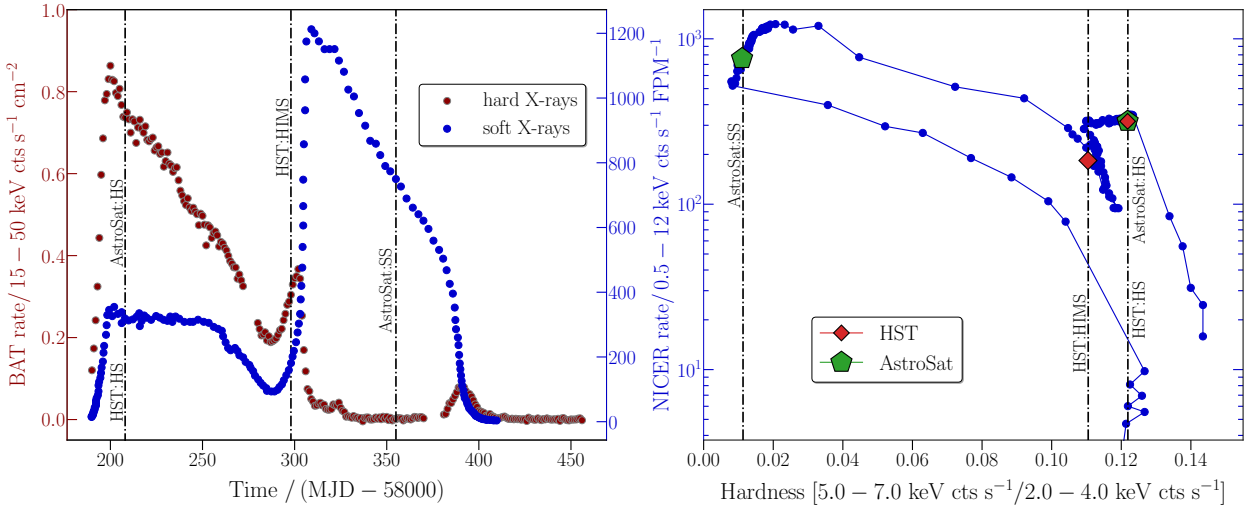

FIGURE 3.1: *Left panel*: Swift/BAT (hard X-rays, dark red) and NICER (soft X-rays, blue) light curves of the outburst of MAXI J1820+070 in 2018. *Right panel*: NICER Hardness-Intensity diagram (HID) of the source, averaged by day (in blue). In both cases, we have superimposed the timing of our ultraviolet observations for comparison. On the right panel, the times of our HST (dark orange) and AstroSat (light green) observations are noted by different colour, signifying the respective accretion state of the system. The transition between the two accretion states is evident in both panels.

2018, 2019; Sánchez-Sierras and Muñoz-Darias, 2020; Castro Segura et al., 2022; Fijma et al., 2023), and to shed light on the periodic and aperiodic variability produced at intermediate disc radii. MAXI J1820+070 provides us with a rare opportunity make progress in this area. Here, I present the first multi-epoch UV characterisation of a BHXT across both outburst states, which allows us to shed light on some of these issues.

The outbursts of BHXTs are typically interpreted in the context of the *disc instability model* (DIM; e.g. Lasota 2001; Hameury 2020 for a recent review), according to which the accretion discs in these systems are subject to a thermal-viscous instability related to the ionisation of hydrogen. To what extent X-ray irradiation plays a significant role in controlling the behaviour of the dsscs in BHXTs is still a matter of debate (e.g. van Paradijs and McClintock, 1994; van Paradijs, 1996; King and Ritter, 1998; Dubus et al., 1999, 2001; Tetarenko et al., 2018b). Strongly irradiated accretion discs are needed, though, to explain the longer and brighter eruptions of these systems and their light curve phenomenology. The outer disc is heated by radiation emitted in the inner regions, which keeps it ionised and prevents an early return to quiescence. It also means that the outer disc produces most of the UV/optical, and sometimes infrared, flux. This picture can be tested by modelling the UV SED with irradiated disc models.

The spectral lines seen in the UV also provide important diagnostics. For example, the He II λ1640Å recombination line is an effective bolometer for the (usually unobservable) extreme UV band above 54 eV. Moreover, UV line *ratios* can be used to shed light on the evolutionary history of the binary, since they depend strongly on the degree of CNO processing the accreting material has been subjected to (e.g. Mauche et al., 1997; Haswell et al., 2002; Gänsicke et al., 2003; Froning

et al., 2011, 2014; Castro Segura et al., 2024). Perhaps most importantly, however, the strong UV resonance lines (N V λ1240Å, Si IV λ1400Å, C IV λ1550Å) are highly sensitive outflow tracers.

The observable wind signatures presented by spectral lines take the form of blue-shifted absorption or P-Cygni profiles. In XRBs, such signatures have been found in both the corona- and disc-dominated states. However, clear *X-ray* wind signatures have so far only been seen in the soft state (e.g. Miller et al., 2006c; Ponti et al., 2012, 2014; Díaz Trigo and Boirin, 2016, and references therein), even though hard-state outflows have been identified both in optical/near-infrared (e.g. Muñoz-Darias et al., 2016, 2018, 2019; Jiménez-Ibarra et al., 2019) and UV spectra (Castro Segura et al., 2022; Fijma et al., 2023). This raises several important questions (e.g. Muñoz-Darias et al., 2019; Sánchez-Sierras and Muñoz-Darias, 2020; Muñoz-Darias and Ponti, 2022). Is the same wind present throughout the eruption, perhaps in different ionisation states? And is this wind multi-phase (e.g. clumpy) and/or spatially stratified? Or are we seeing completely distinct types of outflows in different bands (e.g. cool, magnetically driven winds in the UV, optical and near-infrared bands vs hot, thermally driven winds in X-ray bands)? Resolving these issues will require panchromatic spectroscopic observations across different spectral states. In this context, the present study provides the first data set allowing a search for UV wind signatures in different stages of a single outburst.

Finally, time variability in the form of stochastic flickering and QPOs is ubiquitous among XRBs (and, in fact, among all accreting systems). The standard interpretation of this variability is that each annulus of the disc is susceptible to fluctuations on its own viscous timescale. These fluctuations then propagate inwards, so that correlated variability we see in different wavelengths is the cumulative product of variations across a wide range of disc radii. Irradiation and reprocessing can introduce additional correlations between different wavebands on timescales corresponding to the light travel time from the center of the disc to the relevant emitting region. MAXI J1820+070 is already known to display correlated variability between X-rays and optical at the peak of its outburst (e.g. Stiele and Kong, 2020; Paice et al., 2021; Thomas et al., 2022). Our UV data allows us to test whether / to what extent the same behaviour is present in this intermediate waveband. This issue and the respective timing analysis are the subject of Chapter 4.

In this work, I focus on three distinct snapshots of MAXI J1820+070 obtained during this outburst with the *Hubble Space Telescope* (HST) and AstroSat observatories. The timing of the observations is shown in Figure 3.1, where I relate them to the overall X-ray behaviour of the system. For this purpose I have combined data from both the *Neil Gehrels Swift Observatory* (Swift/BAT; Gehrels et al. 2004; Krimm et al. 2013) and *Neutron star Interior Composition Explorer* (NICER; Gendreau et al. 2016) to construct both the overall X-ray light curve and the HID of the system. The rest of the current chapter is structured as follows. The following section, Section 3.2, provides the reader with a description of the employed observations. The Section 3.3 outlines all the results of the UV campaign. The presented analysis covers various aspects, including extinction estimation, UV wind detection, spectral changes in the UV throughout the different states, UV SED modelling using irradiation models and more.

3.2 Observations

3.2.1 HST observations

MAXI J1820+070 was observed on 2018 March 31st and June 29th (Proposal ID: 15454, PI: Knigge) by the *Space Telescope Imaging Spectrograph* (STIS; Kimble et al., 1998; Woodgate et al., 1998) onboard HST. Each epoch consisted of a five-orbit HST visit, with three orbits dedicated to the far-UV and the remaining two to the near-UV part of the spectrum. The first visit took place in the *hard* state right after the outburst peak. However, the second visit took place three months later, during the *hard-intermediate* state, just before the start of the hard-to-soft state transition.

The MAMA detectors were employed to obtain the observations in TIME-TAG mode in order to provide information on the fast (dynamical timescale) variability of the system. The initial observation, denoted as HST:HS, captured the system in a luminous hard state on MJD=58208.5, just few days after outburst peak. The $0''.2 \times 0''.2$ detector slit and the *echelle* E140M/1425Å, E230M/1978, 2707Å gratings were utilised, providing us with a spectral resolution of R $= \lambda/\Delta\lambda$ = 45800 and 30000 in the far- and near-UV regions, respectively. The subsequent observation, designated as HST:HIMS, took place on MJD=58298.5, just days before the state transition. In this epoch, we used the $52'' \times 0''.2$ slit coupled with the *first-order* G140L/1425Å and G230L/2376Å gratings. Here, the spectral resolution is not constant but wavelength-dependent at both sides of the spectrum. In particular, it ranges between 960-1440 in the far-UV and between 500-1010 in the near-UV wavelengths, respectively. A summary of the instrumental setups and their characteristics can be found in Table 3.1.

All the data were reduced using the *calstis* pipeline to extract one-dimensional spectra for each visit. For our first epoch, blaze correction of the individual orders of the echelle spectra and trimming of their overlapping regions were applied so we could combine them into a single spectrum. On the other hand, the construction of the HIMS first-order spectrum suffered from two challenges. First, there was a flux inconsistency between the far- and near-UV exposures – in particular, the near-UV (G230L) ods802050 exposure appeared to be 27% brighter than the corresponding far-UV (G140L) one in the overlap regions between the two. While it cannot be ruled out that this offset is real (i.e. intrinsic to variability associated with the source), I adjusted the near-UV time-weighted average to match its far-UV counterpart. This adjustment involved determining a scaling factor based on the median value of the continuum windows on both sides of the spectrum. The purpose of this choice was to facilitate our subsequent analysis by creating a single HIMS spectrum. Second, I observed a mismatch between the far- and near-UV line centers. As the setup in this epoch is constrained by the lack of spectral resolution and low signal-to-noise, I used the echelle spectrum and the location of several interstellar lines as my guide to account for these wavelengths shifts. In the end, I shifted the far-UV wavelengths by 1Å and the near-UV wavelengths by 2.5Å to correct for these offsets.

TABLE 3.1: Log of observations discussed in this work. All the observations were taken at the hard and hard-intermediate state except for the second AstroSat observation that is taken at the soft state. The last column represents the notation that I am going to use throughout this thesis.

ObsID	Setup	Onset (MJD)	Exposure (ks)	Notation
ods801010	STIS/E140M/1425Å	58208.52	2.151	
ods801020	—"—	58208.57	2.730	
ods801030	—"—	58208.64	2.730	HST:HS
ods801040	STIS/E230M/1978Å	58208.71	2.730	
ods801050	STIS/E230M/2707Å	58208.77	2.730	
ods802010	STIS/G140L/1425Å	58298.50	2.105	
ods802020	—"—	58298.56	2.730	
ods802030	—"—	58298.63	2.730	HST:HIMS
ods802040	STIS/G230L/2376Å	58298.70	2.730	
ods802050	—"—	58298.76	2.670	
T02_038T01_900001994	UVIT/FUV-G1	58207.50	11.39	AstroSat:HS
T02_066T01_900002324	UVIT/FUV-G1	58355.47	2.845	AstroSat:SS

3.2.2 AstroSat observations

AstroSat constitutes India's first space telescope, launched in 2015. Even though it is a multi-wavelength mission, it is mostly dedicated to high energy studies from UV to hard X-rays. Of great importance to us is the telescope at the UV wavelengths.

The *Ultraviolet Imaging Telescope* instrument (UVIT; Tandon et al., 2017, 2020) features three channels sensitive to three different bands: far-UV ($1200 - 1800$Å), near-UV ($2000 - 3000$Å), and visible ($3200 - 5500$Å). While far-UV and near-UV are used for scientific observations, the visible channel primarily aids in pointing drift correction. Both the far-UV and near-UV channels are equipped with broadband filters for imaging, providing a point spread function (PSF) of $1.0''$-$1.5''$, and include slit-less gratings for low-resolution spectroscopy. The far-UV channel contains two orthogonally arranged slit-less gratings (FUV-G1 and FUV-G2) to minimise contamination along the dispersion direction from nearby sources. Both channels operate in the photon counting mode. Further details on grating performance and calibration can be found in Dewangan (2021).

Level-1 data on MAXI J1820+070 were sourced from the AstroSat archive and processed with the CCDLAB pipeline (Postma and Leahy, 2017). Drift-corrected, dispersed images were generated orbit-wise and then aligned to produce a single image per observation. Spectral extraction was performed using the UVITTOOLS package[1], following Dewangan (2021) and Kumar et al. (2023). The source's zeroth-order image position in the grating images was located, and one-dimensional count spectra for the FUV gratings in the -2 order were extracted using a 50-pixel cross-dispersion width (see Banerjee et al. (2024) for more details). Background count spectra were also extracted

[1]Details about the package's requirements and documentation can be found at https://github.com/gulabd/UVITTools.jl.

similarly from source-free regions and used to correct the source spectra. The grating responses were updated to match the simultaneous hard state HST spectrum of the source, and these files are produced as explained in Dewangan (2021).

3.3 Results

3.3.1 Reddening and HI column density

Most BH binaries are located at kiloparsec (kpc) distances in the Galactic plane. As a result, they tend to suffer from strong extinction and reddening, making them difficult to observe especially at UV wavelengths. In fact, only 8 out of 68 BH binary systems are characterised by reddening values $E_{B-V} \leq 0.3$ (Corral-Santana et al., 2016). In addition to MAXI J1820+070 (whose extinction properties I discuss below), these low-reddening systems are GRS 1009-45 (della Valle et al., 1997), XTE J1118+480 (Garcia et al., 2000), Swift J1357.2-0933, XTE J1817-330 (Schlafly and Finkbeiner, 2011), MAXI J1305-704 (Mata Sánchez et al., 2021) and MAXI J0637-430 (Tetarenko et al., 2021b). Thanks to their relatively low and well-constrained extinction values, the intrinsic luminosities of these systems can be inferred with some confidence (this is true if the distance to the source is known).

In order to determine the line-of-sight extinction and reddening towards MAXI J1820+070, I use two different methods. Initially, I employ the strength of the λ2175Å dust absorption feature (near-UV hump) to determine the appropriate reddening value at the line-of-sight to the source. Dust grains and their properties along different lines-of-sight play a significant role at the determination of the extinction and the definition of their wavelength-dependent extinction curves. I fit a series of parameterised extinction curves, all of them dependent on the A_v and R_v parameters. For reference, I note $E_{B-V}=A_v/R_v$, where I set $R_v=3.1$, its standard value for typical Galactic sources. Using Fitzpatrick's reddened-law (Fitzpatrick, 1999) to match the λ2175Å interstellar dip of our "featureless"/continuum HST:HIMS spectrum, I estimate an extinction value of $E_{B-V} = 0.20 \pm 0.05$ (*sys*), where systematic uncertainties contribute to the error estimate. Figure 3.2 illustrates how the spectrum changes under different extinction values.

In addition, we exploit the well-established correlation between reddening and neutral atomic hydrogen column density (N_H) at any line-of-sight (e.g. Bohlin et al., 1978; Liszt, 2014). In this case, I determine the HI column density by modelling the damped Lyman-α (Lyα) absorption profile, evident in our HST:HS spectrum. I follow Bohlin (1975) and model this profile by an $Ce^{-\tau}$ factor, where C is the continuum level, and the optical depth, τ, is given by

$$\tau(\lambda) = 4.26 \times 10^{-20} N_H / (6.04 \times 10^{-10} + (\lambda - \lambda_0)^2). \quad (3.1)$$

Here, $\lambda_0 = 1215.67$Å, the rest wavelength of the Lyα line. I then estimate N_H by trial and error within a range of values centered on the total line-of-sight column density. Examples of these

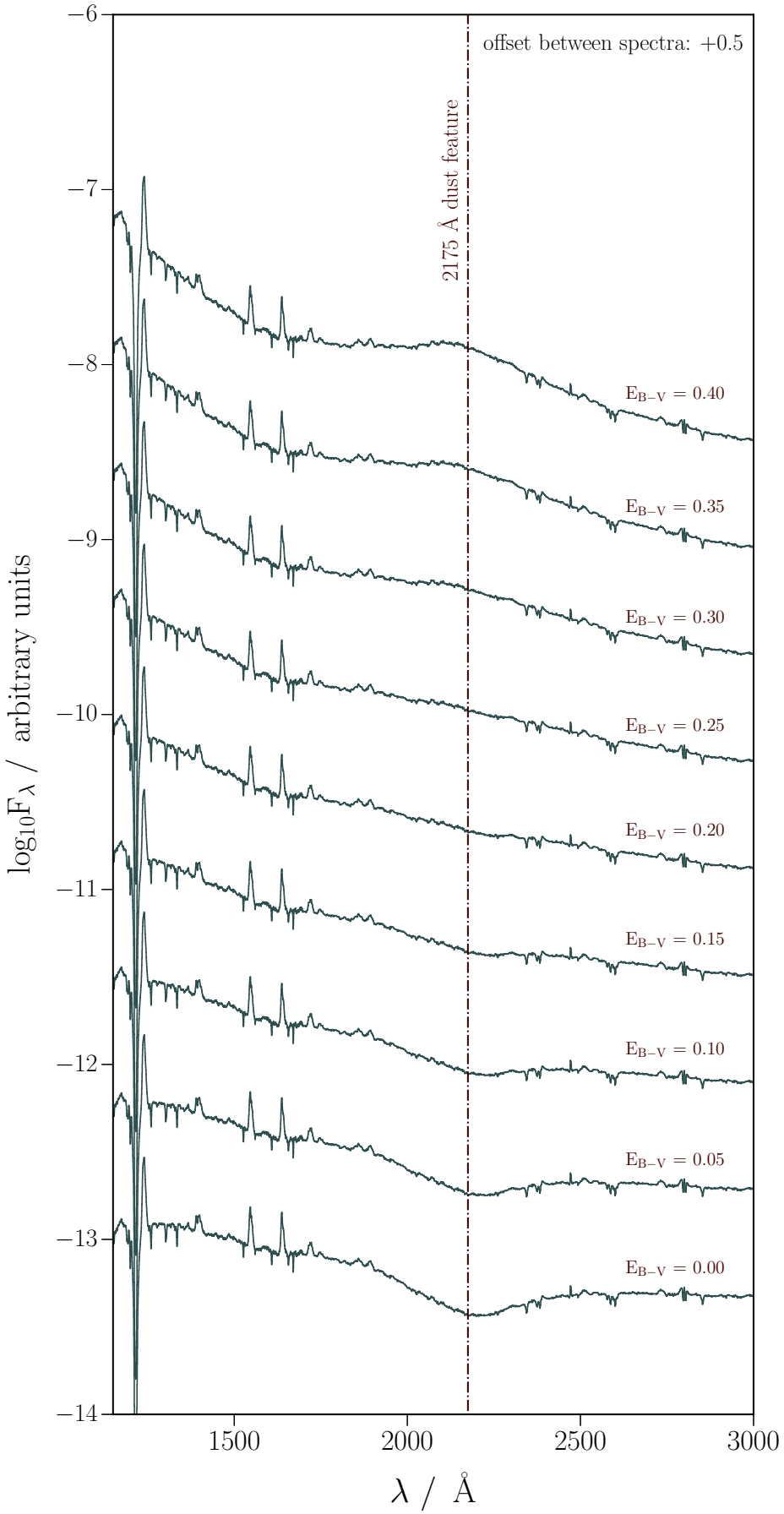

FIGURE 3.2: Estimation of the reddening E_{B-V} through the λ2175Å interstellar extinction feature. Assuming $R_v = 3.1$ and Fitzpatrick's extinction law (Fitzpatrick, 1999), I model the HST:HIMS spectrum and I find the reddening value, which makes the near-UV bump to disappear. The found value that I adopt in this paper is $E_{B-V} = 0.20$.

fits are shown in Figure 3.3, where the best-fit model corresponds to a column density value of $N_H = 10^{21}$ cm^{-2}. The corresponding reddening value then is determined via two standard N_H/E_{B-V} relations from the literature: $N_H/E_{B-V} = 5.8 \times 10^{21}$ cm^{-2} mag^{-1} (Bohlin et al., 1978) and $N_H/E_{B-V} = 8.3 \times 10^{21}$ cm^{-2} mag^{-1} for $|b| < 30^o$ (Liszt, 2014). The resulting estimates for E_{B-V} towards MAXI J1820+070 are 0.17 and 0.12, respectively. These values are slightly lower, but remain consistent with the one inferred from the UV SED.

Similar reddening results are obtained when employing slightly different N_H values derived from other observational studies. For example, high-resolution 21-cm radio observations (HI4PI Collaboration et al., 2016) and fitting of the absorbed X-ray spectrum (Koljonen et al., 2023) yield a column density of $N_H = 1.3 \times 10^{21}$cm^{-2}. On the other hand, modelling of diffuse interstellar bands (such as the λ5780Å line in *VLT*/X-Shooter spectra) results in a column estimate of $N_H = (1.4 \pm 0.4) \times 10^{21}$cm^{-2} (also in Koljonen et al., 2023). These estimates are consistent with predictions based on the Galactic dust distribution (see Koljonen et al. 2023 and references therein). Throughout this work, I adopt $E_{B-V} = 0.20$ as the reddening value.

3.3.2 Overview: spectroscopic evolution through the outburst

Our first objective is to shed light on the UV spectral evolution of MAXI J1820+070 as it passes from the hard to the soft state during its 2018 outburst. The luminous hard state near outburst peak was covered by (quasi-)simultaneous HST and AstroSat observations. The hard-intermediate state just before the state transition was caught by our second HST observation, while the soft state was captured only by low-resolution AstroSat spectroscopy. The evolution of the source's spectrum among these three stages is shown in Figure 3.4.

Overall, the HST spectra are characterised by blue continua and broad emission lines. Despite the significant flux decrease (by a factor of 3), and the system's transition from the hard to the soft state immediately after the second HST epoch, no major characteristic differences are observed between these two observations. The continuum shape remains consistent across our spectra and is reasonably well-approximated by a power-law with an index close to the characteristic value for a viscously-dominated accretion disc ($F_\lambda \propto \lambda^{-\beta}$, $\beta = 7/3$). This is surprising, since the disc regions producing the UV continuum may be expected to be heated by irradiation, rather than viscous dissipation. At wavelengths sufficiently far away from the Wien and Rayleigh-Jeans tails, an irradiation-dominated disc would tend to produce a power-law continuum with $\beta = 1$, significantly shallower than observed (Frank et al., 2002). I will return to this issue below in Section 3.3.4.

Both epochs display the same set of strong, double-peaked emission lines, representing both low- and high-ionisation atomic transitions. At shorter wavelengths, the usual resonance UV lines such as N V λ1240Å, Si IV λ1400Å, C IV λ1550Å or HeII λ1640Å are seen in emission. The damped Lyα absorption line produced by absorption in the ISM contaminates the far-UV end of the spectrum. At the very opposite end, the prominent Mg II λ2800Å line in emission is apparent.

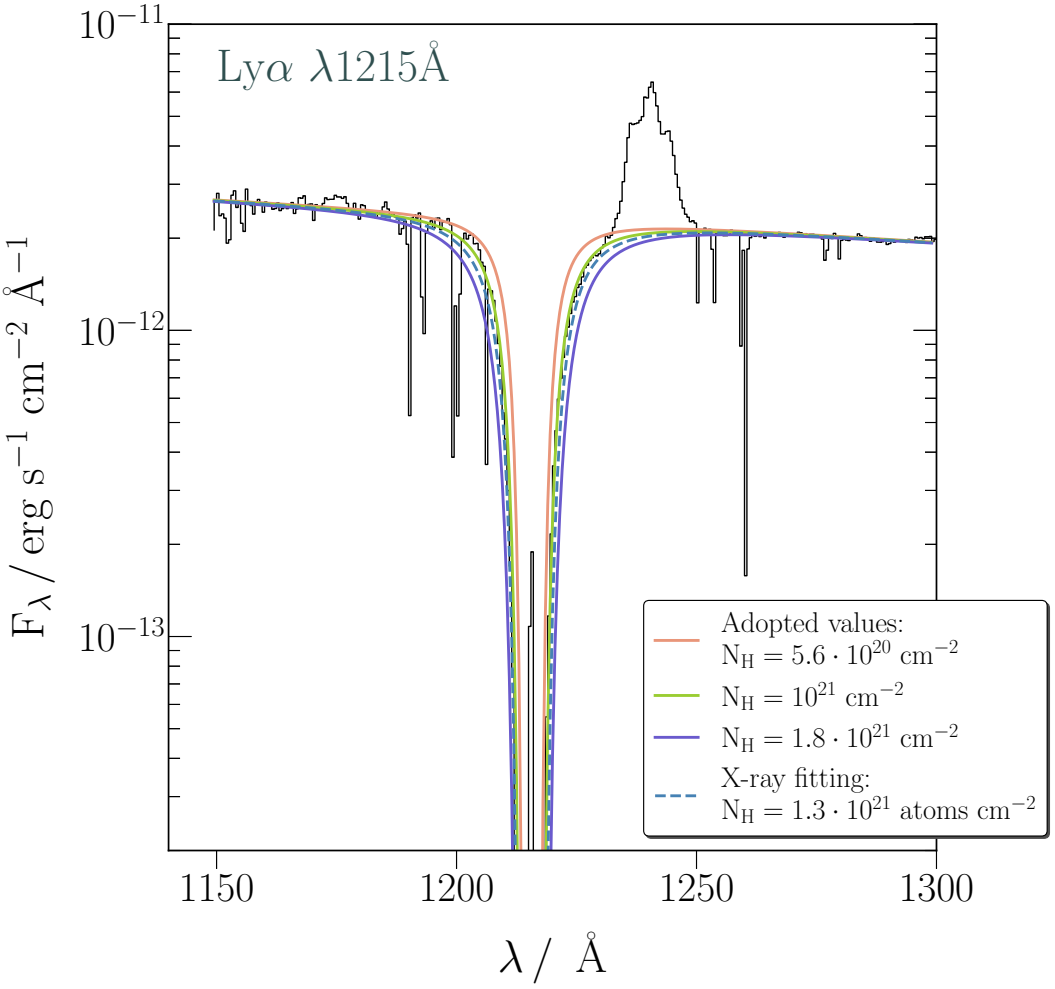

FIGURE 3.3: Focus on the interstellar Lyα line of our HST:HS spectrum in order to model its damped profile. The different fits are represented by different solid colour lines, whose corresponding column density is specified in the legend. The light blue dashed line signifies the column density, derived from X-ray spectral fitting (Koljonen et al., 2023). The optimal model, represented by a light green colour, corresponds to a column density of $N_H = 10^{21}$cm^{-2}.

The AstroSat spectra also capture the far-UV wavelengths, but − due to the lower resolution and signal-to-noise of these data sets − only the strongest lines are detected. As AstroSat constitutes our sole insight into the system's soft state, I exploit our simultaneous hard state observations to calibrate and facilitate comparisons between the HST and AstroSat spectra. For these comparisons, I degrade the HST spectra to the same resolution as the AstroSat observations using a simple Gaussian filter. The result is illustrated in Figure 3.5. A good agreement is achieved between the (quasi-)simultaneous HST/AstroSat hard state observations, whereas there is a hint of line strengthening in the soft state, especially for the Si IV and C IV profiles. The good agreement of the HST/AstroSat observations at the hard state are partly artificial as the AstroSat spectrum was calibrated based on the HST (quasi-)simultaneous spectrum (mentioned earlier in Section 3.2.2).

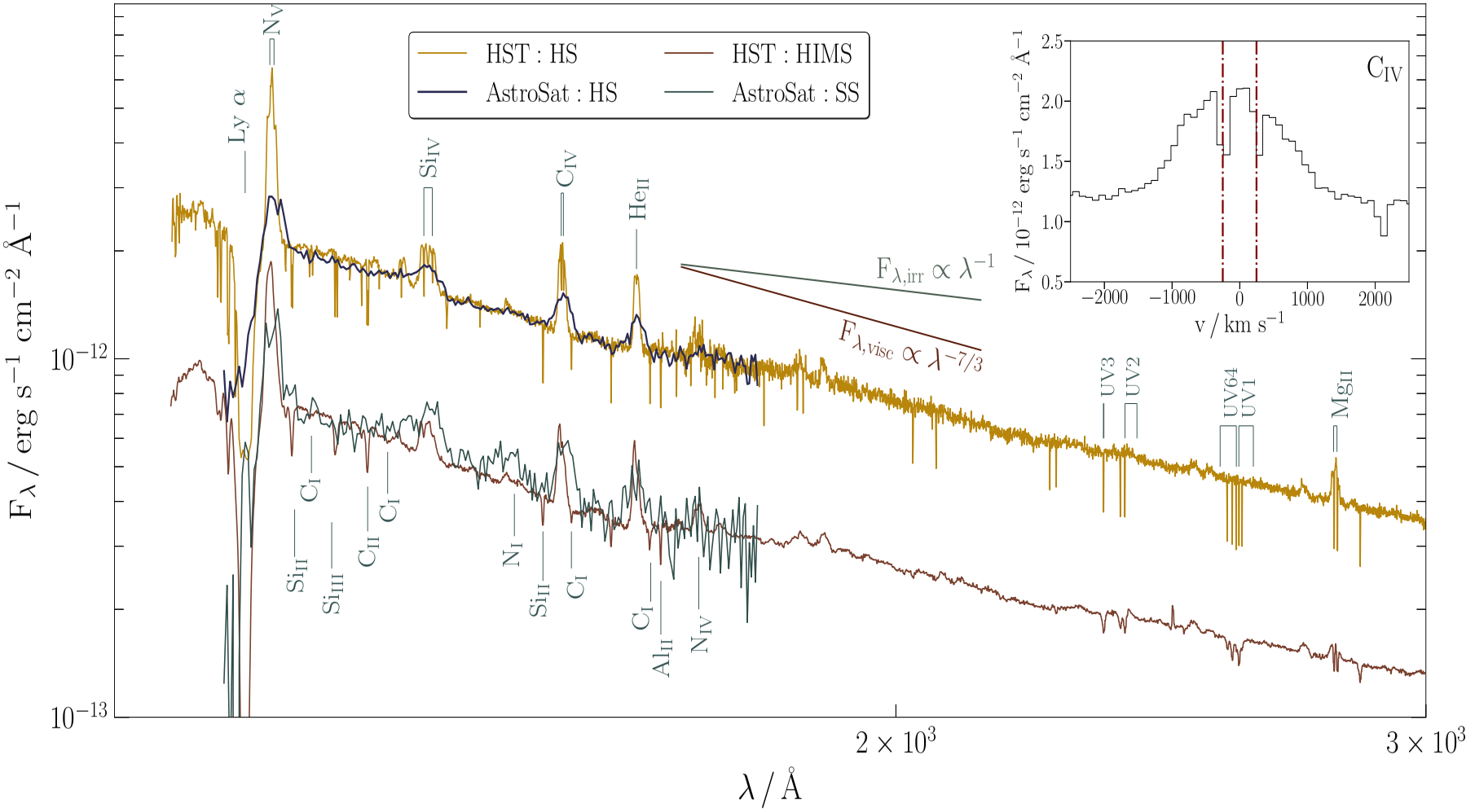

FIGURE 3.4: The dereddened time-averaged spectral evolution of the source across three distinct stages of its outburst, accompanied by line identifications. This work covers three key points of the source's outburst: a) a luminous hard state, combining HST/AstroSat observations b) HST observations of a hard-intermediate state before the state transition and c) AstroSat observations of the soft state. The HST spectra cover the far- and near-UV regions (1150-3000Å) whereas the AstroSat observations cover only the 1200-1800Å range. The slope indices of both a standard Shakura-Sunyaev accretion disc ($F_{\lambda,visc} \propto \lambda^{-7/3}$) and an irradiated disc ($F_{\lambda,irr} \propto \lambda^{-1}$) are illustrated. For clarity, I cut the interstellar lines by 70% of their flux, compared to the original lines. An inset plot zooms in on the C IV λ1550Å profile, emphasising the absence of evidence of an outflow.

3.3.3 Emission line shapes and fluxes

All of the observed lines appeared to be double-peaked or consistent with being double-peaked (within the limit of the diverse spectral resolutions of our instrumental setups). Assuming that the observed emission lines are produced at the atmosphere of the accretion disc, their shapes can help us to specify the physical conditions in the line-forming region(s) and define their evolution during the time between the observations.

Broadened, double-peaked emission profiles are characteristic of geometrically thin Keplerian accretion discs, where the two peaks correspond to regions of the disc rotating towards (blue-shifted component) or away from the observer (red-shifted component), respectively. In this context, I carry out a qualitative analysis of the most prominent observed resonance lines from our dereddened continuum-subtracted spectra. Specifically, I measure properties such as their line fluxes and the corresponding velocities of each of the two components. Then, the fitted emission profile is numerically integrated to extract key parameters.

In my fits, all relevant *atomic* transitions are assumed to produce two kinematically distinct (blue and red) Gaussian emission lines. The two components are constrained to share the same FWHM, but they are allowed to have different normalisations and shifts relative to the relevant rest wavelengths. This is not unexpected, as transient components such as hot spots or interactions at the stream-impact bulge can disrupt the disc's model symmetry. The He II line is adequately described by two such components associated with a single atomic transition. However, most of the lines I consider (specifically N V, Si IV, C IV and Mg II) are resonance doublets, i.e. they consist of *two* well-separated atomic transitions. I therefore have to explicitly account for both doublet components in my fits to these lines. Each of these lines is thus described by a total of four Gaussian emission profiles: an atomic doublet representing the blue kinematic component and an atomic doublet representing the red kinematic component. The wavelength separations between the atomic doublet components are always kept fixed at their known values. The intensity ratio between the doublet components is expected to range between 2:1 (in favour of the blue doublet component) and 1:1, depending on whether the line is optically thin or optically thick. However, I do not enforce this.

The high resolution echelle spectra, obtained in epoch HST:HS (the luminous hard-state), exhibit clear evidence for narrow absorption features close to the rest wavelengths of the Si IV, C IV and Mg II doublets. These absorption features might be intrinsic to the source, but are more likely associated with the ionised phase of the ISM along the line-of-sight. I therefore include narrow (unresolved) doublet absorption features in my models for these lines. The absorption profiles are modelled as $e^{-\tau}$, where, here, τ corresponds to the superposition of the two absorption profiles. The profiles also share the same FWHM and their intensity ratio is specified to range between 2:1 (optically thin) and 1:1 (optically thick) cases. In particular, the only line that it is considered to be formed in an optically-thick region ($\tau >> 1$) of the accretion disc is the Mg II line, as it can be

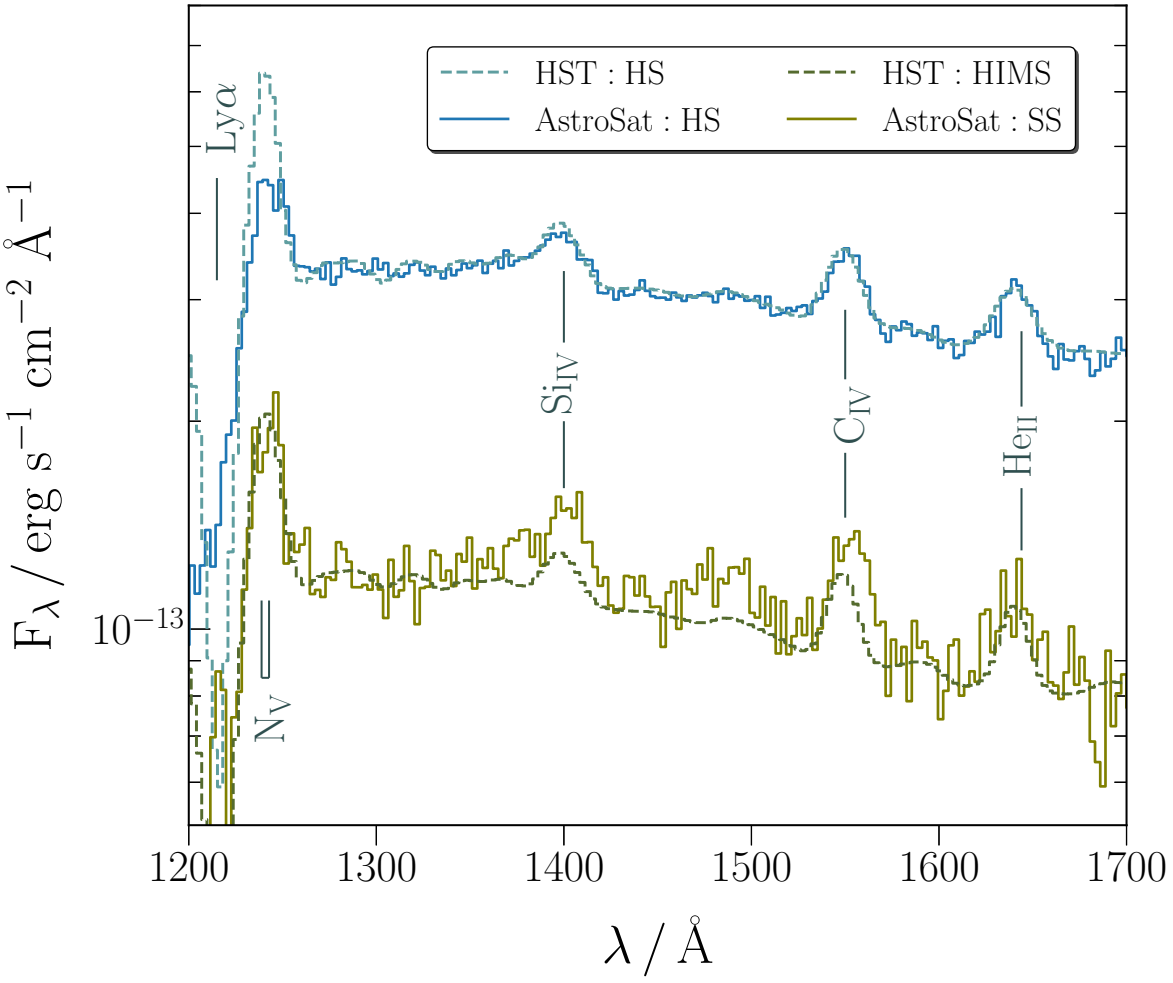

FIGURE 3.5: Far-UV spectral evolution of MAXI J1820+070. I adjusted HST's resolution of the hard and hard-intermediate state epochs to match AstroSat's intrinsic resolution. Apparent agreement among all the observations, taken during the hard state, whereas I observe stronger features when the system is in the soft state. I note that I have limited information regarding the line profiles in the soft state when only four lines are visible.

seen by its profile structure in Figure 3.6. The same figure also shows the rest of the continuum-subtracted line profiles during the first HST epoch along with the Hα Balmer profile, taken by *VLT*/X-shooter, days before our considered HS date[2]. The Hα profile displays broad emission wings, reaching velocities of almost 1800 km s^{-1} (Muñoz-Darias et al., 2019).

In the second HST epoch, described by lower resolution first-order spectra, the absorption profiles are not strikingly evident as in HST:HS and therefore, in my modelling, I fix their properties (amplitude, location and FWHM) to their already-determined values. It is noted that, for the MgII line, in order to facilitate the modelling process, I also fix the intensity ratio and the (common) FWHM of the four-component Gaussian emission profile to the ones of the first HST epoch. In all

[2]The employed optical spectrum of MAXI J1820+070 has been previously published in Muñoz-Darias et al. (2019). It was acquired with *VLT*/X-shooter (Vernet et al., 2011) on 2018 March 22nd (MJD=58199.32), as part of the 0100.D-0292 program. We processed the data using the X-shooter pipeline version 3.6.1 (Freudling et al., 2013).

cases, the constructed model of each of the lines is smoothed to the instrumental resolution of the employed setting and then, it is rebinned to 0.5Å.

Finally, I implement the same method to extract line properties in AstroSat's dereddened spectra. However, in this case, I focus only on the strongest lines (Si IV λ1400Å, C IV λ1550Å, He II λ1640Å) observed in the spectra. Due to the AstroSat's lower resolution, the line profiles of these species are satisfactorily fitted by two Gaussian components, except for the case of the He II line, which is well modelled as just a single Gaussian. I avoid measuring the properties of the N V profile, as it lies too close to the blue edge of the detector to yield reliable measurements.

The line flux and EW uncertainties associated with the fits are estimated through Monte Carlo simulations. First, I estimate the standard deviation (rms), $\sigma_{\rm res}$, between the data and the fitted model. Then, for each line, I generate mock datasets, where the model flux at each wavelength is perturbed by a Gaussian distribution centred on the actual flux with standard deviation $\sigma_{\rm res}$. The line flux and EW for each of these mock sets are then calculated by fitting the new line profile and numerically integrating across it. This iterative process is repeated 1000 times, allowing us to estimate the errors at 1σ confidence level.

The results of our fitting process are presented in Table 3.2. The peak-to-peak velocities, $v_{\rm pp}$, shown also in Figure 3.8, are consistent with the standard picture of an accretion disc where higher ionisation species are formed closer to the central source and are therefore associated with higher velocities. I will discuss the physical implications of the inferred fit parameters more in Section 3.4.1.1.

Our HST spectra show no indication of wind-formed UV features in the hard state, either in the form of blue-shifted absorption or P-Cygni profiles, as can be seen in Figure 3.6. There is also no hint of such features in the AstroSat soft state observations, but the lower signal-to-noise and resolution of those observations would prevent the detection of all but the strongest such features.

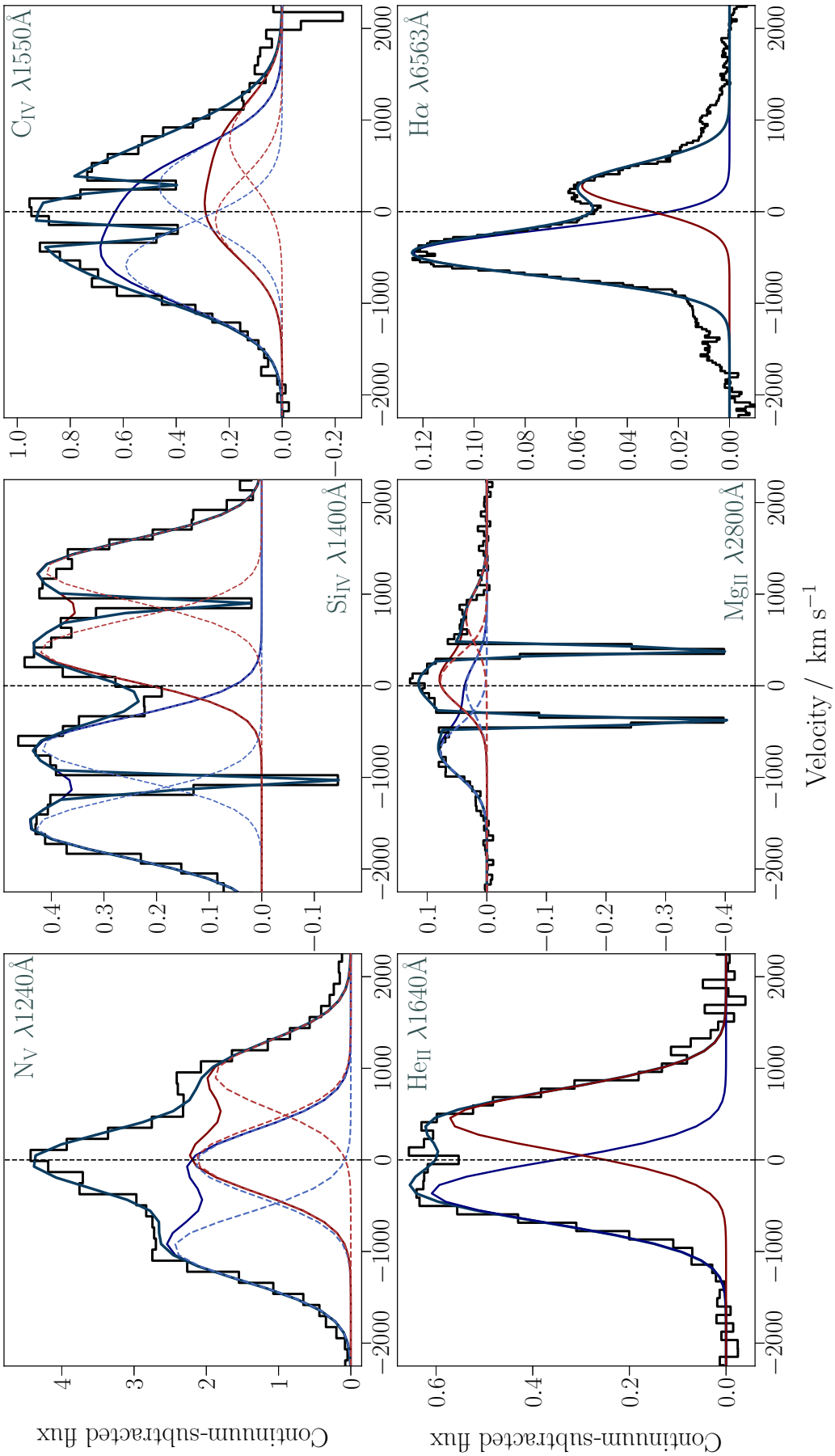

FIGURE 3.6: Continuum-subtracted line profiles of the most prominent UV resonance lines, observed during our HST:HS epoch. Each profile is fitted by a number of Gaussian components to account for each of their individual shapes (dashed lines). Our modelling is based on the fact that each atomic transition produces a distinguised blue and a red emission component. Here, we follow the blue and red colour distinction to demonstrate the relevant created profiles. The last panel shows the *VLT*/X-shooter H6 Balmer line, taken few days before the luminous hard state observation considered here, for comparison. Its profile clearly demonstrates a broad emission line wing.Details of our Gaussian modelling are provided in Table 3.2.

TABLE 3.2: Attributes of the most prominent resonance line profiles in the UV region for all of our epochs. Specifically, I take a closer look at the usual suspects: the N_V λ1240Å, Si_{IV} λ1400Å, C_{IV} λ1550Å, He_{II} λ1640Å and Mg_{II} λ2800Å lines. The table below summarises various line properties, derived from Gaussian fitting of the dereddened continuum-subtracted spectra. Key properties include the integrated fluxes (in 10^{-12} erg s^{-1} cm^{-2} Å^{-1}) and EWs along with their associated errors. Additional parameters of the fitting such as the FWHM, the individual component velocity, the peak-to-peak separation (all in km s^{-1}), the doublet amplitude ratio as well as the ratio between their red/blue component are also shown. The quoted errors correspond to 1σ.

Line	F_λ (cgs)	$F_{\lambda,\text{downgraded}}$ † (cgs)	EW (Å)	FWHM (km s^{-1})	σ (km s^{-1})	v_{pp} (km s^{-1})	Doublet amplitude ratio	Red-to-blue amplitude ratio
HST:HS								
N_V	32.62 ± 0.92	–	16.03 ± 0.80	1818	365	923	1.14	0.88
Si_{IV}	6.50 ± 0.22	6.35 ± 0.33	4.00 ± 0.16	3554	332	867	1.02	0.98
C_{IV}	8.71 ± 0.26	6.41 ± 0.15	7.53 ± 0.28	1773	446	869	1.27	0.43
He_{II}	5.43 ± 0.18	5.37 ± 0.08	5.11 ± 0.19	1515	335	784	0.94	–
Mg_{II}	1.44 ± 0.04	–	3.59 ± 0.12	1359	273	687	2.24	1.0
HST:HIMS								
N_V	13.08 ± 0.47	–	21.21 ± 1.33	2354	651	1366	3.48	1.07
Si_{IV}	2.14 ± 0.04	–	3.98 ± 0.08	3801	466	1018	1.29	0.94
C_{IV}	2.62 ± 0.03	–	6.78 ± 0.09	2231	460	983	0.52	0.46
He_{II}	1.92 ± 0.04	–	5.66 ± 0.14	1482	390	998	0.48	–
Mg_{II}	0.43 ± 0.01	–	2.95 ± 0.07	1390	273	882	0.33	1.0
AstroSat:HS								
Si_{IV}	7.23 ± 0.72	–	4.66 ± 0.48	–	–	–	–	–
C_{IV}	6.00 ± 0.43	–	4.98 ± 0.41	–	–	–	–	–
He_{II}	4.84 ± 0.39	–	4.5 ± 0.39	–	–	–	–	–
AstroSat:SS								
Si_{IV}	3.57 ± 0.41	–	6.28 ± 0.76	–	–	–	–	–
C_{IV}	3.59 ± 0.39	–	8.65 ± 1.01	–	–	–	–	–
He_{II}	3.17 ± 0.74	–	9.13 ± 2.32	–	–	–	–	–
X-shooter:HS								
Hα	0.247 ± 0.003	–	7.03 ± 0.08	649	248	732	2.14	–

Notes: † Line flux measurements from the downgraded dereddened continuum-subtracted spectra for an immediate comparison to the AstroSat:SS estimates. This comparison is imminently seen in Figure 3.9 where I follow the line flux evolution of the source throughout the three epochs of the outburst. The respective uncertainties are estimated through Monte Carlo simulations.
‡ The *VLT*/X-shooter observation is taken few days before the HST:HS epoch, on 2018 March 22nd (or in MJD:58199.32).

3.3.4 Irradiated disc modelling

X-ray irradiation constitutes a crucial, yet not well-understood, ingredient to elucidate the long duration and the high luminosity of sporadic eruptions in BHXTs. The reprocessing of X-ray photons at the disc surface stands as an additional contributor to heating in the outer disc regions, thereby generating the UV and optical light, emitted within these discs (van Paradijs and McClintock, 1994; van Paradijs, 1996). It remains a question, though, how the reprocessing picture is shaped as the accretion states and luminosity change and whether a simple irradiated disc model could sufficiently explain the observed UV spectral shape.

The behaviour of MAXI J1820+070 suggests that this system may belong in this category, susceptible to such characteristics. However, modelling of its continuum indicates otherwise, as its power-law index closely resembles that of an "unirradiated" viscous disc. In this study, I will first introduce the model and the irradiation contribution to the energy balance in the disc while I use the HST:HIMS spectrum as the testbed to examine whether a simple irradiated disc model can replicate the spectral shape of the observed UV SED.

Our model describes the disc as a collection of concentric circular annuli, each of which is characterised by an effective temperature $T_{\rm eff}(R)$. The disc extends from the ISCO, $R = R_{\rm ISCO}$, to an outer radius, $R = R_{\rm disc}$. The effective temperature is set by the requirement that the rate at which an annulus radiates energy away, $\sigma_{\rm SB}T_{\rm eff}^4$, must balance the rate at which energy is deposited into it by viscous dissipation and irradiation. The treatment of irradiated discs and how irradiation changes the temperature distribution has already been given in Section 1.3.4. I mention here the relevant relations, only as a reminder.

The viscous heating rate can be written as

$$\sigma_{\rm SB}T_{\rm eff,visc}^4 = \frac{3GM_{\rm BH}\dot{M}_{\rm acc}}{8\pi R^3}\left[1-\left(\frac{R_{\rm ISCO}}{R}\right)^{1/2}\right], \tag{3.2}$$

where $M_{\rm BH}$ is the mass of the BH, and $\dot{M}_{\rm acc}$ is the accretion rate.

The heating rate due to irradiation can be modelled as

$$\sigma_{\rm SB}T_{\rm eff,irr}^4 = \left(\frac{L_{\rm irr}}{4\pi R^2}\right)\left(\frac{H}{R}\right)\gamma\,(1-A)\,, \tag{3.3}$$

where $L_{\rm irr}$ is the irradiating luminosity (assumed to originate from a central point source), and A is the albedo (so that $1-A$ is the fraction of the light incident on the annulus that is absorbed). The quantity H/R is the aspect ratio of the disc, which can be shown to scale as

$$\frac{H}{R} = \left(\frac{H}{R}\right)_{R_{\rm disc}}\left(\frac{R}{R_{\rm disc}}\right)^{\gamma}, \tag{3.4}$$

where γ is taken to be $1/8$ in the absence of irradiation and $2/7$ if irradiation dominates the heating rate (Frank et al., 2002). Strictly speaking, γ is therefore a function of radius, but I neglect this here and simply set $\gamma = 2/7$ everywhere. This approximation means that I will slightly overestimate the influence of irradiation, but only in disc regions where irradiation is relatively unimportant. Putting all of this together, the effective temperature of the disc can be calculated by requiring that total heating should be matched by radiative cooling, i.e.

$$\sigma_{SB} T_{eff}^4 = \sigma_{SB} T_{eff,visc}^4 + \sigma_{SB} T_{eff,irr}^4. \tag{3.5}$$

In order to calculate the spectrum of the disc, I assume that each annulus radiates as a modified blackbody,

$$B_{\nu,mod}(f, T_{eff}) = \frac{2h\nu^3}{f^4 c^2 \left[e^{\frac{h\nu}{fkT_{eff}}} - 1 \right]}. \tag{3.6}$$

Here, f is the so-called "spectral hardening factor" (Shimura and Takahara, 1995), which approximately corrects for the effects of Compton scattering in the disc atmosphere. This factor is not actually a constant, but rather is a function of temperature, surface density and radius (and, for BHs, spin parameter). In the SED model, I parameterise f using the analytical fitting function provided by Davis and El-Abd (2019), as

$$f = 1.48 + 0.33(\log \dot{M}_{acc} + 1) + 0.02(\log[M/M_\odot] - 1) + 0.07(log\alpha + 1). \tag{3.7}$$

In calculating the required surface density, I take into account the relevant relativistic correction factors (Novikov and Thorne, 1973; Davis and El-Abd, 2019).

Empirically, the SEDs of X-ray binaries exhibit at least one additional high-energy component, which is usually attributed to a hot, compact and optically thin "corona" located close to the accretor. I model this component, which usually dominates in the hard X-ray regime, as a simple power-law,

$$I_{\nu,cor} = I_{\nu_0,cor} \left(\frac{\nu}{\nu_0} \right)^{-(\alpha+2)}. \tag{3.8}$$

With the definition of α, I have $I_{\lambda,cor} \propto \lambda^\alpha$, and I adopt $\nu_0 = 3 \times 10^{18}$ Hz (corresponding to $\lambda = 1$ Å) as the reference frequency. However, this component is not relevant to our application.

My primary focus is to assess if irradiation significantly impacts the outer accretion disc regions and can reproduce the shape and flux level of the far- and near-UV SED. To achieve this, I opt

to model the spectrum prior to the state transition (HST:HIMS) as it provides us a unique opportunity for a direct comparison of our model, which is close in time and luminosity, with the one employed by Koljonen et al. (2023), henceforth referred to as the "reference model".

I first try to find the optimal model that describes the UV SED. I allow the mass accretion rate ($\dot{M}_{acc}$), outer disc radius (R_{out}) and albedo (A_{out}) to vary, taking into account both irradiation heating and viscous dissipation. It is important to note that we cannot avoid the mathematical degeneracy between albedo and scale-height, so I opt to fix the latter for simplicity. I assume a Schwarzschild (non-spinning) BH (Guan et al., 2021; Zhao et al., 2021), scale-height H/R=0.10, reddening E_{B-V}= 0.20 (see Section 3.3.1) while the orbital characteristics (d, M_{BH}, i, q) of the system are already determined (Atri et al., 2020; Torres et al., 2020). In particular, I adopt $M_{BH} = 8.5 M_{\odot}$ and $i = 65^{o}$ in our modelling, while all the distances are measured with respect to the gravitational radius, $R_G = GM_{BH}/c^2$.

The best-fitting model SED is shown in Figure 3.7 (upper panel). As already noted above, the observed spectral shape of the UV continuum is close to that of a standard accretion without any irradiation. In line with this, the UV emitting regions in our best-fitting model are *viscously-dominated*, with very little, contribution from irradiation. However, the best-fit model parameters $-$ $\dot{M}_{acc} = 10^{-7}\ M_{\odot}\ yr^{-1} \simeq 0.5\dot{M}_{Edd}$, $R_{out} = 10^{6} R_G$, $A_{out} = 0.93$ $-$ are physically implausible. In particular, the outer disc radius is far in excess of the *tidal disc radius* of the BH accretor, which is equal to $R_{tidal} = 10^{5.4} R_G$.

Can a physically more plausible irradiated disc model still reproduce the SED acceptably? Naively, for any reasonable values of the disc parameters ($\dot{M}_{acc}, R_{out}, A_{out}$), irradiation should play a crucial role. To address this question more directly, I construct a small grid of models that allows us to understand how changes in these parameters affect the overall SED (and the irradiation contribution, specifically). The grid is roughly centred on the "reference" disc SED model of Koljonen et al. (2023). This model is derived by fitting the X-ray-optical SED of MAXI J1820+070 at the soft state, days after the hard/soft state transition. The corresponding reference parameters are $\dot{M}_{acc} = 2.37 \times 10^{-8}\ M_{\odot}\ yr^{-1}$, $R_{out} = 10^{5.3} R_G$ and A_{out} = 0.90. For all models in our grid, I fix $L_x = 1.35 \times 10^{38} erg\ s^{-1}$ (Koljonen et al., 2023). The attempted comparison is justified as the two epochs are close enough in time that I do not expect the values of the considered parameters to change significantly.

Figure 3.7 (lower triplet of panels) shows the reference and test models that make up our small grid overlaid on the second hard state UV SED. The reference model is clearly too red and underestimates the far-UV flux level. Moreover, even though the test models confirm that reasonable changes to the model parameters can certainly modify the UV continuum, they also suggest that such changes cannot simultaneously match the brightness and shape of the observed SED. I will discuss the implications of this result in Section 3.4.3.

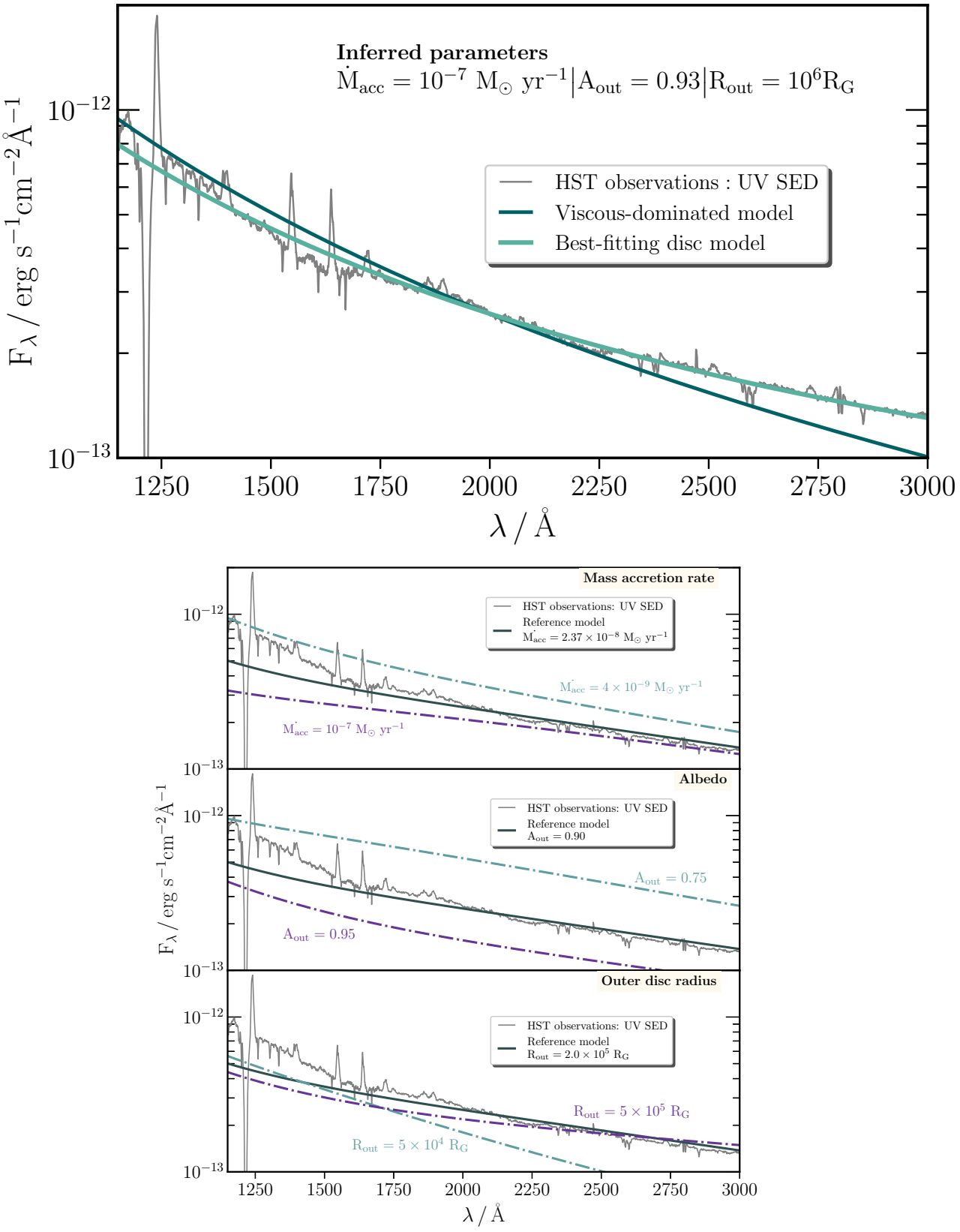

FIGURE 3.7: *Upper panel*: The best-fitting model for our UV SED is very close to a pure viscous-dominated disc. This model yields to a set of unreasonable values for the $\dot{M}_{acc}, A_{out}, R_{out}$ parameters, considered here. *Lower panel*: Parameter sensitivity analysis in our modelling to evaluate the dependency and impact of the considered disc factors on the final output. Each panel corresponds to one of these factors, where I explore a plausible range of their parameter space (dashdot lines), overlaid on the observed HST:HIMS UV spectrum of MAXI J1820+070 (in grey). The reference disc SED, modelled by Koljonen et al. (2023), is depicted in dark grey in all the panels.

3.4 Discussion

3.4.1 The spectral journey through the accretion states

3.4.1.1 Probing the accretion states

Accretion states in BHXTs are usually defined in terms of their X-ray properties. Do their UV properties reflect the same phenomenological picture?

MAXI J1820+070 provided us with a rare opportunity to investigate, for the first time in the UV band, the long-term spectral evolution of a BH binary as it transitioned from the hard to the soft state. Interestingly, I find that the UV behaviour remains consistent among both states: there are no distinct signatures that would signal the state transition or the different phases of the hard-state decay. The UV spectra exhibit the same Doppler-broadened, double-peaked line profiles, which are most likely emitted by an optically thin layer of the disc's atmosphere.

Given the velocities determined from our modelling of the line profiles, I can estimate the location of the corresponding line-forming regions by assuming that the peak-to-peak separation of a given line corresponds to the Keplerian velocity near (the outer edge of) the disc region in which the line is produced. This line formation radius estimate is therefore given by

$$R = \pm\frac{GM_{BH}\sin^2 i}{v_{pp}^2} \Rightarrow R = \frac{c^2\sin^2 i}{v_{pp}^2}[R_G], \tag{3.9}$$

where the latter equation is expressed in terms of R_G. This quantity is shown for each line in each HST epoch in Figure 3.8, where I also relate this to the ionisation potential of the relevant species. As expected, the higher ionisation lines are generated at smaller radii, where temperatures are higher, while the lower ionisation lines originate in the cooler parts of the disc further out.

Figure 3.9 compares the fluxes of the key lines (i.e. N V λ1240Å, Si IV λ1400Å, C IV λ1550Å or He II λ1640Å, Mg II λ2800Å) between our three independent epochs: the luminous hard state (HST:HS), the hard-intermediate state just before the state transition (HST:HIMS) and the soft state (AstroSat:SS). Two key features are apparent. First, the line fluxes decline by approximately a factor of 3 between the hard and hard-intermediate state observations. This is similar to the drop in the UV continuum flux between these epochs, i.e. the EWs of the lines remain almost unchanged. Second, line fluxes then increase again − by roughly a factor of 2 − between HST:HIMS and the soft state.

The strengthening of the UV lines across the hard-to-soft state transition may be expected, given the increase in extreme UV (EUV) and soft X-ray luminosity across this transition (Figure 3.1). The line strength evolution between the hard state and hard-intermediate state observations seems less obvious. Even though the soft X-ray luminosity in HST:HIMS *is* lower than that in HST:HS (Figure 3.1), the difference amounts to less than a factor of 2. Moreover, one might expect the

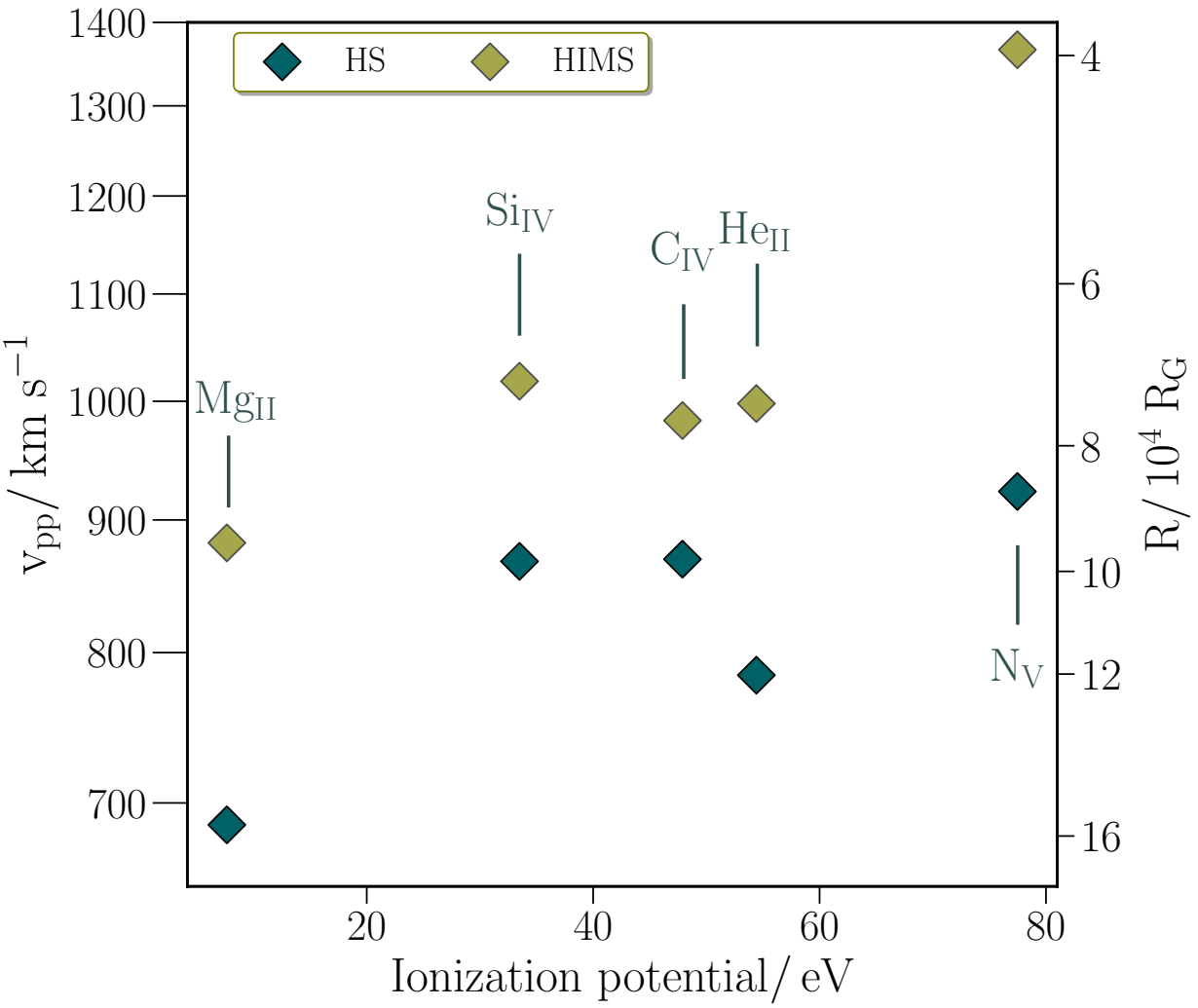

FIGURE 3.8: The peak-to-peak velocities of the main atomic species for both the HST hard (HS – in teal) and hard-intermediate state epochs (HIMS – in olive), as a function of their ionisation potential. On a secondary axis, I depict the corresponding radii where these species are formed in the disc. High-ionisation emission lines are formed closer to the central object whereas low-ionisation species are situated further out at the outer disc.

strong hard X-ray component in HST:HS to *inhibit* the formation of the UV lines, by over-ionising the material in the disc atmosphere.

However, it is important to remember that the radial locations of the line-forming regions are not the same in HST:HS and HST:HIMS. Figure 3.8 shows that all of the characteristic line-formation radii move *inward* – by slightly less than a factor of 2 – between HST:HS and HST:HIMS. This is consistent with each line being formed preferentially at a characteristic ionisation parameter, $U \propto L/n_e R^2$. If the density in the line-forming layers of the disc atmosphere is roughly constant, I expect the characteristic line-forming radius for a given line to scale with luminosity as $R \propto L^{1/2}$. The evolution I see in line flux and velocity evolution between HST:HS and HST:HIMS is therefore likely due to the combination of these factors.

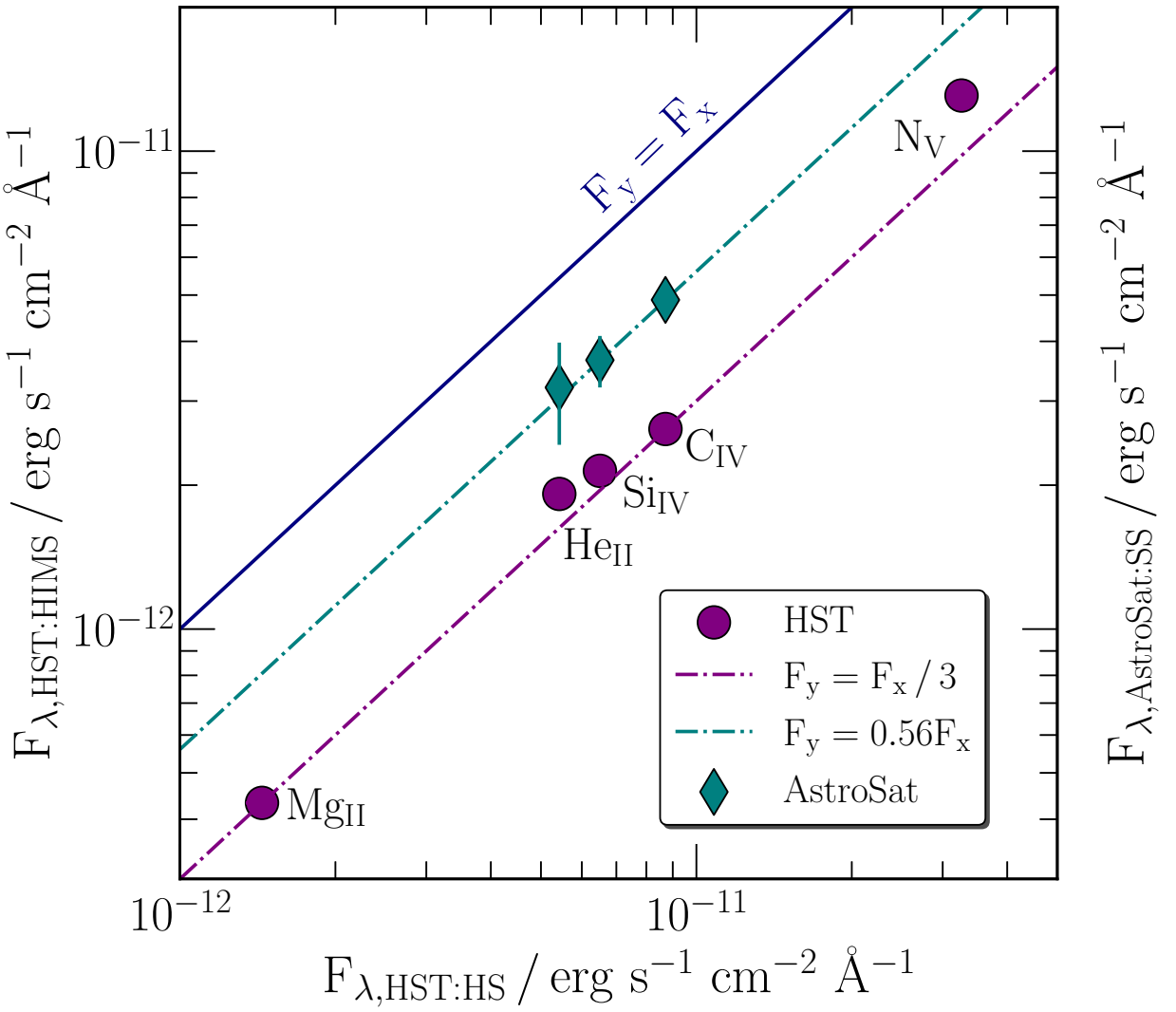

FIGURE 3.9: The plot compares the line fluxes of MAXI J1820+070 across our considered epochs. We use the HST:HS fluxes as our reference point along the x-axis and compare them with their HST:HIMS (purple colour) and AstroSat:SS (teal colour) counterparts. For a fair comparison between the HST and AstroSat fluxes (as different settings are employed), we applied a correction to the AstroSat:SS fluxes. The correction includes the introduction of a factor, f_{corr}, which is defined as the ratio of the line fluxes obtained from HST:HS to their adjusted counterparts. The straight lines indicate scaling relations between these datasets, serving as a visual guide to assess flux variations across the state transition.

3.4.1.2 Absence of evidence for UV winds

The classic observational wind signatures are blue-shifted absorption or P-Cygni line profiles, although these features are strongly inclination-dependent (e.g. Ponti et al., 2012; Díaz Trigo et al., 2014; Díaz Trigo and Boirin, 2016). The response of these signatures to X-ray luminosity variations and state transitions is of great interest, but difficult to explore.

In this study, only the hard state HST observation has the signal-to-noise and resolution to allow a sensitive search for UV wind signatures in MAXI J1820+070. However, I find no evidence for these in the usual UV resonance lines (see Figure 3.6 for more information).

The absence of outflow signatures prompts the question: is the wind truly absent or are we merely unable to detect it? Notably, winds in the hard state have been detected both in the optical (Muñoz-Darias et al., 2019) and near-infrared (Sánchez-Sierras and Muñoz-Darias, 2020) spectra of this source. These detections mainly manifested as P-Cygni and blue emission line wing features in the Balmer/Helium and Paschen lines, respectively.

Among known LMXBs, clear UV wind signatures have so far only been seen in Swift J1858.6-0814 (Castro Segura et al., 2022) and UW CrB (Fijma et al., 2023). However, there are very few systems with UV observations in which such signatures could have been found. Moreover, the signatures in Swift J1858.6-0814 are weak and transient, making them quite difficult to detect. The absence of evidence for a "warm" outflow can therefore not yet be interpreted as evidence for its absence. More UV data − for multiple systems and across different accretion states − will be needed to address this issue.

3.4.2 The evolutionary history of the binary

The relative strengths of the UV resonance lines can serve as sensitive indicators of the physical conditions in the line-emitting gas. However, they can also be used as a complementary tool to determine the evolution of a system by estimating the initial mass of the donor and its evolutionary history. More specifically, the abundance and/or depletion of elements, such as N V and C IV, have been linked to the life stage and status of the companion. The key physics here is that the CNO cycle becomes the dominant nuclear process in stars with an initial mass of $M_2 \geq 1.4\ M_\odot$ (Clayton, 1983). Hence, the abundance ratio N V/C IV emerges as a reliable signature to discern whether the gas stream of the accreting material has undergone CNO-processing (e.g. Mauche et al., 1997; Haswell et al., 2002; Gänsicke et al., 2003; Froning et al., 2011, 2014; Castro Segura et al., 2024).

The relevant line ratios of MAXI J1820+070 are plotted in Figure 3.10 along with the corresponding ratios for other systems, ranging from CVs to LMXBs. It appears that our source displays line ratios that are characteristic of "normal" CVs, suggesting that the accreting material has *not* undergone CNO processing. For reference, Figure 3.10 also includes comparison systems with

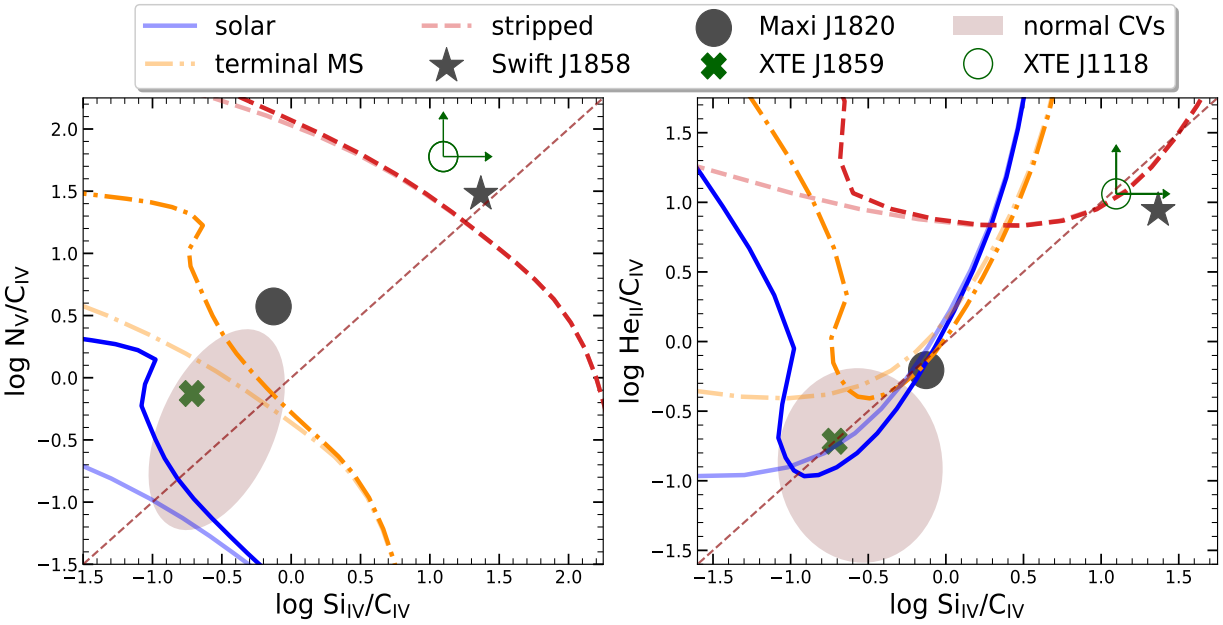

FIGURE 3.10: Far-UV emission-line flux ratios for LMXBs: XTE J1118 + 480, XTE J1859 + 226 (Haswell et al., 2002), Swift J1858.6-0814 (Castro Segura et al., 2024). The region of the parameter space occupied by the 'normal' CVs presented in Mauche et al. (1997); Gänsicke et al. (2003) is indicated with the shaded region, which encloses 2.5σ of a 2D-Gaussian distribution. The lines are predicted line ratios as a function of the ionisation parameter computed with CLOUDY for an optically thin parcel of gas irradiated with a simple accretion disc presented in Castro Segura et al. (2024). Solid, dash-dot and dashed lines are models carried out with solar abundances, M $\approx 1.5 - 2 M_\odot$ terminal MS and the equilibrium CNO-cycle core of a M $\approx 2 M_\odot$ star respectively. The latter is labelled as stripped, as we consider to have representative abundances of a stripped star with its convective CNO core exposed. The models include the O IV multiplet within range of the Si IV doublet, for reference lines including the emission only from Si IV are shown with the same linestyle but higher transparency. The measurements of MAXI J1820+070 (filled black circle) at different epochs overlay in the plot, for clarity a single measurement is shown. MAXI J1820+070 lies very close to the theoretical predictions for a terminal MS star.

anomalous line ratios. In these systems, the donor star is usually thought to have had an initial mass $\gtrsim 2\ M_\odot$. Its envelope was then stripped during a thermal timescale mass-transfer phase, leading to present-day surface abundances that reflect the earlier phase of CNO processing in the core (Schenker et al., 2002).

Given the well-determined distance (d $= 2.96 \pm 0.33$ kpc) of MAXI J1820+070 (Atri et al., 2020) and its low reddening value, there have already been efforts to determine its binary parameters. These suggest a BH primary with mass $M_{BH} = (5.95 \pm 0.22) \sin^{-3} i\ M_\odot$ and a K-type (subgiant) companion (Torres et al., 2020; Mikołajewska et al., 2022). The results here imply that this donor is not the descendant of an initially much more massive star.

3.4.3 Is irradiation important?

As shown in Section 3.3.4, the UV continuum shape, shown in Figure 3.7, cannot be adequately described by a simple irradiated disc model with physically plausible parameters. This is mainly because the spectral shape is close to that of a viscously-dominated, unirradiated disc. For physically reasonable parameters, the model is a poor match to the data, especially at the shortest far-UV wavelengths. Yet X-ray irradiation is certainly *expected* to heat up the outer parts of the disc.

A related puzzle is that one might expect reprocessing to be quite sensitive to both the luminosity and SED of the X-ray radiation field. Yet the observed UV spectra are actually fairly similar across all three spectral states. The UV continuum luminosity tracks the drop in X-ray luminosity between the hard and hard-intermediate states, but then actually stays constant across the hard-to-soft state transition. The emission line strengths also track the declining X-ray luminosity between the hard and hard-intermediate states, before partially recovering in the soft state. However, the headline result is that both the continuum spectral shape and the dominant emission lines remain virtually unchanged, even as the system moves through three very different accretion states.

We can gain some insight into the implications of these observational findings by examining the physics underlying our simple irradiated disc model. In this model, X-rays are produced by a point-like, isotropically emitting source at the centre of the disc. Some of these X-ray photons impact the disc surface and are absorbed there. This heats up the irradiated parts of the disc, thus increasing the effective temperature and modifying the radial intensity profile.

In reality, the details of this process are complex. The geometry and location of the X-ray emitting "corona" are highly uncertain, but clearly important. Similarly, the shape and scale-height of the disc $-$ $H/R|_R$ $-$ are key factors in determining what fraction of X-ray photons are intercepted by the disc. However, the relevant scale-height here is *not* really the pressure scale-height, but rather the height above the disc at which it presents an optical depth of $\simeq 1$ *to the irradiating photons*. Finally, the detailed physics governing the reprocessing of X-rays in the disc atmosphere are clearly far more complex than what can be captured by a single efficiency parameter (i.e. the albedo).

It is easy to see that some or all of these processes are expected to depend on the accretion state of the source. For example, the opacity the disc atmosphere presents to incoming X-ray photons, as well as the efficiency with which those photons are reprocessed, are sensitive to whether these photons are soft or hard. And yet the presumably reprocessing-dominated UV emission-line spectrum remains qualitatively unchanged.

Part of the explanation may be that the relevant parts of the disc do not see the same X-ray SED that we do, as observers, and that the formation of UV emission lines is mainly controlled by EUV photons. For reference, by "extreme-UV", here we mean photons with energy between, say,

13.6 eV and 100 eV (check Figure 3.8, which includes the ionisation potentials of the relevant species). In fact, the He II recombination line is generally thought to be a reliable bolometer for the extreme-UV luminosity above 54 eV (or, in this case, the fraction of this luminosity that is intercepted by the disc).

As noted above, the He II emission line flux drops by $\simeq \times 3$ between the luminous hard state and hard-intermediate state (HST:HS and HST:HIMS, respectively) before partially recovering in the soft state (AstroSat:SS). On the one hand, these relatively modest variations are in line with the modest changes in the observed emission line spectra. And indeed the soft X-ray flux also only varies by a comparable amount (see Figure 3.1).

On the other hand, the He II line flux is clearly not proportional to the soft X-ray flux: the latter is comparable in the hard and hard-intermediate states, but a factor of $\simeq \times 3$ higher in the soft state. Moreover, the *hard* X-ray component completely dominates in HST:HS, is comparable to the soft X-ray component in HST:HIMS, and is all but completely quenched in AstroSat:SS. So, somehow, the UV line-forming regions must be shielded from the ionising effects of the energetic X-ray photons produced in the hard state.

The main conclusion from all these considerations is that the physics governing the reprocessing of X-rays in the outer disc regions is (a) complex and (b) poorly described by simple models. We therefore strongly encourage theoretical efforts to construct physically realistic models of irradiated accretion disc atmospheres.

3.5 Summary

I have presented the first multi-epoch, time-resolved and spectrally-resolved UV characterisation of the transient X-ray binary MAXI J1820+070. The obtained observations are in three distinct stages of the outburst: a luminous hard state after the eruption peak, a hard-intermediate state just before the state transition and finally the soft state.

The primary conclusions of this program are the following:

- I have determined the interstellar reddening and extinction towards the source via the λ2175Å absorption feature (near-UV bump) and Lyα modelling. The estimate of the reddening is quoted as $E_{B-V} = 0.20 \pm 0.05$.
- I track the spectral evolution of MAXI J1820+070 throughout its outburst. Surprisingly, I see no major differences in the appearance of the UV emission line spectrum across the three distinct spectral states. The UV spectra are characterised by blue continua superposed broad, double-peaked emission lines, such as N V λ1240Å, Si IV λ1400Å, C IV λ1550Å, He II λ1640Å, Mg II λ2800Å.

- I do not find evidence of an outflow in the form of blueshifted absorption or P-Cygni profiles in any of the considered lines that are mentioned above.
- I use the relative strengths of the UV resonance lines to constrain the evolutionary history of the binary, showing that the donor has not undergone CNO processing in the past and presumably, now, lies at the end of the MS or at the subgiant branch.
- Simple irradiated disc models with physically plausible parameters fail to adequately describe the observed UV continuum shape. This is mainly because the observed spectral slope is close to that for an unirradiated, viscous-dominated accretion disc.

Acknowledgements

I would like to acknowledge the help of Dr. Noel Castro-Segura for producing the line ratio plot of LMXBs, after I provided to him the information of my modelling. Furthemore, I would like to thank Dr. Douglas Buisson for providing me the *NICER* data products in order to construct the X-ray light curve and the hardness-intensity diagram of the source.

Chapter 4

Ultraviolet timing analysis in the BHXT MAXI J1820+070

"The thought is a deed. Of all deeds she fertilises the world most."

Emile Zola

4.1 Introduction

This chapter constitutes the last part of my analysis of the BHXT MAXI J1820+070. Here, I construct both light curves and power density spectra (PDS) in order to study the evolution of UV variability in our time-resolved HST observations, covering the hard and hard-intermediate states. This is particularly interesting as the emission produced in the *outer* accretion disc is likely to peak in this waveband. The following sections describe the employed methods, the results and the subsequent discussion for the tentative discovery of a UV QPO almost at the same frequency, as seen in X-rays and optical bands, during the same time of the source's eruption.

4.2 Method and Results

4.2.1 Light curves

I first constructed wavelength-integrated light curves from our time-resolved observations and then the corresponding PDS, where the variability amplitude (power) is expressed as a function of frequency. The light curves are generated using the LIGHTCURVE package.[1] They are both

[1]The original code is available at `https://github.com/justincely/lightcurve`, but I have adapted the code to suit my requirements.

background-subtracted and corrected for buffer dumps. An overview of the light curves for all epochs can be seen in Figure 4.1. Rapid, aperiodic variability is apparent throughout the observations. More specifically, the far-UV light curves obtained during the HST:HS observations clearly exhibit flaring activity with a fractional rms amplitude of $\simeq 10\%$ while the corresponding flaring amplitude in the near-UV is $\simeq 7\%$.

Rather suspiciously, all of the light curves, obtained from the HST:HIMS visit, exhibit a slow rise in count rate at the beginning of each orbit (second column of Figure 4.1). Following discussions with the STScI office and a detailed inspection of the cross-dispersion profiles during this visit, I tentatively attribute these variations to instrumental focus changes. I therefore opt to filter out these slow variations by fitting a second-order polynomial to the respective light curves and then normalising to this fit. The polynomial fits are shown overlaid on the raw HST:HIMS light curves in Figure 4.1. I then measure the fractional rms amplitudes of the short-term variability in each orbit, which is $\simeq 4\%$ and $\simeq 3\%$ in the far- and near-UV, respectively.

4.2.2 Construction of power density spectra

The PDS were constructed by following the methodology by Vaughan (2005). For a light curve with K points and ΔT sampling rate, the periodogram is given by the modulus-squared of the discrete Fourier transform (DFT), $X(f_j)$, defined as

$$I(f_j) = \frac{2\Delta T}{< x >^2 N} |X_j|^2, \tag{4.1}$$

and evaluated at the Fourier frequencies $f_j = j/K\Delta T$ with j=1,2,..., K/2. These frequencies range from the fundamental to the Nyquist frequency. Its normalisation, $\frac{2\Delta T}{<x>^2 N}$, is in $(\mathrm{rms/mean})^2 \mathrm{Hz}^{-1}$, expressing the power in fractional units (van der Klis, 1989, 1997; Vaughan et al., 2003; Vaughan, 2005).

Periodograms, however, serve as an estimate of the true underlying power spectrum, $P(f_j)$, as fluctuations arise at each frequency due to the finite length of our observations and the stochastic nature of the DFT. These fluctuations follow a χ^2_2 distribution[2] and therefore, the periodogram, $I(f_j)$, can be approximated as being distributed proportionally to χ^2_2, scaled by $P(f_j)$, as

$$I(f_j) = P(f_j)\chi^2_2/2. \tag{4.2}$$

One of my aims here is to examine the datasets for the presence of significant sharp features, e.g., low-frequency quasi-periodic oscillations (LF-QPOs), as seen in X-ray and optical studies

[2]The DFT of a stochastic process has real and imaginary terms, which are independent and normally-distributed. It is mentioned that the squared sum of two independent Gaussian variables, $|X_j|^2 = \mathrm{Re}(X_j)^2 + \mathrm{Im}(X_j)^2$, follows a χ^2 distribution of two degrees of freedom.

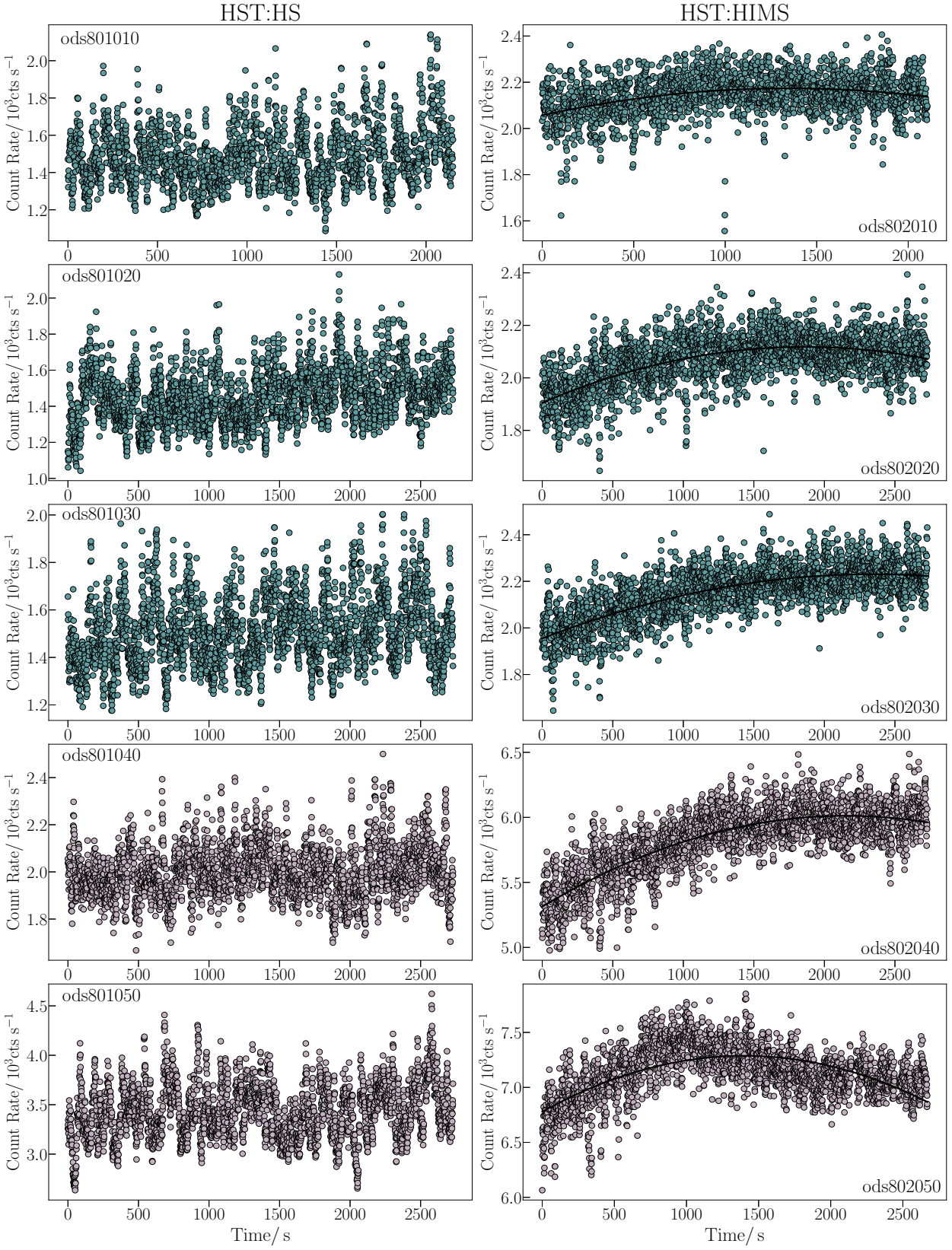

FIGURE 4.1: Far- and near-UV light curves of MAXI J1820+070, extracted at one-second resolution, for both of the hard state observations, taken by HST. As noted, the left column showcases light curves of the first luminous hard state (HST:HS) while the right column features the corresponding light curves of the second hard state (HST:HIMS). For our HST:HIMS observations, I overlaid our polynomial fit, correcting for the presented turnover. The two colours are utilised to distinguish between the far- (teal) and near-UV observations (dusty pink). For completion, I have also noted the obsID of the considered observations at each of the panels.

(e.g. Stiele and Kong, 2020; Mudambi et al., 2020; Paice et al., 2021; Thomas et al., 2022; Mao et al., 2022). Overall, the UV PDS exhibit a pattern consistent with that seen in other sources and at other wavelengths. The "continuum", i.e. broadband noise, can be aptly described by a single-bend power-law with two distinct power indices, delineated by the break frequency. At the highest frequencies, the power spectra are governed by Poisson noise. Finally, especially during our HST:HS observations, I do observe a weak yet discernible signature of a QPO close to the break frequency, within the frequency range dominated by red noise, and at a frequency that is similar to QPOs detected in other bands.

I decided to take a closer look at the PDS in which I tentatively detect a peak. Specifically, in order to determine the statistical significance of these detections, I fit each observed PDS with two models, one with and one without a QPO component. The intrinsic "continuum" in both models is described as a broken (or bending) power-law, while the QPO is approximated as a Lorentzian of a centroid frequency, ν_c, and FWHM width W_q.

The full PDS model that includes the QPO is given by Summons et al. (2007) as

$$P(\nu) = \frac{A_{BPL}\nu^{\alpha_L}}{1+(\frac{\nu}{\nu_B})^{\alpha_L-\alpha_H}} + \frac{B_{QPO}Q\nu_c}{\nu_c^2+4Q^2(\nu_c-\nu)^2} + C_{PS}. \tag{4.3}$$

Here, the first term describes the broken power-law (BPL) continuum with ν_B the break frequency, and α_L, α_H, the low- and high-frequency indices. The second term accounts for the presence of QPO with the parameter Q, known as the quality factor (measure of coherence), aptly connected to the centroid frequency as ν_c/W_q. The third term, C_{PS}, describes the variability associated with Poisson noise. The parameters A_{BPL} and B_{QPO} serve as normalisation constants for the individual components. In the model without a QPO, the second term is simply set to zero.

Following Vaughan (2005), I use the maximum likelihood estimation (MLE) method and S-statistic in order to find the optimal parameters of the two models. As already mentioned in 2.4.2.2, this approach tries to identify the model that maximises the likelihood function ($\mathcal{L}$) or, equivalently, minimises the negative log-likelihood. Here, the negative log-likelihood is defined through the S-statistic as $S = -2\ln\mathcal{L}$. To set the stage, we first consider the statistical distribution of the periodogram (our data). It is easy to derive that the periodogram, $I(f_j)$, is exponentially-distributed if we recall that the probability density function (PDF) of a χ^2 distribution is equal to $e^{-x/2}/2$ (for $x \geq 0$). Specifically, the PDF of our periodogram, at each frequency (excluding the Nyquist frequency), can be written as

$$p(I(f_j)) = \frac{1}{P(f_j)} e^{-I(f_j)/P(f_j)}. \tag{4.4}$$

As the periodogram values at different frequencies are statistically independent, the likelihood of observing the periodogram is given by

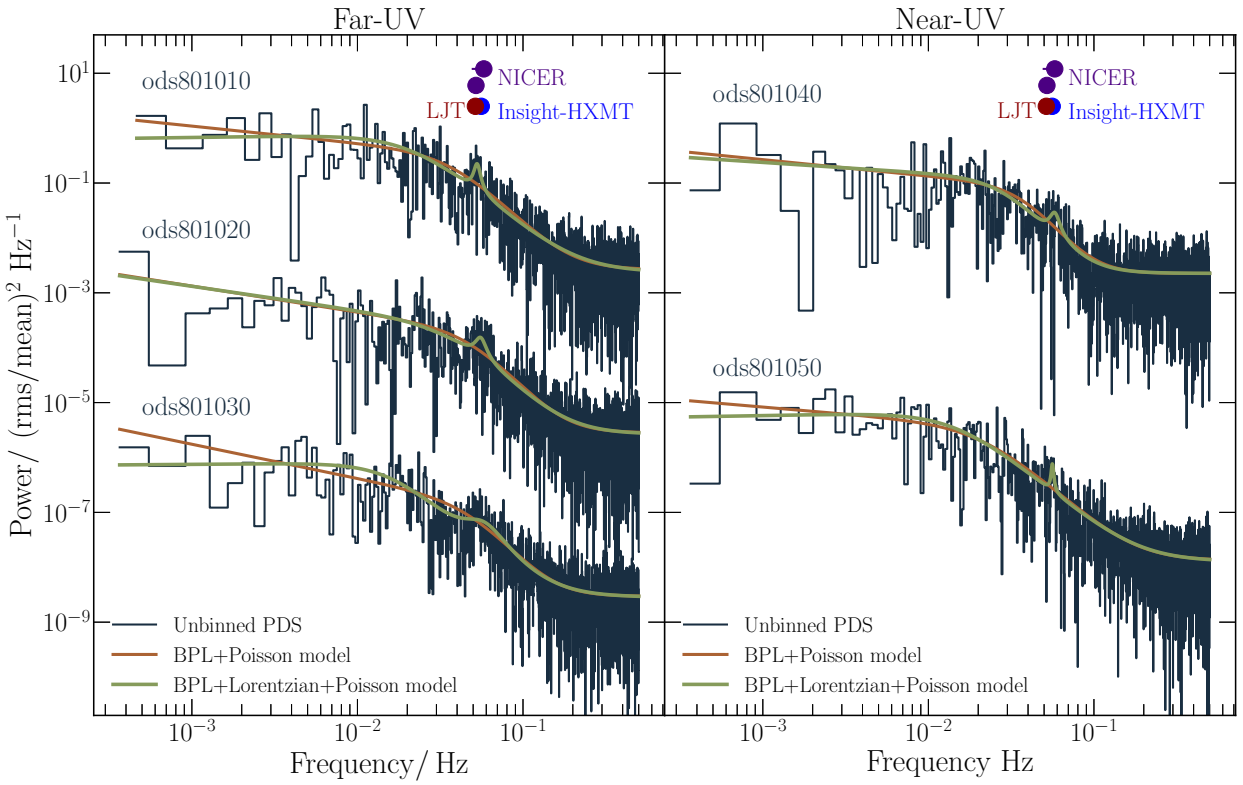

FIGURE 4.2: PDS for both the far- (left) and near-UV (right) wavelengths during our HST:HS epoch are presented. The different solid lines represent the best-fitting models, incorporating the Lorentzian contribution. Tentative evidence for the presence of a LF-QPO is observed in the far-UV, which is absent in the near-UV observations. For reference, characteristic centroid QPO frequencies, estimated in the X-ray (NICER: Stiele and Kong 2020, Insight-HMXT/HE: Mao et al. 2022) and optical (LJT/YFOSC: Yu et al., 2018b; Mao et al., 2022) bands, close to our observation time, are displayed.

$$\mathcal{L} = \prod_{j=1}^{n-1} p(I(f_j)) = \prod_{j=1}^{n-1} \frac{1}{P(f_j)} e^{-I(f_j)/P(f_j)}, \tag{4.5}$$

whereas the S-statistic takes the following form

$$S = -2\ln\mathcal{L} = 2\sum_{j=1}^{n-1} \left\{ \ln(P(f_j)) + \frac{I(f_j)}{P(f_j)} \right\}. \tag{4.6}$$

The S-statistic constitutes a metric that will allow us to facilitate the comparison among different models and find the one that best describes the observed periodogram of the source. In the performed modelling, all model parameters are allowed to vary. The goodness-of-fit in both cases − models with or without the Lorentzian contribution − is assessed using the Kolmogorov-Smirnov (KS) test. For unbinned periodograms, the test compares the data/model residual ratio, i.e. $2I(f_j)/P(f_j)$, with the theoretical χ^2_2 distribution (of two degrees of freedom). The uncertainties

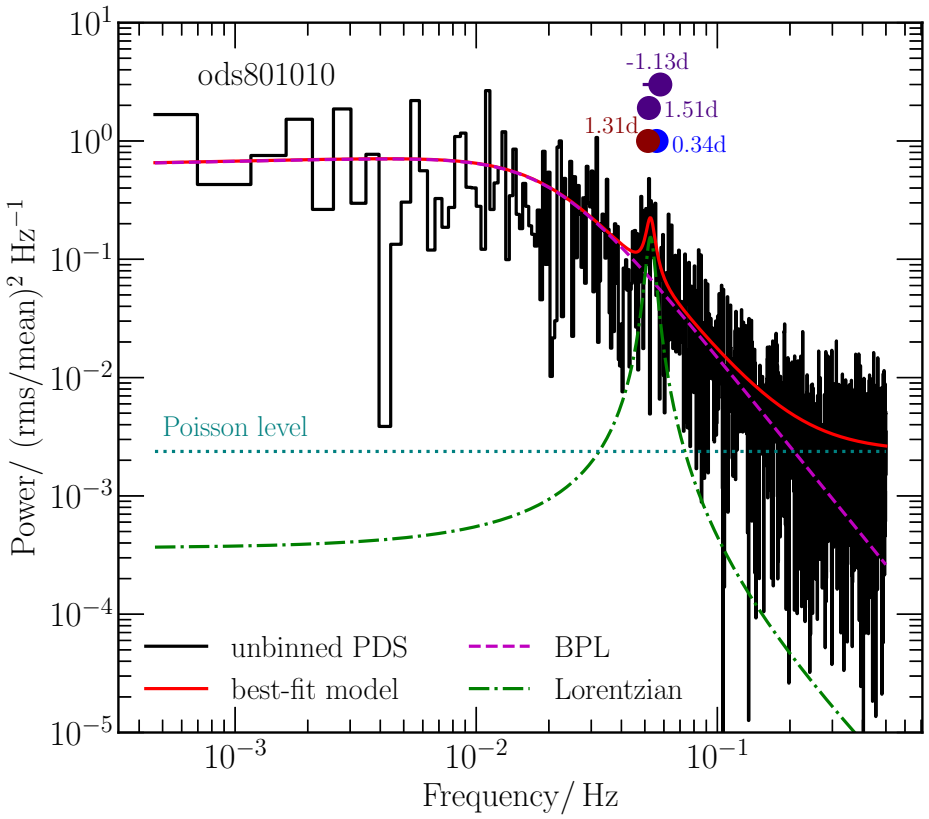

FIGURE 4.3: Example of a far-UV PDS of our source during our HST:HS observations, showing a weak signature of a QPO. The solid red line represents the overall best-fit model while the dashed and dash-dotted lines highlight the two main model contributions (BPL: magenta, Lorentzian: green). The level of Poison noise is seen as a teal dotted line. The X-ray and optical QPO frequencies, mentioned in Figure 4.2, offer valuable context for comparison.

in my best-fit parameters are estimated by Monte Carlo simulations. For each dataset, I generate 1000 mock exponentially-distributed PDS and fit them in the same manner as described above. This iterative process provides me with the best-fit parameters and S-statistic for each mock dataset, allowing me to estimate the 1σ errors. The best-fitting parameters and their uncertainties, as well as details of my fitting results, are summarised in Table 4.1.

Figure 4.2 presents the different PDS for both the far- and near-UV regions, where I have also superimposed both the QPO and no-QPO models. In Figure 4.3, I additionally illustrate the contributions of the different components. In both cases, I indicate the estimated centroid frequencies both in X-ray (Stiele and Kong, 2020; Mao et al., 2022) and optical (Mao et al., 2022) wavelengths, with respect to the time of the UV observations. Here, both the employed X-ray and optical datasets are in almost the same period as our UV observations are taken. Taken separately, both models provide statistically acceptable fits to the data.

TABLE 4.1: Best-fitting model parameters of the considered models for the HST:HS PDS both at the far- and near-UV range. The letter indices describe the parameters involved: [(a)] normalisation constant of the broken power-law model, [(b)] low-frequency (before the break) power-law index, [(c)] high-frequency power-law index, [(d)] break frequency, [(e)] normalisation constant of the Lorentzian, describing the QPO, [(f)] quality factor defined as ν_c/W_q, where W_q the FWHM of the Lorentzian, [(g)] centroid frequency of the QPO peak, [(h)] Poisson constant, [(i)] goodness-of-fit p-value obtained via the KS-test, [(j)] statistical significance of the QPO obtained through the LRT test. All the uncertainties are quoted to 1σ confidence level.

ObsID	$\log A^{(a)}_{BPL}$	$\alpha^{(b)}_{L}$	$\alpha^{(c)}_{H}$	$\nu^{(d)}_{B}$ (mHz)	$\log B^{(e)}_{QPO}$	$\log Q^{(f)}$	$\nu^{(g)}_{c}$ (mHz)	$C^{(h)}_{PS}$	KS-test [(i)]	$\Delta S^{(j)}$
HS: far-UV @1425 Å										
ods801010	-0.044 ± 0.53	0.042 ± 0.23	-2.52 ± 0.19	20.93 ± 5.42	-3.10 ± 0.25	1.01 ± 0.49	52.79 ± 1.63	$(2.38 \pm 0.21)\ 10^{-3}$	0.74	
	-0.9 ± 0.35	-0.31 ± 0.16	-3.09 ± 0.26	38.60 ± 7.53	–	–	–	$(2.63 \pm 0.19)\ 10^{-3}$	0.62	0.044
ods801020	-1.20 ± 0.40	-0.44 ± 0.18	-2.95 ± 0.35	37.44 ± 11.25	-3.07 ± 0.30	0.77 ± 0.47	55.34 ± 2.48	$(2.67 \pm 0.19)\ 10^{-3}$	0.97	
	-1.30 ± 0.25	-0.475 ± 0.13	-3.47 ± 0.27	49.85 ± 7.24	–	–	–	$(2.81 \pm 0.15)\ 10^{-3}$	0.86	0.014
ods801030	-0.057 ± 0.58	0.04 ± 0.24	-2.95 ± 0.98	16.00 ± 4.55	-2.75 ± 0.24	0.18 ± 0.19	54.65 ± 5.82	$(2.84 \pm 0.14)\ 10^{-3}$	0.46	
	-1.63 ± 0.28	-0.62 ± 0.14	-3.56 ± 0.32	49.31 ± 8.48	–	–	–	$(2.96 \pm 0.13)\ 10^{-3}$	0.61	0.044
HS: near-UV @1978 Å										
ods801040	-1.22 ± 0.38	-1.98 ± 0.18	-3.63 ± 0.55	28.88 ± 5.11	-3.80 ± 0.28	0.82 ± 0.40	57.81 ± 2.11	$(2.26 \pm 0.083)\ 10^{-3}$	0.48	
	-1.48 ± 0.29	-0.30 ± 0.14	-3.88 ± 0.41	37.40 ± 5.10	–	–	–	$(2.25 \pm 0.080)\ 10^{-3}$	0.39	0.0067
HS: near-UV @2707 Å										
ods801050	-0.075 ± 0.055	0.054 ± 0.22	-2.49 ± 0.15	14.65 ± 3.29	-3.97 ± 0.96	1.44 ± 3.00	56.13 ± 0.90	$(1.28 \pm 0.087)\ 10^{-3}$	0.74	
	-0.85 ± 0.45	-0.256 ± 0.19	-2.70 ± 0.17	21.64 ± 4.69	–	–	–	$(1.33 \pm 0.082)\ 10^{-3}$	0.83	0.069

In order to test whether QPOs are significantly detected, I once again follow Vaughan (2005) in estimating their statistical significance. Specifically, I use the likelihood ratio test (LRT) to check if the additional freedom associated with the QPO model is warranted by the data. The test statistic here is

$$\Delta S = S_1 - S_2 = -2\ln[\mathcal{L}_1/\mathcal{L}_2], \tag{4.7}$$

where the indices 1 and 2 represent the likelihoods and S-statistic for the simpler and complex model, respectively. If the models are nested, and the simpler model is correct, the variable ΔS is $\chi^2_\nu-$distributed, where ν is the number of additional free parameters. In my case, ΔS therefore follows a χ^2_3 distribution under the null hypothesis that the no-QPO model is correct (since the QPO term requires three additional parameters). The p-values associated with this null hypothesis turn out to be 0.044, 0.014, 0.044 for the far-UV and 0.0067, 0.069 for the near-UV range. These values correspond to 2-3σ detections of the QPOs $-$ suggestive, but not definitive. Given that the locations of the putative UV QPOs are consistent with those seen in other bands, I tend to think that they are real and worthy of consideration.

I have also constructed PDS from both the raw and corrected light curves of our HST:HIMS observations. Notably, all the raw PDS exhibit an unusual excess at low frequencies, in line with our suspicion that the slow variations in these data sets are instrumental artefacts. This low-frequency excess disappears once the polynomial fit is used to "correct" the light curves. An illustrative example of this process is presented in Figure 4.4. There are no hints of QPO feature in HST:HIMS, in any of the visits associated with this epoch. Given this, and also the inevitable uncertainty associated with our polynomial correction, I choose not to perform detailed PDS modelling for this epoch.

4.3 Discussion

4.3.1 Evidence of a UV QPO signal?

Only a handful of systems to date are known to display LF-QPOs in multiple wave bands (mostly in the optical/infrared and in X-rays; check Motch et al., 1982, 1983; Hynes et al., 2003; Durant et al., 2009; Gandhi et al., 2010, for more information). The only system known to exhibit an analogous signal in the UV is the BHXT XTE J1118+480 (Hynes et al., 2003). The mentioned studies are based on panchromatic, (quasi-)simultaneous observations of BHXTs and correspond to periods when the systems are in the low hard state. It is still unclear, though, whether the X-ray and longer-wavelength signals are physically associated and how the latter are actually produced (e.g. Markoff et al., 2001; Veledina et al., 2013; Veledina and Poutanen, 2015; Hynes et al., 2003; Gandhi et al., 2017).

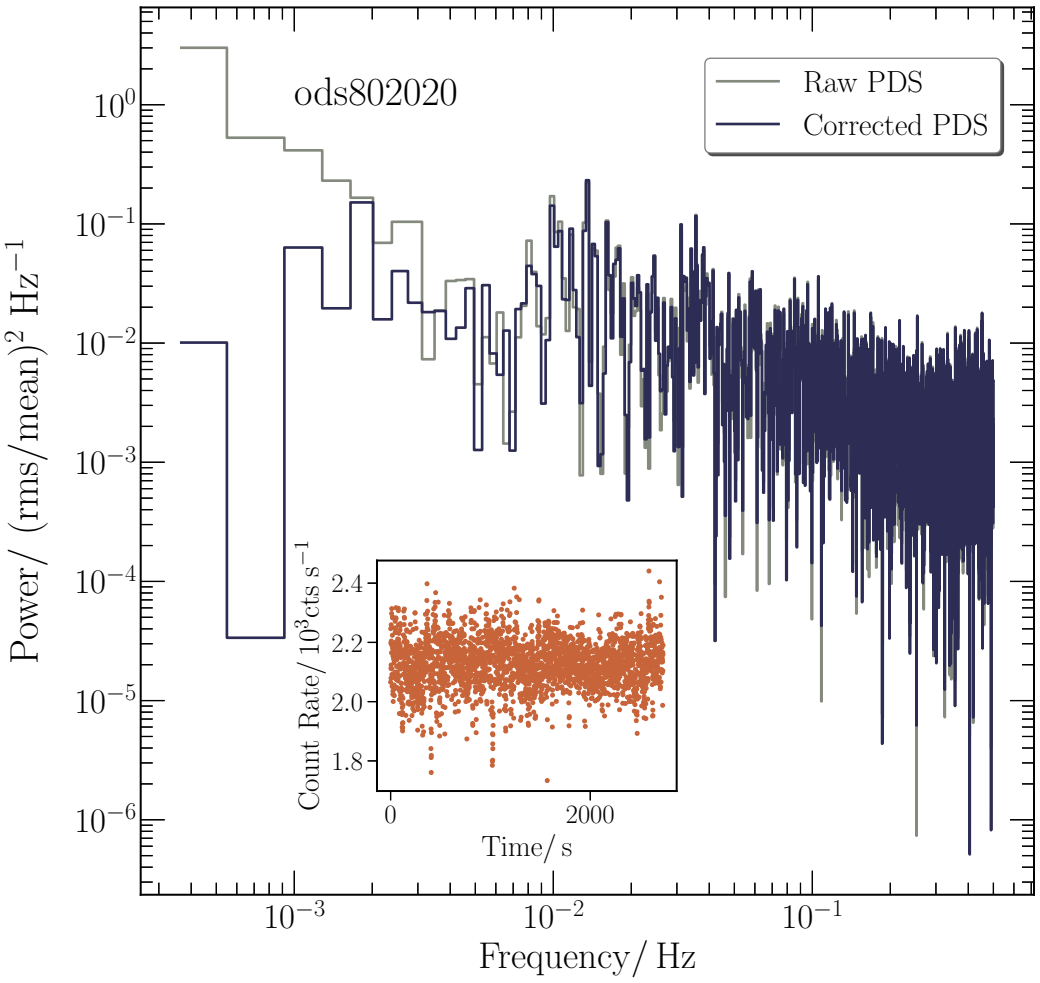

FIGURE 4.4: Representative far-UV PDS of the HST:HIMS epoch of MAXI J1820+070. We overlaid both the raw and corrected PDS to illustrate the difference prior and after the applied correction. The corresponding corrected light curve is placed as an inset.

In this work, the time-resolved observations allow me to search for UV QPO signatures only in the *hard* state. Nevertheless, MAXI J1820+070 is already known to display simultaneous X-ray and optical LF-QPOs in the hard state, as reported by Mao et al. (2022) and Thomas et al. (2022). The mentioned studies present observations captured at similar times to our UV observations. In this state, the observed X-ray QPOs, the so-called type-C QPOs, may be associated with a precessing hot flow near the inner edge of the disc (e.g. Stella and Vietri, 1998; Ingram et al., 2009; Ingram and Motta, 2019), instabilities in the disc (e.g. Tagger and Pellat, 1999; Varnière et al., 2002, 2012) or corona variability (e.g. Titarchuk and Fiorito, 2004; Cabanac et al., 2010). On the other hand, in the optical band, detections of QPOs are limited, and the observed signals are usually attributed to precession (Veledina et al., 2013), thermal reprocessing (Veledina and Poutanen, 2015) or jet synchrotron emission variations (e.g. Markoff et al., 2001; Hynes et al., 2003; Gandhi et al., 2017).

Almost the time of the observations, Mao et al. (2022) and Thomas et al. (2022) find that both X-ray and optical signals share similar centroid QPO frequencies and evolve similarly over time. However, optical variations are more coherent, i.e. $Q_{X-ray} < Q_{opt}$ (check Table 1 in Mao et al.,

2022). This implies that disc reprocessing is not the dominant mechanism, and Ma et al. (2021) suggest instead that the jet may precess at the QPO frequency.

My work provides provisional evidence for the existence of UV LF-QPOs with centroid frequencies closely resembling those observed in other bands. My modelling suggests − albeit I take into account only the observations that I *do* detect a QPO − that the coherence in the UV is lower than the equivalent one in optical and X-rays (for almost the same centroid frequencies). It seems unlikely that synchrotron radiation could be responsible for QPOs in the UV band. The current results suggest that the "same" type-C QPOs in different bands can be produced in three distinct regions − the inner accretion flow (producing X-ray QPOs), the jet (producing optical QPOs) and the outer disc (producing UV QPOs via reprocessing). In the UV, reprocessing may constitute the primary mechanism, which is in line with the lower coherence I observe. This evidence is worthy of consideration and indeed, more data in the UV are needed in order to solidify the presence of the UV QPOs and this connection between the different bands.

Chapter 5

Conclusions and future work

"Wise as you will have become, so full of experience,
you will have understood by then what these Ithacas mean."

-C.P. Cavafy, Ithaca

5.1 The journey or the destination?

The submission of this thesis marks the endpoint of some amazing years filled with research, determination and curiosity. From the start, my research interests were focused on observational studies of accretion discs and on the evolution of accreting compact binaries. Throughout my period of candidature, then, I performed time-resolved UV spectroscopy on two remarkable objects, the DN WZ Sge and the BHXT MAXI J1820+070. Maybe one of the few − if any − similarities between them is that even though they have been well-studied in the past, certain aspects of their nature have been left unexplored. I would like to think that the research presented in this thesis has made a contribution to our understanding of transient accretion and to the journey to unravel some of the mysteries in these two sources. This section is devoted to summaries of my findings, but I will also provide suggestions for promising routes for future work.

5.1.1 The DN WZ Sge

WZ Sge is the prototype of a growing category ($\sim$ 100 systems as reported in Kato, 2015) of highly evolved, low-accretion rate DNe. It erupts almost every 30 years. Due to its long recurrence timescale, only four eruptions have been reported (1913, 1946, 1978, 2001), and only the last two have been well-documented. However, the intricate and complex structure of its light curve (and the ones of similar systems) still remains to be understood within the framework of the DIM (or its modifications).

In my study, I focused on one particular feature, a distinctive *"dip"*, in the light curve of WZ Sge's 2001 superoutburst. This drop in luminosity precedes a series of rebrightenings before the final transition of the source towards quiescence. This type of feature is not exclusive to our source, but is also seen in the light curves of other objects, including LMXBs, HMXBs and YSOs.

Campana et al. (2018) have suggested that what they call the "knee", observed in these light curves, marks a transition into and out of a magnetic propeller state. Perhaps the most compelling example supporting this idea is the millisecond X-ray pulsar SAX J1808.4-3658, where the knee in the X-ray light curve is associated with a transition into a propeller state (Gilfanov et al., 1998). This is also an appealing scenario for WZ Sge. Indeed, the source has been suspected to have a magnetic WD due to the discovery of optical and X-ray pulsations during its quiescent periods.

The first project of my candidature revolved around testing this idea using time-resolved HST UV spectroscopy of the WZ Sge's 2001 superoutburst. The description of the current analysis has been given in Chapter 2. The observations for this project were taken at three key epochs during the eruption decay − before, during and after the dip. The observation during the dip is the most crucial for us, as it is the one in which the propeller may operate. In the propeller state, it is expected that distinct spectral signatures − similar to the flare signatures observed in the magnetic propeller system AE Aqr − may be seen. For this reason, I constructed both mean and variability spectra and also performed a linear decomposition of the time-resolved spectra for each of the visits, all in an attempt to isolate both the constant and time-dependent (i.e.propeller) signatures of the system. My analysis showed that all the stages of the outburst are characterised by the same narrow absorption features, none of which are state-dependent. As a result, one may question if there is a causal and unique connection between the luminosity drops in the light curves of magnetic rotators and propeller transitions. Even though Campana et al. (2018) recognise this issue, it may be wiser to treat each case independently, particularly in systems where the magnetic field is only loosely constrained.

Could we go then even further or are we influenced by bias in our interpretation? Indeed, AE Aqr is considered the best-known magnetic propeller WD system, yet, it remains unclear whether its unique characteristics represent typical behaviour in the UV and how it compares to WZ Sge. To better understand this, it would be interesting to identify common properties among other magnetic CVs. A particularly relevant follow-up case could be the newly-established "AE Aqr-twin", LAMOST J024048.51+195226.9 (Garnavich et al., 2021; Pelisoli et al., 2022), whose UV signatures during its transition into propeller mode could provide valuable insights. As the sample of magnetic propeller systems increases, our confidence in understanding their behaviour will strengthen. On the other hand, should we insist on the magnetic nature of the WD accretor in WZ Sge? As previously mentioned, WZ Sge constitutes the prototypical system of a family of low-accretion DNe that shows similar outburst light curve phenomenology. If, in fact, the observed dip corresponds to a transition into a propeller state, does this imply that all WZ Sge-like systems possess a magnetic accretor? To date, no observations support this hypothesis.

Maybe the answer lies in revisiting the DIM and its modifications. The dip feature observed in the light curve of WZ Sge (and similar systems) is not a unique phenomenon, but may be related to the subsequent rebrightenings. In this scenario, external factors such as irradiation could sustain mass transfer, leading to a series of echo-outbursts on small timescales (e.g., Hameury and Lasota, 2017). It is possible that the reflares were on track to reach the amplitude of the dip but never did. This type of interpretation aligns with the idea that the dip follows the broader picture of disc instabilities in DNe and it is not an isolated event. To address this idea, an interesting case study would be to obtain time-resolved UV spectroscopy of a high-inclination system and perform Hα tomography or eclipse mapping in order to monitor the motion of the bright spot and the impact of material with the disc.

Furthermore, in this chapter, I modelled the newly-found narrow absorption features, detected in the dip, the disc-dominated plateau and the echo-outburst phases of the outburst. This modelling suggests the existence of a high-density, moderate-temperature, low-velocity veiling curtain along the line-of-sight. As I noted in Chapter 2, this curtain was also present a bit later, close to the end of the superoutburst, as described by Long et al. (2004). These absorption features imply the presence of an unknown physical component in the system, which remains persistently present around the source.

Determining the nature of this component is important, but the level of difficulty is uncertain. Is this a rare occurrence, or is it more common than we realise? A promising approach is the performance of a radial velocity study of a high-inclination system, as it may allow us to associate the motion of the veil with one (or maybe more) components of the binary system. It is noted that similar signatures have also been found in other systems (Horne et al., 1994; Baptista et al., 1998; Froning et al., 2011; Šimon, 2024), although it is not clear whether their origin is the same. This raises the question that such structures may not be as rare as previously thought. An interesting follow-up study would involve investigating archival UV data by combining data from both the International Ultraviolet Explorer (IUE) and HST to search for these signatures in DNe and NLs. Such an analysis would help distinguish whether veiling curtains are truly rare structures or simply overlooked.

To sum up, my analysis led to the following results:

- *Magnetic propeller:* There are no distinctive features (like the emission lines observed in AE Aqr) that are solely seen in the dip phase. However, all epochs exhibit the same narrow absorption features.
- *Identification of the narrow features*: Modelling of these narrow absorption features shows that there is a high-density, moderate temperature veil around the system, seen in all stages of the outburst decline. The same veil was also present later, as described by Long et al. (2004).

This work advances our understanding of the transient accretion process(es) that take place in WZ Sge and related systems. WZ Sge has been suspected to be a magnetic rotator for several decades

now (e.g. Lasota et al., 1999; Matthews et al., 2007; Warner and Pretorius, 2008; Kuulkers et al., 2011), in spite of a lack of clear evidence and competing arguments (e.g. Hameury et al., 2000; Hameury and Lasota, 2021). As this effort was not successful to prove the existence of propeller in WZ Sge, this is a confirmation that we will need to return back to basics – are there additional physical processes that may be responsible for the complex pattern of WZ Sge-type light curves? It would be important to focus on these issues *now* as the next superoutburst of WZ Sge could be imminent. It is already 24 years (as of the time of writing) since its previous one (July 2001). Yet, this study represents the *first attempt* to look at and characterise the spectral signatures in the UV at different stages of the eruption decay.

5.1.2 The BHXT MAXI J1820+070

The last two chapters of my thesis concern the first multi-epoch time-resolved UV characterisation of the BHXT MAXI J1820+070 during all stages of its 2018 outburst. This is the first time that such a dataset has been obtained in the UV, since most compact binary systems suffer from high reddening, which prevents such observations. The UV data here were obtained as part of a coordinated effort involving both HST and AstroSat, which allowed us to capture MAXI J1820+070 in three different stages of its eruption: before, during and after a state transition. More specifically, the three epochs can be characterised as:

- HST:HS/AstroSat:HS – the luminous hard state $\longrightarrow$ HST/AstroSat observations
- HST:HIMS – the hard-intermediate state before the transition $\longrightarrow$ HST observations
- AstroSat:SS – the soft state $\longrightarrow$ AstroSat observations

This unique dataset has allowed me to explore a wide range of important topics. First, I determined the extinction to the source through two different methods: (i) using the near-UV hump seen at λ2175Å and (ii) using the correlation between reddening and atomic hydrogen density. My work indicates a low extinction value towards the source ($E_{B-V} = 0.20$). Furthermore, I studied the spectral evolution of MAXI J1820+070 throughout its outburst. A striking result is that the UV behaviour remains almost unchanged among the different accretion states – it does not evolve strongly with time, as happens in X-rays, for example. In the UV, there are no crucial differences associated between the different X-ray states, which correspond to different accretion flows/-geometries close to the central object. The HST spectra, which cover the first two epochs, are characterised by the same double-peaked, Doppler-broadened emission lines, while their overall spectral slope is closer to the one predicted for a viscous-dissipation-dominated (rather than irradiation-dominated) disc.

Moreover, there is no sign of blue-shifted absorption or P-Cygni features in the HST:HS observations, i.e. there is no detection of hard-state UV winds. Such wind signatures have been found in

two systems so far, Swift J1858.6-0814 (Castro Segura et al., 2022) and the UW Crb (Fijma et al., 2023). It should be noted, however, that these signatures are not easy to observe, as they are quite variable. The fact that there are so few observations in the UV band to date makes it difficult to determine the significance and occurrence rate of these signatures.

I also modelled the most prominent UV emission lines in our spectra in order to extract properties such as the lines fluxes and the corresponding velocities. I note that the AstroSat spectrum, probing the soft state, is described by relatively low resolution and signal-to-noise, so that only the strongest features are discernible. This analysis can be used to identify the line-forming regions of these species in the accretion disc. My results confirm that indeed, higher ionisation lines are formed closer to the compact object, while the lower ionisation species are formed further out, in the outer disc. Furthermore, I found that there is strengthening of the integrated line fluxes between the hard state and the soft state. The latter is expected as there is an increase in EUV and soft X-ray photons during the transition. On the other hand, the strengthening of the lines between the hard state and the hard-intermediate state is perplexing. This may signal that the UV line-forming region is hampered from receiving hard X-ray photons. Of course, the location of the line-forming region is not the same in both states, as it varies with luminosity.

In BHXTs, it is expected that X-ray irradiation plays a crucial role in the manifestation of eruptions in these systems, as well as in the energy balance and stability of their accretion discs. That said, I modelled the HST:HIMS UV SED in order to evaluate if irradiation matches its shape and flux level. The optimal model to fit our UV SED results in a number of unfeasible parameters for our system. In order to quantify and understand this, I created a small grid varying parameters such as the accretion rate, outer disc radius and albedo. The key result of this expedition is that, for all sets of reasonable parameters, the model could not replicate the observed flux level and the curvature of the spectrum, especially in the far-UV wavelengths.

Finally, I constructed both far-UV and near-UV light curves and PDS in order to study the variability and the emergence of features such as QPOs. In MAXI J1820+070, variability has been observed both in X-rays and optical (e.g. Stiele and Kong, 2020; Paice et al., 2021; Thomas et al., 2022; Mao et al., 2022). Variability in the UV is less explored. The only system in which UV QPOs have been detected is the case of the BHXT XTE J1118+480 (Hynes et al., 2003). Here, I find that all our spectra can be fitted by a broken-power law for both the far-UV and near-UV wavelengths of the hard state. On the other hand, tentative evidence is found for the presence of a UV QPO around $\sim 18s$ in the far-UV, around the same location that has been seen in both X-rays and optical almost during the same time.

These results would not be permitted without HST's astounding capabilities. Unfortunately, as I previously mentioned, UV wavelengths can suffer significant extinction, and this rare opportunity may not arise again. Coupled with the fact that the HST will soon be decommissioned, it becomes clear that we must act now. This urgency highlights the need to expand our sample of BHXTs (but in general, LMXBs), observed in different states of outburst. If this expedition is combined with simultaneous observations in other bands, it will advance our grasp of these sources and

unravel their mysteries. One obvious avenue is the ToO (Target of Opportunity) proposals to capture any extraordinary event as fast as it erupts. This type of observations allow us not to lose the opportunity to overlook these phenomena and act rapidly so as to put together a multi-wavelength campaign to characterise these sources in total.

Having UV data for a sample of sources, we can identify trends and common patterns, enabling a deeper exploration of various aspects observed in MAXI J1820+070. For example, we can systematically monitor the presence of UV outflows in the hard state of BH binaries. As winds are time-dependent phenomena, isolated snapshots are insufficient for their detection. Instead, systems should be continuously monitored across their outburst for reliable identification of outflow features. Furthermore, the plethora of UV observations would allow us to study timing properties, such as the detection of UV QPOs in the power spectra of these sources. So far, there is only one system with confirmed UV QPOs, with tentative evidence in MAXI J1820+070. Expanding our sample is crucial in the pursuit of these features and the discovery of the physical mechanism driving them.

From a theoretical point of view, there is significant room for progression. I would like to bring our attention back to the limitations in our understanding of X-ray irradiation and the implementation of the current irradiated disc models. The challenge lies not only in the simplistic assumptions during our modelling but also in the diversity of the different models and parameters. To address this issue, we have to return back to physics and implement more realistic conditions in the existent models. This includes taking into account the different shapes and properties of the corona and going beyond using blackbodies as an appropriate model of disc's radiation. This process would have a huge impact in our comprehension of which processes play a significant role in these systems.

Bibliography

Meil Abada-Simon, Alain Lecacheux, Tim S. Bastian, Jay A. Bookbinder, and George A. Dulk. The Spectrum and Variability of Radio Emission from AE Aquarii. *Astrophysical Journal*, 406: 692, April 1993. .

M. A. Abramowicz, M. Calvani, and L. Nobili. Thick accretion disks with super-Eddington luminosities. *Astrophysical Journal*, 242:772–788, December 1980. .

M. A. Abramowicz, B. Czerny, J. P. Lasota, and E. Szuszkiewicz. Slim Accretion Disks. *Astrophysical Journal*, 332:646, September 1988. .

K. Aizu. X-Ray Emission Region of a White Dwarf with Accretion. *Progress of Theoretical Physics*, 49(4):1184–1194, April 1973. .

K. Alabarta, D. Altamirano, M. Méndez, V. A. Cúneo, F. M. Vincentelli, N. Castro-Segura, F. García, B. Luff, and A. Veledina. Failed-transition outbursts in black hole low-mass X-ray binaries. *Monthly Notices of the Royal Astronomical Society*, 507(4):5507–5522, November 2021. .

J. Aleksić, S. Ansoldi, L. A. Antonelli, P. Antoranz, A. Babic, P. Bangale, J. A. Barrio, J. Becerra González, W. Bednarek, E. Bernardini, B. Biasuzzi, A. Biland, O. Blanch, S. Bonnefoy, G. Bonnoli, F. Borracci, T. Bretz, E. Carmona, A. Carosi, P. Colin, E. Colombo, J. L. Contreras, J. Cortina, S. Covino, P. Da Vela, F. Dazzi, A. De Angelis, G. De Caneva, B. De Lotto, E. de Oña Wilhelmi, C. Delgado Mendez, M. Doert, D. Dominis Prester, D. Dorner, M. Doro, S. Einecke, D. Eisenacher, D. Elsaesser, M. V. Fonseca, L. Font, K. Frantzen, C. Fruck, D. Galindo, R. J. García López, M. Garczarczyk, D. Garrido Terrats, M. Gaug, N. Godinović, A. González Muñoz, S. R. Gozzini, D. Hadasch, Y. Hanabata, M. Hayashida, J. Herrera, D. Hildebrand, J. Hose, D. Hrupec, W. Idec, V. Kadenius, H. Kellermann, K. Kodani, Y. Konno, J. Krause, H. Kubo, J. Kushida, A. La Barbera, D. Lelas, N. Lewandowska, E. Lindfors, S. Lombardi, M. López, R. López-Coto, A. López-Oramas, E. Lorenz, I. Lozano, M. Makariev, K. Mallot, G. Maneva, N. Mankuzhiyil, K. Mannheim, L. Maraschi, B. Marcote, M. Mariotti, M. Martínez, D. Mazin, U. Menzel, J. M. Miranda, R. Mirzoyan, A. Moralejo, P. Munar-Adrover, D. Nakajima, A. Niedzwiecki, K. Nilsson, K. Nishijima, K. Noda, N. Nowak, R. Orito, A. Overkemping, S. Paiano, M. Palatiello, D. Paneque, R. Paoletti, J. M. Paredes, X. Paredes-Fortuny, M. Persic, P. G. Prada Moroni, E. Prandini, S. Preziuso, I. Puljak, R. Reinthal, W. Rhode, M. Ribó, J. Rico, J. Rodriguez Garcia, S. Rügamer, A. Saggion, T. Saito, K. Saito, K. Satalecka, V. Scalzotto, V. Scapin, C. Schultz,

T. Schweizer, A. Sillanpää, J. Sitarek, I. Snidaric, D. Sobczynska, F. Spanier, V. Stamatescu, A. Stamerra, T. Steinbring, J. Storz, M. Strzys, L. Takalo, H. Takami, F. Tavecchio, P. Temnikov, T. Terzić, D. Tescaro, M. Teshima, J. Thaele, O. Tibolla, D. F. Torres, T. Toyama, A. Treves, M. Uellenbeck, P. Vogler, R. M. Wagner, and R. Zanin. MAGIC search for VHE γ-ray emission from AE Aquarii in a multiwavelength context. *Astronomy and Astrophysics*, 568:A109, August 2014. .

Pau Amaro-Seoane, Jeff Andrews, Manuel Arca Sedda, Abbas Askar, Quentin Baghi, Razvan Balasov, Imre Bartos, Simone S. Bavera, Jillian Bellovary, Christopher P. L. Berry, Emanuele Berti, Stefano Bianchi, Laura Blecha, Stéphane Blondin, Tamara Bogdanović, Samuel Boissier, Matteo Bonetti, Silvia Bonoli, Elisa Bortolas, Katelyn Breivik, Pedro R. Capelo, Laurentiu Caramete, Federico Cattorini, Maria Charisi, Sylvain Chaty, Xian Chen, Martyna Chruślińska, Alvin J. K. Chua, Ross Church, Monica Colpi, Daniel D'Orazio, Camilla Danielski, Melvyn B. Davies, Pratika Dayal, Alessandra De Rosa, Andrea Derdzinski, Kyriakos Destounis, Massimo Dotti, Ioana Dutan, Irina Dvorkin, Gaia Fabj, Thierry Foglizzo, Saavik Ford, Jean-Baptiste Fouvry, Alessia Franchini, Tassos Fragos, Chris Fryer, Massimo Gaspari, Davide Gerosa, Luca Graziani, Paul Groot, Melanie Habouzit, Daryl Haggard, Zoltan Haiman, Wen-Biao Han, Alina Istrate, Peter H. Johansson, Fazeel Mahmood Khan, Tomas Kimpson, Kostas Kokkotas, Albert Kong, Valeriya Korol, Kyle Kremer, Thomas Kupfer, Astrid Lamberts, Shane Larson, Mike Lau, Dongliang Liu, Nicole Lloyd-Ronning, Giuseppe Lodato, Alessandro Lupi, Chung-Pei Ma, Tomas Maccarone, Ilya Mandel, Alberto Mangiagli, Michela Mapelli, Stéphane Mathis, Lucio Mayer, Sean McGee, Barry McKernan, M. Coleman Miller, David F. Mota, Matthew Mumpower, Syeda S. Nasim, Gijs Nelemans, Scott Noble, Fabio Pacucci, Francesca Panessa, Vasileios Paschalidis, Hugo Pfister, Delphine Porquet, John Quenby, Angelo Ricarte, Friedrich K. Röpke, John Regan, Stephan Rosswog, Ashley Ruiter, Milton Ruiz, Jessie Runnoe, Raffaella Schneider, Jeremy Schnittman, Amy Secunda, Alberto Sesana, Naoki Seto, Lijing Shao, Stuart Shapiro, Carlos Sopuerta, Nicholas C. Stone, Arthur Suvorov, Nicola Tamanini, Tomas Tamfal, Thomas Tauris, Karel Temmink, John Tomsick, Silvia Toonen, Alejandro Torres-Orjuela, Martina Toscani, Antonios Tsokaros, Caner Unal, Verónica Vázquez-Aceves, Rosa Valiante, Maurice van Putten, Jan van Roestel, Christian Vignali, Marta Volonteri, Kinwah Wu, Ziri Younsi, Shenghua Yu, Silvia Zane, Lorenz Zwick, Fabio Antonini, Vishal Baibhav, Enrico Barausse, Alexander Bonilla Rivera, Marica Branchesi, Graziella Branduardi-Raymont, Kevin Burdge, Srija Chakraborty, Jorge Cuadra, Kristen Dage, Benjamin Davis, Selma E. de Mink, Roberto Decarli, Daniela Doneva, Stephanie Escoffier, Poshak Gandhi, Francesco Haardt, Carlos O. Lousto, Samaya Nissanke, Jason Nordhaus, Richard O'Shaughnessy, Simon Portegies Zwart, Adam Pound, Fabian Schussler, Olga Sergijenko, Alessandro Spallicci, Daniele Vernieri, and Alejandro Vigna-Gómez. Astrophysics with the Laser Interferometer Space Antenna. *Living Reviews in Relativity*, 26(1):2, December 2023. .

Anne M. Archibald, Ingrid H. Stairs, Scott M. Ransom, Victoria M. Kaspi, Vladislav I. Kondratiev, Duncan R. Lorimer, Maura A. McLaughlin, Jason Boyles, Jason W. T. Hessels, Ryan Lynch, Joeri van Leeuwen, Mallory S. E. Roberts, Frederick Jenet, David J. Champion, Rachel Rosen, Brad N.

Barlow, Bart H. Dunlap, and Ronald A. Remillard. A Radio Pulsar/X-ray Binary Link. *Science*, 324(5933):1411, June 2009. .

Philip J. Armitage. Lecture notes on accretion disk physics. *arXiv e-prints*, art. arXiv:2201.07262, January 2022. .

P. Atri, J. C. A. Miller-Jones, A. Bahramian, R. M. Plotkin, A. T. Deller, P. G. Jonker, T. J. Maccarone, G. R. Sivakoff, R. Soria, D. Altamirano, T. Belloni, R. Fender, E. Koerding, D. Maitra, S. Markoff, S. Migliari, D. Russell, T. Russell, C. L. Sarazin, A. J. Tetarenko, and V. Tudose. A radio parallax to the black hole X-ray binary MAXI J1820+070. *Monthly Notices of the Royal Astronomical Society*, 493(1):L81–L86, March 2020. .

M. Cristina Baglio, Dave M. Russell, and Fraser Lewis. Optical observations of MAXI J1820+070 suggest it is a black hole X-ray binary. *The Astronomer's Telegram*, 11418:1, March 2018.

Arash Bahramian and Nathalie Degenaar. Low-Mass X-ray Binaries. In *Handbook of X-ray and Gamma-ray Astrophysics. Edited by Cosimo Bambi and Andrea Santangelo*, page 120. 2023. .

Steven A. Balbus and John F. Hawley. A Powerful Local Shear Instability in Weakly Magnetized Disks. I. Linear Analysis. *Astrophysical Journal*, 376:214, July 1991. .

Cosimo Bambi, Laura W. Brenneman, Thomas Dauser, Javier A. García, Victoria Grinberg, Adam Ingram, Jiachen Jiang, Honghui Liu, Anne M. Lohfink, Andrea Marinucci, Guglielmo Mastroserio, Riccardo Middei, Sourabh Nampalliwar, Andrzej Niedźwiecki, James F. Steiner, Ashutosh Tripathi, and Andrzej A. Zdziarski. Towards Precision Measurements of Accreting Black Holes Using X-Ray Reflection Spectroscopy. *Space Science Reviews*, 217(5):65, August 2021. .

Srimanta Banerjee, Gulab C. Dewangan, Christian Knigge, Maria Georganti, Poshak Gandhi, N. P. S. Mithun, Payaswini Saikia, Dipankar Bhattacharya, David M. Russell, Fraser Lewis, and Andrzej A. Zdziarski. A multi-wavelength study of the hard and soft states of MAXI J1820+070 during its 2018 outburst. *arXiv e-prints*, art. arXiv:2402.08237, February 2024. .

Raymundo Baptista, Keith Horne, Richard A. Wade, Ivan Hubeny, Knox S. Long, and Rene G. M. Rutten. HST spatially resolved spectra of the accretion disc and gas stream of the nova-like variable UX Ursae Majoris. *Monthly Notices of the Royal Astronomical Society*, 298(4):1079–1091, August 1998. .

J. Barker and U. Kolb. The minimum period problem in cataclysmic variables. *Monthly Notices of the Royal Astronomical Society*, 340(2):623–631, April 2003. .

M. C. Begelman, C. F. McKee, and G. A. Shields. Compton heated winds and coronae above accretion disks. I. Dynamics. *Astrophysical Journal*, 271:70–88, August 1983. .

T. Belloni, J. Homan, P. Casella, M. van der Klis, E. Nespoli, W. H. G. Lewin, J. M. Miller, and M. Méndez. The evolution of the timing properties of the black-hole transient GX 339-4 during its 2002/2003 outburst. *Astronomy and Astrophysics*, 440(1):207–222, September 2005. .

T. M. Belloni, A. Sanna, and M. Méndez. High-frequency quasi-periodic oscillations in black hole binaries. *Monthly Notices of the Royal Astronomical Society*, 426(3):1701–1709, November 2012. .

Tomaso M. Belloni and Sara E. Motta. Transient Black Hole Binaries. In Cosimo Bambi, editor, *Astrophysics of Black Holes: From Fundamental Aspects to Latest Developments*, volume 440 of *Astrophysics and Space Science Library*, page 61, January 2016.

Tomaso M. Belloni and Luigi Stella. Fast Variability from Black-Hole Binaries. *Space Science Reviews*, 183(1-4):43–60, September 2014. .

D. Bhattacharya and E. P. J. van den Heuvel. Formation and evolution of binary and millisecond radio pulsars. *Physics Reports*, 203(1-2):1–124, January 1991. .

A. A. Blinova, M. M. Romanova, G. V. Ustyugova, A. V. Koldoba, and R. V. E. Lovelace. Comparisons of MHD propeller model with observations of cataclysmic variable AE Aqr. *Monthly Notices of the Royal Astronomical Society*, 487(2):1754–1763, August 2019. .

R. C. Bohlin. Copernicus observations of interstellar absorption at Lyman Alpha. *Astrophysical Journal*, 200:402–414, September 1975. .

R. C. Bohlin, B. D. Savage, and J. F. Drake. A survey of interstellar H I from Lalpha absorption measurements. II. *Astrophysical Journal*, 224:132–142, August 1978. .

C. C. G. Bowden, S. M. Bradbury, P. M. Chadwick, J. E. Dickinson, N. A. Dipper, P. J. Edwards, E. W. Lincoln, T. J. L. McComb, K. J. Orford, S. M. Rayner, and K. E. Turver. 350 GeV gamma rays from AE Aqr. *Astroparticle Physics*, 1(1):47–59, November 1992. .

Joe Bright, Sara Motta, and Rob Fender. AMI radio detection of the black hole candidate MAXI J1820+070 during the soft to hard transition. *The Astronomer's Telegram*, 12061:1, September 2018.

V. Buat-Ménard, J. M. Hameury, and J. P. Lasota. Z Cam stars: A particular response to a general phenomenon. *Astronomy and Astrophysics*, 369:925–931, April 2001. .

V. Buat-Menard, J.-M. Hameury, and J.-P. Lasota. The nature of dwarf nova outbursts. *Astronomy and Astrophysics*, 366:612–622, 2001. .

David A. H. Buckley, Kazuhiro Sekiguchi, Christian Motch, Darragh O'Donoghue, An-Le Chen, Alex Schwarzenberg-Czerny, Wolfgang Pietsch, and Margaret K. Harrop-Allin. RX J1712.6-2414: a polarized intermediate polar from the ROSAT Galactic Plane Survey. *Monthly Notices of the Royal Astronomical Society*, 275(4):1028–1048, August 1995. .

D. J. K. Buisson, A. C. Fabian, D. Barret, F. Fürst, P. Gandhi, J. A. García, E. Kara, K. K. Madsen, J. M. Miller, M. L. Parker, A. W. Shaw, J. A. Tomsick, and D. J. Walton. MAXI J1820+070 with NuSTAR I. An increase in variability frequency but a stable reflection spectrum: coronal properties and implications for the inner disc in black hole binaries. *Monthly Notices of the Royal Astronomical Society*, 490(1):1350–1362, November 2019. .

O. W. Butters, S. Katajainen, A. J. Norton, H. J. Lehto, and V. Piirola. Circular polarization survey of intermediate polars I. Northern targets in the range 17 h < RA < 23 h. *Astronomy and Astrophysics*, 496(3):891–902, March 2009. .

C. Cabanac, G. Henri, P. O. Petrucci, J. Malzac, J. Ferreira, and T. M. Belloni. Variability of X-ray binaries from an oscillating hot corona. *Monthly Notices of the Royal Astronomical Society*, 404(2): 738–748, May 2010. .

S. Campana, L. Stella, G. L. Israel, A. Moretti, A. N. Parmar, and M. Orlandini. The Quiescent X-Ray Emission of Three Transient X-Ray Pulsars. *Astrophysical Journal*, 580(1):389–393, November 2002. .

S. Campana, L. Stella, S. Mereghetti, and D. de Martino. A universal relation for the propeller mechanisms in magnetic rotating stars at different scales. *Astronomy and Astrophysics*, 610:A46, 02 2018. .

J. Casares, M. Mouchet, I. G. Martinez-Pais, and E. T. Harlaftis. A coordinated campaign on the intermediate polar AE AQR - I. The system parameters. *Monthly Notices of the Royal Astronomical Society*, 282(1):182–190, 09 1996. .

P. Casella, T. Belloni, J. Homan, and L. Stella. A study of the low-frequency quasi-periodic oscillations in the X-ray light curves of the black hole candidate <ASTROBJ>XTE J1859+226</ASTROBJ>. *Astronomy and Astrophysics*, 426:587–600, November 2004. .

P. Casella, V. Testa, D. M. Russell, T. M. Belloni, and T. J. Maccarone. Declining near-infrared flux from the black-hole candidate MAXI J1820+070 (ASASSN-18ey) in transition. *The Astronomer's Telegram*, 11833:1, July 2018.

N. Castro Segura, C. Knigge, K. S. Long, D. Altamirano, M. Armas Padilla, C. Bailyn, D. A. H. Buckley, D. J. K. Buisson, J. Casares, P. Charles, J. A. Combi, V. A. Cúneo, N. D. Degenaar, S. del Palacio, M. Díaz Trigo, R. Fender, P. Gandhi, M. Georganti, C. Gutiérrez, J. V. Hernandez Santisteban, F. Jiménez-Ibarra, J. Matthews, M. Méndez, M. Middleton, T. Muñoz-Darias, M. Özbey Arabacı, M. Pahari, L. Rhodes, T. D. Russell, S. Scaringi, J. van den Eijnden, G. Vasilopoulos, F. M. Vincentelli, and P. Wiseman. A persistent ultraviolet outflow from an accreting neutron star binary transient. *Nature*, 603(7899):52–57, March 2022. .

N. Castro Segura, C. Knigge, J. H. Matthews, F. M. Vincentelli, P. Charles, K. S. Long, D. Altamirano, D. A. H. Buckley, D. Modiano, M. A. P. Torres, D. J. K. Buisson, S. Fijma, K. Alabarta, N. Degenaar, M. Georganti, and M. C. Baglio. Shedding far-ultraviolet light on the donor star and evolutionary state of the neutron-star LMXB Swift J1858.6-0814. *Monthly Notices of the Royal Astronomical Society*, 527(2):2508–2522, January 2024. .

Gilles Chabrier, Isabelle Baraffe, Mark Phillips, and Florian Debras. Impact of a new H/He equation of state on the evolution of massive brown dwarfs. New determination of the hydrogen burning limit. *Astronomy and Astrophysics*, 671:A119, March 2023. .

Sudip Chakraborty, Nilam Navale, Ajay Ratheesh, and Sudip Bhattacharyya. A spectral study of the black hole X-ray binary MAXI J1820+070 with AstroSat and NuSTAR. *Monthly Notices of the Royal Astronomical Society*, 498(4):5873–5884, November 2020. .

G. Chanmugam and A. Ray. The rotational and orbital evolution of cataclysmic binaries containing magnetic white dwarfs. *Astrophysical Journal*, 285:252–257, October 1984. .

Donald D Clayton. *Principles of stellar evolution and nucleosynthesis*. University of Chicago press, 1983.

M. S. B. Coleman, I. Kotko, O. Blaes, J. P. Lasota, and S. Hirose. Dwarf nova outbursts with magnetorotational turbulence. *Monthly Notices of the Royal Astronomical Society*, 462(4):3710–3726, November 2016. .

S. Corbel, M. A. Nowak, R. P. Fender, A. K. Tzioumis, and S. Markoff. Radio/X-ray correlation in the low/hard state of GX 339-4. *Astronomy and Astrophysics*, 400:1007–1012, March 2003. .

M. Coriat, R. P. Fender, and G. Dubus. Revisiting a fundamental test of the disc instability model for X-ray binaries. *Monthly Notices of the Royal Astronomical Society*, 424(3):1991–2001, August 2012. .

J. M. Corral-Santana, J. Casares, T. Muñoz-Darias, F. E. Bauer, I. G. Martínez-Pais, and D. M. Russell. BlackCAT: A catalogue of stellar-mass black holes in X-ray transients. *Astronomy and Astrophysics*, 587:A61, March 2016. .

Mark Cropper. The Polars. *Space Science Reviews*, 54(3-4):195–295, December 1990. .

Caroline R. D'Angelo and Hendrik C. Spruit. Episodic accretion on to strongly magnetic stars. *Monthly Notices of the Royal Astronomical Society*, 406(2):1208–1219, August 2010. .

Caroline R. D'Angelo and Hendrik C. Spruit. Accretion discs trapped near corotation. *Monthly Notices of the Royal Astronomical Society*, 420(1):416–429, February 2012. .

Shane W. Davis and Samer El-Abd. Spectral Hardening in Black Hole Accretion: Giving Spectral Modelers an f. *Astrophysical Journal*, 874(1):23, March 2019. .

O. C. de Jager, P. J. Meintjes, D. O'Donoghue, and E. L. Robinson. The discovery of a brake on the white dwarf in AE Aquarii. *Monthly Notices of the Royal Astronomical Society*, 267:577–588, 04 1994.

M. de Kool. Common Envelope Evolution and Double Cores of Planetary Nebulae. *Astrophysical Journal*, 358:189, July 1990. .

B. De Marco, A. A. Zdziarski, G. Ponti, G. Migliori, T. M. Belloni, A. Segovia Otero, M. A. Dziełak, and E. V. Lai. The inner flow geometry in MAXI J1820+070 during hard and hard-intermediate states. *Astronomy and Astrophysics*, 654:A14, October 2021. .

M. della Valle, S. Benetti, E. Cappellaro, and C. Wheeler. The optical counterpart of GRS 1009-45 (X-ray Nova Velorum 1993). *Astronomy and Astrophysics*, 318:179–186, February 1997.

G. C. Dewangan. Calibration of AstroSat/UVIT gratings and spectral responses. *Journal of Astrophysics and Astronomy*, 42(2):49, October 2021. .

J. D. M. Dewi and T. M. Tauris. On the energy equation and efficiency parameter of the common envelope evolution. *Astronomy and Astrophysics*, 360:1043–1051, August 2000. .

M. Díaz Trigo and L. Boirin. Accretion disc atmospheres and winds in low-mass X-ray binaries. *Astronomische Nachrichten*, 337(4-5):368, May 2016. .

M. Díaz Trigo, S. Migliari, J. C. A. Miller-Jones, and M. Guainazzi. XMM-Newton observations reveal the disappearance of the wind in 4U 1630-47. *Astronomy and Astrophysics*, 571:A76, November 2014. .

Chris Done, Marek Gierliński, and Aya Kubota. Modelling the behaviour of accretion flows in X-ray binaries. Everything you always wanted to know about accretion but were afraid to ask. *Astronomy and Astrophysics Reviews*, 15(1):1–66, December 2007. .

G. Dubus, J. M. Hameury, and J. P. Lasota. The disc instability model for X-ray transients: Evidence for truncation and irradiation. *Astronomy and Astrophysics*, 373:251–271, July 2001. .

Guillaume Dubus, Jean-Pierre Lasota, Jean-Marie Hameury, and Phil Charles. X-ray irradiation in low-mass binary systems. *Monthly Notices of the Royal Astronomical Society*, 303(1):139–147, February 1999. .

Gaspard Duchêne and Adam Kraus. Stellar Multiplicity. *Annual Review of Astronomy and Astrophysics*, 51(1):269–310, August 2013. .

M. Durant, P. Gandhi, T. Shahbaz, H. H. Peralta, and V. S. Dhillon. Multiwavelength spectral and high time resolution observations of SWIFTJ1753.5-0127: new activity? *Monthly Notices of the Royal Astronomical Society*, 392(1):309–324, January 2009. .

J. Echevarría, Robert Connon Smith, R. Costero, S. Zharikov, and R. Michel. High-dispersion absorption-line spectroscopy of AE Aqr. *Monthly Notices of the Royal Astronomical Society*, 387 (4):1563–1574, July 2008. .

P. P. Eggleton. Aproximations to the radii of Roche lobes. *Astrophysical Journal*, 268:368–369, May 1983. .

Kareem El-Badry, Hans-Walter Rix, and Tyler M. Heintz. A million binaries from Gaia eDR3: sample selection and validation of Gaia parallax uncertainties. *Monthly Notices of the Royal Astronomical Society*, 506(2):2269–2295, September 2021. .

M. Eracleous and K. Horne. The speedy magnetic propeller in the cataclysmic variable AE aquarii. *Astrophysical Journal*, 471(1):427–446, 11 1996. .

M. Eracleous, K. Horne, E. L. Robinson, E.-H. Zhang, T. R. Marsh, and J. H. Wood. The Ultraviolet Pulsations of the Cataclysmic Variable AE Aquarii as Observed with the Hubble Space Telescope. *Astrophysical Journal*, 433:313, sep 1994. .

Ann A. Esin, Jeffrey E. McClintock, and Ramesh Narayan. Advection-dominated accretion and the spectral states of black hole x-ray binaries: Application to nova muscae 1991. *Astrophysical Journal*, 489(2):865, nov 1997. . URL https://dx.doi.org/10.1086/304829.

I.N. Evans. *FOS Instrument Science Report CAL/FOS-104*, 1993.

Yi-Zhong Fan, Ming-Zhe Han, Jin-Liang Jiang, Dong-Sheng Shao, and Shao-Peng Tang. Maximum gravitational mass M_{TOV}=2.2 $5_{-0.07}{}^{+0.08}M_{\odot}$ inferred at about 3% precision with multi-messenger data of neutron stars. *Physical Review D*, 109(4):043052, February 2024. .

R. P. Fender, T. M. Belloni, and E. Gallo. Towards a unified model for black hole X-ray binary jets. *Monthly Notices of the Royal Astronomical Society*, 355(4):1105–1118, December 2004. .

R. P. Fender, J. Homan, and T. M. Belloni. Jets from black hole X-ray binaries: testing, refining and extending empirical models for the coupling to X-rays. *Monthly Notices of the Royal Astronomical Society*, 396(3):1370–1382, July 2009. .

Rob Fender and Elena Gallo. An Overview of Jets and Outflows in Stellar Mass Black Holes. *Space Science Reviews*, 183(1-4):323–337, September 2014. .

Lilia Ferrario, D. T. Wickramasinghe, and Gary Schmidt. Analysis of new spectropolarimetric data of AR UMa. *Monthly Notices of the Royal Astronomical Society*, 338(2):340–346, January 2003. .

Lilia Ferrario, Domitilla de Martino, and Boris T. Gänsicke. Magnetic White Dwarfs. *Space Science Reviews*, 191(1-4):111–169, October 2015. .

J. Ferreira, G. Marcel, P. O. Petrucci, J. Rodriguez, J. Malzac, R. Belmont, M. Clavel, G. Henri, S. Corbel, and M. Coriat. Are low-frequency quasi-periodic oscillations in accretion flows the disk response to jet instability? *Astronomy and Astrophysics*, 660:A66, April 2022. .

S. Fijma, N. Castro Segura, N. Degenaar, C. Knigge, N. Higginbottom, J. V. Hernández Santisteban, and T. J. Maccarone. A transient ultraviolet outflow in the short-period X-ray binary UW CrB. *Monthly Notices of the Royal Astronomical Society*, 526(1):L149–L154, November 2023. .

Edward L. Fitzpatrick. Correcting for the Effects of Interstellar Extinction. *Publications of the Astronomical Society of the Pacific*, 111(755):63–75, January 1999. .

R. H. Fowler. On dense matter. *Monthly Notices of the Royal Astronomical Society*, 87:114–122, December 1926. .

J. Frank, A. King, and D. Raine. *Accretion Power in Astrophysics: Third edition*. Cambridge University Press, New York, 02 2002.

W. Freudling, M. Romaniello, D. M. Bramich, P. Ballester, V. Forchi, C. E. García-Dabló, S. Moehler, and M. J. Neeser. Automated data reduction workflows for astronomy. The ESO Reflex environment. *Astronomy and Astrophysics*, 559:A96, November 2013. .

Cynthia S. Froning, Knox S. Long, and Raymundo Baptista. Hubble Space Telescope Observations of the Nova-like Cataclysmic Variable V348 Puppis. *Astronomical Journal*, 126(2):964–974, August 2003. .

Cynthia S. Froning, Andrew G. Cantrell, Thomas J. Maccarone, Kevin France, Juthika Khargharia, Lisa M. Winter, Edward L. Robinson, Robert I. Hynes, Jess W. Broderick, Sera Markoff, Manuel A. P. Torres, Michael Garcia, Charles D. Bailyn, J. Xavier Prochaska, Jessica Werk, Chris Thom, Stéphane Béland, Charles W. Danforth, Brian Keeney, and James C. Green. Multiwavelength Observations of A0620-00 in Quiescence. *Astrophysical Journal*, 743(1):26, December 2011. .

Cynthia S. Froning, Thomas J. Maccarone, Kevin France, Lisa Winter, Edward L. Robinson, Robert I. Hynes, and Fraser Lewis. Multiwavelength Observations of Swift J1753.5-0127. *Astrophysical Journal*, 780(1):48, January 2014. .

Gaia Collaboration, A. G. A. Brown, A. Vallenari, T. Prusti, J. H. J. de Bruijne, C. Babusiaux, M. Biermann, O. L. Creevey, D. W. Evans, L. Eyer, A. Hutton, F. Jansen, C. Jordi, S. A. Klioner, U. Lammers, L. Lindegren, X. Luri, F. Mignard, C. Panem, D. Pourbaix, S. Randich, P. Sartoretti, C. Soubiran, N. A. Walton, F. Arenou, C. A. L. Bailer-Jones, U. Bastian, M. Cropper, R. Drimmel, D. Katz, M. G. Lattanzi, F. van Leeuwen, J. Bakker, C. Cacciari, J. Castañeda, F. De Angeli, C. Ducourant, C. Fabricius, M. Fouesneau, Y. Frémat, R. Guerra, A. Guerrier, J. Guiraud, A. Jean-Antoine Piccolo, E. Masana, R. Messineo, N. Mowlavi, C. Nicolas, K. Nienartowicz, F. Pailler, P. Panuzzo, F. Riclet, W. Roux, G. M. Seabroke, R. Sordo, P. Tanga, F. Thévenin, G. Gracia-Abril, J. Portell, D. Teyssier, M. Altmann, R. Andrae, I. Bellas-Velidis, K. Benson, J. Berthier, R. Blomme, E. Brugaletta, P. W. Burgess, G. Busso, B. Carry, A. Cellino, N. Cheek, G. Clementini, Y. Damerdji, M. Davidson, L. Delchambre, A. Dell'Oro, J. Fernández-Hernández, L. Galluccio, P. García-Lario, M. Garcia-Reinaldos, J. González-Núñez, E. Gosset, R. Haigron, J. L. Halbwachs, N. C. Hambly, D. L. Harrison, D. Hatzidimitriou, U. Heiter, J. Hernández, D. Hestroffer, S. T. Hodgkin, B. Holl, K. Janßen, G. Jevardat de Fombelle, S. Jordan, A. Krone-Martins, A. C. Lanzafame, W. Löffler, A. Lorca, M. Manteiga, O. Marchal, P. M. Marrese, A. Moitinho, A. Mora, K. Muinonen, P. Osborne, E. Pancino, T. Pauwels, J. M. Petit, A. Recio-Blanco, P. J. Richards, M. Riello, L. Rimoldini, A. C. Robin, T. Roegiers, J. Rybizki, L. M. Sarro, C. Siopis, M. Smith, A. Sozzetti, A. Ulla, E. Utrilla, M. van Leeuwen, W. van Reeven, U. Abbas, A. Abreu Aramburu, S. Accart, C. Aerts, J. J. Aguado, M. Ajaj, G. Altavilla, M. A. Álvarez, J. Álvarez Cid-Fuentes, J. Alves, R. I. Anderson, E. Anglada Varela, T. Antoja, M. Audard, D. Baines, S. G. Baker, L. Balaguer-Núñez, E. Balbinot, Z. Balog, C. Barache, D. Barbato, M. Barros, M. A. Barstow, S. Bartolomé, J. L. Bassilana, N. Bauchet, A. Baudesson-Stella, U. Becciani, M. Bellazzini, M. Bernet, S. Bertone, L. Bianchi, S. Blanco-Cuaresma, T. Boch, A. Bombrun, D. Bossini, S. Bouquillon, A. Bragaglia, L. Bramante, E. Breedt, A. Bressan, N. Brouillet, B. Bucciarelli, A. Burlacu, D. Busonero, A. G. Butkevich, R. Buzzi, E. Caffau, R. Cancelliere, H. Cánovas,

T. Cantat-Gaudin, R. Carballo, T. Carlucci, M. I. Carnerero, J. M. Carrasco, L. Casamiquela, M. Castellani, A. Castro-Ginard, P. Castro Sampol, L. Chaoul, P. Charlot, L. Chemin, A. Chiavassa, M. R. L. Cioni, G. Comoretto, W. J. Cooper, T. Cornez, S. Cowell, F. Crifo, M. Crosta, C. Crowley, C. Dafonte, A. Dapergolas, M. David, P. David, P. de Laverny, F. De Luise, R. De March, J. De Ridder, R. de Souza, P. de Teodoro, A. de Torres, E. F. del Peloso, E. del Pozo, M. Delbo, A. Delgado, H. E. Delgado, J. B. Delisle, P. Di Matteo, S. Diakite, C. Diener, E. Distefano, C. Dolding, D. Eappachen, B. Edvardsson, H. Enke, P. Esquej, C. Fabre, M. Fabrizio, S. Faigler, G. Fedorets, P. Fernique, A. Fienga, F. Figueras, C. Fouron, F. Fragkoudi, E. Fraile, F. Franke, M. Gai, D. Garabato, A. Garcia-Gutierrez, M. García-Torres, A. Garofalo, P. Gavras, E. Gerlach, R. Geyer, P. Giacobbe, G. Gilmore, S. Girona, G. Giuffrida, R. Gomel, A. Gomez, I. Gonzalez-Santamaria, J. J. González-Vidal, M. Granvik, R. Gutiérrez-Sánchez, L. P. Guy, M. Hauser, M. Haywood, A. Helmi, S. L. Hidalgo, T. Hilger, N. Hładczuk, D. Hobbs, G. Holland, H. E. Huckle, G. Jasniewicz, P. G. Jonker, J. Juaristi Campillo, F. Julbe, L. Karbevska, P. Kervella, S. Khanna, A. Kochoska, M. Kontizas, G. Kordopatis, A. J. Korn, Z. Kostrzewa-Rutkowska, K. Kruszyńska, S. Lambert, A. F. Lanza, Y. Lasne, J. F. Le Campion, Y. Le Fustec, Y. Lebreton, T. Lebzelter, S. Leccia, N. Leclerc, I. Lecoeur-Taibi, S. Liao, E. Licata, E. P. Lindstrøm, T. A. Lister, E. Livanou, A. Lobel, P. Madrero Pardo, S. Managau, R. G. Mann, J. M. Marchant, M. Marconi, M. M. S. Marcos Santos, S. Marinoni, F. Marocco, D. J. Marshall, L. Martin Polo, J. M. Martín-Fleitas, A. Masip, D. Massari, A. Mastrobuono-Battisti, T. Mazeh, P. J. McMillan, S. Messina, D. Michalik, N. R. Millar, A. Mints, D. Molina, R. Molinaro, L. Molnár, P. Montegriffo, R. Mor, R. Morbidelli, T. Morel, D. Morris, A. F. Mulone, D. Munoz, T. Muraveva, C. P. Murphy, I. Musella, L. Noval, C. Ordénovic, G. Orrù, J. Osinde, C. Pagani, I. Pagano, L. Palaversa, P. A. Palicio, A. Panahi, M. Pawlak, X. Peñalosa Esteller, A. Penttilä, A. M. Piersimoni, F. X. Pineau, E. Plachy, G. Plum, E. Poggio, E. Poretti, E. Poujoulet, A. Prša, L. Pulone, E. Racero, S. Ragaini, M. Rainer, C. M. Raiteri, N. Rambaux, P. Ramos, M. Ramos-Lerate, P. Re Fiorentin, S. Regibo, C. Reylé, V. Ripepi, A. Riva, G. Rixon, N. Robichon, C. Robin, M. Roelens, L. Rohrbasser, M. Romero-Gómez, N. Rowell, F. Royer, K. A. Rybicki, G. Sadowski, A. Sagristà Sellés, J. Sahlmann, J. Salgado, E. Salguero, N. Samaras, V. Sanchez Gimenez, N. Sanna, R. Santoveña, M. Sarasso, M. Schultheis, E. Sciacca, M. Segol, J. C. Segovia, D. Ségransan, D. Semeux, S. Shahaf, H. I. Siddiqui, A. Siebert, L. Siltala, E. Slezak, R. L. Smart, E. Solano, F. Solitro, D. Souami, J. Souchay, A. Spagna, F. Spoto, I. A. Steele, H. Steidelmüller, C. A. Stephenson, M. Süveges, L. Szabados, E. Szegedi-Elek, F. Taris, G. Tauran, M. B. Taylor, R. Teixeira, W. Thuillot, N. Tonello, F. Torra, J. Torra, C. Turon, N. Unger, M. Vaillant, E. van Dillen, O. Vanel, A. Vecchiato, Y. Viala, D. Vicente, S. Voutsinas, M. Weiler, T. Wevers, Ł. Wyrzykowski, A. Yoldas, P. Yvard, H. Zhao, J. Zorec, S. Zucker, C. Zurbach, and T. Zwitter. Gaia Early Data Release 3. Summary of the contents and survey properties. *Astronomy and Astrophysics*, 649:A1, May 2021. .

E. Gallo, R. P. Fender, and G. G. Pooley. A universal radio-X-ray correlation in low/hard state black hole binaries. *Monthly Notices of the Royal Astronomical Society*, 344(1):60–72, September 2003.

E. Gallo, J. C. A. Miller-Jones, D. M. Russell, P. G. Jonker, J. Homan, R. M. Plotkin, S. Markoff, B. P. Miller, S. Corbel, and R. P. Fender. The radio/X-ray domain of black hole X-ray binaries at the lowest radio luminosities. *Monthly Notices of the Royal Astronomical Society*, 445(1):290–300, November 2014. .

Elena Gallo, Nathalie Degenaar, and Jakob van den Eijnden. Hard state neutron star and black hole X-ray binaries in the radio:X-ray luminosity plane. *Monthly Notices of the Royal Astronomical Society*, 478(1):L132–L136, July 2018.

P. Gandhi, V. S. Dhillon, M. Durant, A. C. Fabian, A. Kubota, K. Makishima, J. Malzac, T. R. Marsh, J. M. Miller, T. Shahbaz, H. C. Spruit, and P. Casella. Rapid optical and X-ray timing observations of GX339-4: multicomponent optical variability in the low/hard state. *Monthly Notices of the Royal Astronomical Society*, 407(4):2166–2192, October 2010. .

P. Gandhi, M. Bachetti, V. S. Dhillon, R. P. Fender, L. K. Hardy, F. A. Harrison, S. P. Littlefair, J. Malzac, S. Markoff, T. R. Marsh, K. Mooley, D. Stern, J. A. Tomsick, D. J. Walton, P. Casella, F. Vincentelli, D. Altamirano, J. Casares, C. Ceccobello, P. A. Charles, C. Ferrigno, R. I. Hynes, C. Knigge, E. Kuulkers, M. Pahari, F. Rahoui, D. M. Russell, and A. W. Shaw. An elevation of 0.1 light-seconds for the optical jet base in an accreting Galactic black hole system. *Nature Astronomy*, 1:859–864, October 2017. .

Boris T. Gänsicke, Gary D. Schmidt, Stefan Jordan, and Paula Szkody. Phase-resolved Hubble Space Telescope/STIS Spectroscopy of the Exposed White Dwarf in the High-Field Polar AR Ursae Majoris. *Astrophysical Journal*, 555(1):380–392, July 2001. .

Boris T. Gänsicke, Paula Szkody, Domitilla de Martino, Klaus Beuermann, Knox S. Long, Edward M. Sion, Christian Knigge, Tom Marsh, and Ivan Hubeny. Anomalous Ultraviolet Line Flux Ratios in the Cataclysmic Variables 1RXS J232953.9+062814, CE 315, BZ Ursae Majoris, and EY Cygni, Observed with the Hubble Space Telescope Space Telescope Imaging Spectrograph. *Astrophysical Journal*, 594(1):443–448, September 2003. .

M. Garcia, W. Brown, M. Pahre, J. McClintock, P. Callanan, and P. Garnavich. XTE J1118+480. *IAU Cirulars*, 7392:2, April 2000.

Peter Garnavich, Colin Littlefield, R. M. Wagner, Jan van Roestel, Amruta D. Jaodand, Paula Szkody, and John R. Thorstensen. Confirmation of a Second Propeller: A High-inclination Twin of AE Aquarii. *Astrophysical Journal*, 917(1):22, August 2021. .

N. Gehrels, G. Chincarini, P. Giommi, K. O. Mason, J. A. Nousek, A. A. Wells, N. E. White, S. D. Barthelmy, D. N. Burrows, L. R. Cominsky, K. C. Hurley, F. E. Marshall, P. Mészáros, P. W. A. Roming, L. Angelini, L. M. Barbier, T. Belloni, S. Campana, P. A. Caraveo, M. M. Chester, O. Citterio, T. L. Cline, M. S. Cropper, J. R. Cummings, A. J. Dean, E. D. Feigelson, E. E. Fenimore, D. A. Frail, A. S. Fruchter, G. P. Garmire, K. Gendreau, G. Ghisellini, J. Greiner, J. E. Hill, S. D. Hunsberger, H. A. Krimm, S. R. Kulkarni, P. Kumar, F. Lebrun, N. M. Lloyd-Ronning, C. B. Markwardt, B. J. Mattson, R. F. Mushotzky, J. P. Norris, J. Osborne, B. Paczynski, D. M. Palmer,

H. S. Park, A. M. Parsons, J. Paul, M. J. Rees, C. S. Reynolds, J. E. Rhoads, T. P. Sasseen, B. E. Schaefer, A. T. Short, A. P. Smale, I. A. Smith, L. Stella, G. Tagliaferri, T. Takahashi, M. Tashiro, L. K. Townsley, J. Tueller, M. J. L. Turner, M. Vietri, W. Voges, M. J. Ward, R. Willingale, F. M. Zerbi, and W. W. Zhang. The Swift Gamma-Ray Burst Mission. *Astrophysical Journal*, 611(2): 1005–1020, August 2004. .

Keith C. Gendreau, Zaven Arzoumanian, Phillip Adkins, Cheryl L. Albert, John F. Anders, Andrew T. Aylward, Charles Baker, Erin Balsamo, William A. Bamford, Suyog S. Benegalrao, Daniel L. Berry, Shiraz Bhalwani, J. Kevin Black, Carl Blaurock, Ginger Bronke, Gary L. Brown, Jason Budinoff, Jeffrey D. Cantwell, Thoniel Cazeau, Philip T. Chen, Thomas G. Clement, Andrew T. Colangelo, Jerry S. Coleman, Jonathan D. Coopersmith, William E. Dehaven, John P. Doty, Mark Egan, Teruaki Enoto, Terry W.-M. Fan, Deneen M. Ferro, R. Foster, Nicholas M. Galassi, Luis D. Gallo, Christopher M. Green, Dave Grosh, Kong Q. Ha, Monther A. Hasouneh, Kristofer B. Heefner, Phyllis Hestnes, Lisa J. Hoge, Tawanda M. Jacobs, John Leif Jørgensen, Michael A. Kaiser, James W. Kellogg, Steven Kenyon, Richard Koenecke, Robert Kozon, Beverly LaMarr, Mike D. Lambertson, Anne M. Larson, Steven Lentine, Jesse Lewis, Michael G. Lilly, Kuochia Alice Liu, Andrew Malonis, Sridhar S. Manthripragada, Craig B. Markwardt, Bryan D. Matonak, Isaac E. Mcginnis, Roger L. Miller, Alissa L. Mitchell, Jason W. Mitchell, Jelila S. Mohammed, Charles Monroe, K Garcia, Peter Mule, Louis T. Nagao, Son N. Ngo, Eric D. Norris, Dwight A. Norwood, Joseph Novotka, Takashi Okajima, L. Olsen, Chimaobi O. Onyeachu, Henry Y. Orosco, Jacqualine R. Peterson, Kristina N. Pevear, Karen K. Pham, Sue E. Pollard, John S. Pope, Daniel Powers, Charles E. Powers, Samuel R. Price, Gregory Y. Prigozhin, Julian B. Ramirez, Winston J. Reid, Ronald A. Remillard, Eric M. Rogstad, Glenn P. Rosecrans, John N. Rowe, Jennifer A. Sager, Claude A. Sanders, Bruce Savadkin, Maxine R. Saylor, Alexander F. Schaeffer, Nancy S. Schweiss, Sean R. Semper, Peter J. Serlemitsos, Larry V. Shackelford, Yang Soong, Jonathan Struebel, Michael Vezie, Joel Villasenor, Luke Winternitz, George I. Wofford, Michael R. Wright, Mike Y. Yang, and Wayne H. Yu. The neutron star interior composition explorer (nicer): design and development. *SPIE Proceedings*, 9905:420–435, July 2016. .

P. Ghosh and F. K. Lamb. Accretion by rotating magnetic neutron stars. II. Radial and vertical structure of the transition zone in disk accretion. *Astrophysical Journal*, 232:259–276, August 1979a. .

P. Ghosh and F. K. Lamb. Accretion by rotating magnetic neutron stars. III. Accretion torques and period changes in pulsating X-ray sources. *Astrophysical Journal*, 234:296–316, November 1979b. .

P. Ghosh, F. K. Lamb, and C. J. Pethick. Accretion by rotating magnetic neutron stars. I. Flow of matter inside the magnetosphere and its implications for spin-up and spin-down of the star. *Astrophysical Journal*, 217:578–596, October 1977. .

M. Gilfanov. X-Ray Emission from Black-Hole Binaries. In Tomaso Belloni, editor, *Lecture Notes in Physics, Berlin Springer Verlag*, volume 794, page 17. 2010. .

M. Gilfanov, M. Revnivtsev, R. Sunyaev, and E. Churazov. The millisecond X-ray pulsar/burster SAX J1808.4-3658: the outburst light curve and the power law spectrum. *Astronomy and Astrophysics*, 338:L83–L86, 10 1998.

F. Giovannelli. The Golden Age of Cataclysmic Variables and Related Objects (A Very Personal Review). In *The Golden Age of Cataclysmic Variables and Related Objects IV*, page 1, September 2017. .

Patrick Godon, Edward M. Sion, Fuhua Cheng, Boris T. Gänsicke, Steve Howell, Christian Knigge, Warren M. Sparks, and Sumner Starrfield. Modeling the Heating and Cooling of WZ Sagittae Following the 2001 July Outburst. *Astrophysical Journal*, 602(1):336–341, February 2004. .

J. E. Grove, W. N. Johnson, R. A. Kroeger, K. McNaron-Brown, J. G. Skibo, and B. F. Phlips. Gamma-Ray Spectral States of Galactic Black Hole Candidates. *Astrophysical Journal*, 500(2): 899–908, June 1998. .

J. Guan, L. Tao, J. L. Qu, S. N. Zhang, W. Zhang, S. Zhang, R. C. Ma, M. Y. Ge, L. M. Song, F. J. Lu, T. P. Li, Y. P. Xu, Y. Chen, X. L. Cao, C. Z. Liu, L. Zhang, Y. N. Wang, Y. P. Chen, Q. C. Bu, C. Cai, Z. Chang, L. Chen, T. X. Chen, Y. B. Chen, W. W. Cui, Y. Y. Du, G. H. Gao, H. Gao, Y. D. Gu, C. C. Guo, D. W. Han, Y. Huang, J. Huo, S. M. Jia, W. C. Jiang, J. Jin, L. D. Kong, B. Li, C. K. Li, G. Li, W. Li, X. Li, X. B. Li, X. F. Li, Z. W. Li, X. H. Liang, J. Y. Liao, B. S. Liu, H. W. Liu, H. X. Liu, X. J. Liu, X. F. Lu, Q. Luo, T. Luo, X. Ma, B. Meng, Y. Nang, J. Y. Nie, G. Ou, X. Q. Ren, N. Sai, X. Y. Song, L. Sun, Y. Tan, C. Wang, L. J. Wang, P. J. Wang, W. S. Wang, Y. S. Wang, X. Y. Wen, B. B. Wu, B. Y. Wu, M. Wu, G. C. Xiao, S. Xiao, S. L. Xiong, R. J. Yang, S. Yang, Y. J. Yang, Y. J. Yang, Q. B. Yi, Q. Q. Yin, Y. You, F. Zhang, H. M. Zhang, J. Zhang, P. Zhang, W. C. Zhang, Y. F. Zhang, Y. H. Zhang, H. S. Zhao, X. F. Zhao, S. J. Zheng, Y. G. Zheng, and D. K. Zhou. Physical origin of the non-physical spin evolution of MAXI J1820 + 070. *Monthly Notices of the Royal Astronomical Society*, 504(2):2168–2180, June 2021. .

J. M. Hameury. A review of the disc instability model for dwarf novae, soft X-ray transients and related objects. *Advances in Space Research*, 66(5):1004–1024, 09 2020. .

J. M. Hameury and J. P. Lasota. Anomalous Z Cam stars: a response to mass-transfer outbursts. *Astronomy and Astrophysics*, 569:A48, September 2014. .

J. M. Hameury and J. P. Lasota. Dwarf nova outbursts in intermediate polars. *Astronomy and Astrophysics*, 602:A102, June 2017. .

J. M. Hameury and J. P. Lasota. Modelling rebrightenings, reflares, and echoes in dwarf nova outbursts. *Astronomy and Astrophysics*, 650:A114, June 2021. .

J. M. Hameury, J. P. Lasota, and J. M. Huré. A model for WZ SGE with 'standard' values of alpha. *Monthly Notices of the Royal Astronomical Society*, 287(4):937–940, 06 1997. .

J. M. Hameury, J. P. Lasota, C. Knigge, and E. G. Körding. Hystereses in dwarf nova outbursts and low-mass X-ray binaries. *Astronomy and Astrophysics*, 600:A95, April 2017. .

Jean-Marie Hameury, Kristen Menou, Guillaume Dubus, Jean-Pierre Lasota, and Jean-Marc Hure. Accretion disc outbursts: a new version of an old model. *Monthly Notices of the Royal Astronomical Society*, 298(4):1048–1060, August 1998. .

Jean-Marie Hameury, Jean-Pierre Lasota, and Brian Warner. The zoo of dwarf novae: illumination, evaporation and disc radius variation. *Astronomy and Astrophysics*, 353:244–252, 01 2000.

R. J. Harms, E. Beaver, E. M. Burbidge, R. Angel, F. Bartko, W. Bloomquist, J. C. Flemming, R. Bohlin, A. F. Davidsen, and H. Ford. Faint-object spectrograph for Space Telescope. In C. L. Wyman, editor, *Space optics*, volume 183 of *Society of Photo-Optical Instrumentation Engineers (SPIE) Conference Series*, pages 74–87, January 1979. .

C. A. Haswell, R. I. Hynes, A. R. King, and K. Schenker. The ultraviolet line spectrum of the soft X-ray transient XTE J1118+480: a CNO-processed core exposed. *Monthly Notices of the Royal Astronomical Society*, 332(4):928–932, June 2002. .

Coel Hellier. *Cataclysmic Variable Stars*. 2001.

Coel Hellier and A. P. Beardmore. The accretion flow in the discless intermediate polar V2400 Ophiuchi. *Monthly Notices of the Royal Astronomical Society*, 331(2):407–416, March 2002. .

Juan Venancio Hernández Santisteban. *Multi-wavelength Observations of Accreting Compact Objects*. PhD thesis, University of Southampton, November 2016.

HI4PI Collaboration, N. Ben Bekhti, L. Flöer, R. Keller, J. Kerp, D. Lenz, B. Winkel, J. Bailin, M. R. Calabretta, L. Dedes, H. A. Ford, B. K. Gibson, U. Haud, S. Janowiecki, P. M. W. Kalberla, F. J. Lockman, N. M. McClure-Griffiths, T. Murphy, H. Nakanishi, D. J. Pisano, and L. Staveley-Smith. HI4PI: A full-sky H I survey based on EBHIS and GASS. *Astronomy and Astrophysics*, 594:A116, October 2016. .

N. Higginbottom, D. Proga, C. Knigge, and K. S. Long. Thermal Disk Winds in X-Ray Binaries: Realistic Heating and Cooling Rates Give Rise to Slow, but Massive, Outflows. *Astrophysical Journal*, 836(1):42, February 2017. .

Nick Higginbottom, Christian Knigge, Knox S. Long, James H. Matthews, Stuart A. Sim, and Henrietta A. Hewitt. Radiation-hydrodynamic simulations of thermally driven disc winds in X-ray binaries: a direct comparison to GRO J1655-40. *Monthly Notices of the Royal Astronomical Society*, 479(3):3651–3662, September 2018. .

Nick Higginbottom, Christian Knigge, Knox S. Long, James H. Matthews, and Edward J. Parkinson. The luminosity dependence of thermally driven disc winds in low-mass X-ray binaries. *Monthly Notices of the Royal Astronomical Society*, 484(4):4635–4644, April 2019. .

Nick Higginbottom, Christian Knigge, Stuart A. Sim, Knox S. Long, James H. Matthews, Henrietta A. Hewitt, Edward J. Parkinson, and Sam W. Mangham. Thermal and radiation driving can produce observable disc winds in hard-state X-ray binaries. *Monthly Notices of the Royal Astronomical Society*, 492(4):5271–5279, March 2020. .

Shigenobu Hirose, Omer Blaes, Julian H. Krolik, Matthew S. B. Coleman, and Takayoshi Sano. Convection Causes Enhanced Magnetic Turbulence in Accretion Disks in Outburst. *Astrophysical Journal*, 787(1):1, May 2014. .

J. Homan, A. L. Stevens, D. Altamirano, K. Gendreau, Z. Arzoumanian, T. E. Strohmayer, P. Uttley, E. M. Cackett, E. Kara, Dheeraj R. Pasham, and Nicer Team. MAXI J1820+070 continuing its rapid evolution toward the hard state. *The Astronomer's Telegram*, 12068:1, September 2018a.

J. Homan, P. Uttley, K. Gendreau, Z. Arzoumanian, M. Saylor, J. F. Steiner, D. Pasham, A. L. Stevens, D. Altamirano, E. Kara. A. C. Fabian, S. Eikenberry, and Nicer Team. Continuing NICER observations of the state transition in ASASSN-18ey/MAXI J1820+070. *The Astronomer's Telegram*, 11823:1, July 2018b.

J. Homan, P. Uttley, K. Gendreau, Z. Arzoumanian, M. Saylor, J. F. Steiner, D. Pasham, A. L. Stevens, D. Altamirano, E. Kara, A. C. Fabian, and Nicer Team. A rapid state transition in MAXI J1820+070. *The Astronomer's Telegram*, 11820:1, July 2018c.

Jeroen Homan and Tomaso Belloni. The Evolution of Black Hole States. *Astrophysics and Space Science*, 300(1-3):107–117, November 2005.

Jeroen Homan, Rudy Wijnands, Michiel van der Klis, Tomaso Belloni, Jan van Paradijs, Marc Klein-Wolt, Rob Fender, and Mariano Méndez. Correlated X-Ray Spectral and Timing Behavior of the Black Hole Candidate XTE J1550-564: A New Interpretation of Black Hole States. *Astrophysical Journal, Supplement*, 132(2):377–402, February 2001. .

Jeroen Homan, Joseph Neilsen, Jessamyn L. Allen, Deepto Chakrabarty, Rob Fender, Joel K. Fridriksson, Ronald A. Remillard, and Norbert Schulz. Evidence for Simultaneous Jets and Disk Winds in Luminous Low-mass X-Ray Binaries. *Astrophysical Journal, Letters*, 830(1):L5, October 2016. .

Jeroen Homan, Joe Bright, Sara E. Motta, Diego Altamirano, Zaven Arzoumanian, Arkadip Basak, Tomaso M. Belloni, Edward M. Cackett, Rob Fender, Keith C. Gendreau, Erin Kara, Dheeraj R. Pasham, Ronald A. Remillard, James F. Steiner, Abigail L. Stevens, and Phil Uttley. A Rapid Change in X-Ray Variability and a Jet Ejection in the Black Hole Transient MAXI J1820+070. *Astrophysical Journal, Letters*, 891(2):L29, March 2020. .

Keith Horne, T. R. Marsh, F. H. Cheng, Ivan Hubeny, and Theirry Lanz. HST Eclipse Mapping of Dwarf Nova OY Carinae in Quiescence: an "Fe II Curtain" with Mach 6 Velocity Dispersion Veils the White Dwarf. *Astrophysical Journal*, 426:294, May 1994. .

Ivan Hubeny and Thierry Lanz. A brief introductory guide to TLUSTY and SYNSPEC. *arXiv e-prints*, art. arXiv:1706.01859, June 2017.

R. I. Hynes. The Optical and Ultraviolet Spectral Energy Distributions of Short-Period Black Hole X-Ray Transients in Outburst. *Astrophysical Journal*, 623(2):1026–1043, April 2005. .

R. I. Hynes, C. A. Haswell, W. Cui, C. R. Shrader, K. O'Brien, S. Chaty, D. R. Skillman, J. Patterson, and Keith Horne. The remarkable rapid X-ray, ultraviolet, optical and infrared variability in the black hole XTE J1118+480. *Monthly Notices of the Royal Astronomical Society*, 345(1):292–310, October 2003. .

Jr. Iben, Icko and A. V. Tutukov. On the Evolution of Symbiotic Stars and Other Binaries with Accreting Degenerate Dwarfs. *Astrophysical Journal, Supplement*, 105:145, July 1996. .

A. F. Illarionov and R. A. Sunyaev. Why the Number of Galactic X-ray Stars Is so Small? *Astronomy and Astrophysics*, 39:185, February 1975.

Akira Imada, Hideyuki Izumiura, Daisuke Kuroda, Kenshi Yanagisawa, Nobuyuki Kawai, Toshihiro Omodaka, and Ryo Miyanoshita. Discovery of Superhumps during a Normal Outburst of SU Ursae Majoris. *Publications of the Astronomical Society of Japan*, 64:L5, October 2012. .

Adam Ingram, Chris Done, and P. Chris Fragile. Low-frequency quasi-periodic oscillations spectra and Lense-Thirring precession. *Monthly Notices of the Royal Astronomical Society*, 397(1):L101–L105, July 2009. .

Adam R. Ingram and Sara E. Motta. A review of quasi-periodic oscillations from black hole X-ray binaries: Observation and theory. *New Astronomy Review*, 85:101524, September 2019. .

P. B. Isakova, N. R. Ikhsanov, A. G. Zhilkin, D. V. Bisikalo, and N. G. Beskrovnaya. Features of the matter flows in the peculiar cataclysmic variable AE Aquarii. *Astronomy Reports*, 60(5):498–508, May 2016. .

R. Ishioka, M. Uemura, K. Matsumoto, H. Ohashi, T. Kato, G. Masi, R. Novak, J. Pietz, B. Martin, D. Starkey, S. Kiyota, A. Oksanen, M. Moilanen, L. Cook, L. Kral, T. Hynek, M. Kolasa, T. Vanmunster, M. Richmond, J. Kern, S. Davis, D. Crabtree, K. Beaulieu, T. Davis, M. Aggleton, K. Gazeas, P. Niarchos, A. Yushchenko, F. Mallia, M. Fiaschi, G. A. Good, D. Boyd, Y. Sano, K. Morikawa, M. Moriyama, R. Mennickent, J. Arenas, T. Ohshima, and T. Watanabe. First detection of the growing humps at the rapidly rising stage of dwarf novae AL Com and WZ Sge. *Astronomy and Astrophysics*, 381:L41–L44, jan 2002. .

Ryoko Ishioka, Taichi Kato, Makoto Uemura, Jochen Pietz, Tonny Vanmunster, Tom Krajci, Ken'ichi Torii, Kenji Tanabe, Seiichiro Kiyota, Kenzo Kinugasa, Gianluca Masi, Koichi Morikawa, Lewis M. Cook, Patrick Schmeer, and Hitoshi Yamaoka. Period Change of Superhumps in a WZ Sge-Type Dwarf Nova, HV Virginis. *Publications of the Astronomical Society of Japan*, 55:683–690, June 2003. .

N. Ivanova, S. Justham, X. Chen, O. De Marco, C. L. Fryer, E. Gaburov, H. Ge, E. Glebbeek, Z. Han, X. D. Li, G. Lu, T. Marsh, P. Podsiadlowski, A. Potter, N. Soker, R. Taam, T. M. Tauris, E. P. J. van den Heuvel, and R. F. Webbink. Common envelope evolution: where we stand and how we can move forward. *Astronomy and Astrophysics Reviews*, 21:59, February 2013. .

Natalia Ivanova, Stephen Justham, and Paul Ricker. *Common Envelope Evolution*. 2020. .

H. Th. Janka, K. Langanke, A. Marek, G. Martínez-Pinedo, and B. Müller. Theory of core-collapse supernovae. *Physics Reports*, 442(1-6):38–74, April 2007. .

Hans-Thomas Janka. Explosion Mechanisms of Core-Collapse Supernovae. *Annual Review of Nuclear and Particle Science*, 62(1):407–451, November 2012. .

F. Jiménez-Ibarra, T. Muñoz-Darias, J. Casares, M. Armas Padilla, and J. M. Corral-Santana. An equatorial outflow in the black hole optical dipper Swift J1357.2-0933. *Monthly Notices of the Royal Astronomical Society*, 489(3):3420–3426, November 2019. .

S. Jones, R. Hirschi, K. Nomoto, T. Fischer, F. X. Timmes, F. Herwig, B. Paxton, H. Toki, T. Suzuki, G. Martínez-Pinedo, Y. H. Lam, and M. G. Bertolli. Advanced Burning Stages and Fate of 8-10 M $_\odot$ Stars. *Astrophysical Journal*, 772(2):150, August 2013. .

Wenhua Ju, James M. Stone, and Zhaohuan Zhu. Global MHD Simulations of Accretion Disks in Cataclysmic Variables. I. The Importance of Spiral Shocks. *Astrophysical Journal*, 823(2):81, June 2016. .

Wenhua Ju, James M. Stone, and Zhaohuan Zhu. Global MHD Simulations of Accretion Disks in Cataclysmic Variables (CVs). II. The Relative Importance of MRI and Spiral Shocks. *Astrophysical Journal*, 841(1):29, May 2017. .

Vassiliki Kalogera and Gordon Baym. The Maximum Mass of a Neutron Star. *Astrophysical Journal, Letters*, 470:L61, October 1996. .

E. Kara, J. F. Steiner, A. C. Fabian, E. M. Cackett, P. Uttley, R. A. Remillard, K. C. Gendreau, Z. Arzoumanian, D. Altamirano, S. Eikenberry, T. Enoto, J. Homan, J. Neilsen, and A. L. Stevens. The corona contracts in a black-hole transient, January 2019. URL https://eprints.soton.ac.uk/427946/.

Amanda I. Karakas and John C. Lattanzio. The Dawes Review 2: Nucleosynthesis and Stellar Yields of Low- and Intermediate-Mass Single Stars. *Publications of the Astronomical Society of Australia*, 31:e030, July 2014. .

S. Katajainen, O. Butters, A. J. Norton, H. J. Lehto, V. Piirola, and A. Berdyugin. Discovery of Polarized Emission from Two Soft X-ray-emitting Intermediate Polars: UU Col and NY Lup. *Astrophysical Journal*, 724(1):165–170, November 2010. .

T. Kato. WZ Sge-type dwarf novae. *Publications of the Astronomical Society of Japan*, 67:108, dec 2015. .

Taichi Kato. Three Z Camelopardalis-type dwarf novae exhibiting IW Andromedae-type phenomenon. *Publications of the Astronomical Society of Japan*, 71(1):20, January 2019. .

Taichi Kato and Yoji Osaki. Analysis of Three SU UMa-Type Dwarf Novae in the Kepler Field. *Publications of the Astronomical Society of Japan*, 65:97, October 2013. .

Taichi Kato, Makoto Uemura, Ryoko Ishioka, Daisaku Nogami, Chatief Kunjaya, Hajime Baba, and Hitoshi Yamaoka. Variable Star Network: World Center for Transient Object Astronomy and Variable Stars. *Publications of the Astronomical Society of Japan*, 56:S1–S54, March 2004. .

T. Kawamuro, H. Negoro, T. Yoneyama, S. Ueno, H. Tomida, M. Ishikawa, Y. Sugawara, N. Isobe, R. Shimomukai, T. Mihara, M. Sugizaki, S. Nakahira, W. Iwakiri, F. Yatabe, Y. Takao, M. Matsuoka, N. Kawai, S. Sugita, T. Yoshii, Y. Tachibana, S. Harita, K. Morita, A. Yoshida, T. Sakamoto, M. Serino, Y. Kawakubo, Y. Kitaoka, T. Hashimoto, H. Tsunemi, M. Nakajima, T. Kawase, A. Sakamaki, W. Maruyama, Y. Ueda, T. Hori, A. Tanimoto, S. Oda, T. Morita, S. Yamada, Y. Tsuboi, Y. Nakamura, R. Sasaki, H. Kawai, T. Sato, M. Yamauchi, C. Hanyu, K. Hidaka, K. Yamaoka, and M. Shidatsu. MAXI/GSC detection of a probable new X-ray transient MAXI J1820+070. *The Astronomer's Telegram*, 11399:1, March 2018.

Mukremin Kilic, K. Z. Stanek, and M. H. Pinsonneault. The Future Is Now: The Formation of Single Low-Mass White Dwarfs in the Solar Neighborhood. *Astrophysical Journal*, 671(1):761–766, December 2007. .

R. A. Kimble, B. E. Woodgate, C. W. Bowers, S. B. Kraemer, M. E. Kaiser, T. R. Gull, S. R. Heap, A. C. Danks, A. Boggess, R. F. Green, J. B. Hutchings, E. B. Jenkins, C. L. Joseph, J. L. Linsky, S. P. Maran, H. W. Moos, F. Roesler, J. G. Timothy, D. E. Weistrop, J. F. Grady, J. J. Loiacono, L. W. Brown, M. D. Brumfield, D. A. Content, L. D. Feinberg, M. N. Isaacs, C. A. Krebs, V. L. Krueger, R. W. Melcher, F. J. Rebar, H. D. Vitagliano, J. J. Yagelowich, W. W. Meyer, D. F. Hood, V. S. Argabright, S. I. Becker, M. Bottema, R. R. Breyer, R. L. Bybee, P. R. Christon, A. W. Delamere, D. A. Dorn, S. Downey, P. A. Driggers, D. C. Ebbets, J. S. Gallegos, H. Garner, J. C. Hetlinger, R. L. Lettieri, C. W. Ludtke, D. Michika, R. Nyquist, D. M. Rose, R. B. Stocker, J. F. Sullivan, C. N. Van Houten, R. A. Woodruff, S. A. Baum, G. F. Hartig, V. Balzano, C. Biagetti, J. C. Blades, R. C. Bohlin, M. Clampin, R. Doxsey, H. C. Ferguson, P. Goudfrooij, S. J. Hulbert, R. Kutina, M. McGrath, D. J. Lindler, T. L. Beck, J. K. Feggans, P. C. Plait, J. L. Sandoval, R. S. Hill, N. R. Collins, R. H. Cornett, W. B. Fowler, R. J. Hill, W. B. Landsman, E. M. Malumuth, C. Standley, M. Blouke, A. Grusczak, R. Reed, R. D. Robinson, J. A. Valenti, and T. Wolfe. The On-Orbit Performance of the Space Telescope Imaging Spectrograph. *Astrophysical Journal, Letters*, 492(2): L83–L93, January 1998. .

A. R. King and H. Ritter. The light curves of soft X-ray transients. *Monthly Notices of the Royal Astronomical Society*, 293(1):L42–L48, January 1998. .

C. Knigge, R. I. Hynes, D. Steeghs, K. S. Long, S. Araujo-Betancor, and T. R. Marsh. Discovery of 15 second oscillations in [ITAL]hubble space telescope[/ITAL] observations of WZ sagittae following the 2001 outburst. *Astrophysical Journal*, 580(2):L151–L155, 12 2002. .

Christian Knigge. The donor stars of cataclysmic variables. *Monthly Notices of the Royal Astronomical Society*, 373(2):484–502, December 2006. .

Christian Knigge, Knox S. Long, William P. Blair, and Richard A. Wade. Disks, Winds, and Veiling Curtains: Dissecting the Ultraviolet Spectrum of the Dwarf Nova Z Camelopardalis in Outburst. *Astrophysical Journal*, 476(1):291–310, February 1997. .

Christian Knigge, Knox S. Long, Richard A. Wade, Raymundo Baptista, Keith Horne, Ivan Hubeny, and René G. M. Rutten. Hubble Space Telescope Eclipse Observations of the Nova-like Cataclysmic Variable UX Ursae Majoris. *Astrophysical Journal*, 499(1):414–428, May 1998. .

Christian Knigge, Isabelle Baraffe, and Joseph Patterson. The Evolution of Cataclysmic Variables as Revealed by Their Donor Stars. *Astrophysical Journal, Supplement*, 194(2):28, June 2011. .

K. I. I. Koljonen, K. S. Long, J. H. Matthews, and C. Knigge. The origin of optical emission lines in the soft state of X-ray binary outbursts: the case of MAXI J1820+070. *Monthly Notices of the Royal Astronomical Society*, 521(3):4190–4206, May 2023. .

Elmar Körding, Michael Rupen, Christian Knigge, Rob Fender, Vivek Dhawan, Matthew Templeton, and Tom Muxlow. A Transient Radio Jet in an Erupting Dwarf Nova. *Science*, 320(5881): 1318, June 2008. .

Robert P. Kraft. Studies of Stellar Rotation. V. The Dependence of Rotation on Age among Solar-Type Stars. *Astrophysical Journal*, 150:551, November 1967. .

Robert P. Kraft, Jon Mathews, and Jesse L. Greenstein. Binary Stars among Cataclysmic Variables. II. Nova WZ Sagittae: a Possible Radiator of Gravitational Waves. *Astrophysical Journal*, 136: 312–315, July 1962. .

H. A. Krimm, S. T. Holland, R. H. D. Corbet, A. B. Pearlman, P. Romano, J. A. Kennea, J. S. Bloom, S. D. Barthelmy, W. H. Baumgartner, J. R. Cummings, N. Gehrels, A. Y. Lien, C. B. Markwardt, D. M. Palmer, T. Sakamoto, M. Stamatikos, and T. N. Ukwatta. The Swift/BAT Hard X-Ray Transient Monitor. *Astrophysical Journal, Supplement*, 209(1):14, November 2013. .

Pavel Kroupa. On the variation of the initial mass function. *Monthly Notices of the Royal Astronomical Society*, 322(2):231–246, April 2001. .

W. Krzeminski. Nova WZ Sagittae: an Extremely Short-Period Eclipsing Binary. *Publications of the Astronomical Society of the Pacific*, 74(436):66, February 1962. .

Shrabani Kumar, G. C. Dewangan, K. P. Singh, P. Gandhi, I. E. Papadakis, P. Tripathi, and L. Mallick. Far-ultraviolet Spectroscopy of Active Galactic Nuclei with ASTROSAT/UVIT. *Astrophysical Journal*, 950(2):90, June 2023. .

E. Kuulkers, A. A. Henden, R. K. Honeycutt, W. Skidmore, E. O. Waagen, and G. A. Wynn. Secular changes in the quiescence of WZ Sagittae: the development of a cavity in the inner disk. *Astronomy and Astrophysics*, 528:A152, April 2011. .

D. Q. Lamb and A. R. Masters. X and UV radiation from accreting magnetic degenerate dwarfs. *Astrophysical Journal, Letters*, 234:L117–L122, December 1979. .

L Landau and E Lifshitz. The classical theory of fields (reading, mass.; addison, 1951.

J.-P. Lasota. The disc instability model of dwarf novae and low-mass x-ray binary transients. *New Astronomy Review*, 45:449, 06 2001. .

J. P. Lasota, J. M. Hameury, and J. M. Huré. Dwarf novae at low mass transfer rates. *Astronomy and Astrophysics*, 302:L29, 10 1995.

J. P. Lasota, E. Kuulkers, and P. Charles. WZ Sagittae as a DQ Herculis star. *Monthly Notices of the Royal Astronomical Society*, 305(2):473–480, 04 1999. .

Shing-Chi Leung, Ken'ichi Nomoto, and Tomoharu Suzuki. Electron-capture Supernovae of Super-AGB Stars: Sensitivity on Input Physics. *Astrophysical Journal*, 889(1):34, January 2020. .

D. N. C. Lin and J. Papaloizou. Tidal torques on accretion discs in binary systems with extreme mass ratios. *Monthly Notices of the Royal Astronomical Society*, 186:799–812, March 1979. .

Harvey Liszt. N(H I)/E(B - V). *Astrophysical Journal*, 780(1):10, January 2014. .

D. Liu, B. Wang, H. Ge, X. Chen, and Z. Han. The progenitors of type-Ia supernovae in semidetached binaries with red giant donors. *Astronomy and Astrophysics*, 622:A35, February 2019. .

W. M. Liu, L. Yungelson, and A. Kuranov. He-star donor AM CVn stars and their progenitors as LISA sources. *Astronomy and Astrophysics*, 668:A80, December 2022. .

M. Livio and J. E. Pringle. Dwarf nova outbursts - the ultraviolet delay and the effect of a weakly magnetized white dwarf. *Monthly Notices of the Royal Astronomical Society*, 259:23P, 12 1992.

Mario Livio and Noam Soker. The Common Envelope Phase in the Evolution of Binary Stars. *Astrophysical Journal*, 329:764, June 1988. .

K. S. Long, C. S. Froning, B. Gänsicke, C. Knigge, E. M. Sion, and P. Szkody. WZ Sagittae: FUSE Spectroscopy of the 2001 Outburst. *Astrophysical Journal*, 591(2):1172–1183, jul 2003. .

Knox S. Long, Edward M. Sion, Boris T. Gänsicke, and Paula Szkody. WZ Sagittae: Hubble Space Telescope Spectroscopy of the Cooling of the White Dwarf after the 2001 Outburst. *Astrophysical Journal*, 602(2):948–959, 02 2004. .

M. Long, M. M. Romanova, and R. V. E. Lovelace. Locking of the Rotation of Disk-Accreting Magnetized Stars. *Astrophysical Journal*, 634(2):1214–1222, December 2005. .

R. V. E. Lovelace, M. M. Romanova, and G. S. Bisnovatyi-Kogan. Spin-up/spin-down of magnetized stars with accretion discs and outflows. *Monthly Notices of the Royal Astronomical Society*, 275(2):244–254, July 1995. .

Xiang Ma, Lian Tao, Shuang-Nan Zhang, Liang Zhang, Qing-Cui Bu, Ming-Yu Ge, Yu-Peng Chen, Jin-Lu Qu, Shu Zhang, Fang-Jun Lu, Li-Ming Song, Yi-Jung Yang, Feng Yuan, Ce Cai, Xue-Lei Cao, Zhi Chang, Gang Chen, Li Chen, Tian-Xiang Chen, Yi-Bao Chen, Yong Chen, Wei Cui, Wei-Wei Cui, Jing-Kang Deng, Yong-Wei Dong, Yuan-Yuan Du, Min-Xue Fu, Guan-Hua Gao, He Gao, Min Gao, Yu-Dong Gu, Ju Guan, Cheng-Cheng Guo, Da-Wei Han, Yue Huang, Jia Huo, Long Ji, Shu-Mei Jia, Lu-Hua Jiang, Wei-Chun Jiang, Jing Jin, Yong-Jie Jin, Ling-Da Kong, Bing Li, Cheng-Kui Li, Gang Li, Mao-Shun Li, Ti-Pei Li, Wei Li, Xian Li, Xiao-Bo Li, Xu-Fang Li, Yan-Guo Li, Zheng-Wei Li, Xiao-Hua Liang, Jin-Yuan Liao, Bai-Sheng Liu, Cong-Zhan Liu, Guo-Qing Liu, Hong-Wei Liu, Xiao-Jing Liu, Yi-Nong Liu, Bo Lu, Xue-Feng Lu, Qi Luo, Tao Luo, Bin Meng, Yi Nang, Jian-Yin Nie, Ge Ou, Na Sai, Ren-Cheng Shang, Xin-Ying Song, Liang Sun, Ying Tan, Yuo-Li Tuo, Chen Wang, Guo-Feng Wang, Juan Wang, Ling-Jun Wang, Wen-Shuai Wang, Yu-Sa Wang, Xiang-Yang Wen, Bai-Yang Wu, Bo-Bing Wu, Mei Wu, Guang-Cheng Xiao, Shuo Xiao, Fu-Guo Xie, Shao-Lin Xiong, He Xu, Yu-Peng Xu, Jia-Wei Yang, Sheng Yang, Yan-Ji Yang, Qi-Bin Yi, Qian-Qing Yin, Yuan You, Ai-Mei Zhang, Cheng-Mo Zhang, Fan Zhang, Hong-Mei Zhang, Juan Zhang, Tong Zhang, Wan-Chang Zhang, Wei Zhang, Wen-Zhao Zhang, Yi Zhang, Yi-Fei Zhang, Yong-Jie Zhang, Yue Zhang, Zhao Zhang, Zhi Zhang, Zi-Liang Zhang, Hai-Sheng Zhao, Xiao-Fan Zhao, Shi-Jie Zheng, Deng-Ke Zhou, Jian-Feng Zhou, Yu-Xuan Zhu, Yue Zhu, and Ren-Lin Zhuang. Discovery of oscillations above 200 keV in a black hole X-ray binary with Insight-HXMT. *Nature Astronomy*, 5:94–102, January 2021. .

K. Makishima, Y. Maejima, K. Mitsuda, H. V. Bradt, R. A. Remillard, I. R. Tuohy, R. Hoshi, and M. Nakagawa. Simultaneous X-Ray and Optical Observations of GX 339-4 in an X-Ray High State. *Astrophysical Journal*, 308:635, September 1986. .

Dong-Ming Mao, Wen-Fei Yu, Ju-Jia Zhang, Zhen Yan, Stefano Rapisarda, Xiao-Feng Wang, and Jin-Ming Bai. Optical and X-Ray Observations of MAXI J1820+070 During the Early Outburst Phase in 2018: Zooming in the Low Frequency QPOs. *Research in Astronomy and Astrophysics*, 22(4):045009, April 2022. .

G. Marcel, J. Ferreira, P. O. Petrucci, S. Barnier, J. Malzac, A. Marino, M. Coriat, M. Clavel, C. Reynolds, J. Neilsen, R. Belmont, and S. Corbel. A unified accretion-ejection paradigm for black hole X-ray binaries. VI. Radiative efficiency and radio-X-ray correlation during four outbursts from GX 339-4. *Astronomy and Astrophysics*, 659:A194, March 2022. .

A. Marino, S. Barnier, P. O. Petrucci, M. Del Santo, J. Malzac, J. Ferreira, G. Marcel, A. Segreto, S. E. Motta, A. D'Aì, T. Di Salvo, S. Guillot, and T. D. Russell. Tracking the evolution of the accretion flow in MAXI J1820+070 during its hard state with the JED-SAD model. *Astronomy and Astrophysics*, 656:A63, December 2021. .

S. Markoff, H. Falcke, and R. Fender. A jet model for the broadband spectrum of XTE J1118+480. Synchrotron emission from radio to X-rays in the Low/Hard spectral state. *Astronomy and Astrophysics*, 372:L25–L28, June 2001. .

S. Markoff, M. Nowak, S. Corbel, R. Fender, and H. Falcke. Exploring the role of jets in the radio/X-ray correlations of GX 339-4. *Astronomy and Astrophysics*, 397:645–658, January 2003.

T. R. Marsh, V. S. Dhillon, and S. R. Duck. Low-Mass White Dwarfs Need Friends - Five New Double-Degenerate Close Binary Stars. *Monthly Notices of the Royal Astronomical Society*, 275: 828, August 1995. .

D. Mata Sánchez, A. Rau, A. Álvarez Hernández, T. F. J. van Grunsven, M. A. P. Torres, and P. G. Jonker. Dynamical confirmation of a stellar mass black hole in the transient X-ray dipping binary MAXI J1305-704. *Monthly Notices of the Royal Astronomical Society*, 506(1):581–594, September 2021. .

J. H. Matthews, C. Knigge, K. S. Long, S. A. Sim, and N. Higginbottom. The impact of accretion disc winds on the optical spectra of cataclysmic variables. *Monthly Notices of the Royal Astronomical Society*, 450(3):3331–3344, July 2015. .

O. M. Matthews, R. Speith, G. A. Wynn, and R. G. West. Magnetically moderated outbursts of WZ Sagittae. *Monthly Notices of the Royal Astronomical Society*, 375(1):105–114, feb 2007. .

C. W. Mauche. Chandra Low Energy Transmission Grating Spectrum of SS Cygni in Outburst. *Astrophysical Journal*, 610(1):422–426, 07 2004.

Christopher W. Mauche. The white dwarf in AE Aqr brakes harder. *Monthly Notices of the Royal Astronomical Society*, 369(4):1983–1987, July 2006. .

Christopher W. Mauche, Y. Paul Lee, and Timothy R. Kallman. Ultraviolet Emission-line Ratios of Cataclysmic Variables. *Astrophysical Journal*, 477(2):832–847, March 1997. .

Margaret Walton Mayall. Nova Sagittarii 1913, 1946. *Harvard College Observatory Bulletin*, 918:3–5, December 1946.

P. J. Meintjes and O. C. de Jager. Propeller spin-down and the non-thermal emission from AE Aquarii. *Monthly Notices of the Royal Astronomical Society*, 311(3):611–620, January 2000. .

P. J. Meintjes, O. C. de Jager, B. C. Raubenheimer, H. I. Nel, A. R. North, D. A. H. Buckley, and C. Koen. Simultaneous Optical and TeV Gamma-Ray Observations of the Cataclysmic Variable AE Aquarii. *Astrophysical Journal*, 434:292, October 1994. .

I. A. Mereminskiy, S. A. Grebenev, S. V. Molkov, I. A. Zaznobin, G. A. Khorunzhev, R. A. Burenin, and M. V. Eselevich. Low-frequency QPOs in MAXI J1820+070 as seen by INTEGRAL/SPI. *The Astronomer's Telegram*, 11488:1, March 2018.

F. Meyer and E. Meyer-Hofmeister. Accretion disk evaporation by a coronal siphon flow. *Astronomy and Astrophysics*, 288:175–182, 08 1994.

F. Meyer and E. Meyer-Hofmeister. Su uma stars: Rebrightenings after superoutburst. *Publications of the Astronomical Society of Japan*, 67:52, 06 2015. .

S. Migliari and R. P. Fender. Jets in neutron star X-ray binaries: a comparison with black holes. *Monthly Notices of the Royal Astronomical Society*, 366(1):79–91, February 2006. .

Joanna Mikołajewska and Michael M. Shara. The Massive CO White Dwarf in the Symbiotic Recurrent Nova RS Ophiuchi. *Astrophysical Journal*, 847(2):99, October 2017. .

Joanna Mikołajewska, Andrzej A. Zdziarski, Janusz Ziółkowski, Manuel A. P. Torres, and Jorge Casares. The Donor of the Black Hole X-Ray Binary MAXI J1820+070. *Astrophysical Journal*, 930 (1):9, May 2022. .

J. M. Miller, J. Raymond, J. Homan, A. C. Fabian, D. Steeghs, R. Wijnands, M. Rupen, P. Charles, M. van der Klis, and W. H. G. Lewin. Simultaneous Chandra and RXTE Spectroscopy of the Microquasar H1743-322: Clues to Disk Wind and Jet Formation from a Variable Ionized Outflow. *Astrophysical Journal*, 646(1):394–406, July 2006a. .

J. M. Miller, J. Raymond, J. Homan, A. C. Fabian, D. Steeghs, R. Wijnands, M. Rupen, P. Charles, M. van der Klis, and W. H. G. Lewin. Simultaneous Chandra and RXTE Spectroscopy of the Microquasar H1743-322: Clues to Disk Wind and Jet Formation from a Variable Ionized Outflow. *Astrophysical Journal*, 646(1):394–406, July 2006b. .

J. M. Miller, J. Raymond, C. S. Reynolds, A. C. Fabian, T. R. Kallman, and J. Homan. The Accretion Disk Wind in the Black Hole GRO J1655-40. *Astrophysical Journal*, 680(2):1359–1377, June 2008. .

Jon M. Miller, John Raymond, Andy Fabian, Danny Steeghs, Jeroen Homan, Chris Reynolds, Michiel van der Klis, and Rudy Wijnands. The magnetic nature of disk accretion onto black holes. *Nature*, 441(7096):953–955, June 2006c. .

J. C. A. Miller-Jones, G. R. Sivakoff, D. Altamirano, M. Coriat, S. Corbel, V. Dhawan, H. A. Krimm, R. A. Remillard, M. P. Rupen, D. M. Russell, R. P. Fender, S. Heinz, E. G. Körding, D. Maitra, S. Markoff, S. Migliari, C. L. Sarazin, and V. Tudose. Disc-jet coupling in the 2009 outburst of the black hole candidate H1743-322. *Monthly Notices of the Royal Astronomical Society*, 421(1): 468–485, March 2012. .

James C. A. Miller-Jones, Arash Bahramian, Jerome A. Orosz, Ilya Mandel, Lijun Gou, Thomas J. Maccarone, Coenraad J. Neijssel, Xueshan Zhao, Janusz Ziółkowski, Mark J. Reid, Phil Uttley, Xueying Zheng, Do-Young Byun, Richard Dodson, Victoria Grinberg, Taehyun Jung, Jeong-Sook Kim, Benito Marcote, Sera Markoff, María J. Rioja, Anthony P. Rushton, David M. Russell, Gregory R. Sivakoff, Alexandra J. Tetarenko, Valeriu Tudose, and Joern Wilms. Cygnus X-1 contains a 21-solar mass black hole—Implications for massive star winds. *Science*, 371(6533): 1046–1049, March 2021. .

I. F. Mirabel and L. F. Rodríguez. A superluminal source in the Galaxy. *Nature*, 371(6492):46–48, September 1994. .

K. Mitsuda, H. Inoue, K. Koyama, K. Makishima, M. Matsuoka, Y. Ogawara, N. Shibazaki, K. Suzuki, Y. Tanaka, and T. Hirano. Energy spectra of low-mass binary X-ray sources observed from Tenma. *Publications of the Astronomical Society of Japan*, 36:741–759, January 1984.

Sigenori Miyamoto, Sayuri Iga, Shunji Kitamoto, and Yasuhide Kamado. Another Canonical Time Variation of X-Rays from Black Hole Candidates in the Very High Flare State? *Astrophysical Journal, Letters*, 403:L39, January 1993. .

C. Motch, S. A. Ilovaisky, and C. Chevalier. Discovery of fast optical activity in the X-ray source GX 339-4. *Astronomy and Astrophysics*, 109:L1–L4, May 1982.

C. Motch, M. J. Ricketts, C. G. Page, S. A. Ilovaisky, and C. Chevalier. Simultaneous X-ray/optical observations of GX 339-4 during the May 1981 optically bright state. *Astronomy and Astrophysics*, 119:171–176, March 1983.

S. Motta, T. Muñoz-Darias, P. Casella, T. Belloni, and J. Homan. Low-frequency oscillations in black holes: a spectral-timing approach to the case of GX 339-4. *Monthly Notices of the Royal Astronomical Society*, 418(4):2292–2307, December 2011. .

S. E. Motta. Quasi periodic oscillations in black hole binaries. *Astronomische Nachrichten*, 337(4-5): 398, May 2016. .

S. E. Motta, J. Bright, and R. Fender. Swift observes MAXI J1820+070 in transition from the soft to the hard-intermediate state. *The Astronomer's Telegram*, 12064:1, September 2018.

T. Muñoz-Darias, S. Motta, and T. M. Belloni. Fast variability as a tracer of accretion regimes in black hole transients. *Monthly Notices of the Royal Astronomical Society*, 410(1):679–684, January 2011. .

T. Muñoz-Darias, J. Casares, D. Mata Sánchez, R. P. Fender, M. Armas Padilla, M. Linares, G. Ponti, P. A. Charles, K. P. Mooley, and J. Rodriguez. Regulation of black-hole accretion by a disk wind during a violent outburst of V404 Cygni. *Nature*, 534(7605):75–78, June 2016. .

T. Muñoz-Darias, F. Jiménez-Ibarra, G. Panizo-Espinar, J. Casares, D. Mata Sánchez, G. Ponti, R. P. Fender, D. A. H. Buckley, P. Garnavich, M. A. P. Torres, M. Armas Padilla, P. A. Charles, J. M. Corral-Santana, J. J. E. Kajava, E. J. Kotze, C. Littlefield, J. Sánchez-Sierras, D. Steeghs, and J. Thomas. Hard-state Accretion Disk Winds from Black Holes: The Revealing Case of MAXI J1820+070. *Astrophysical Journal, Letters*, 879(1):L4, July 2019.

Teo Muñoz-Darias and Gabriele Ponti. Simultaneous X-ray and optical spectroscopy of V404 Cygni supports the multi-phase nature of X-ray binary accretion disc winds. *Astronomy and Astrophysics*, 664:A104, August 2022. .

Teo Muñoz-Darias, Manuel A. P. Torres, and Michael R. Garcia. The low-luminosity accretion disc wind of the black hole transient V4641 Sagittarii. *Monthly Notices of the Royal Astronomical Society*, 479(3):3987–3995, September 2018. .

Sneha Prakash Mudambi, Bari Maqbool, Ranjeev Misra, Sabhya Hebbar, J. S. Yadav, Shivappa B. Gudennavar, and Bubbly S. G. Unveiling the Temporal Properties of MAXI J1820+070 through AstroSat Observations. *Astrophysical Journal, Letters*, 889(1):L17, January 2020. .

K. Mukai. X-Ray Emissions from Accreting White Dwarfs: A Review. *Publications of the Astronomical Society of the Pacific*, 129(976):062001, June 2017. .

Chikako Nakata, Tomohito Ohshima, Taichi Kato, Daisaku Nogami, Gianluca Masi, Enrique de Miguel, Joseph Ulowetz, Colin Littlefield, William N. Goff, Thomas Krajci, Hiroyuki Maehara, William Stein, Richard Sabo, Ryo Noguchi, Rikako Ono, Miho Kawabata, Hisami Furukawa, Katsura Matsumoto, Takehiro Ishibashi, Pavol A. Dubovsky, Igor Kudzej, Shawn Dvorak, Franz-Josef Hambsch, Roger D. Pickard, Etienne Morelle, Eddy Muyllaert, Stefano Padovan, and Arne Henden. WZ Sge-Type Dwarf Novae with Multiple Rebrightenings: MASTER OT J211258.65+242145.4 and MASTER OT J203749.39+552210.3. *Publications of the Astronomical Society of Japan*, 65:117, December 2013. .

Ramesh Narayan and Insu Yi. Advection-dominated Accretion: A Self-similar Solution. *Astrophysical Journal, Letters*, 428:L13, June 1994. .

Ramesh Narayan and Insu Yi. Advection-dominated Accretion: Underfed Black Holes and Neutron Stars. *Astrophysical Journal*, 452:710, October 1995. .

H. Negoro, M. Nakajima, A. Sakamaki, W. Maruyama, T. Mihara, S. Nakahira, F. Yatabe, Y. Takao, M. Matsuoka, T. Sakamoto, M. Serino, S. Sugita, Y. Kawakubo, T. Hashimoto, A. Yoshida, N. Kawai, M. Sugizaki, Y. Tachibana, K. Morita, S. Ueno, H. Tomida, M. Ishikawa, Y. Sugawara, N. Isobe, R. Shimomukai, Y. Ueda, A. Tanimoto, T. Morita, S. Yamada, Y. Tsuboi, W. Iwakiri, R. Sasaki, H. Kawai, T. Sato, H. Tsunemi, T. Yoneyama, M. Yamauchi, K. Hidaka, S. Iwahori, T. Kawamuro, K. Yamaoka, and M. Shidatsu. MAXI/GSC detection of a rapid increase in the hard X-ray flux of MAXI J1820+070. *The Astronomer's Telegram*, 12057:1, September 2018.

Joseph Neilsen and Julia C. Lee. Accretion disk winds as the jet suppression mechanism in the microquasar GRS 1915+105. *Nature*, 458(7237):481–484, March 2009. .

G. Nelemans, F. Verbunt, L. R. Yungelson, and Simon F. Portegies Zwart. Reconstructing the evolution of double helium white dwarfs: envelope loss without spiral-in. *Astronomy and Astrophysics*, 360:1011–1018, August 2000. .

G. Nelemans, L. R. Yungelson, and S. F. Portegies Zwart. Short-period AM CVn systems as optical, X-ray and gravitational-wave sources. *Monthly Notices of the Royal Astronomical Society*, 349(1): 181–192, March 2004. .

Harry Nelson and Tim Nelson. *A Guide to Unbinned Maximum Likelihood Fits*. 1998.

Ulrich M. Noebauer, Knox S. Long, Stuart A. Sim, and Christian Knigge. The Geometry and Ionization Structure of the Wind in the Eclipsing Nova-like Variables RW Tri and UX UMa. *Astrophysical Journal*, 719(2):1932–1945, August 2010. .

K. Nomoto. Evolution of 8-10 solar mass stars toward electron capture supernovae. I - Formation of electron-degenerate O + NE + MG cores. *Astrophysical Journal*, 277:791–805, February 1984. .

Ken'ichi Nomoto. Evolution of 8–10 M_{sun} Stars toward Electron Capture Supernovae. II. Collapse of an O + NE + MG Core. *Astrophysical Journal*, 322:206, November 1987. .

I. D. Novikov and K. S. Thorne. Astrophysics of black holes. In *Black Holes (Les Astres Occlus)*, pages 343–450, January 1973.

Jerome A. Orosz, Jeffrey E. McClintock, Ramesh Narayan, Charles D. Bailyn, Joel D. Hartman, Lucas Macri, Jiefeng Liu, Wolfgang Pietsch, Ronald A. Remillard, Avi Shporer, and Tsevi Mazeh. A 15.65-solar-mass black hole in an eclipsing binary in the nearby spiral galaxy M 33. *Nature*, 449(7164):872–875, October 2007. .

Jerome A. Orosz, Danny Steeghs, Jeffrey E. McClintock, Manuel A. P. Torres, Ivan Bochkov, Lijun Gou, Ramesh Narayan, Michael Blaschak, Alan M. Levine, Ronald A. Remillard, Charles D. Bailyn, Morgan M. Dwyer, and Michelle Buxton. A New Dynamical Model for the Black Hole Binary LMC X-1. *Astrophysical Journal*, 697(1):573–591, May 2009. .

Jerome A. Orosz, James F. Steiner, Jeffrey E. McClintock, Michelle M. Buxton, Charles D. Bailyn, Danny Steeghs, Alec Guberman, and Manuel A. P. Torres. The Mass of the Black Hole in LMC X-3. *Astrophysical Journal*, 794(2):154, October 2014. .

Y. Osaki. A model for the superoutburst phenomenon of SU Ursae MAjoris stars. *Publications of the Astronomical Society of Japan*, 41:1005–1033, 01 1989.

Y. Osaki. A Model for WZ Sagittae-Type Dwarf Novae: SU UMa/WZ SGE Connection. *Publications of the Astronomical Society of Japan*, 47:47–58, 02 1995.

Y. Osaki. Dwarf-nova outbursts. *Publications of the Astronomical Society of the Pacific*, 108:39, 01 1996. .

Y. Osaki and T. Kato. A further study of superoutbursts and superhumps in SU UMa stars by the Kepler light curves of V1504 Cygni and V344 Lyrae. *Publications of the Astronomical Society of Japan*, 66(1):15, 02 2014.

Y. Osaki and F. Meyer. Early humps in WZ Sge stars. *Astronomy and Astrophysics*, 383:574–579, February 2002. .

Y. Osaki, F. Meyer, and E. Meyer-Hofmeister. Repetitive rebrightening of EG Cancri: Evidence for viscosity decay in the quiescent disk? *Astronomy and Astrophysics*, 370:488–495, May 2001. .

M. Özbey Arabacı, E. Kalemci, T. Dinçer, C. D. Bailyn, D. Altamirano, and T. Ak. Multiwavelength observations of MAXI J1820+070 during its outburst decay and subsequent mini-outburst. *Monthly Notices of the Royal Astronomical Society*, 514(3):3894–3909, August 2022. .

B. Paczyński. Gravitational Waves and the Evolution of Close Binaries. *Acta Astronomica*, 17:287, January 1967.

B. Paczyński. Evolutionary Processes in Close Binary Systems. *Annual Review of Astronomy and Astrophysics*, 9:183, January 1971. .

B. Paczynski. Common Envelope Binaries. In Peter Eggleton, Simon Mitton, and John Whelan, editors, *Structure and Evolution of Close Binary Systems*, volume 73 of *IAU Symposium*, page 75, January 1976.

K. L. Page and A. W. Shaw. X-Ray Emission Mechanisms in Accreting White Dwarfs. In *Handbook of X-ray and Gamma-ray Astrophysics*, page 107. 2022. .

J. A. Paice, P. Gandhi, T. Shahbaz, A. Veledina, J. Malzac, D. A. H. Buckley, P. A. Charles, K. Rajwade, V. S. Dhillon, S. P. Littlefair, T. R. Marsh, P. Uttley, F. M. Vincentelli, and R. Misra. The evolution of rapid optical/X-ray timing correlations in the initial hard state of MAXI J1820+070. *Monthly Notices of the Royal Astronomical Society*, 505(3):3452–3469, August 2021. .

A. F. Pala, B. T. Gänsicke, E. Breedt, C. Knigge, J. J. Hermes, N. P. Gentile Fusillo, M. A. Hollands, T. Naylor, I. Pelisoli, M. R. Schreiber, S. Toonen, A. Aungwerojwit, E. Cukanovaite, E. Dennihy, C. J. Manser, M. L. Pretorius, S. Scaringi, and O. Toloza. A Volume-limited Sample of Cataclysmic Variables from Gaia DR2: Space Density and Population Properties. *Monthly Notices of the Royal Astronomical Society*, 494(3):3799–3827, May 2020. .

J. Patterson. Rapid oscillations in cataclysmic variables. III. an oblique rotator in AE Aqr. *Astrophysical Journal*, 234:978–992, 12 1979. .

J. Patterson. Rapid oscillations in cataclysmic variables. IV. WZ Sagittae. *Astrophysical Journal*, 241: 235–246, 10 1980. .

J. Patterson, J. T. McGraw, L. Coleman, and J. L. Africano. A photometric study of the dwarf nova WZ SGE in outburst. *Astrophysical Journal*, 248:1067–1075, 09 1981. .

J. Patterson, H. Richman, J. Kemp, and K. Mukai. Rapid oscillations in cataclysmic variables. XIII. WZ sagittae revisited. *Publications of the Astronomical Society of the Pacific*, 110(746):403–414, 04 1998. .

J Patterson, G Masi, M.W. Richmond, B. Martin, E. Beshore, D.R. Skillman, J. Kemp, T. Vanmunster, R. Rea, W. Allen, S. Davis, T. Davis, A.A. Henden, D. Starkey, J. Foote, A. Oksanen, L.M. Cook, R.E. Fried, D. Husar, R. Novák, T. Campbell, J. Robertson, T. Krajci, E. Pavlenko, N. Mirabal, P.G. Niarchos, O. Brettman, and S. Walker. The 2001 superoutburst of WZ sagittae. *Publications of the Astronomical Society of the Pacific*, 114(797):721–747, 07 2002.

Joseph Patterson. The DQ Herculis Stars. *Publications of the Astronomical Society of the Pacific*, 106: 209, March 1994. .

Joseph Patterson. Accretion-Disk Precession and Substellar Secondaries in Cataclysmic Variables. *Publications of the Astronomical Society of the Pacific*, 113(784):736–747, June 2001. .

Joseph Patterson, Jonathan Kemp, David A. Harvey, Robert E. Fried, Robert Rea, Berto Monard, Lewis M. Cook, David R. Skillman, Tonny Vanmunster, Greg Bolt, Eve Armstrong, Jennie McCormick, Thomas Krajci, Lasse Jensen, Jerry Gunn, Neil Butterworth, Jerry Foote, Marc

Bos, Gianluca Masi, and Paul Warhurst. Superhumps in Cataclysmic Binaries. XXV. q_{crit}, epsilon(q), and Mass-Radius. *Publications of the Astronomical Society of the Pacific*, 117(837):1204–1222, November 2005. .

E. P. Pavlenko. Wz SGE Stars. *Odessa Astronomical Publications*, 20:168, January 2007.

K. J. Pearson, Keith Horne, and Warren Skidmore. Fireball models for flares in AE Aquarii. *Monthly Notices of the Royal Astronomical Society*, 338(4):1067–1083, February 2003. .

I. Pelisoli, T. R. Marsh, V. S. Dhillon, E. Breedt, A. J. Brown, M. J. Dyer, M. J. Green, P. Kerry, S. P. Littlefair, S. G. Parsons, D. I. Sahman, and J. F. Wild. Found: a rapidly spinning white dwarf in LAMOST J024048.51+195226.9. *Monthly Notices of the Royal Astronomical Society*, 509:L31–L36, January 2022. .

Geraldine J. Peters and Raphael Hirschi. The Evolution of High-Mass Stars. In Terry D. Oswalt and Martin A. Barstow, editors, *Planets, Stars and Stellar Systems. Volume 4: Stellar Structure and Evolution*, volume 4, page 447. 2013. .

G. Ponti, R. P. Fender, M. C. Begelman, R. J. H. Dunn, J. Neilsen, and M. Coriat. Ubiquitous equatorial accretion disc winds in black hole soft states. *Monthly Notices of the Royal Astronomical Society*, 422(1):L11–L15, May 2012. .

G. Ponti, S. Bianchi, T. Muñoz-Darias, K. De, R. Fender, and A. Merloni. High ionisation absorption in low mass X-ray binaries. *Astronomische Nachrichten*, 337(4-5):512–517, May 2016. .

Gabriele Ponti, Teodoro Muñoz-Darias, and Robert P. Fender. A connection between accretion state and Fe K absorption in an accreting neutron star: black hole-like soft-state winds? *Monthly Notices of the Royal Astronomical Society*, 444(2):1829–1834, October 2014. .

Joseph E Postma and Denis Leahy. CCDLAB: A graphical user interface FITS image data reducer, viewer, and canadian UVIT data pipeline. *Publications of the Astronomical Society of the Pacific*, 129(981):115002, oct 2017. . URL https://doi.org/10.1088/1538-3873/aa8800.

Stephen B. Potter, Encarni Romero-Colmenero, Marissa Kotze, Ewald Zietsman, O. W. Butters, Nikki Pekeur, and David A. H. Buckley. On the spin modulated circular polarization from the intermediate polars NY Lup and IGR J15094-6649. *Monthly Notices of the Royal Astronomical Society*, 420(3):2596–2602, March 2012. .

P. Pradhan, E. Bozzo, and B. Paul. Supergiant fast X-ray transients versus classical supergiant high mass X-ray binaries: Does the difference lie in the companion wind? *Astronomy and Astrophysics*, 610:A50, February 2018. .

Magaretha L. Pretorius, Christian Knigge, and Axel D. Schwope. The space density of magnetic cataclysmic variables. *Monthly Notices of the Royal Astronomical Society*, 432(1):570–583, June 2013. .

J. E. Pringle and M. J. Rees. Accretion Disc Models for Compact X-Ray Sources. *Astronomy and Astrophysics*, 21:1, October 1972.

G. Ramsay, M. J. Green, T. R. Marsh, T. Kupfer, E. Breedt, V. Korol, P. J. Groot, C. Knigge, G. Nelemans, D. Steeghs, P. Woudt, and A. Aungwerojwit. Physical properties of AM CVn stars: New insights from Gaia DR2. *Astronomy and Astrophysics*, 620:A141, December 2018. .

Ronald A. Remillard and Jeffrey E. McClintock. X-ray properties of black-hole binaries. *Annual Review of Astronomy and Astrophysics*, 44(1):49–92, 2006.

H. Ritter and R. Schroeder. The physical parameters of WZ Sge. II. Eclipse analysis. *Astronomy and Astrophysics*, 76:168–175, July 1979.

E. L. Robinson, R. E. Nather, and J. Patterson. A photometric study of the recurrent nova WZ Sagittae at minimum light. *Astrophysical Journal*, 219:168–182, 01 1978. .

M. M. Romanova, G. V. Ustyugova, A. V. Koldoba, and R. V. E. Lovelace. Magnetohydrodynamic Simulations of Disk-Magnetized Star Interactions in the Quiescent Regime: Funnel Flows and Angular Momentum Transport. *Astrophysical Journal*, 578(1):420–438, October 2002. .

M. M. Romanova, O. D. Toropina, Yu. M. Toropin, and R. V. E. Lovelace. Magnetohydrodynamic Simulations of Accretion onto a Star in the "Propeller" Regime. *Astrophysical Journal*, 588(1): 400–407, May 2003. .

Gustavo E. Romero, M. Boettcher, S. Markoff, and F. Tavecchio. Relativistic Jets in Active Galactic Nuclei and Microquasars. *Space Science Reviews*, 207(1-4):5–61, July 2017. .

S. R. Rosen, R. K. Prinja, J. E. Drew, K. O. Mason, and S. B. Howell. Phase-resolved Hubble Space Telescope ultraviolet spectroscopy of V795 HER. *Monthly Notices of the Royal Astronomical Society*, 299(2):305–318, September 1998. .

David M. Russell, Maria Cristina Baglio, and Fraser Lewis. MAXI J1820+070 is close to quiescence. *The Astronomer's Telegram*, 12534:1, February 2019.

Maurizio Salaris and Santi Cassisi. *Evolution of Stars and Stellar Populations*. 2005.

Edwin E. Salpeter. The Luminosity Function and Stellar Evolution. *Astrophysical Journal*, 121:161, January 1955. .

H. Sana, S. E. de Mink, A. de Koter, N. Langer, C. J. Evans, M. Gieles, E. Gosset, R. G. Izzard, J. B. Le Bouquin, and F. R. N. Schneider. Binary Interaction Dominates the Evolution of Massive Stars. *Science*, 337(6093):444, July 2012. .

J. Sánchez-Sierras and T. Muñoz-Darias. Near-infrared emission lines trace the state-independent accretion disc wind of the black hole transient MAXI J1820+070. *Astronomy and Astrophysics*, 640:L3, August 2020. .

Curtis J. Saxton, Kinwah Wu, Mark Cropper, and Gavin Ramsay. Two-temperature accretion flows in magnetic cataclysmic variables: structures of post-shock emission regions and X-ray spectroscopy. *Monthly Notices of the Royal Astronomical Society*, 360(3):1091–1104, July 2005. .

N. Scepi, G. Lesur, G. Dubus, and M. Flock. Impact of convection and resistivity on angular momentum transport in dwarf novae. *Astronomy and Astrophysics*, 609:A77, January 2018. .

K. Schenker, A. R. King, U. Kolb, G. A. Wynn, and Z. Zhang. AE Aquarii: how cataclysmic variables descend from supersoft binaries. *Monthly Notices of the Royal Astronomical Society*, 337 (3):1105–1112, December 2002. .

Edward F. Schlafly and Douglas P. Finkbeiner. Measuring Reddening with Sloan Digital Sky Survey Stellar Spectra and Recalibrating SFD. *Astrophysical Journal*, 737(2):103, August 2011. .

Jeremy D. Schnittman, Jeroen Homan, and Jon M. Miller. A Precessing Ring Model for Low-Frequency Quasi-periodic Oscillations. *Astrophysical Journal*, 642(1):420–426, May 2006. .

M. R. Schreiber, J. M. Hameury, and J. P. Lasota. Delays in dwarf novae I: The case of SS Cygni. *Astronomy and Astrophysics*, 410:239–252, October 2003. .

Matthias R. Schreiber, Diogo Belloni, Boris T. Gänsicke, Steven G. Parsons, and Monica Zorotovic. The origin and evolution of magnetic white dwarfs in close binary stars. *Nature Astronomy*, 5: 648–654, April 2021. .

R. Schwarz, A. D. Schwope, A. Staude, T. Urrutia, A. Rau, and G. Hasinger. RX J0524+42: A New Asynchronous Magnetic CV. In Sonja Vrielmann and Mark Cropper, editors, *IAU Colloq. 190: Magnetic Cataclysmic Variables*, volume 315 of *Astronomical Society of the Pacific Conference Series*, page 230, December 2004.

A. D. Schwope, D. A. H. Buckley, D. O'Donoghue, G. Hasinger, J. Truemper, and W. Voges. RX J2115.7-5840: a short-period, asynchronous polar. *Astronomy and Astrophysics*, 326:195–202, October 1997. .

N. I. Shakura and R. A. Sunyaev. Black holes in binary systems. observational appearance. *Astronomy and Astrophysics*, 24:337, 1973.

Toshiya Shimura and Fumio Takahara. Emission Spectrum Integrated over an Accretion Disk: Comparison with Observations of Active Galactic Nuclei. *Astrophysical Journal*, 440:610, February 1995. .

Frank Shu, Joan Najita, Eve Ostriker, Frank Wilkin, Steven Ruden, and Susana Lizano. Magneto-centrifugally Driven Flows from Young Stars and Disks. I. A Generalized Model. *Astrophysical Journal*, 429:781, July 1994. .

A. Silber, H. V. Bradt, M. Ishida, T. Ohashi, and R. A. Remillard. H0538+608 (= BY Camelopardalis): an Asynchronously Rotating AM Herculis Binary? *Astrophysical Journal*, 389: 704, April 1992. .

M. Sirk and R. Bohlin. *FOS Instrument Science Report CAL/FOS-026*, 1986.

Warren Skidmore, William F. Welsh, Janet H. Wood, M. S. Catalán, and Keith Horne. Analysis of the oscillations in HST observations of the quiescent SU UMa type dwarf nova WZ Sagittae. *Monthly Notices of the Royal Astronomical Society*, 310(3):750–758, December 1999. .

A. Skumanich. Time Scales for Ca II Emission Decay, Rotational Braking, and Lithium Depletion. *Astrophysical Journal*, 171:565, February 1972. .

J. Smak. WZ SGE as a Dwarf Nova. *Acta Astronomica*, 43:101–119, April 1993.

J. Smak. Unsolved problems of dwarf nova outbursts. *New Astronomy Review*, 44(1-2):171–175, 04 2000.

J. Smak. New Interpretation of Superhumps. *Acta Astronomica*, 59(1):121–130, March 2009a. .

J. Smak. On the Origin of Tilted Disks and Negative Superhumps. *Acta Astronomica*, 59(4):419–430, December 2009b. .

J. Smak. On the Critical Mass Ratio for the 3:1 Resonance in Accretion Disks. *Acta Astronomica*, 70 (4):313–315, December 2020. .

Jozef Smak and Elizabeth O. Waagen. The 1985 Superoutburst of U Geminorum. Detection of Superhumps. *Acta Astronomica*, 54:433–442, December 2004.

J. E. Solheim. AM CVn Stars: Status and Challenges. *Publications of the Astronomical Society of the Pacific*, 122(896):1133, October 2010. .

H. C. Spruit and R. G. M. Rutten. The stream impact region in the disc of WZ SGE. *Monthly Notices of the Royal Astronomical Society*, 299(3):768–776, September 1998. .

D. Steeghs, T. Marsh, C. Knigge, P. F. L. Maxted, E. Kuulkers, and W. Skidmore. Emission from the secondary star in the old cataclysmic variable WZ sagittae. *Astrophysical Journal*, 562(2): L145–L148, 12 2001.

Danny Steeghs, Steve B. Howell, Christian Knigge, Boris T. Gänsicke, Edward M. Sion, and William F. Welsh. Dynamical constraints on the component masses of the cataclysmic variable WZ sagittae. *Astrophysical Journal*, 667(1):442–447, 09 2007. .

Luigi Stella and Mario Vietri. Lense-Thirring Precession and Quasi-periodic Oscillations in Low-Mass X-Ray Binaries. *Astrophysical Journal, Letters*, 492(1):L59–L62, January 1998. .

Luigi Stella, Mario Vietri, and Sharon M. Morsink. Correlations in the Quasi-periodic Oscillation Frequencies of Low-Mass X-Ray Binaries and the Relativistic Precession Model. *Astrophysical Journal, Letters*, 524(1):L63–L66, October 1999. .

H. Stiele and A. K. H. Kong. A Timing Study of MAXI J1820+070 Based on Swift/XRT and NICER Monitoring in 2018/19. *Astrophysical Journal*, 889(2):142, February 2020. .

H. S. Stockman, Gary D. Schmidt, and D. Q. Lamb. V1500 Cygni: Discovery of a Magnetic Nova. *Astrophysical Journal*, 332:282, September 1988. .

D. P. Summons, P. Arévalo, I. M. McHardy, P. Uttley, and A. Bhaskar. Timing evidence in determining the accretion state of the Seyfert galaxy NGC 3783. *Monthly Notices of the Royal Astronomical Society*, 378(2):649–656, June 2007. .

R. A. Syunyaev and N. I. Shakura. Disk reservoirs in binary systems and prospects for observing them. *Soviet Astronomy Letters*, 3:138–141, June 1977.

Paula Szkody, Meagan Albright, Albert P. Linnell, Mark E. Everett, Russet McMillan, Gabrelle Saurage, Joseph Huehnerhoff, Steve B. Howell, Mike Simonsen, and Nick Hunt-Walker. A Study of the Unusual Z Cam Systems IW Andromedae and V513 Cassiopeia. *Publications of the Astronomical Society of the Pacific*, 125(934):1421, December 2013. .

Ronald E. Taam and Eric L. Sandquist. Common Envelope Evolution of Massive Binary Stars. *Annual Review of Astronomy and Astrophysics*, 38:113–141, January 2000. .

M. Tagger and R. Pellat. An accretion-ejection instability in magnetized disks. *Astronomy and Astrophysics*, 349:1003–1016, September 1999. .

SN Tandon, Annapurni Subramaniam, V Girish, J Postma, K Sankarasubramanian, S Sriram, CS Stalin, Chayan Mondal, S Sahu, P Joseph, et al. In-orbit calibrations of the ultraviolet imaging telescope. *The Astronomical Journal*, 154(3):128, 2017.

SN Tandon, J Postma, P Joseph, A Devaraj, A Subramaniam, IV Barve, K George, SK Ghosh, V Girish, JB Hutchings, et al. Additional calibration of the ultraviolet imaging telescope on board astrosat. *The Astronomical Journal*, 159(4):158, 2020.

A. J. Tetarenko, G. Petitpas, G. R. Sivakoff, J. C. A. Miller-Jones, T. D. Russell, G. Schieven, and Jacpot Xrb Collaboration. (Sub)-millimetre Observations of MAXI J1820+070 (ASASSN-18ey) Suggest Jet Quenching on July 6. *The Astronomer's Telegram*, 11831:1, July 2018a.

A. J. Tetarenko, P. Casella, J. C. A. Miller-Jones, G. R. Sivakoff, J. A. Paice, F. M. Vincentelli, T. J. Maccarone, P. Gandhi, V. S. Dhillon, T. R. Marsh, T. D. Russell, and P. Uttley. Measuring fundamental jet properties with multiwavelength fast timing of the black hole X-ray binary MAXI J1820+070. *Monthly Notices of the Royal Astronomical Society*, 504(3):3862–3883, July 2021a. .

B. E. Tetarenko, G. Dubus, J. P. Lasota, C. O. Heinke, and G. R. Sivakoff. Understanding X-ray irradiation in low-mass X-ray binaries directly from their light-curves. *Monthly Notices of the Royal Astronomical Society*, 480(1):2–16, October 2018b. .

B. E. Tetarenko, J. P. Lasota, C. O. Heinke, G. Dubus, and G. R. Sivakoff. Strong disk winds traced throughout outbursts in black-hole X-ray binaries. *Nature*, 554(7690):69–72, February 2018c. .

B. E. Tetarenko, A. W. Shaw, E. R. Manrow, P. A. Charles, J. M. Miller, T. D. Russell, and A. J. Tetarenko. Using optical spectroscopy to map the geometry and structure of the irradiated

accretion discs in low-mass X-ray binaries: the pilot study of MAXI J0637-430. *Monthly Notices of the Royal Astronomical Society*, 501(3):3406–3420, March 2021b. .

Jessymol K. Thomas, David A. H. Buckley, Philip A. Charles, John A. Paice, Stephen B. Potter, James F. Steiner, Jean-Pierre Lasota, P. Gandhi, Lian Tao, Xiang Ma, Yi-Jung Yang, Youli Tuo, and Shuang-Nan Zhang. Synchronous X-ray/optical quasi-periodic oscillations from the black hole LMXB MAXI J1820+070. *Monthly Notices of the Royal Astronomical Society*, 513(1):L35–L39, June 2022. .

Lev Titarchuk and Ralph Fiorito. Spectral Index and Quasi-Periodic Oscillation Frequency Correlation in Black Hole Sources: Observational Evidence of Two Phases and Phase Transition in Black Holes. *Astrophysical Journal*, 612(2):988–999, September 2004. .

M. A. P. Torres, J. Casares, F. Jiménez-Ibarra, A. Álvarez-Hernández, T. Muñoz-Darias, M. Armas Padilla, P. G. Jonker, and M. Heida. The Binary Mass Ratio in the Black Hole Transient MAXI J1820+070. *Astrophysical Journal, Letters*, 893(2):L37, April 2020. .

M. A. Tucker, B. J. Shappee, T. W. S. Holoien, K. Auchettl, J. Strader, K. Z. Stanek, C. S. Kochanek, A. Bahramian, ASAS-SN, Subo Dong, J. L. Prieto, J. Shields, Todd A. Thompson, John F. Beacom, L. Chomiuk, ATLAS, L. Denneau, H. Flewelling, A. N. Heinze, K. W. Smith, B. Stalder, J. L. Tonry, H. Weiland, A. Rest, M. E. Huber, D. M. Rowan, and K. Dage. ASASSN-18ey: The Rise of a New Black Hole X-Ray Binary. *Astrophysical Journal, Letters*, 867(1):L9, November 2018. .

Makoto Uemura, Taichi Kato, Tomohito Ohshima, and Hiroyuki Maehara. Reconstruction of the Structure of Accretion Disks in Dwarf Novae from the Multi-Band Light Curves of Early Superhumps. *Publications of the Astronomical Society of Japan*, 64:92, October 2012. .

E. P. J. Van Den Heuvel. Late stages of close binary systems. *Symposium - International Astronomical Union*, 73:35–61, 1976. .

Edward P. J. van den Heuvel. High-Mass X-ray Binaries: progenitors of double compact objects. In Lidia M. Oskinova, Enrico Bozzo, Tomasz Bulik, and Douglas R. Gies, editors, *High-mass X-ray Binaries: Illuminating the Passage from Massive Binaries to Merging Compact Objects*, volume 346 of *IAU Symposium*, pages 1–13, December 2019. .

M. van der Klis. Fourier techniques in X-ray timing. In H. Ögelman and E. P. J. van den Heuvel, editors, *Timing Neutron Stars*, volume 262 of *NATO Advanced Study Institute (ASI) Series C*, page 27, January 1989.

M. van der Klis. Kilohertz Quasi-Periodic Oscillations in Low-Mass X-Ray Binaries. In D. Maoz, A. Sternberg, and E. M. Leibowitz, editors, *Astronomical Time Series*, volume 218 of *Astrophysics and Space Science Library*, page 121, January 1997.

J. van Paradijs. On the Accretion Instability in Soft X-Ray Transients. *Astrophysical Journal, Letters*, 464:L139, June 1996. .

J. van Paradijs and J. E. McClintock. Absolute visual magnitudes of low-mass X-ray binaries. *Astronomy and Astrophysics*, 290:133–136, October 1994.

P. Varnière, J. Rodriguez, and M. Tagger. Accretion-ejection instability and QPO in black-hole binaries. II. Relativistic effects. *Astronomy and Astrophysics*, 387:497–506, May 2002. .

P. Varnière, M. Tagger, and J. Rodriguez. A possible interpretation for the apparent differences in LFQPO types in microquasars. *Astronomy and Astrophysics*, 545:A40, September 2012. .

S. Vaughan. A simple test for periodic signals in red noise. *Astronomy and Astrophysics*, 431:391–403, February 2005. .

S. Vaughan, R. Edelson, R. S. Warwick, and P. Uttley. On characterizing the variability properties of X-ray light curves from active galaxies. *Monthly Notices of the Royal Astronomical Society*, 345 (4):1271–1284, November 2003. .

Alexandra Veledina and Juri Poutanen. Reprocessing model for the optical quasi-periodic oscillations in black hole binaries. *Monthly Notices of the Royal Astronomical Society*, 448(1):939–945, March 2015. .

Alexandra Veledina, Juri Poutanen, and Indrek Vurm. Hot accretion flow in black hole binaries: a link connecting X-rays to the infrared. *Monthly Notices of the Royal Astronomical Society*, 430(4): 3196–3212, April 2013. .

J. Vernet, H. Dekker, S. D'Odorico, L. Kaper, P. Kjaergaard, F. Hammer, S. Randich, F. Zerbi, P. J. Groot, J. Hjorth, I. Guinouard, R. Navarro, T. Adolfse, P. W. Albers, J. P. Amans, J. J. Andersen, M. I. Andersen, P. Binetruy, P. Bristow, R. Castillo, F. Chemla, L. Christensen, P. Conconi, R. Conzelmann, J. Dam, V. de Caprio, A. de Ugarte Postigo, B. Delabre, P. di Marcantonio, M. Downing, E. Elswijk, G. Finger, G. Fischer, H. Flores, P. François, P. Goldoni, L. Guglielmi, R. Haigron, H. Hanenburg, I. Hendriks, M. Horrobin, D. Horville, N. C. Jessen, F. Kerber, L. Kern, M. Kiekebusch, P. Kleszcz, J. Klougart, J. Kragt, H. H. Larsen, J. L. Lizon, C. Lucuix, V. Mainieri, R. Manuputy, C. Martayan, E. Mason, R. Mazzoleni, N. Michaelsen, A. Modigliani, S. Moehler, P. Møller, A. Norup Sørensen, P. Nørregaard, C. Péroux, F. Patat, E. Pena, J. Pragt, C. Reinero, F. Rigal, M. Riva, R. Roelfsema, F. Royer, G. Sacco, P. Santin, T. Schoenmaker, P. Spano, E. Sweers, R. Ter Horst, M. Tintori, N. Tromp, P. van Dael, H. van der Vliet, L. Venema, M. Vidali, J. Vinther, P. Vola, R. Winters, D. Wistisen, G. Wulterkens, and A. Zacchei. X-shooter, the new wide band intermediate resolution spectrograph at the ESO Very Large Telescope. *Astronomy and Astrophysics*, 536:A105, December 2011. .

Vojtěch Šimon. The Long-term Activity of the Postnovae Q Cygni and BK Lyncis. *Astronomical Journal*, 167(4):152, April 2024. .

B. Warner. *Cataclysmic Variable Stars*. 2003.

B. Warner, M. Livio, and C. A. Tout. Dwarf nova outbursts in truncated accretion discs: down with low alphas. *Monthly Notices of the Royal Astronomical Society*, 282(3):735–738, 10 1996.

Brian Warner and Magaretha L. Pretorius. Dwarf nova oscillations and quasi-periodic oscillations in cataclysmic variables - VI. Spin rates, propellering and coherence. *Monthly Notices of the Royal Astronomical Society*, 383(4):1469–1476, February 2008. .

R. F. Webbink. Double white dwarfs as progenitors of R Coronae Borealis stars and type I supernovae. *Astrophysical Journal*, 277:355–360, February 1984. .

William F. Welsh, Keith Horne, and Richard Gomer. A study of the absorption lines from the donor star in the exotic cataclysmic variable AE Aquarii. *Monthly Notices of the Royal Astronomical Society*, 275(3):649–670, August 1995. .

William F. Welsh, Keith Horne, and Richard Gomer. Doppler signatures of Hα flares in AE Aquarii. *Monthly Notices of the Royal Astronomical Society*, 298(1):285–302, July 1998. .

Robert Whitehurst. Numerical simulations of accretion discs - I. Superhumps : a tidal phenomenon of accretion discs. *Monthly Notices of the Royal Astronomical Society*, 232:35–51, May 1988. .

D. T. Wickramasinghe, Kinwah Wu, and Lilia Ferrario. Intermediate polars as low-field magnetic cataclysmic variables. *Monthly Notices of the Royal Astronomical Society*, 249:460–467, April 1991. .

C. M. Wood, J. C. A. Miller-Jones, J. Homan, J. S. Bright, S. E. Motta, R. P. Fender, S. Markoff, T. M. Belloni, E. G. Körding, D. Maitra, S. Migliari, D. M. Russell, T. D. Russell, C. L. Sarazin, R. Soria, A. J. Tetarenko, and V. Tudose. The varying kinematics of multiple ejecta from the black hole X-ray binary MAXI J1820 + 070. *Monthly Notices of the Royal Astronomical Society*, 505 (3):3393–3403, August 2021. .

B. E. Woodgate, R. A. Kimble, C. W. Bowers, S. Kraemer, M. E. Kaiser, A. C. Danks, J. F. Grady, J. J. Loiacono, M. Brumfield, L. Feinberg, T. R. Gull, S. R. Heap, S. P. Maran, D. Lindler, D. Hood, W. Meyer, C. Vanhouten, V. Argabright, S. Franka, R. Bybee, D. Dorn, M. Bottema, R. Woodruff, D. Michika, J. Sullivan, J. Hetlinger, C. Ludtke, R. Stocker, A. Delamere, D. Rose, I. Becker, H. Garner, J. G. Timothy, M. Blouke, C. L. Joseph, G. Hartig, R. F. Green, E. B. Jenkins, J. L. Linsky, J. B. Hutchings, H. W. Moos, A. Boggess, F. Roesler, and D. Weistrop. The Space Telescope Imaging Spectrograph Design. *Publications of the Astronomical Society of the Pacific*, 110 (752):1183–1204, October 1998. .

Kinwah Wu. Accretion onto Magnetic White Dwarfs. *Space Science Reviews*, 93:611–649, August 2000. .

Kinwah Wu, G. Chanmugam, and G. Shaviv. Structure of Steady State Accretion Shocks with Several Cooling Functions: Closed Integral-Form Solution. *Astrophysical Journal*, 426:664, May 1994. .

G. A. Wynn and A. R. King. Diamagnetic accretion in intermediate polars - I. Blob orbits and spin evolution. *Monthly Notices of the Royal Astronomical Society*, 275(1):9–21, 07 1995. .

G. A. Wynn, A. R. King, and K. Horne. A magnetic propeller in the cataclysmic variable AE Aquarii. *Monthly Notices of the Royal Astronomical Society*, 286(2):436–446, 04 1997. .

Tomohiro Yoshitake, Megumi Shidatsu, Yoshihiro Ueda, Shin Mineshige, Katsuhiro L. Murata, Ryo Adachi, Hiroyuki Maehara, Daisaku Nogami, Hitoshi Negoro, Nobuyuki Kawai, Masafumi Niwano, Ryohei Hosokawa, Tomoki Saito, Yumiko Oasa, Takuya Takarada, Takumi Shigeyoshi, and Oister Collaboration. Multiwavelength observations of the black hole X-ray binary MAXI J1820+070 in the rebrightening phase. *Publications of the Astronomical Society of Japan*, 74(4):805–814, August 2022. .

Wenfei Yu, Jie Lin, Dongming Mao, Jujia Zhang, Zhen Yan, and Jinming Bai. Further detection of the optical low frequency QPO in the black hole transient MAXI J1820+070. *The Astronomer's Telegram*, 11591:1, May 2018a.

Wenfei Yu, Jujia Zhang, Zhen Yan, Xiaofeng Wang, and Jinming Bai. Detection of optical and X-ray QPOs at similar frequencies in MAXI J1820+070. *The Astronomer's Telegram*, 11510:1, April 2018b.

Luca Zampieri, Michele Fiori, Aleksandr Burtovoi, Giampiero Naletto, Cesare Barbieri, Paolo Ochner, Gabriele Umbriaco, and Mauro Barbieri. Low-frequency optical QPO in MAXI J1820+070 detected with IFI+IQUEYE@Galileo. *The Astronomer's Telegram*, 11723:1, June 2018.

C. Zanni and J. Ferreira. MHD simulations of accretion onto a dipolar magnetosphere. II. Magnetospheric ejections and stellar spin-down. *Astronomy and Astrophysics*, 550:A99, February 2013. .

A. A. Zdziarski and M. Gierliński. Radiative Processes, Spectral States and Variability of Black-Hole Binaries. *Progress of Theoretical Physics Supplement*, 155:99–119, January 2004. .

Xueshan Zhao, Lijun Gou, Yanting Dong, Youli Tuo, Zhenxuan Liao, Yufeng Li, Nan Jia, Ye Feng, and James F. Steiner. Estimating the Black Hole Spin for the X-Ray Binary MAXI J1820+070. *Astrophysical Journal*, 916(2):108, August 2021. .